Physical and Practical Limits of A Biomolecular Control System Using Nanoparticles and Electromagnetic Field Irradiation

by

Joshua Daniel Alper

B.S., University of Rochester (1999)
M.Eng., Tufts University (2002)

Submitted to the Department of Mechanical Engineering
in partial fulfillment of the requirements for the degree of

Doctor of Philosophy

at the

MASSACHUSETTS INSTITUTE OF TECHNOLOGY

February 2010

Author .....
Department of Mechanical Engineering
December 21, 2009

Certified by .....
Kimberly Hamad-Schifferli
Esther and Harold E. Edgerton Assistant Professor of Mechanical Engineering and Biological Engineering
Thesis Supervisor

Accepted by .....
David E. Hardt
Chairman, Department Committee on Graduate Theses

Physical and Practical Limits of A Biomolecular Control System Using Nanoparticles and Electromagnetic Field Irradiation

by

Joshua Daniel Alper

Submitted to the Department of Mechanical Engineering
on December 21, 2009, in partial fulfillment of the
requirements for the degree of
Doctor of Philosophy

Abstract

Many nanometer length scale engineering applications of mechanics and biology including computation, sensing, self-assembly, transport, and molecular machine design take advantage of natural biomolecular machinery. Further development of these technologies requires direct, external biomolecular control. This thesis proposes a simple control technique: a biomolecular "on/off" activity switch in which metallic nanoparticles (NPs) are conjugated to target biomolecules and irradiated with an electromagnetic field. Due to their unique physical properties, the NPs specifically absorb the field's energy. They convert the energy to heat, and then they transport it to the conjugated target biomolecules. The heat affects a change in the targeted biomolecules, selectively actuating their activity.

This thesis is on the mechanisms by which both ultrafast pulsed laser irradiation and radio frequency alternating magnetic fields (RFMFs) can be used as energy sources for the proposed biomolecular activity switch. The thesis reports on the quantification of a fs-pulsed laser triggered release mechanism that actuates activity of the molecules released from NPs. The release mechanism is governed by NP surface chemistry. The operating window for the critical parameters governing release including NP properties and laser fluence is defined. The thesis also reports on transmission pump-probe experiments that show the thermal interface conductance (G) of NPs is critical to nanoscale thermal transport, and that G is a strong function of the NP's surface chemistry. The thesis concludes that an ultrafast pulsed laser actuated biomolecular activity switch is feasible if the critical parameters are carefully controlled. However, experimental studies revealed that using RFMFs in this biomolecular activity switching technique is not feasible. These results are validated by theoretical and analytical studies of nanoscale heat generation and transport in the system.

The results presented in this thesis have implications on the design of the biomolecular activity switch, and many of the results are also applicable to other nanoscale

thermal applications including hyperthermia cancer treatments and triggered drug delivery techniques.

Thesis Supervisor: Kimberly Hamad-Schifferli
Title: Esther and Harold E. Edgerton Assistant Professor of Mechanical Engineering and Biological Engineering

Acknowledgments

My colleagues at MIT, my friends, and my family have made my time in graduate school a rewarding and fun experience. I would like to thank everyone how has contributed positively to my experience.

First, I would like to thank my thesis advisor Professor Kimberly Hamad-Schifferli. From the moment she invited me to join the lab she has allowed me to pursue my own scientific direction. Her guidance and advice through out has been helpful. I have learned so much about being a scientific researcher, a teacher, a manager, and a mentor from her. For all these reasons and more, I am grateful to her.

I would also like thank my thesis committee for their advice. Just when it seemed no progress was even possible, they would come up with a suggestion that would redirect me toward a successful path. Thank you Andrei Tokmakoff and Matt Lang. They have both been very supportive of my work over the years.

None of the work done in this thesis was done in a vacuum. Too many people have helped me along way to acknowledge them all. I would like to thank all the past and current members of the Hamad-Schifferli lab for their scientific support and camaraderie. Kate, Victor, and Shahriar made the countless hours in the lab so much more enjoyable. Once they had all moved on, the music both literally and figuratively left 56-354. I would also like to thank all of the undergraduates I had to opportunity to work with. Monica, Katie, Pablo, Sana, Alex and Jess contributed so much effort to this work. I am indebted to them all.

My collaborators at MIT really enabled me to perform this research. I would like to thank Lauren DeFlores, Kevin Jones, and Andrei Tokmakoff from the Tokmakoff lab in the Chemistry Department at MIT. Without them helping me and being so accommodating, I never would have been able to get this thesis done. I am so grateful to them for their generosity. I would also like to thank Aaron Schmidt, Mateo Chisea, Kimberlee Collins and Gang Chen from the Chen lab in the Mechanical Engineering Department at MIT. Again, their help was instrumental in getting the results for this thesis.

I'd also like to thank the people who run the shared facilities at MIT. The Biophysical Instrumentation Facility for the Study of Complex Macromolecular Systems (NSF-0070319 and NIH GM68762) is gratefully acknowledged. In particular I'd like to thank Debby Pheasant for all her help with many of the instruments in the BIF. The Edgerton Center Student Shop filled a huge gap in my education as a mechanical engineer and taught me to use the lathe, mill, and other machine shop tools. The Shared Experimental Facilities (SEFs) in the The Center for Materials Science and Engineering, especially Yong Zhang, Shaoyan Chu, and Libby Shaw. One of MIT's greatest strengths is its facilities and the people who run them. Without access to the state of the art equipment, and without expert training, I would have gotten no reasonable results.

Beyond the thesis work, I would like to specifically thank a few others at MIT. Jeff and Erin helped get me through many of the courses I took, and they were excellent study partners for the qualification exam. Without them pushing me, I am not sure I would have been able to study hard enough. But beyond that, their keen intelligence and their perspective, often so different from my own, really enabled me learn mechanical engineering better than I ever could have on my own. Thank you to Roger Kamm, Al Grodzinsky, Carol Livermore, and all the other instructors and TAs I worked with as a teaching assistant. It was a great learning experience observing such great teaching from the inside. I hope to use much of what I learned from them someday as a faculty member myself.

I'd like to thank my network of friends outside of MIT. Even graduate students need to have a little fun outside the lab. Brendan and Charles in particular provided the encouragement I often needed to relax – something that I found was difficult to do without a driving force. It is so easy to get sucked into work. My fiends did a great job of making sure I was able to get away from it all, even if just for a couple hours at a time.

Finally, and most importantly, I thank my family. My wife, Gretchen, has been unbelievably supportive through out my 5 years at MIT. She has sacrificed much, and done everything she possibly could, to enable my success in graduate school. She

has truly been a partner with me in this. I love her, and I am immensely indebted to her for all that she has done. I look forward to sharing the fruits of our labor in the decades to come. Our parents have been very supportive and understanding through out the entire process. They have been particularly great with the grandchildren. Zach and Zoë are just about the perfect children, and I thank them for being so understanding about letting Daddy go to school. I do not know how anyone gets through graduate school without the loving support of a family as great as mine. I love them so much and thank graciously them for everything.

Contents

1 Introduction **23**

1.1 Motivation : Why biomolecular control? 23

1.2 State of the art biomolecular control systems 25

1.2.1 Chemical 27

1.2.2 Electronic interfaces 28

1.2.3 Direct thermal 29

1.2.4 Photoactivated 31

1.2.5 Mechanical interactions 33

1.3 Hallmarks of effective control system 33

1.3.1 External actuation 34

1.3.2 Specific 34

1.3.3 Reversible 35

1.4 The biomolecular control system: a biomolecular activity switch . . . 36

1.4.1 Nanoparticles 37

1.4.2 The field 37

1.4.3 Conjugation 37

1.4.4 The biomolecule 40

1.4.5 Local thermal confinement 41

1.4.6 Model of control as a reaction 43

1.4.7 Biomolecular control system efficiency 44

1.4.8 A robust biomolecular control system 45

1.5 Specific biomolecular control system strategies 46

1.5.1 Denaturation of attached protein 46
1.5.2 Separation of multi-part systems 47
1.5.3 Inhabitation of active site and release 49
1.6 This thesis 50

2 Magnetic field heating **51**
2.1 Magnetic nanoparticles 51
2.2 Analysis of heating mechanisms 54
2.2.1 Hysteresis 54
2.2.2 Néel relaxation 55
2.2.3 Brownian relaxation 57
2.2.4 Power 57
2.3 Our setup 58
2.3.1 Current generating equipment 60
2.3.2 Coils 61
2.3.3 Shielding 68
2.3.4 Transmission line effects 69
2.4 Global heating of ferrofluids 72
2.5 Local heating of magnetic nanoparticles 77
2.5.1 Theoretical analytical temperature profiles in magnetic field heating 77
2.5.2 Magnetoferritin experiments 79
2.5.3 Discussion of local heating using magnetic fields 85

3 Laser mediated control **89**
3.1 Optically active NPs 90
3.1.1 Gold nanoparticles 90
3.1.2 Gold nanorods 91
3.1.3 The “optical window” 92
3.1.4 Mie/Gans theory 93
3.1.5 Synthesis techniques 95

3.1.6 Ligands . . . 97
3.1.7 Characterization Techniques . . . 104
3.1.8 Analysis of limits on NR AR . . . 112
3.1.9 Analysis on the effect of NR polydispersity . . . 113
3.2 Analysis of heating mechanisms . . . 114
3.2.1 Photon-electron thermalization . . . 114
3.2.2 Electron-phonon thermalization . . . 114
3.2.3 Phonon-phonon thermalization . . . 115
3.3 Finite element analysis of NR heating . . . 115
3.4 Temperature as a function of space and time . . . 117
3.4.1 Analysis of pulse length . . . 119
3.4.2 Multiple pulses . . . 121
3.5 The laser setup . . . 123
3.5.1 Femtosecond laser . . . 123
3.5.2 Pump-probe system . . . 123
3.6 Thermal properties of NR ligands . . . 125
3.6.1 NR synthesis . . . 126
3.6.2 NR characterization . . . 127
3.6.3 Transient absorption procedure . . . 131
3.6.4 Results and discussion . . . 132
3.6.5 Conclusions . . . 141
3.7 Global heating effects . . . 142
3.8 Local heating effects . . . 143
3.8.1 Nanorod melting . . . 143
3.8.2 The effect of NR concentration . . . 146

4 Proof of concept using the release strategy : operating window and mechanism description 149

4.1 Experimental plan . . . 150
4.2 Materials and methods . . . 152

4.2.1 NR synthesis . . . 152
4.2.2 NR characterization . . . 152
4.2.3 R_{18} loading of NRs . . . 152
4.2.4 Laser induced release . . . 153
4.2.5 Laser accelerated loading . . . 153
4.2.6 Water bath induced release . . . 153
4.2.7 Water bath accelerated loading . . . 153
4.2.8 Fluorescence spectroscopy . . . 154
4.2.9 Coverage of NRs . . . 155
4.3 Results and discussion . . . 155
4.3.1 Characterization of NRs . . . 155
4.3.2 Pulsed laser irradiation accelerates R_{18} release . . . 157
4.3.3 Controls on the release of R_{18} . . . 160
4.3.4 Exchange Mechanism . . . 164
4.3.5 CTAB influences the binding and release of R_{18} . . . 167
4.3.6 Bulk heating accelerates R_{18} release and binding . . . 167
4.3.7 Pulsed laser irradiation accelerates R_{18} binding . . . 168
4.3.8 Excess CTAB inhibits laser induced R_{18} binding . . . 168
4.3.9 NR melting correlates to the upper limits of laser accelerated release . . . 171
4.4 Summary and broader impact of the proof of concept experiment . . . 172

5 Conclusions and future considerations 173

5.1 Major conclusions . . . 174
5.1.1 The biomolecular switch is feasable . . . 174
5.1.2 Limits on the electromagnetic field . . . 174
5.1.3 Limits on the nanoparticle . . . 176
5.1.4 Limits on the conjugation . . . 178
5.1.5 Limits on the biomolecule . . . 180
5.2 Broader implications . . . 181

5.3 Future considerations 181
5.3.1 Near term "enabling" studies key to achieving external biomolecular control 181
5.3.2 Near term demonstration of biomolecular switch with a biological target 182
5.3.3 The potential of this biomolecular control mechanism 186

A Symbols and acronyms **189**

List of Figures

1-1 State of the art biomolecular control systems 26
1-2 Example from literature of chemical control of ATP hydrolysis 28
1-3 Demonstration of direct thermal control over actin filament sliding . . 30
1-4 Demonstration of photoactivated bistable photoswitch actuating RNAse S activity 32
1-5 Specificity analogy to archery 35
1-6 Schematic of biomolecular activity switch 36
1-7 Example typical biomoleculenanoparticle conjugation chemistries . . . 38
1-8 Required energy delivery duration as a function of desired local thermal confinement area 41
1-9 Local thermal confinement analogy to filling a bucket with water . . . 42
1-10 Energy landscape of the biomolecular switch as a simple chemical reaction 43
1-11 Schematic of local denaturation strategy 47
1-12 Schematic of two part separation strategy 48
1-13 Schematic of release strategy 49

2-1 TEM analysis of magentite nanofluid 52
2-2 Crystal structure of ferritin 53
2-3 Magnetic hysteresis loop of a ferromagnetic material. 55
2-4 Schematic demonstrating the difference between Néel and Brownian relaxation. 56
2-5 Frequency dependency of effective magnetic relaxation time constant 59
2-6 Schematic of RFMF generating apparatus 59

2-7 H field in and around a coil 62
2-8 Results of coil cooling 63
2-9 Standard CD curves of secondary structure 64
2-10 Schematic for the CD cuvette. 64
2-11 Diagram of CD sample within the coil. 65
2-12 Photograph of the customized CD sample drawer with coil 66
2-13 Schematic of the light path of a fluorometer. 67
2-14 Schematic of a generic transmission line circuit. 70
2-15 Schematic of the model of a RFMF producing coil as determined from an impedance analyzer. 70
2-16 VNA output for the coil in the CD drawer. 71
2-17 Simulation of current in the coil accounting for transmission line effects 72
2-18 Schematic diagram of the heat flux in a global heating experiment. . 73
2-19 Plot of the mean particle spacing as a function of concentration. . . . 74
2-20 Global heating of EMG507 75
2-21 Power output per particle of EMG 507 ferrofluids near an impedance matched frequency. 76
2-22 Schematic of magnetoferritin synthesis procedure. 80
2-23 Effects of temperature on CD spectra of ferritin. 82
2-24 XPS spectra of various iron compounds. 83
2-25 XPS spectra of synthesized NPs 83
2-26 SQUID data of synthesized NPs 84
2-27 Local heating results for Magnetoferritin. 85

3-1 The “optical window.” 92
3-2 Calculated absorption spectra of gold NRs using Gans theory 94
3-3 The effect of silver in NR synthesis 98
3-4 Hexadecyltrimethylammonium bromide (CTAB) 99
3-5 CTAB micelle schematic 100
3-6 Mercaptohexanoic acid (MHA), carbon chain length = 6 carbons . . . 101

3-7 Mercaptoundecanoic acid (MUDA), carbon chain length = 11 carbons 101
3-8 Mercaptohexadecanoic acid (MHDA), carbon chain length = 16 carbons 101
3-9 Methyl-polyethylene glycol-thiol (mPEG-Thiol) 102
3-10 Polyelectrolytes for coating NRs, PSS and PDADMAC 104
3-11 Typical TEM of NRs 105
3-12 Simulated vs measured absorption spectra of NRs 107
3-13 Simulated absorption spectra of NR samples of various polydispersity 108
3-14 Absorption spectrum of MCA coated NRs 108
3-15 Longitudinal SPR of MCA-NRs a function of the length of the alkyl chain. 109
3-16 Ferguson plots for the gel calibration size standards 111
3-17 Schematic of NR vibration modes 115
3-18 NR finite element model 117
3-19 Temperature field around NR after laser 118
3-20 Temperature as a function of r at multiple times after irradiation by a 100 fs laser pulse. 119
3-21 FEA results on the laser pulse length 120
3-22 Relative peak temperatures of NR and protein with varying pulse length 121
3-23 FEA results on the laser pulse train 122
3-24 Pump-probe system. 124
3-25 Characterization of NRs for CTAB thermal interface conductance experiments 127
3-26 Characterization of NRs for MCA, PEG and polyelectrolyte thermal interface conductance experiments 128
3-27 Typical distribution of NR aspect ratios, lengths, and diameters . . . 129
3-28 Size of gold nanorods by Ferguson plot analysis. 130
3-29 Transient absorption spectra of CTAB-NRs 133
3-30 Transient absorption of CTAB-NRs in 50 mM CTAB and the best fit model of thermal dissipation 134

3-31 Transient absorption of CTAB-NRs in 5 mM CTAB and the best fit model of thermal dissipation 134
3-32 Transient absorption of CTAB-NRs in 1 mM CTAB and the best fit model of thermal dissipation 135
3-33 Transient absorption spectra for MCA-NRs 136
3-34 Transient absorption spectra for PEG-NRs 137
3-35 Transient absorption spectra for polyelectrolyte-NRs 137
3-36 Transient absorption of PEG-NRs and polyelectrolyte-NRs, and the best fit model of thermal dissipation 138
3-37 Thermal interface conductance and SPR wavelength in relation to CTAB concentration 141
3-38 Global heating experiment results on NRs 143
3-39 Effect of bulk heating a NR sample on their absorption spectra 144
3-40 Absorption of melted NRs 145
3-41 TEM of NR melting 145
3-42 Effect of concentration on biomolecular switch specificity 146

4-1 Schematic of R_{18} release 151
4-2 R_{18} Fluorescence intensity calibration curve 154
4-3 TEM of NRs for proof of the release strategy 155
4-4 Characterization of NRs for proof of the release strategy 156
4-5 R_{18} coverage assay example data 157
4-6 Release of R_{18} from NRs 158
4-7 Release rate of R_{18} from NRs 159
4-8 Additional example data (see figure 4-6) from release of R_{18} from NRs 161
4-9 Control for bulk heating due to the laser. 162
4-10 Absorption spectrum of R_{18}. 163
4-11 Fluorescence intensity of R_{18} in 10 mM CTAB after 10 minutes of laser irradiation. 164

4-12 Fluorescence intensity of R_{18} in the supernatant after release from small aspect ratio NRs. 165
4-13 Fluorescence intensity of R_{18} as a function of CTAB concentration . . 165
4-14 Induced release and binding of R_{18} when heated in a water bath . . . 169
4-15 Binding of R_{18} to NRs under laser irradiation 170
4-16 Optical absorption of NRs after femtosecond pulsed laser exposure . . 171

5-1 Gramicidin 183
5-2 Schematic of NR-thrombin-aptamer system. 185

List of Tables

2.1 Properties of FerroTec magnetic nanoparticles. 52

2.2 Maximum gap size in an EMI shield. 69

2.3 Power output for selected magnetic nanoparticles 76

3.1 Light penetration depth of selected tissues 93

3.2 NR syntheses for ligand interface conductivity experiments 127

3.3 Thermal interface conductance for all tested ligands 139

4.1 NR syntheses for proof of the release strategy 152

4.2 R_{18} release rates due to laser irradiation 159

4.3 R_{18} release and binding rates due to water bath heating 168

4.4 R_{18} binding rates due to laser irradiation 170

A.1 Definition of symbols used 189

A.1 Definition of symbols used, continued. 190

A.1 Definition of symbols used, continued. 191

A.1 Definition of symbols used, continued. 192

A.2 Definition of acronyms used 192

A.2 Definition of acronyms used, continued. 193

A.2 Definition of acronyms used, continued. 194

Chapter 1

Introduction

In this chapter I will cover the motivation for this work. This will include a brief review of external biomolecular control systems. It will cover what we consider to be the hallmarks of an ideal biomolecular control system. Finally, I will discuss the basis for our biomolecular control system including some details on the critical components and some strategies for accomplishing biomolecular control.

1.1 Motivation : Why biomolecular control?

> Scientists investigate that which
> already is; Engineers create that
> which has never been.
>
> Albert Einstein

The primary goal of science is to describe the world, to make sense of it, and to be able to predict it. The role of engineering is to take what the scientists teach us and to use the knowledge to control our world. Engineers make science useful. As engineers, we have successfully used science to control many aspects of our world. We can control our local environment by heating and cooling our houses. We can control the flow of electrons to make computers by manipulating semiconductors. We can control the way we get around by manipulating metals and fuels to make cars. Our

ability to control materials across many length and time scales is astounding. There is a hole. We have very little direct control over biological molecules.

Biomolecules form the foundation for all functions of life. DNA encodes the genome, enzymes catalyze complex reactions, carbohydrates store energy for future use, and lipids provide the membranes that ensure order at a microscopic level.[173] Nature, through billions of years of evolution has found ways to control these interactions. Temperature, pH, ionic strength, chemical concentrations, chemical reactions, and physical interactions are just a few ways that nature controls biological molecules. The results speak for themselves.

In recent years, scientists and engineers have been interested in engineering biology. Some of the most promising biological engineering designs exploit nature's building blocks by using modified natural systems or artificial systems comprised of natural proteins.[87, 166] In their native biomolecular systems, these molecules would be controlled by chemical, mechanical, thermodynamic or even electrical means. However, for engineers to harness the full potential of natural biomolecules, it is necessary to control them specifically and externally.[52] Direct, external, spatio-temporal control over protein activity would enable greater precision in the study and engineering of biology.

One clear area that would greatly benefit from direct biomolecular control is molecular and cellular biology. The ability to directly control protein activity would enable a biologist to study what one type of protein does within a cell by observing how the cell reacts in real-time to having the protein active and then suddenly not active. This would improve on the technique of creating genetic mutant knockouts as both states could be tested in exactly the same system. It would simplify and accelerate the rate at which biological research is done.

Another example application for biomolecular control is in drug activation, particularly in combination therapies where the sequence of activation is critical.[154] Additionally, precise spatio-temporal control could mitigate many of the side affects associated with systemic delivery of drugs, notably chemotheraperies.[22, 41] A targeted, systemically introduced drug only accumulates on the cancer sites, but it could

cause problems before it finds its way there. If this targeted drug were externally activated, it would be even more precise. Additionally, external activation could potentially limit the number of times the drug must be introduced, if the actuation step were repeatable.

Beyond the biological and medical sciences, there are potential applications for biomolecular control in computation,[1, 17] in biotech manufacturing, and sensing. Though there are many examples of successful systems without direct external biomolecular control, their potential could be enhanced with it.

These are just some of the potential applications for a direct, external, spatiotemporally precise biomolecular control system. Development of this technology would add a set of tools to the engineering biology toolbox. Enabling technologies like this one are clearly important for many applications today, but they often have impacts that are farther reaching in the future.

Another motivation for achieving direct external control over biomolecules is as an enabling technology for designed molecular machinery. There is much interest in affecting mechanical changes at the molecular length-scale. Recent work has focused on designing proteins to achieve these goals, with a particular focus on the individual components necessary.[75] However, as progress is made in molecular machine design, the means to externally control them is increasingly necessary.

1.2 State of the art biomolecular control systems

There are many excellent scientific studies which address controlling molecular machinery at the molecular scale. The techniques they employ often imitate nature, and include chemical,[106] electrical,[182] laser induced thermal,[82, 86, 143] direct thermal,[113, 134, 135] and photoactivated [109] control techniques. Most of these studies try to achieve an "on/off" control mechanism. However, none of these systems are ideal.

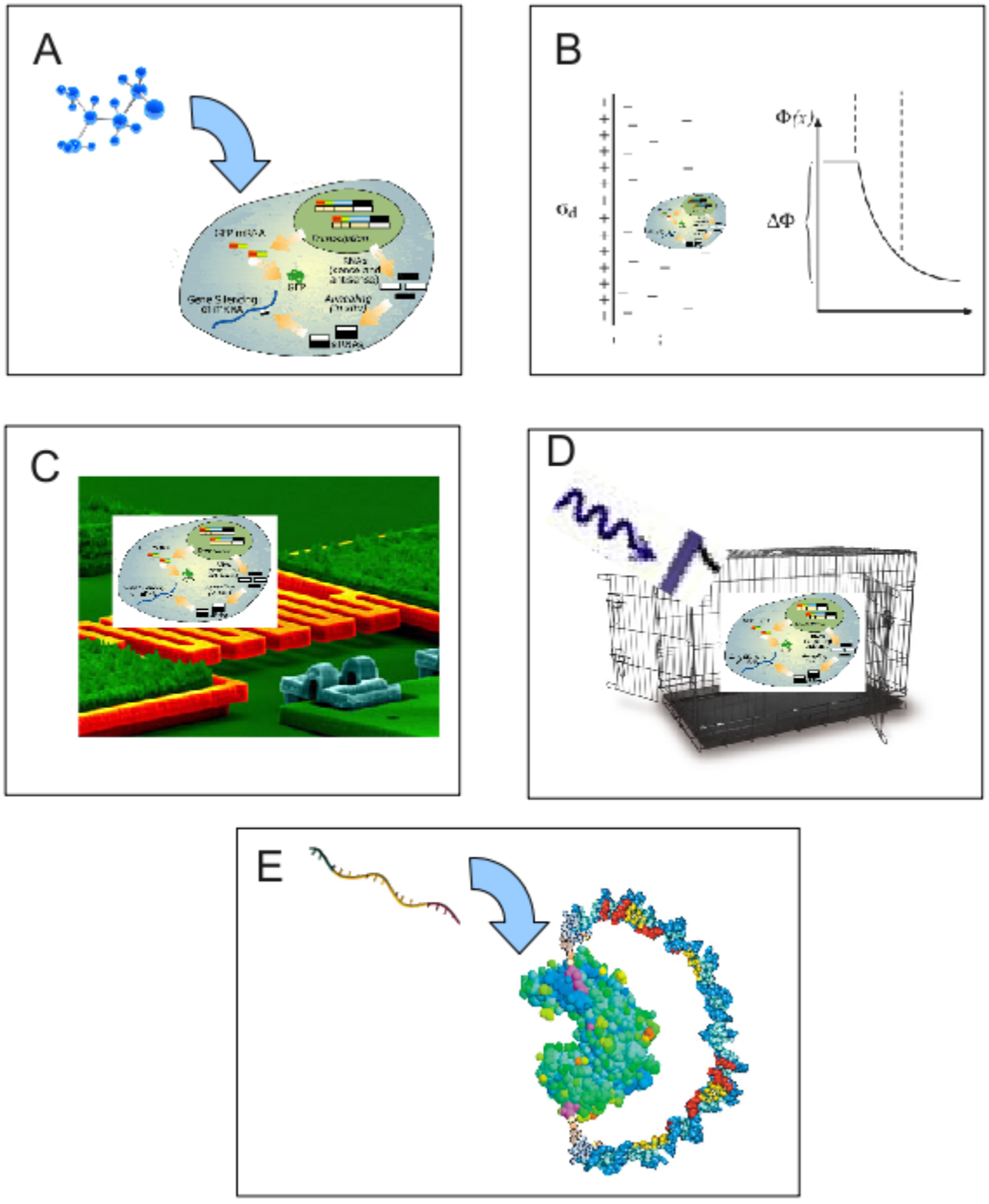

Figure 1-1: Schematics of state of the art biomolecular control systems. A. Chemical, B. Electrical interfaces, C. Direct thermal, D. Photoactivated, E. Mechanical. See the following sections for a description of each control method.

1.2.1 Chemical

One of the most common natural regulation pathways for biomolecular activity is "on/off" switching when a chemical, be it a small molecule, a peptide or another protein, binds to an enzyme. This could be competitive, non-competitive or mixed competitive inhibition, depending on if the regulatory molecule binds to the same site as the substrate.[173] There are millions of examples of chemical control, like regulation of muscle contraction by calcium ion interaction with tropomyosin or regulation of ATPases with ATP concentration.

Because there are so many examples in nature, this has also been a common control technique engineered into biological systems by scientists. A nice example is some work that was done on a molecular motor comprised of the cytoplasmic F_1 fragment of ATP synthase (F_1-ATPase). The group reporting the results designed a domain into the F_1-ATPase with a zinc binding site that serves as an allosteric inhibitor of function. They demonstrated that it works as an "on/off" switch.[106] The addition of Zn^{2+} ions suppressed the ATPase activity. Subsequent addition of a zinc chelator (1,10-phenanthroline) restored activity. They demonstrated repeatability by cycling addition of Zn^{2+} and 1,10-phenanthroline (see figure 1-2).[106] There is significant interest in this control technique. Other examples of the chemical control mechanism include control of kinesin activity by Zn^{2+} ions[56] and Ca^{2+} ions.[95]

This control system is elegant, and rapid. For certain applications, the chemical control system is nearly ideal, if the actuation chemical is relatively inert to the remainder of the system. But as a general purpose system, it has a major drawback. As the cycles are repeated, the accumulation of Zn^{2+} and chelator degrades the performance of the switching mechanism. Without a mechanism to washout the accumulated chemical control agents, the switch may only be actuated a couple of times, as can be seen in figure 1-2. Repeated additions of these chemicals also could affect other Zn^{2+} sensitive molecules within the entire biomolecular system. Additionally, 1,10-phenanthroline and other chelators are known to be both toxic and carcinogenic so that their use is not ideal.

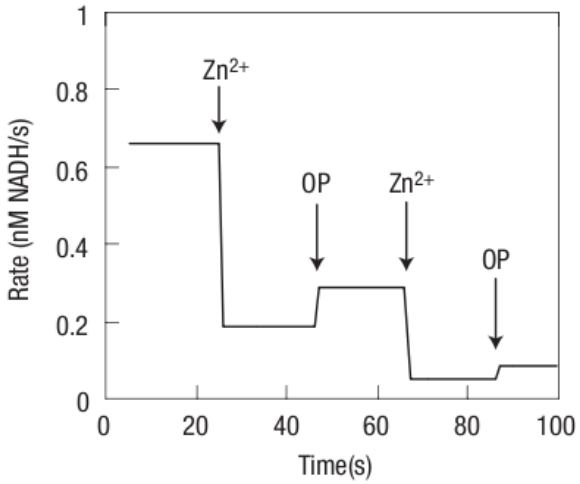

Figure 1-2: Example from literature of chemical control: Steady-state kinetics of ATP hydrolysis in mutant F_1-ATPase enzymes. Two cycles of successive additions of 100 μM Zn^{2+} and 150 μM 1,10-phenanthroline (OP). Note that activity, as evidenced by NADH production rate, drops with addition of Zn^{2+} and is restored by addition of OP. Reprinted by permission from Macmillan Publishers Ltd: *Nature Materials* **1**, 173 - 177, copyright 2002 [106]

1.2.2 Electronic interfaces

Another system controls biomolecular activity by regulating the ionic and electrostatic environment within the Debye double layer ($\sim$1 nm for physiologic saline) near an electrode. This scheme was demonstrated by controlling the polymerization of actin filaments. The normally active actin monomers were suspended in a buffer that was depleted of Mg^{2+}, which is necessary for polymerization, rendering them inactive. Upon application of an electrical potential Mg^{2+} ions migrate to the negative electrode surface, locally activating biomolecular function.[182] This system is ideal if the target molecule is bound to a surface. It is very rapid, as electrical migration times over the debye length are extremely short. If the applied voltage is high enough, the level of exclusion of charged counter-ions can be very small, allowing for high switching efficiency.

This control system has some major drawbacks that limit its general utility. It takes advantage of some very specific properties of the targeted biomolecules, and it requires altering the native buffer concentration. Since it affects all molecules within

a Debye lengths of the electrode, it is not specific to the targeted molecule. Equally bad, there are a number of unaffected actin monomers not within the Debye layer. The diffusion of the monomers in and out of the Debye layer makes it difficult to uniformly affect a majority of targeted molecules. Finally, the induced electrostatic interactions between the electrode and the biological system could be problematic.

1.2.3 Direct thermal

Since there are many thermally responsive materials, using direct heating of a biosystem could, if carefully designed, control biomolecular activity. One example of a direct thermally actuated biomolecular control system uses a thermally responsive supramolecular hydrogel to control the molecular motor F_1-ATPase.[184] The supramolecular hydrogel entraps the protein without denaturing it. When the glycosyl amino acetate-based hydrogel (a fibrous networks consisting of GalNAc-succglu(*O*-methyl-*cyc*-pentyl)$_2$[93] is heated, it collapses on the molecule restricting it mechanically. This switches its activity off. Upon cooling, this process fully reverses. This system is easy to achieve, at it generally only requires the assembly of a MEMS device, and not much biochemistry at all. It is in expensive and relatively rapid.

However, despite the claim that the heating can be localized by using MEMS heating devices,[184] this control technique will actuate anything in the system that is large enough to be ensnared by the collapsing hydrogel. Conversely, this control system can only actuate biomolecules that are large enough to be affected by the hydrogel. Additionally, the heating must be carefully controlled, because both the hydrogel and biomolecules are temperature sensitive. Care must be taken to apply just enough heat to contract the hydrogel without affecting the biomolecules. This balance might not be possible, if the biomolecules are more sensitive to the temperature than the hydrogel.

Others have use thermally sensitive polymers in other ways. An example is that PNIPAm (poly(*N*-isopropylacrylamide)) was conjugated to the distal end of a DNA strand. At elevated temperature PNIPAm collapses on itself. In this state it sterically hinders the natural recognition of the restriction-modification enzyme.[135] Upon

cooling, the PNIPAm relaxes, and restriction-modification enzymes can again recognize the DNA. So PNIPAm acts as a switch. However, this control technique suffers from similar issues as the entrapping hydrogel, as it really just scales the concept down to the single molecule scale. It also requires biochemical modification of the target molecule, which is not ideal.

Another example of direct thermal control is to exploit the thermally sensitive nature of the biomolecule itself. Arrhenius kinetics predicts that reaction rates increase exponentially with temperature. This is true for the ATPase activity of kinesin.[85, 86] This was shown to be useful in the control of the velocity of actin sliding in an acto-

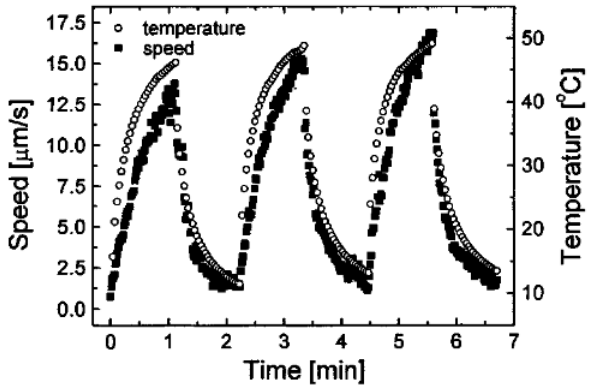

Figure 1-3: Demonstration of direct thermal control. An actin filament sliding speed response as a function of time upon slow cyclical heating and cooling for three cycles with temperature data. Reprinted with permission from Goran Mihajlovic, Nicolas M. Brunet, Jelena Trbovic, Peng Xiong, Stephan von Molnar, and P. Bryant Chase. All-electrical switching and control mechanism for actomyosin-powered nanoactuators. *Applied Physics Letters*, 85(6):10601062, 2004. Copyright 2004, American Institute of Physics.

myosin sliding filament assay (see figure 1-3).[113]

Controlling the activity of kinesin with the direct thermal technique is a special case. The biomolecular components are robust enough to remain active with the application of heat. This is not generally true, and often other changes caused by heating the entire system can counteract the intended purpose of speeding up the kinetics of a chemical reaction.

A final example of using direct thermal control is in the bidirectional control

of DNA hybridization. A group recently showed that by using what they they call "thermally degradable molecular glue" they can control the DNA hybridization/denaturation cycle.[134] The glue mimics base-pairing of DNA and prevents actual hybridization. They demonstrated this method for turning DNA hybridization on and off, and then they applied it to the control of the assembly of gold nanoparticles.[134]

A common issue with all the direct thermal control systems is that they will only work in very specific cases. In a larger system, like a cell, there are too many thermally sensitive molecules and processes for the direct thermal control system to be effective. However, if this heat could be delivered locally just to the molecule of interest, the thermal control technique would be significantly more general.

1.2.4 Photoactivated

Another biomolecular control strategy, one that has a relatively long history (since the 1970s), is to use light as a conditional trigger signal to actuate a photosensitive group which controls the biomolecule of interest.[109] There are two general strategies. The first one, "caging," involves the modification of a the target biomolecule with a photolabile protecting group to make it temporarily inactive. Then the system is irradiated with light to which only the protecting group is sensitive. This releases the protecting group and activates the biomolecule. The most commonly used caging groups are the *ortho*-nitrobenzyl group and its derivatives, and coumarin-based systems.[109] This strategy has been employed in a variety of ways. It has been used to control the local ATP concentration by using DMNPE-caged ATP and UV light exposure, therefore regulating the activity of ATPase enzymes, like kinesin.[61] It has also been used to control glutamate transporting enzymes, also called excitatory amino acid transporters.[164, 165]

The second strategy involves using bistable photoswitches. This has the clear advantage of reversibility, but it is difficult to engineer these groups into biomolecules of interest.[109] One example where the bistable photoswitches were employed successfully was in the control of RNAse S activity.[58] A phenylazophenylalanime bistable

photoswitch was attached to the S-peptide. Upon irradiation with UV light, the activity is suppressed (see figure 1-4).

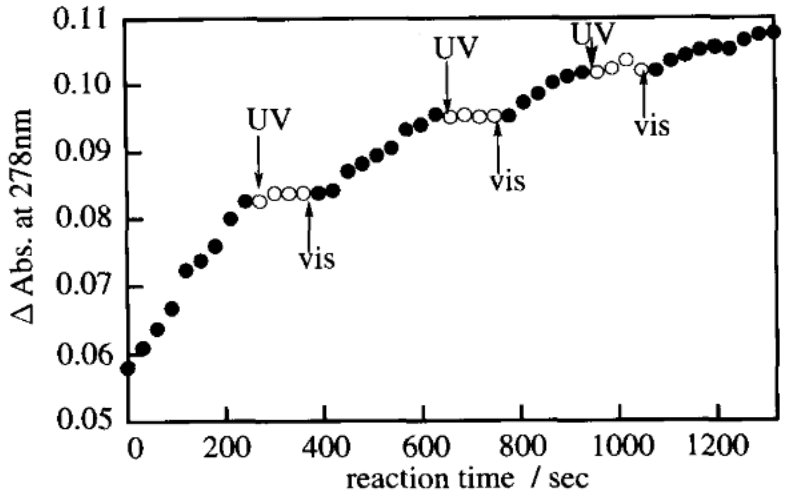

Figure 1-4: Demonstration of photoactivated bistable photoswitch. RNAse S activity is the slope of the change in absorbance of light at $\lambda = 278$ nm which measures the consumption of a poly-U RNA substrate. The changes in activity correspond to the switching of light from UV to Vis and back again. The slope when active decreases over time due to the consumption of the poly-U substrate.[58]

Overall, the photoactivated control technique is an elegant system that can control a biomolecular system with very high speed and accuracy. It is highly specific and quite rapid. However, there are a couple drawbacks of this system. First, the caging technique, though relatively easy to do biochemically, is irreversible. Thus it is not really an "on/off" control system, it is just an activation technique. Additionally some of the leaving groups, nitrosoaldehydes in particular, are biologically harmful. So the bistable photoswitch technique is preferable, but, as noted in [109], it is much more difficult biochemically. Both of these techniques require that, in order to ensure specificity, the modification of the biomolecules be in a purified solution outside of the system of interest. This necessarily requires that the system be devoid of the unmodified biomolecule of interest.

1.2.5 Mechanical interactions

Because of the relatively compliant nature of biomolecules, and because of the strong relationship between structure and function, another path to biomolecular control is through mechanical interactions. This system requires that a molecule be conjugated to the biomolecule of interest that can apply mechanical force. One way to implement this system is to conjugate both ends of a ssDNA to two different parts of an enzyme. In this configuration the enzyme is in its native state because the ssDNA is flexible (persistence length $\lambda_p^{ssDNA} = 1$ nm). When the complementary DNA is added, the ssDNA becomes dsDNA which is semi-rigid ($\lambda_p^{dsDNA} = 50$ nm). This causes the enzyme to take a non-native configuration and disrupts it activity. The stress can be removed by the addition of a DNase which breaks the dsDNA, and the activity is restored.[187] This was demonstrated on guanylate kinase, an enzyme that catalyzes the transfer of a phosphate from ATP to guanosine monophosphate (GMP).[27]

This technique is an elegant use of the entropic spring nature of DNA. For cases where other techniques could fail, due to the mechanical nature of this system, it is quite general. However, it is lacking as a control technique because it is not reversible. Once the DNase is introduced to the system, the control system is disabled. The DNase will continue to chop up the DNA until it is consumed. There will be no way to disable the enzyme activity a second time. Additionally, control by addition of a chemical like a complimentary DNA oligo is not ideal because of the potential for accumulation of DNA in the system in the lack of a washing mechanism.

1.3 Hallmarks of effective control system

There are three hallmarks of an ideal "on/off" biomolecular control mechanism: external, specific, and reversible. Externality allows integration of the biomolecular control mechanism into a larger system of control outside the biological system. Specificity allows the target molecule, and only the target molecule, within the biological system to be actuated. Reversibility allows the switch to be flipped multiple times without incrementally changing the system. Each of the biomolecular control techniques

mentioned in section 1.2 lacks one or more of these hallmarks thus rendering it not ideal.

1.3.1 External actuation

The idea that the biomolecular control system must be externally actuated is important for a couple reasons. First, for an engineered molecular machine, an external control system provides an interface between the macro and nano length scales. The person looking to control the biomolecule lives at the macroscale, so, to effectively gain control over nanoscale biomolecular interactions, that person must be able to flip a macroscale switch have the effects felt within the biomolecular system.

Secondly, for integration into a control algorithm, the biomolecular actuation scheme must be external. The controller is built into a piece of electronics. Even for integration into the simplest PID type controllers, the computer needs to interface with the biomolecules. In general, external actuation is a critical characteristic of any switching mechanism.

1.3.2 Specific

Specificity is critical to any precise control system. For the case of a biomolecular switch this can be broken down into two thoughts. First, the switching mechanism must be able to pick out the targeted molecule. Particularly in cellular research, if the researcher is interested in the effects of a particular molecule, it is important to be able to switch the activity of that molecule of interest. If the system were not specific in this way, if it cannot recognize the intended target, conclusions could be drawn erroneously because of inaccuracy in the targeting of switch. So by specific, we mean able to recognize target the molecule of interest.

Second, the control system should only affect the targeted molecule and not others. Again, as a molecular and cellular biology research tool, if the switch were not accurate it could affect the targeted molecule and many of the molecules in the immediate vicinity. This could lead to confusing results. So, in this case, by specific we mean

able to be local to the targeted molecule.

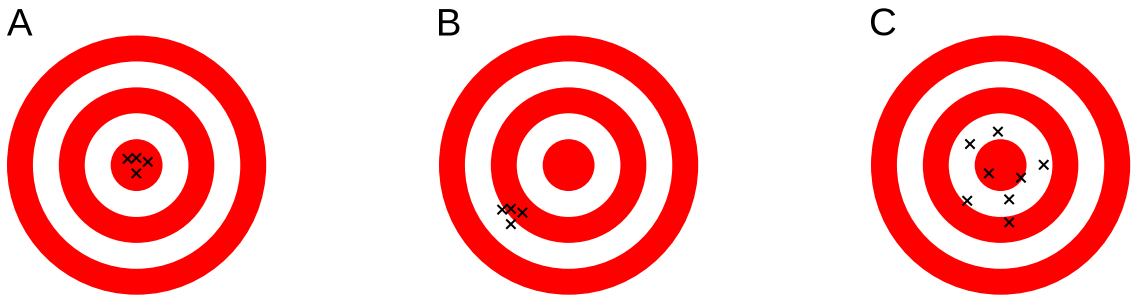

Figure 1-5: Specificity of the biomolecular control system is like archery. A. This targeting system has specificity. B. This targeting system cannot identify the target accurately. C. This targeting system has a large distribution about the intended target.

Archery is a good analogy for biomolecular control specificity. Accomplishing specific control is like being able to hit the bullseye (figure 1-5A). If the control system cannot distinguish the target from other biomolecules, it affect something else as if it were the target, and it is not specific. This can be thought of as mistakingly aiming at and hitting a point other than the bullseye (see figure 1-5B). Also, if the control system does not affect the system locally it will affect things near to the target, and it is not specific. This can be thought of as being inaccurate and hitting points far from the bullseye (see figure 1-5C).

1.3.3 Reversible

An ideal control system is completely reversible. The ideal form of reversibility would have the n^{th} off state be completely indistinguishable from the initial condition. Like switching a lamp on an off, the state of the bulb and the immediate surroundings are basically unchanged over the course of many thousands of cycles.

The rate at which the switch is reversed is also generally important. The faster the reversal rate, the better the control system. There are a number of parameters that affect the on and off switching rates including thermodynamics, temperature dependent biomolecule folding rates, binding and dissociation constants, response

times of actuation equipment and many more. Reversibility is often the most difficult hallmark to achieve, and even more difficult to optimize.

1.4 The biomolecular control system: a biomolecular activity switch

To meet these hallmarks, we need to actuate the activity state of the targeted biomolecule externally, specifically and reversibly. Metallic nanoparticles (NPs) are an ideal material to interface between the macro and nano size scales due to their size ($\sim$ 1 nm), versatile surface chemistry, and unique optical or magnetic properties. The activity switching mechanism requires the conjugation of the targeted biomolecule to a NP by one of a variety of techniques as permitted by the NP's surface chemistry. The NP-biomolecule conjugates are irradiated with an externally actuated electromagnetic field, either a laser or an alternating magnetic field (figure 1-6). The energy

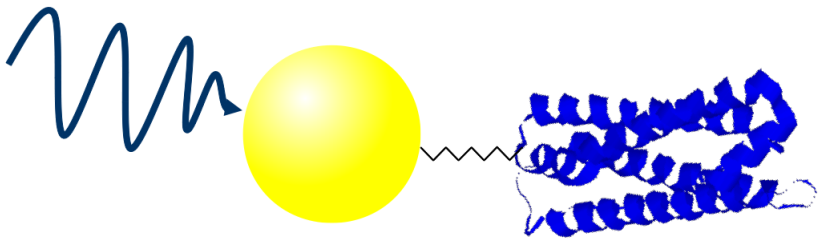

Figure 1-6: Schematic of biomolecular activity switch. There are four key components to the switching mechanism highlighted here. 1. The nanoparticle, 2. the biomolecule, 3. the conjugation of the NP and biomolecule, and 4. the irradiating field.

in the field is specifically absorbed by the NP due to its optical or magnetic properties while other components of the system remain unaffected. The NP converts the energy in the field to heat. This heat is conducted to the targeted biomolecule. If the system is carefully designed, the heat will move the biomoelcule from its equilibrium state by disrupting its structure, actuating its activity. When the field is removed, the system will return to the original equilibrium state, thus achieving reversibility if the critical parameters are carefully controlled.

1.4.1 Nanoparticles

The primary purpose of nanoparticles is to convert the energy from the field to heat. Then they transfer the heat to the conjugated biomolecules.

Generally, NPs are defined as any object larger than a single molecule that acts as a single unit of size 1 – 100 nm. Often NPs are of scientific interest because they have unique, size related properties that differ from the bulk material. The NPs used in this biomolecular control system can be magnetic to convert the energy from a magnetic field, or they can be optically absorptive to convert the energy from laser light. In addition to the energy absorption properties of NPs, their surface chemistry and stabilizing ligand are critical to the success of the activity switch. NPs must be compatible with the conjugation technique, and they should prevent interactions with elements of the biomolecular system that are not targeted. Other NP parameters like size and shape can also be critical.

1.4.2 The field

There are two primary field types for use with this switching mechanism. Radio frequency alternating magnetic fields (RFMFs) can specifically heat magnetic nanoparticles (see chapter 2). Laser irradiation can specifically heat metallic NPs, particularly gold or silver NPs (see chapters 3 and 4). Either of these two choices can be tuned such that only the NPs will absorb the energy. This is critical to achieve the hallmarks of successful biomolecular control.

1.4.3 Conjugation

Depending on the nature of the NP, the ligand and the biomolecule, there are a number of possible conjunction options including adsorption, covalent coupling and specific recognition.[83] When combined with the nature of the biomolecule and the NP's stabilizing ligand, the conjugation can either preserve or disrupt the activity of the biomolecule.[11]

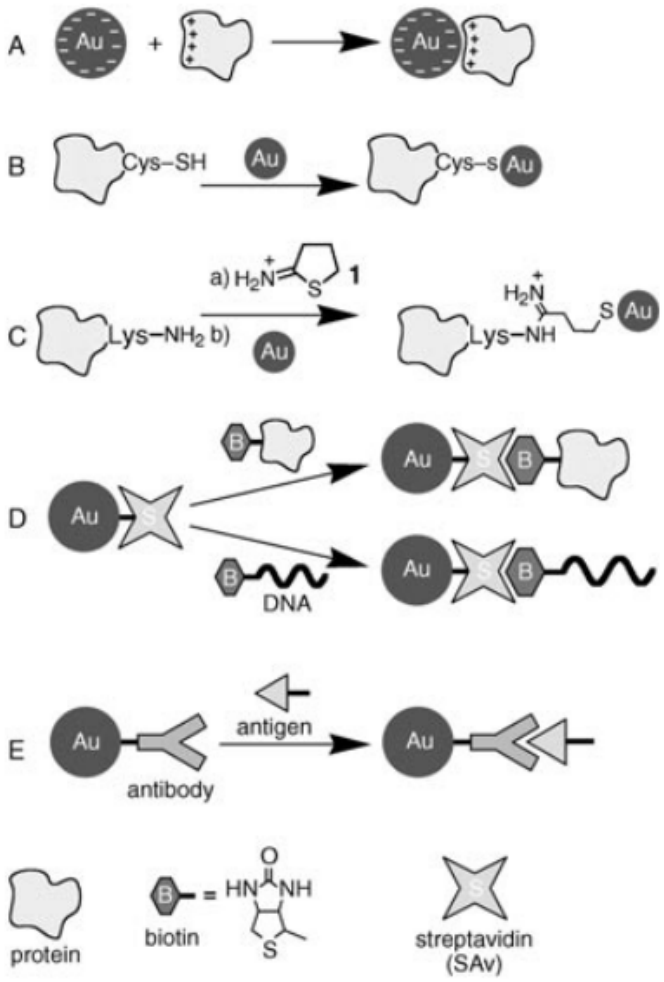

Figure 1-7: Example typical biomoleculenanoparticle conjugation chemistries. A) Electrostatic interactions. B) Covalent binding of NPs on natural thiol groups of the protein. C) Covalent binding of NPs on synthetic thiol groups of the protein. D) Specific bioaffinity interactions of streptavidinbiotin binding. E) Specific bioaffinity interactions of antibodyantigen associations.[83] Eugenii Katz and Itamar Willner : Integrated Nanoparticle-Biomolecule Hybrid Systems: Synthesis, Properties, and Applications. Angewandte Chemie International Edition. 2004. 43. 6042-6108. Copyright Wiley-VCH Verlag GmbH & Co. KGaA. Reproduced with permission.

Biomolecule adsorption

The simplest conjugation procedure is nonspecific adsorption. The most common type is electrostatic adhesion. If the NPs or the ligand on the NPs is charged and the biomolecules are oppositely charged, then they will adhere. Electrostatic interaction conjugation procedures can be controlled by altering the ionic strength of the solvent. Increasing the salt concentration decreases the Debye length and increases the electrostatic charge shielding. This tends to slow electrostatic adhesion. Additionally, because many proteins contain side chains that have titratable groups, the pH of the solution can greatly affect the charge of the proteins, so it must be carefully controlled if electrostatic interactions are to be used as a conjugation technique.

A second common nonspecific adsorption technique takes advantage of hydrophobic interactions. The van der Waals forces involved in these interactions result in hydrophobic regions of biomolecules to reside in hydrophobic ligand layers. As an example, a phospholipid layer on a NP could be used to bind a membrane associated protein to a NP.[97]

Another relatively common technique is to tag the protein with a poly-histadine tail. This will coordinate nonspecifically with a number of different types of nanoparticles depending on their surface ligands.[34, 13]

Covalent coupling

The most common covalent bonding reaction used to conjugate biomolecules to nanoparticles is gold-thiol bonds. This can be through naturally occurring free surface thiol groups on cystein residues in proteins. Generally, for a cystine to be available it cannot be involved in a disulfide bond. Cleaving a disulfide would greatly affect the protein structure. If there are no available cystine residues, they can be genetically engineered in[12] or other amino acids can be modified, for example a lysine can be with 2-iminothiolane (Traut's reagent, **1**; see figure 1-7C).[83]

Specific recognition

Nanoparticles can be functionalized with groups that provide specific affinities to particular biomolecules. Often this functionalization relies on one of the above conjugation techniques, for example, gold-thiol covalent bonding. However the interaction with the biomolecule itself is often not covalent.

A common example of specific recognition is biotin-streptavadin. This conjugation technique is often used with polystyerene beads, but others have used it with gold nanoparticles.[123] It works by biotinylating the biomolecule and conjugating the streptavadin to the NP. Another common specific recognition technique takes advantage of the antibody-antigen binding. The immunoglobulin is conjugated to the nanoparticle. The specific recognition can either be to the biomolecule itself is the antigen, or to the antigen which has been tagged to the biomolecule of interest. A third relatively common specific recognition technique takes advantage of DNA. This can be done either with DNA base-pairing or using a DNA aptamer. Either way a DNA oligo is generally thiolated and covalently bonded to the NP. It interacts with the intended specific binding partner. Whenever DNA is conjugated to NPs care must be taken to ensure it is available to bind to the target biomolecule. The NP's surface ligand can have a strong influence over the DNA confirmation and thus its availability to recognize its binding partner.[132]

1.4.4 The biomolecule

The final key component of the system is the biomolecule itself. If the goal of the biomolecular switch is to control a larger biological system, say in a biotech manufacturing application, identifying a biomolecule whose actuation will have the desired effect on the overall system is critical. If, however, the intention is to study the effect of a particular biomolecule on the system, say in a cell biology study, then there might not be much flexibility in what biomolecule to target. Often selection of the target biomolecule will restrict the choices of NP, field, and conjugation. So, careful selection of a target biomolecule could lead to a simpler overall system.

Some of the biomolecules we studied with include ferritin, cytochrome c, RNase, thrombin, amongst others. They were all selected for particular reasons detailed in the following chapters.

1.4.5 Local thermal confinement

Each of the hallmarks of an ideal biomolecular control system (section 1.3) relies in some way on the temperature of the nanoparticles being elevated with respect to their immediate surroundings. For a NP to affect a change on a conjugated biomolecule, likely less than 10 nm from the surface of the NP, the temperature profile must extend $\sim$ 10 nm. However, for it to not affect anything else, the heated zone should not extend beyond that. This is what is know as "local thermal confinement." To

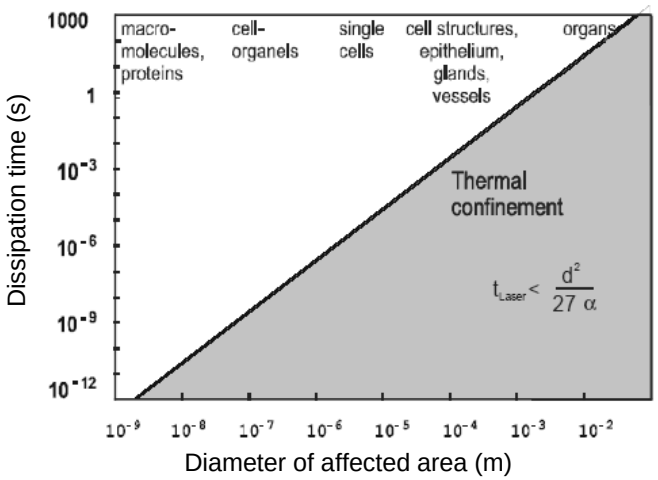

Figure 1-8: Order of magnitude estimate of required energy delivery duration as a function of desired local thermal confinement area. Figure is adapted from Huettmann et al. 2003.[73]

achieve local thermal confinement, the energy input needs to be faster than the energy dissipation time constant (τ_D):[7]

$$\tau_D \propto \frac{d^2}{27\alpha} \tag{1.1}$$

where d is the size of the affected zone and α is the thermal diffusivity of the solvent. Thus, to accumulate enough energy to raise the temperature of the nanoparticle, and subsequently the area immediately surrounding the particle ($\sim$ 10 nm) the total amount of energy necessary to heat that zone ($Q_{NP-biomolecule}$) needs to be absorbed by the NP in $\sim 10^{-12}$ seconds (see figure 1-8). Note that the energy necessary to heat the intended zone ($Q_{NP-biomolecule}$) is

$$Q_{NP-biomolecule} = \rho_{eff} C_{p,eff} \Delta T V \tag{1.2}$$

where ρ_{eff} and $C_{p,eff}$ are the effective density and specific heats of the affected zone respectively, ΔT is the temperature rise and V is the volume of the affected zone.

A nice way to visualize local thermal confinement is with a thought experiment. Imagine filling a bucket with water (see figure 1-9). That bucket has a hole. If you fill the bucket slowly, the water will simply pass through the bucket, without accumulating. If you increase the flux of water into the bucket or decrease the flux of water out of the hole, you will see an appreciable accumulation of water within the bucket before it eventually empties. This is analogous to the concept of local thermal confinement.

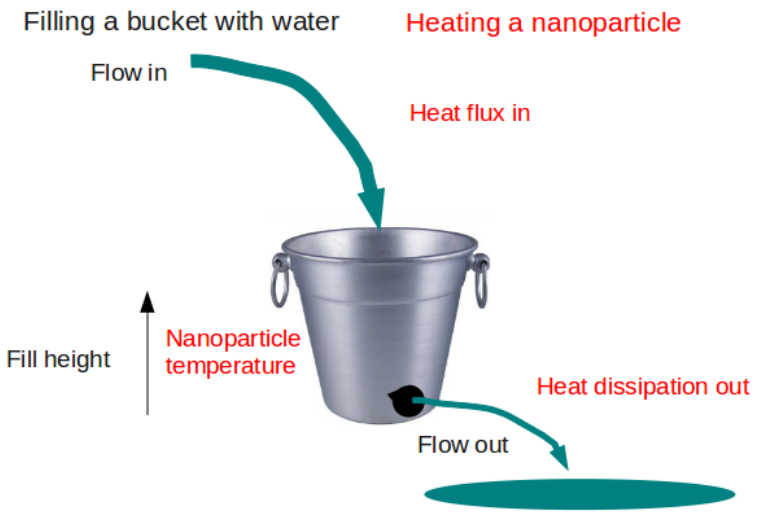

Figure 1-9: Local thermal confinement is like filling a bucket with water, and that bucket has a hole.

1.4.6 Model of control as a reaction

The simplest analytical model of the biomolecular switch is as a chemical reaction. In the default, low energy, state, the system is not being exposed to the field. Assuming the activation energy is significantly than k_BT, where k_B is Boltzmann's constant and k_BT is the magnitude of random thermal energy fluctuations, the likelihood that the system will progress to the actuated state is very low. When the field is activated, there is energy input. If that energy is sufficiently large, there is a significantly increased likelihood that the system will move to the activated state (see figure 1-10).

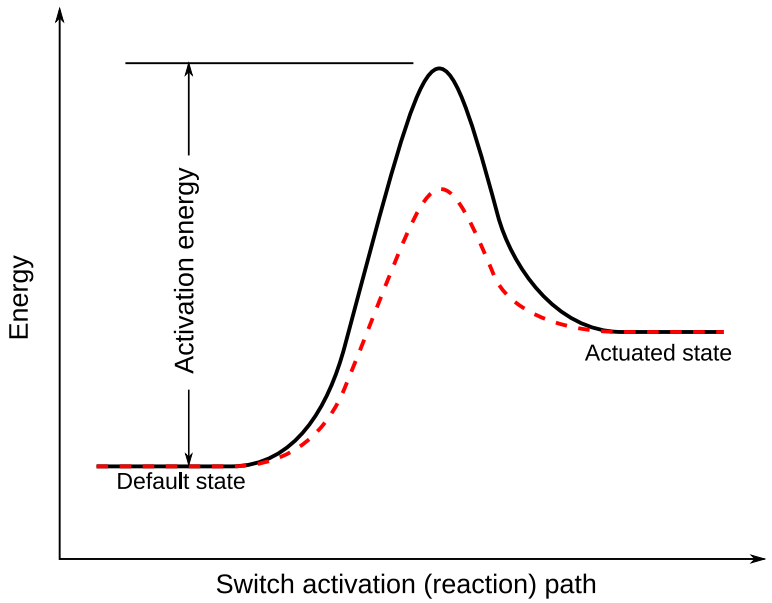

Figure 1-10: The biomolecular switch as a simple chemical reaction. The black line represents the default energy landscape of biomolecular switching. The red dashed line represents a catalyst-like modification to the system that increases the sensitivity of the switch.

The key to designing an implementation of the biomolecular switch is found in this representation. The activation energy necessary must be high enough such that the switch does not actuate on its own. This will ensure that the switch is only actuated externally. It is also necessary that the activation energy be low enough to ensure rapid, efficient switching. Theoretically this can be overcome with a stronger field, but there are other constraints.

There are a number limiting factors within the NP-biomolecule-biological system. The first limiting factor on the field strength is that the entire solution's temperature may rise significantly (called global heating) thus reducing specificity. The second is that the energy may have detrimental unintended effects on the system. For example, a high local temperature may cause a change in the energy conversion properties of the NPs thus reducing repeatability.

There are also a number of limiting factors external to the NP-biomolecule-biological system. An example of an external constraint is that the equipment necessary to generate higher intensity fields may not be available or may be prohibitively expensive. If the fields get too strong it is possible that they will become dangerous and require a significant effort in safety considerations.

So, some level of control over the activation energy is desirable. There are a number of ways to change the energy landscape within the biomolecular switch. The NP's ligand may have an effect. The conjugation technique might be another target. Additionally, it is possible that by adjusting some of the external parameters, if the intended application allows it, the energy landscape can be adjusted. The external parameters that might be adjusted include the ambient temperature, the ionic strength, and the pH of the solvent.

1.4.7 Biomolecular control system efficiency

There are two components to the efficiency of the biomolecular control system. The first is the speed at which the system switches from off to on and vice versa. The second is the percentage of target biomolecules actuated by any control event. They are interrelated because they both have to do with the kinetic and stochastic nature of this system. A highly efficient system would actuate 100% of the targets within an imperceptibly small amount of time.

When thinking about the switching speeds, there are two time scales associated with the biomolecule we should consider. These times scales are strongly dependent on the local environment of the biomolecule, in the case of the biomolecular switch, that includes the NR and the ligand.

The first of these time constants is $\tau_{switching}$, which is the timescale associated with the target being actuated. It is the time that the target needs to be at the elevated temperature to affect the changes that result in switching. $\tau_{switching}$ is likely dependent on the temperature, similar to Arrhenius kinetics. A higher temperature should lead to a faster $\tau_{switching}$.

The second of these time constants is $\tau_{recovery}$, which is the timescale associated with the target returning to its default state. It is the time that the target needs to be at T_∞ before it is driven to its default state thermodynamically. $\tau_{recovery}$ likely depends on the nature of the target's energy landscape. The further it got away from the default state, and the deeper the local energy minimum it happens to be in, the longer $\tau_{recovery}$ will be.

For the biomolecular switch to be effective $\tau_{switching}$ must be less than the time for which the target it heated, and $\tau_{recovery}$ must be longer than the repetition rate of the energy source. For a highly efficient biomolecular switch, one that actuates the target's activity both on and off rapidly, these time constants must be carefully considered.

The other key aspect of efficiency is the proportion of target actually actuated. It is unlikely that any system will be 100% efficient, but when designing each aspect of the biomoecluar switch design, one should consider its effect on efficiency. Further discussion of this aspect of efficiency, see section 3.1.9.

1.4.8 A robust biomolecular control system

Any system, and particularly a control system, is governed by a set of parameters. This section has covered the 4 key characteristics of our proposed biomolecular control system. Each of these characteristics has an associated set of parameters. For the system to work, there are upper and lower bounds on these parameters. These bounds are known as the "operating windows" for each parameter. It is important for each parameter to be within its operating window for the biomolecular switch to be functional. Design engineers need to keep the operating windows in mind as they design their systems. To design robust systems, those that will work under a

wide variety of conditions, the operating windows need to be maximized. Thus, as we define the technologies behind our bimolecular control switch, we have considered some ways to expand the operating windows for key parameters.

1.5 Specific biomolecular control system strategies

The previous sections have given a general overview of the biomolecular activity switching mechanism. The overarching concept is that NPs absorb the energy in an irradiated field. They convert the energy to heat. That heat is transfered to conjugated biomolecules. The heat affects a change in the biomolecules that actuates their activity state. When the field is removed the biomolecules relax back to their default state. There are many ways to implement this. In fact, each type of biomolecule might require its own specially tailored specific control strategy.

We like to think about three specific strategies to accomplish control. They are denaturation of attached biomolecule, separation of a multi-part biomolecule, and release from an activity inhibiting NP.

1.5.1 Denaturation of attached protein

In this strategy, the biomolecules are conjugated to NPs is such a manner that activity is preserved. When the field generating equipment gets an input (control signal) the field irradiates the NPs. This causes denaturation of the biomolecules. Based on the structure-function relationship in biomolecules, the activity is suppressed. When the field is removed, the biomolecule refolds to its native state and activity is restored. See figure 1-11 for a schematic of this strategy which, for brevity will be known as the denaturation strategy.

There are a number of considerations that are critical to accomplish this type of control. First, it is important that the biomolecules can maintain an acceptable level of activity when bound to NPs. This is not trivial because of many complicating factors including the charge and hydrophobicity of the ligand, the conjugation technique, and the potential for steric hindrance of the active site. Additionally if

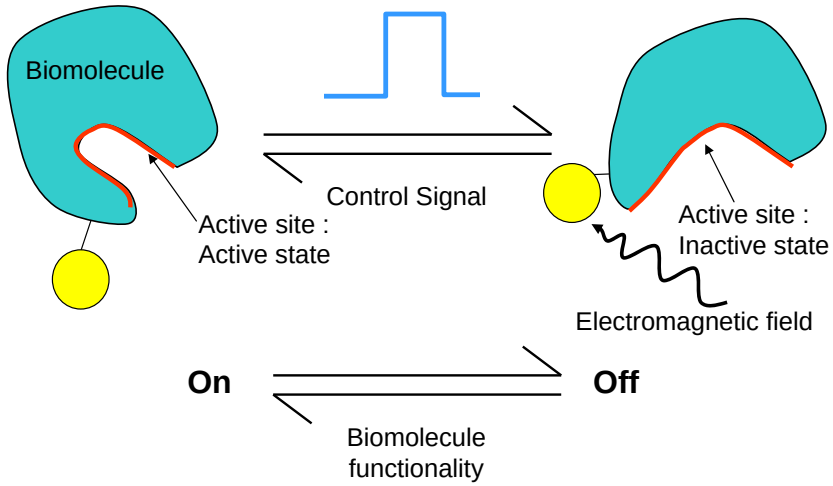

Figure 1-11: Schematic for model for biomolecular activity control : local denaturation

multiple biomolecules are conjugated to the same NP then there is a very high local concentration of the biomolecule in the immediate vicinity of the NPs. Since the kinetics of biomolecular interactions are often concentration dependent, and most kinetics models assume a well mixed solution, it is quite possible that by attaching the biomolecules to NPs the characteristics of the biological system may change. Another consideration that may be difficult to predict is the interaction between the biomolecule and the NP in the denatured state. If there is another, deep energy minimum in the landscape in this state, then the system may not relax to the native state.

Some possible target biomolecules for this control system include ferritin and cytochrome c. At least theoretically, this is a relatively generally applicable strategy.

1.5.2 Separation of multi-part systems

In this strategy multi-part biomolecules, or biomolecules and co-factors, are conjugated to NPs such that the activity is preserved. When the field generating equipment gets an input (control signal) the field irradiates the NPs. This causes the multi-part biomolecules to disassociate. Based on the biomolecules needing both parts, the activity is suppressed. When the field is removed, the parts recombine to form the default,

active state. See figure 1-12 for a schematic of this strategy which, for brevity will be known as the multi-part strategy.

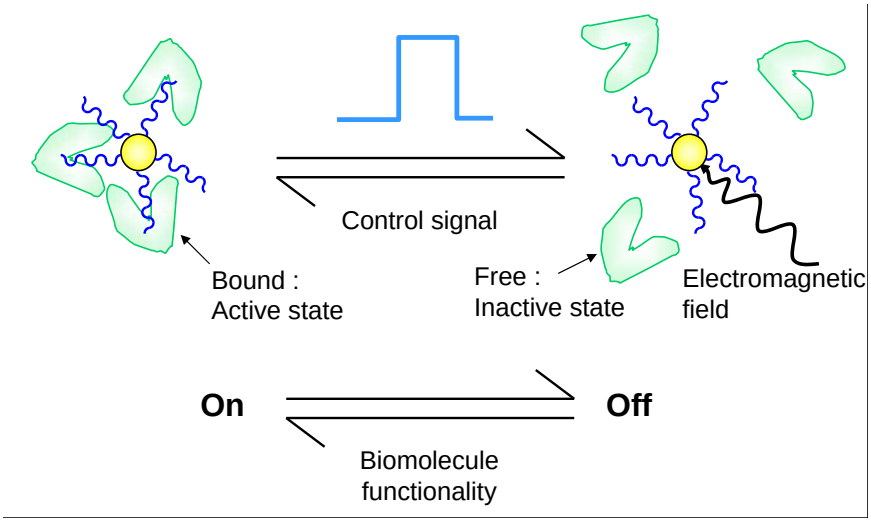

Figure 1-12: Schematic for model for biomolecular activity control : two part separation

Like the denaturation strategy, separation of multi-part systems requires that the biomolecules be active when conjugated to the NPs. This causes the same sorts of issues noted above. The unique challenge of this strategy is that the energy needs to be high enough to cause the two parts to separate, but not so much that the attached parts leave the NPs. If they were to be knocked off, the strategy would not be reversible. Even worse than that, however, is that, since both parts would be released, it might not actuate the activity.

One possible target biomolecules for this control system is RNase S. This is a two-part enzyme formed by a modification of RNase A by a protease called subtilisin. The RNase A is broken into two pieces which are inactive when separate, but, when they are incubated together, they will associate and be active.[146] Another class of targets include proteins with cofactors or multiprotein complexes. An example of this is pyruvate dehydrogenase, an element of the pyruvate dehydrogenase complex (PDC) which contributes to transforming pyruvate into acetyl-CoA, an important link between the glycolysis metobolic pathway and the citric acid cycle.

1.5.3 Inhabitation of active site and release

In this strategy, the biomolecules are conjugated to the NPs is such a manner that the activity is suppressed. When the field generating equipment gets an input (control signal) the field irradiates the NPs. This causes the biomolecules to disassociate from the NPs. Based on the fact that NPs are no longer interacting with the biomolecules, the activity is restored. When the field is removed, the biomolecules re-coordinate with the NPs to restore the default, inactive state. See figure 1-13 for a schematic of this strategy which, for brevity will be known as the release strategy.

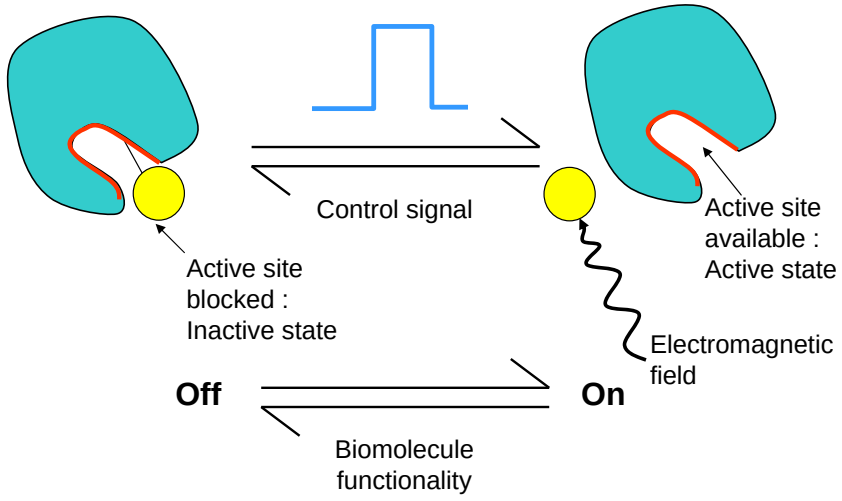

Figure 1-13: Schematic for biomolecular activity control : release

The conjugation of the biomolecules to the NPs in this strategy is potentially simpler than in either the denaturation or multi-part biomolecule strategy because is it more likely that the biomolecule-nanoparticle interaction will suppress activity than preserve it. Release of biomolecules is also a simpler task than denaturation or separation because there is likely a larger acceptable window in the energy parameter. The key here is to get enough energy delivered to knock the biomolecules off the NPs without destroying either the NPs or the biomolecules. The major drawback of this system is that the default state is inactive. For many of the applications for the biomolecular control switch it would most likely be beneficial for the default to be active, as that is likely to be the natural state. This could be mitigated with a detailed

understanding of the biological system in which the switch is being implemented.

There are a number of possible targets for this strategy. In fact, it is the most likely to be general. This system is ideal if the target can only be conjugated in a noncovalent manner. So, any biomolecule that is conjugated with electrostatic or hydrophobic interactions would be ideal. Even biomolecules that are attached by specific biological recognition, like those conjugated by aptamers or antibodies, are likely to find success in the release strategy.

1.6 This thesis

This thesis will discuss baseline and proof-of-concept experiments for the biomolecular switch. It will define the operating window for some of the most critical external and internal parameters that are necessary to achieve biomolecular control. It will also discuss system design considerations that could widen the operating windows. The thesis is designed to serve as a foundation for future work on the biomolecular switch. In chapter 2, I will cover the control system as actuated by radio frequency alternating magnetic fields. This will include details on how the system works theoretically, our experimental setup, and the results of our experiments. I detail the control system as actuated by ultrafast pulsed laser irradiation in chapters 3 and 4. Chapter 3 focuses on how the system works theoretically, and some of the key parameters governing the nanoparticles and their ligands. Chapter 4 focuses on a proof-of-concept demonstration of the biomolecular switch. Finally, in chapter 5, I summarize the most important conclusions, and I describe the implications of the research on achieving a fully functional biomolecular switch.

Chapter 2

Magnetic field heating

The use of magnetic fields and nanoparticles in biological applications has been around since the 1950s.[50] They have been used to simplify the separation of cells and molecules in the liquid phase.[29] They have been used as contrast agents for MRI detection of cancer and other imaging applications.[130] In therapeutics, magnetic nanoparticles have been used for targeted drug delivery[29] and hyperthermia of cancer.[64, 33, 170]

Alternating magnetic fields can heat magnetic nanoparticles. This is the driving force behind hyperthermia and some drug delivery applications. The concept, as applied to the biomolecular control system, is to miniaturize this from the millimeter length scale in most existing applications to the nanometer length scale.

2.1 Magnetic nanoparticles

Most materials with high magnetic moment are toxic and susceptible to oxidation, and thus they are not suitable for biological applications. These include particles made of cobalt and nickel. However, magentite (Fe_3O_4) and maghemite (γ-Fe_2O_3), if properly capped with protecting ligands, are suitable. Gold coated iron oxide nanoparticles are also a popular choice. Additionally, there is some evidence that small gold NPs and iron doped gold NPs are also magnetic.[177, 20]

The chapter covers the use of two types of magnetic nanoparticles. As a baseline

Table 2.1: Properties of FerroTec magnetic nanoparticles.

Nanoparticle	Concentration (μM)	Ligand	Saturation Magnetization (mT)
EMG 507	39	Anionic surfactant	10
EMG 705	77	Anionic surfactant	20

and control for many of the experiments, I used magnetite particles from FerroTec Corp, called EMG 705 and EMG 507 (see figure 2-1). These are high concentration "ferrofluids" with properties given in Table 2.1.

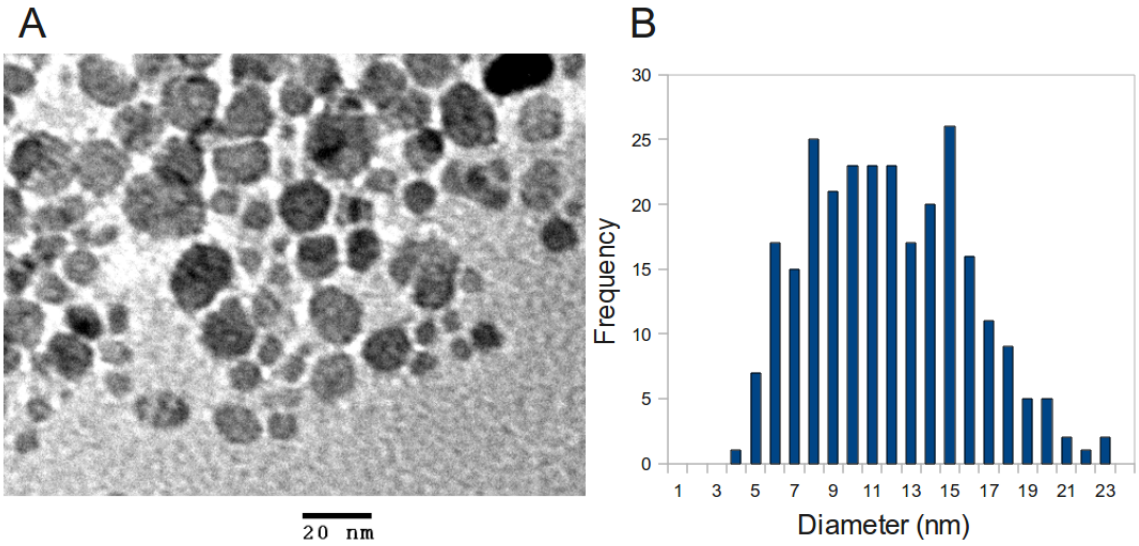

Figure 2-1: A. TEM of unmodified EMG 507 magentite (Fe_3O_4) nanoparticles from FerroTec Corp. B. Histogram of the diameter of EMG 507. The mean diameter is 11.4 $\pm$4.0 nm.

The other type of particle used predominantly in this work is the nanoparticle in magnetoferritin. Ferritin (see figure 2-2A) is a highly conserved, naturally occurring protein that sequesters iron in a goethite (FeOOH) nanoparticle. It is a spherical shell of 24 protein subunits (see figure 2-2B) that can nucleate metallic nanocrystals.[171] Magnetoferritin is made by chemically dissolving ferritin's native nanoparticle, and then synthetically mineralizing a $\sim$ 8 nm Fe_3O_4 particle [111, 183] inside ferritin to form magnetoferritin. We used magnetoferritin because it is an ideal system to study energy transfer from particles to proteins. Its spherical symmetry ensures all the dissipated energy passes through the protein shell. It also eliminates the need for

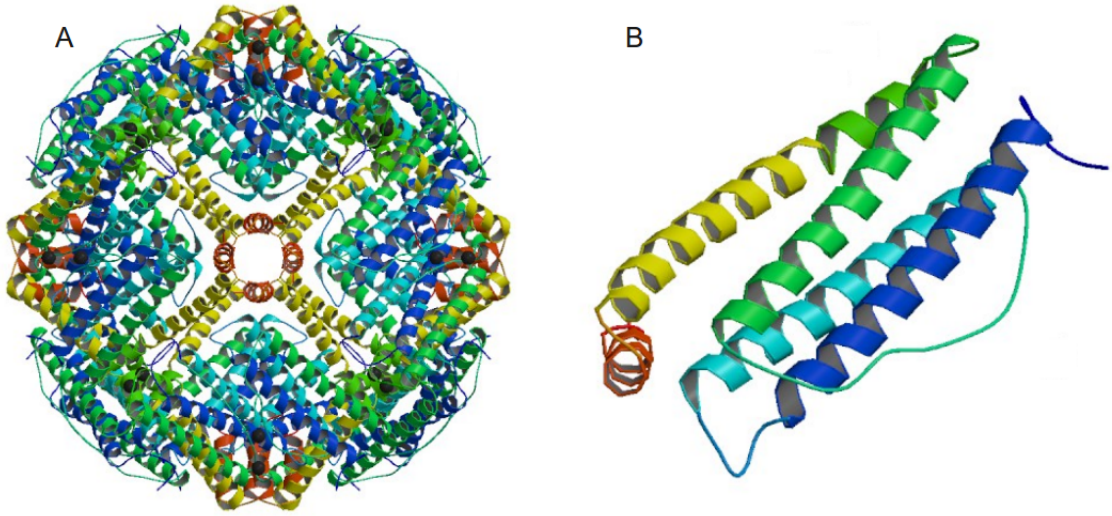

Figure 2-2: Crystal structure of ferritin. A. Ribbon diagram of horse spleen apoferritin complex. It is $\sim$ 450 kDa, $\sim$ 12 nm outer diameter, $\sim$ 8 nm inner diameter. B. Light chain ferritin subunit. It is $\sim$ 19 kDa. Along with heavy chain ($\sim$ 21 kDa not shown), it self assembles into the ferritin spherical protein shell. PDB ID: 1IER [55]

particle-protein conjugation.

Magnetic nanoparticles with diameter $< 30 - 50$ nm are superparamagnetic.[15, 51] The bulk form of the material that makes up superparamagnetic NPs can usually be magnetized in the absence of an applied magnetic field. The energy barrier separating possible orientations of the magnetization (E_{mag}) is

$$E_{mag} = K_1 V \tag{2.1}$$

where K_1 is the anisotropy energy density and V is the particle volume. E_{mag} can be overcome by thermal energy ($k_B T$). The characteristic time τ to overcome the energy barrier is

$$\tau = \tau_0 \exp \frac{E_{mag}}{k_B T} \tag{2.2}$$

where τ_0 is usually 10^{-7} to 10^{-9}.[51] For macroscopic magentite ($V \sim 10^{-6}$ m^3 and $K_1 = 1.35 \times 10^4 \ \frac{J}{m^3}$) at room temperature ($k_B T = 4.14 \times 10^{-21}$ J) $E >> k_B T$. Thus, at room temperature, τ is a *very* long time. The volume for which $\tau \sim 1$ s corresponds to a material size of length scale 10^{-8} m. Thus, particles that are of this

length scale or smaller are called superparamagnetic.[51]

2.2 Analysis of heating mechanisms

As was mentioned previously, when these magnetic nanoparticle are exposed to an alternating magnetic field, they can absorb the energy in that field and convert it to heat. There are three primary physical mechanisms that can lead to the conversion to heat: Néel relaxation, Brownian relaxation and magnetic hysteresis heating. Depending on the material and the geometry of the particle, any of these loss mechanisms could dominate.

2.2.1 Hysteresis

It is a well known phenomenon that when a magnetic field is applied to a magnetic material the atomic dipoles align. The circulation of the electrons within their orbitals, and the circulation of those orbitals about the nucleus, generated magnetic fields. The volume integral of magnetic dipole strength taken over the entire material is the magnetic moment of the material. In general, magnetic flux density (B) of magnetic materials is not linear with the applied magnetic field strength (H). As a H field is applied and then reversed, B follows a hysteresis loop (figure 2-3). A number of magnetic properties of a material can be determined from its hysteresis loop. Saturation magnetization is the magnetic flux density maximum as the applied field approaches infinity. Retentivity is a material's ability to retain residual magnetic flux (see figure 2-3) when H removed after having achieved saturation. Coercive force is the magnitude of the reverse magnetic field which must be applied to make the material's magnetic flux density return to zero (see figure 2-3). Finally, the reluctance, which is the constitutive property relating the magnetic flux density to the applied field can be determined. Reluctance is analogous to the resistance in an electrical circuit. As a magnetic is exposed to an alternating magnetic field, it state will travel around the loop. The energy density state of the material is the area swept out by the H-B curve. With each cycle, the material dissipates the energy equivalent to the

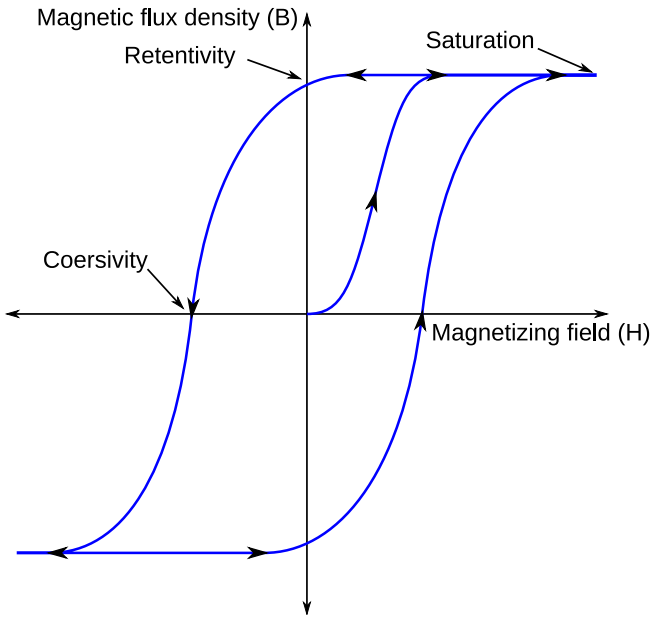

Figure 2-3: Magnetic hysteresis loop of a ferromagnetic material.

area enclosed by the hysteresis loop. This energy is dissipated as heat, thus magnetic materials can exhibit hysteresis heating.

Hysteresis heating only occurs when a material is divided into multiple magnetic domains separated by domain wall energies. When the domains get too small, the domain wall energies dominate the sum of the enclosed magnetic dipole energies. Once this condition is met, the particle will have only a single domain.[51] Particles with only a single domain, or just a few domains, no longer exhibit hysteresis heating. So despite being useful for bulk materials all the way down to nanoparticles with diameter $\sim$ 100 nm, hysteresis heating is not particularly useful in the biomolecular switch.

2.2.2 Néel relaxation

Another energy conversion mechanism is Néel relaxation. When a field is applied to a solution with magnetic particles, they will align with the field. When the field reverses, the particles' magnetic moments now point opposite to the field. This is a high energy state, and the system needs to relax. Néel relaxation occurs when the magnetic moment is able to flip within the particle. In particles with few magnetic

domains it is easier for the domain walls to move than for the particle to physically rotate in the field (see figure 2-4). The energy from having the magnetic moment

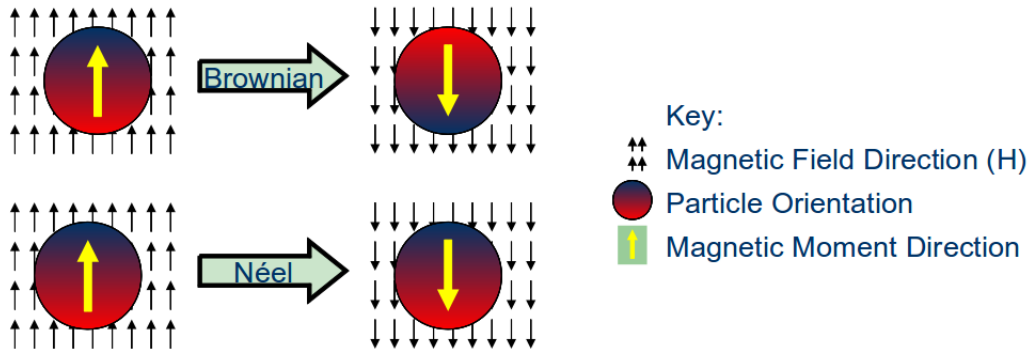

Figure 2-4: Schematic demonstrating the difference between Néel and Brownian relaxation.

relax transfers to phonons in the lattice.[35] The rate at which this occurs of order of the characteristic Néel relaxation time constant (τ_N)[148]

$$\tau_N = \tau_0 \exp \frac{K_1 V}{k_B T} \tag{2.3}$$

where $\tau_0 \sim 10^{-9}$ s. The energy within the particle then is dissipated by the solvent with a time constant τ_D (recall equation 1.1).

The specific energy dissipation per cycle due to Néel relaxation is a function of frequency for frequencies greater than 1 MHz ($E_{\text{Néel}}$)[35] is

$$E_{\text{Néel}} \approx \frac{2}{3}\mu_0 \pi m_S H \frac{\alpha_N}{\omega}. \tag{2.4}$$

At frequency less than 1 MHz, the specific energy dissipation is independent of frequency and is

$$E_{\text{Néel}} \approx 4\mu_0 \pi m_S H \tag{2.5}$$

where $\mu_0 = 4\pi \times 10^{-7} \frac{N}{A^2}$ is the permeability of free space, m_S is the saturation magnetization, H is the magnitude of applied magnetic field, α_N is a measure of the damping, and ω is the angular frequency of the magnetic field.

2.2.3 Brownian relaxation

The last magnetic energy conversion mechanism is the Brownian relaxation mechanism. When a field is applied to a solution with magnetic particles, they will align with the field. When the field reverses, the magnetic moment then points opposite to the field. This is a high energy state and the system needs to relax. Brownian relaxation occurs when the particle rotates within the viscous solvent (see figure 2-4). Energy is dissipated through viscous fluid effects. This occurs with at a rate characterized by a time constant, τ_B[148]

$$\tau_B = \frac{3\eta V_H}{k_B T} \tag{2.6}$$

where η is the coefficient of viscosity of the fluid in the immediate vicinity of the particle, and V_H is the hydrodynamic volume of the particle (note $V_H > V$ due to the thickness of the ligand layer). This means that the Brownian heat dissipation mechanism is highly dependent on the local environment, while this is not true for the Néel relaxation mechanism.[162] There could be significant differences as one moves a system from an *in vitro* experiment to an *in vivo* application.

2.2.4 Power

Before discussing the heat dissipated by these particles, I am going to cover the a couple things about specific absorption rate (SAR). SAR is the generally accepted figure of merit for hyperthermia applications.[35] It is the amount of energy absorbed per second by a unit of mass of sample ($\frac{W}{g}$). The confusion in the literature is often about what mass to use. Sometimes SAR is defined as per unit mass of NPs. Sometimes it is defined as per unit mass of ferrofluid (mass of particles plus mass of solvent). Sometimes it is per unit mass of embedded tissue (if the NPs are injected into a tumor, for instance). In this thesis, I will refer to SAR as the dissipated power per unit mass on NPs. But most often, I will actually be more interested in the power dissipated per particle.

Generally, the contribution of the Néel and Brownian relaxation mechanisms to

the overall power dissipation of an ensemble of NPs in solution is dependent on the size of the particles, the polydispersity of the particles, the anisotropy constant (K_1), and the local viscosity (η) of the sample.[162] That being said, there is a relatively simple, theoretically derived and experimentally proven expression for the power dissipation per particle (P)[148]

$$P = \pi\mu_0\chi_0 H^2 f \frac{2\pi\tau_{eff}}{1+(1\pi f\tau_{eff})^2} \tag{2.7}$$

where H_0 is the magnitude of the magnetic field, $f = \dfrac{\omega}{2\pi}$ is the frequency of the magnetic field, χ_0 is the susceptibility of the NP and τ_{eff} is the effective relaxation time constant τ_{eff}

$$\frac{1}{\tau_{eff}} = \frac{1}{\tau_B} + \frac{1}{\tau_N}. \tag{2.8}$$

χ_0 is field dependent and can be approximated by the Langevin equation

$$\chi_0 = \chi_i \frac{3}{\xi}\left(\coth\xi - \frac{1}{\xi}\right) \tag{2.9}$$

where $\chi_i = \dfrac{\mu_0\phi M_d^2 V}{3k_B T}$ is the initial susceptibility, M_d the domain magnetization of a suspended particle and ϕ is the volume fraction solids in the fluid, and $\xi = \frac{\mu_0 M_d H V}{k_B T}$.

SAR is dominated by the relaxation mechanism with the shortest time constant, since that mechanism will respond first. All other considerations being equal, there is a critical NP size ($D \sim 10$ nm see figure 2-5) below which the heating is dominated by the Néel relaxation mechanism, and above which the heating is dominated by the Brownian mechanism.

2.3 Our setup

Our RFMF control system includes a number of components. There are pieces of equipment necessary to generate the RFMF, to detect what is going on in the experiment, and for safety considerations. Additionally, there are characterization equipment and considerations. See figure 2-6 for a schematic diagram of our setup.

The concept of the setup is that a computer running a custom LabView program

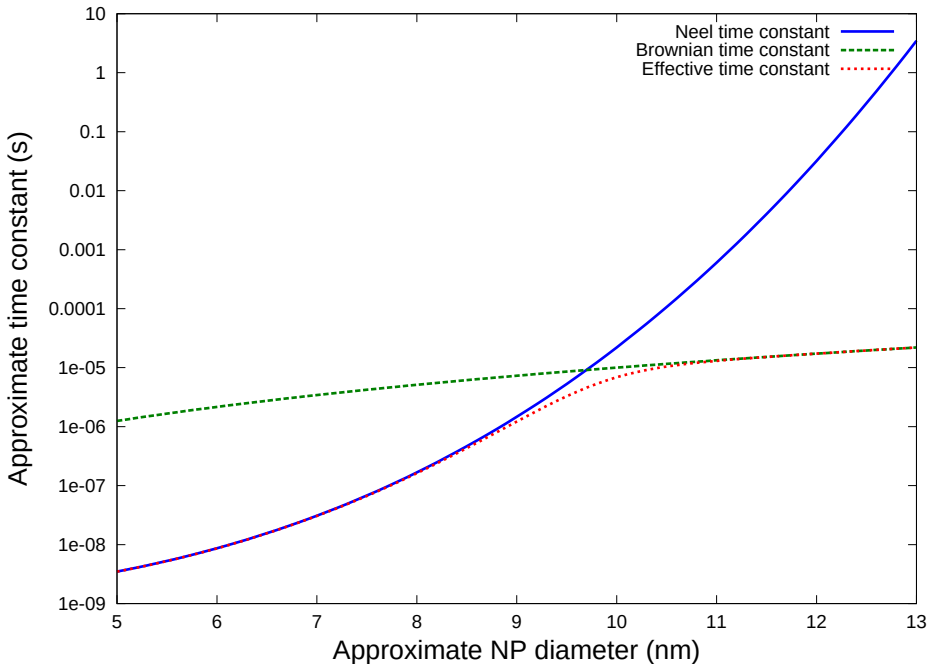

Figure 2-5: Order of magnitude estimates for the Brownian, Néel, and effective time constants as a function of particle diameter.

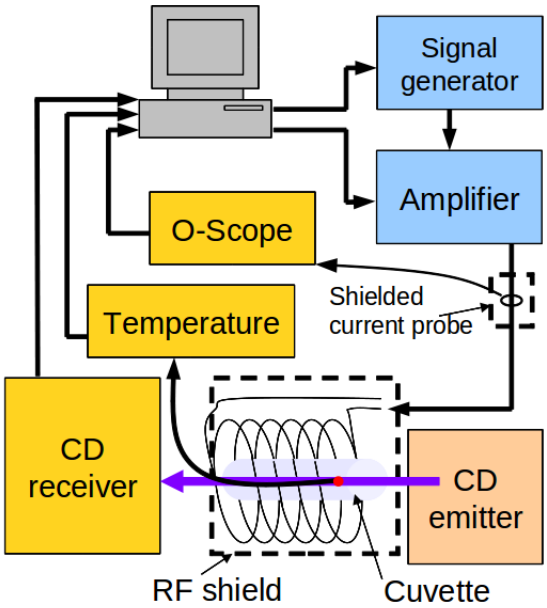

Figure 2-6: Schematic diagram of RFMF generating and experimental results measuring apparatus. Light blue elements generate the field. Peach colored elements generate circularly polarized light for CD. Orange colored elements detect either experimental results or field parameters.

acts as the equipment controller and data collector. It communicates with a signal generator used to generate a sinusoidal voltage signal. This is the input signal for an amplifier that generates a higher amplitude current which is fed through a custom coil. The coil generates a magnetic field. That alternating magnetic field is converted to heat by the nanoparticles. This heat is then conducted to the conjugated biomolecule, actuating its activity.

2.3.1 Current generating equipment

To generate the RFMF field we use a signal generator and an amplifier.

The computer sends the signal generator a command through a GPIB interface telling it what waveform and frequency to output. The signal generator (HP 8648D) can generate waveforms within the 9 kHz to 2 GHz frequency range. We used the sinusoidal waveform output.

This waveform is transfered to an amplifier through BNC terminated coaxial cable. Depending on the frequency of the signal, we use one of a variety of amplifiers from Amplifier Research. For lower frequencies (10 kHz - 250 MHz) we used a 100A250A amplifier. For higher frequencies (800 mHz - 4.2 GHz) we used a 5S1G4 amplifier. Either system accepts a signal through a GPIB interface telling it what amplitude (though annoyingly in an arbitrary unit ranging from 1000 - 4000) to make the output current.

To control the system, we employ a feedback mechanism that measures the current in the system using a current probe. We primarily use Tektronix current probes. The CT-1 is for higher frequencies (up to 1 GHz), and the CT-2 is for lower frequencies (up to 200 MHz). They are inductively coupled current probes that are permanently mounted to the setup. A single conductor must pass through the probe for it to work. They output a voltage proportional to the current passing through. That voltage is fed into an oscilloscope (HP 54615B) where the signal from the current probes were analyzed. The oscilloscope communicates the amplitude and frequency of the voltage through a GPIB back to the LabView where the frequency and amplitude of the current within the system are recorded.

2.3.2 Coils

The key component of the RFMF producing system is the coil used to generate the field. Coil design is critical to achieving the goals of the biomolecular control system. Many practical requirements of the control system influence the size and shape of the coil.

A coil is a passive electrical circuit element that converts current to magnetic fields. The strength of the magnetic field in its core is proportional to the current passing through it. This is a direct consequence of Ampere's and Faraday's laws ($\bigtriangledown \times H = I + \frac{\partial}{\partial t}(\epsilon_0 E)$ and $\bigtriangledown \times E = -\frac{\partial}{\partial t}(\mu_0 H)$ respectively where I is the current and E is the electric field). In circuit analysis, the inductance of a coil (L) is

$$L = \frac{\mu \pi N^2 r^2}{l} \tag{2.10}$$

where μ is the magnetic permeability of the core (note that $\mu = \mu_r \mu_0$ where μ_r is the relative permeability), N is the number of turns in the coil, and l and r are the length and radius of the coil respectively. The voltage ($v(t)$) across a coil is

$$v(t) = L\frac{dI}{dt} \tag{2.11}$$

for linear inductors.

The actual field within the coil is a complicated function of both space and time (see figure 2-7). However, it is instructive to look at the field at the center of coils at the long solenoid limit ($l >> r$ see equation 2.12) and at the short coil limit ($r >> l$ see equation 2.13).

$$H = \frac{NI}{l} \tag{2.12}$$

$$H = \frac{NI}{2r} \tag{2.13}$$

The field within the coil is maximized be increasing the current (I), the number of turns (N), the density of turns ($\frac{N}{l}$) or decreasing radius of the coil. The physical coil parameters are limited by some practical considerations. I found the most restrictive

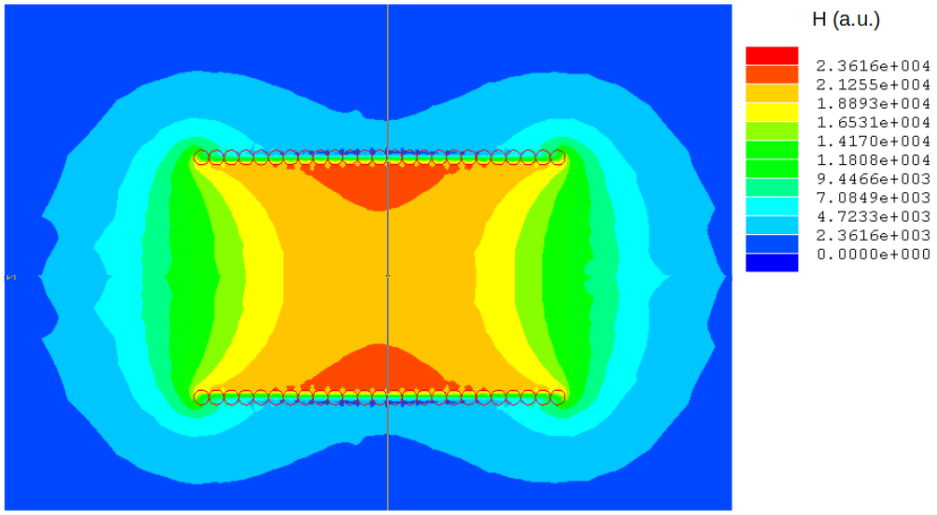

Figure 2-7: Magnetic field strength (H) within and outside an example coil ($N = 25$ and $\frac{l}{r} = 3$). This plot was made using Maxwell SV (a freely distributed lectrical engineering software - www.ansoft.com/maxwellSV.

of those limits to come from the biophysical characterization technique. The current parameter is limited by the ability of the amplifier to generate the necessary current. Assuming a larger amplifier can always be found, the limiting factor may be the heat dissipated but the coil.

Like any circuit element, the coil has some resistance. The heat dissipated by a coil ($P = I^2Z$ where Z is the impedance of the coil) scales by the square of the current (I). So, to ensure that the sample is not being heated by the resistive heating of the coil, cooling may be necessary. I found that about 40 standard cubic feet per hour (SCFH) of air (see figure 2-8) directly impinged on to the coil was sufficient to keep the inner surface of the coil sufficiently cool to both prevent damage to the coil itself, and to keep the sample from being heated. The temperature rise was $\sim 1^\circ$ C.

Coil for CD

One of the most useful biocharacterization techniques while working with the biomolecular switch targeting proteins is circular dichroism (CD). The general concept behind CD is that certain chiral molecules absorb left-hand circularly polarized light differently from right-hand circularly polarized light. The difference between the ab-

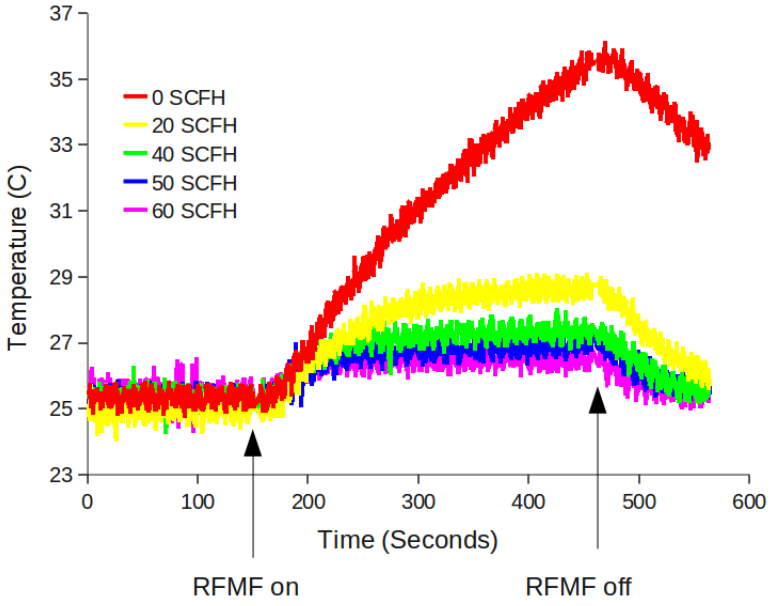

Figure 2-8: Temperature of the inner diameter surface of an example coil with various air flow rates within the cooling chamber around the coil.

sorbance as a function of the wavelength (190 – 250 nm) is the CD spectra. The secondary structure of a protein can be assayed by looking for characteristic CD spectra of the various types of secondary structure (see figure 2-9). CD spectra can be deconvoluted using freely available software such as CDSSTR [158] to give the secondary structure composition of the sample. Thus, the naturation state of a protein can be monitored by observing the transition from the native state to a totally random coil state.

To observe the naturation state of the protein in real-time during exposure to the RFMF, I designed a coil that could go into an Aviv 202 CD spectrometer in the The Biophysical Instrumentation Facility associated with CSBi. The primary design requirements for this coil were that it could be cooled, that it would be properly shielded (see section 2.3.3), and that it could deliver a relatively spatially uniform to the sample in a cuvette while the circularly polarized light probed the secondary structure of the sample. To accomplish these requirements and optimize the CD signal, I designed a custom cuvette (see figure 2-10) that has a 10 mm path length (the distance the light travels through the sample). It is made of strain free quartz, and it positions the sample that is being probed by the CD fully inside the coil (see

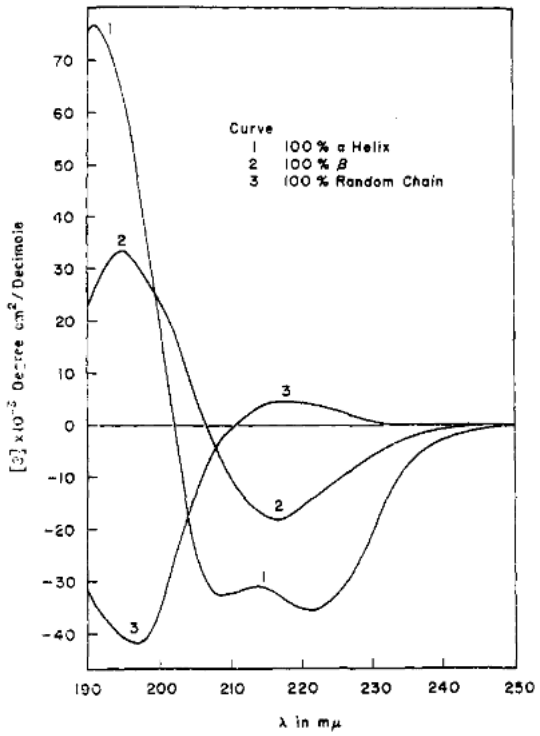

Figure 2-9: Circular dichroism spectra of poly-$_L$-lysine in the α-helical, β-sheet, and random coil conformations. Reprinted with permission from [57]. Copyright 1969 American Chemical Society.

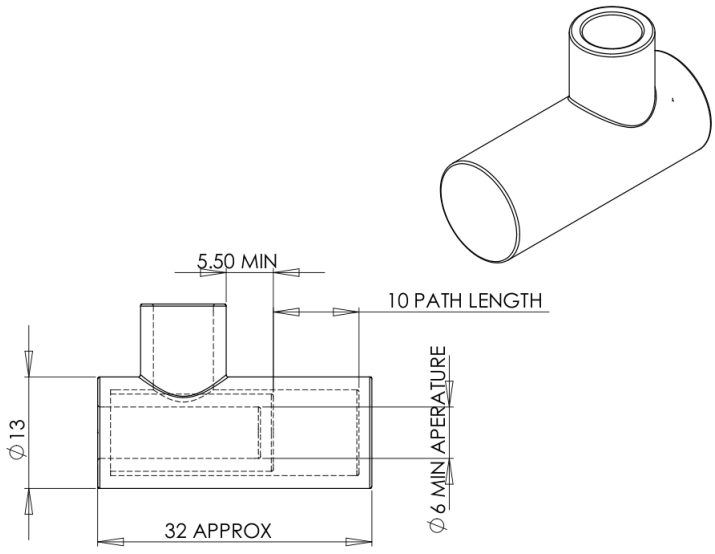

Figure 2-10: Schematic for the CD cuvette.

figure 2-11) and at the focal point of the CD. The diameter of the cuvette is as small as it can be, minimizing the amount of sample needed, yet still allowing the light to pass through based on the beam trace of the light through the CD's optics. The coil is

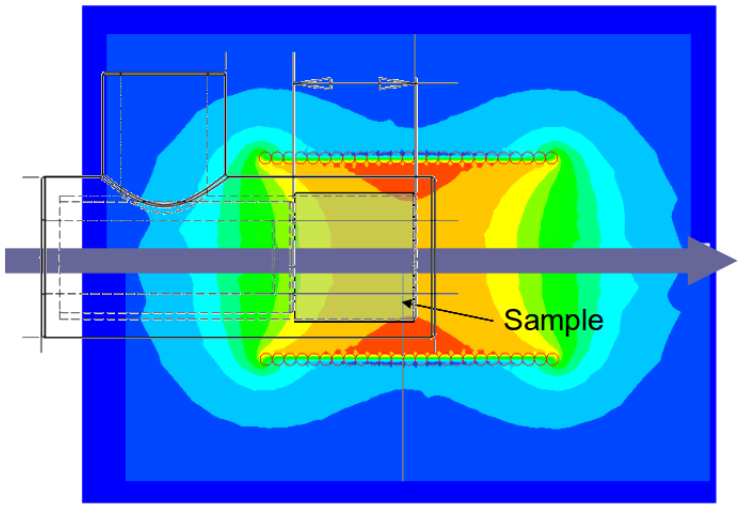

Figure 2-11: Diagram of CD sample within the coil. Color map shows the magnetic field intensity (a.u.) where red is high field and blue is low field strength.

designed to be as small as possible around the outside of the cuvette, thus maximizing the intensity of the magnetic field. The coil is wrapped around a base that is enclosed in an air jacket. This allows for a steady flow of air to be impinged directly on the coil without hitting the sample and adversely affecting the experiment.

The coil assembly is positioned such that the cuvette is directly in the light path of the CD (see figure 2-12). It is positioned and held fixed in all six degrees of freedom by a v-groove with a hard stop to position it along the axis of the groove. This whole thing is mounted onto a custom sample drawer that can slide into the Aviv 202, replacing the standard issue sample drawer. The coil is shielded within the CD to prevent any stray electromagnetic interference (EMI) from affecting the instrument. The shield cover is easily removable, so the gap where the cover meets the base is filled with an EMI gasket. There are a number of inlets and outlets to the sample chamber, and then from within the sample chamber to the shield. These are signal input and output, and cooling air input and output. The connections are made with BNC connectors and fluid quick disconnects respectively for maximum

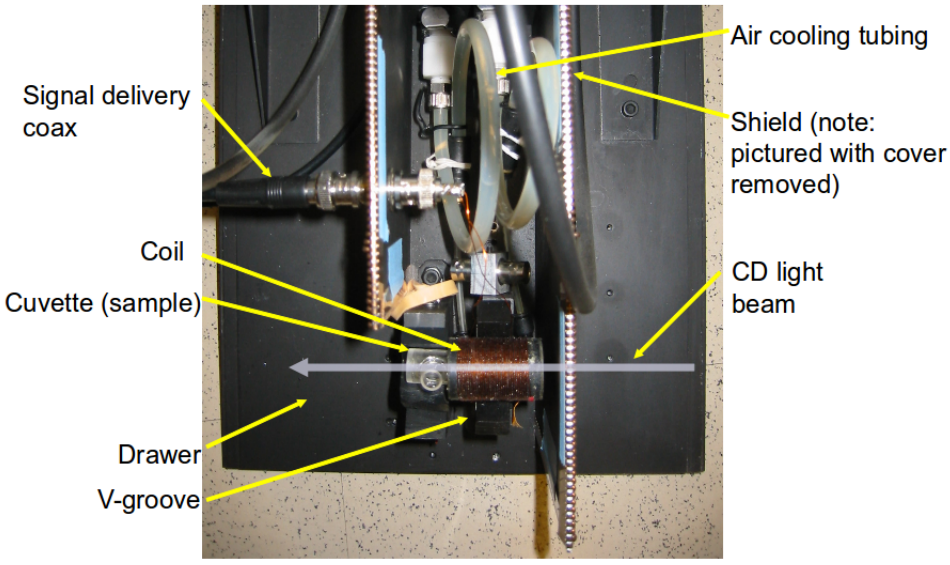

Figure 2-12: Photograph of the customized sample drawer. The top of the image is toward the front access point of the CD.

reconfigurability and flexibility.

The entire setup is specifically designed for the CD, but many of the components can be ported to other designs if necessary. The concept was to keep the system as module and reconfigurable as possible.

Coil for Fluorometer

Another important biophysical characterization technique is fluorescence spectroscopy. Since it is frequently easy to probe biomolecules' activity using fluorescence, I also designed a coil to work with the fluorometer.

Fluorometers pose a somewhat unique challenge for the RFMF system. They usually have their excitation and emission light paths at right angles to each other (see schematic 2-13). A consequence of this geometry is that the sample cannot lie within a solenoid because either the excitation or emission light will be blocked. One way around this is to use a Helmholtz coil. A Helmholtz coil consists of a pair of identical coaxial coils generally spaced such that the distance between the is equal to

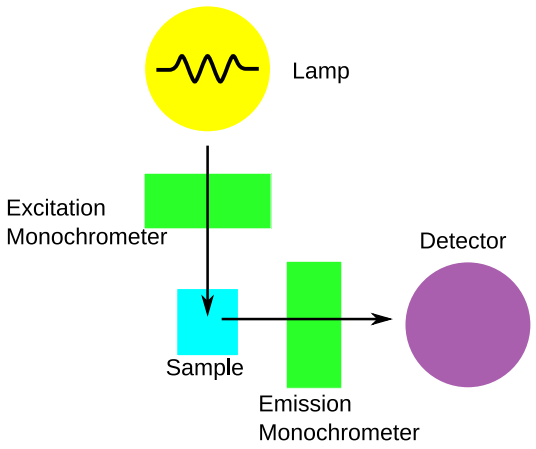

Figure 2-13: Schematic of the light path of a fluorometer.

their radius. This generates a nearly uniform magnetic field (H)

$$H = \left(\frac{4}{5}\right)^{\frac{3}{2}} \frac{N_H I}{r} \tag{2.14}$$

between them where N_H is the number of loops in each half of the Helmholtz coil. I built a Helmholtz coil with materials and techniques very similar to the CD coils for use in the fluorometer.

Coil for UV/Vis

Another widely used biocharacterization technique is spectrophotometry. Spectrophotometry is the precise quantification of a sample's color. Many biological molecules have relatively strong absorption spectra that are useful for a number of analyses. These include the identification of a sample's components based on their unique spectra, and measuring the concentration of these molecules with the Beer-Lambert Law (equation 2.15)

$$A = \epsilon_x(\lambda) C_x l_p \tag{2.15}$$

where

$$A = -\log_{10}\left(\frac{I_1}{I_0}\right) \tag{2.16}$$

is the absorbance of the sample, I_0 and I_1 are the intensities of the incident and transmitted light respectively, $\epsilon_x(\lambda)$ is wavelength dependent the molar extinction coefficient of molecule x, C_x is the concentration of species x, and l_p is the path length of light through the sample. Often spectrophotometry can be used to monitor biophysical changes in a sample, like aggregation, oxidation or reduction of an associated ion, and DNA hybridization.

Because spectrophotometry is such a versatile, it is advantageous to monitor absorbance while a sample is being exposed to an RFMF. I designed a system to incorporate a coil in to the Cary 100 UV/Vis spectrophotometer. Unlike the CD or the fluorometer, there is not enough space to put the sample in the UV/Vis itself. Instead I built a shield for the coil and a fixture to align the fiber ends of a fiber optic adapter. The fiber degrades the signal $\sim 10\%$. To ensure that the sample is within the coil, I used the custom cuvette designed for the CD (see figure 2-10).

2.3.3 Shielding

One complicating factor that cannot be ignored is the need to contain electromagnetic interference (EMI). Stray electromagnetic fields, generally known as EMI can be dangerous, particularly in a lab setting. Stray fields can induce potentially damaging currents in the circuitry of near by equipment or personal electronics like cell phones. As an example, an orbital shaker in the lab was known to increase its speed uncontrollably, one time throwing samples (luckily in plastic microcentrifuge tubes) more than 10 feet away, when the shielding around a coils was not sufficient. Even in cases without noticeable effects, EMI can cause inaccuracies in the output of analytical instruments like spectrophotometers.

The easiest way to mitigate this safety concern is to ensure that all electronic components within the biomoelcular control system are shielded. This means that they are placed within a faraday cage, which is a grounded electrically conducting enclosure with holes significantly smaller than the minimum wavelength of the fields

Table 2.2: Maximum gap size in an EMI shield.

Frequency	Gap size (in)
1 KHz	1.2×10^7
100 KHz	1.2×10^4
10 MHz	120
100 MHz	12
250 MHz	4.7
800 MHz	1.5
1 GHz	1.2
2.5 GHz	0.5

within. For fields with frequency (f) order 1 GHz the wavelength (λ) is

$$\lambda = \frac{c}{f} \tag{2.17}$$

where $c = 3 \times 10^8$ meters per second is the speed of light. So holes should be no larger than $\sim$ 1 inch (see table 2.2). This means that screws should be spaced on this length scale to ensure no EMI leakage, and that any shielding should allow for no gaps of any shape with a dimension larger than 1 inch.

I designed a shield for each of the coils that fit these parameters (see figure 2-12 for shield top mounting points and EMI gasket).

2.3.4 Transmission line effects

The primary challenges associated with the design of the field generating circuitry are that none of the components are ideal and the length of the cables necessary to connect all the components are, even at frequencies as low as 1 MHz, of the same order of magnitude as the wavelength ($\lambda \sim 1$ m). Transmission line effects cannot be ignored since the length of the cables are not $\leq 0.1\lambda$.

At high frequency, circuits experience losses due to energy being absorbed or reflected back to the source. These losses are know as transmission line effects. Transmission line theory states that a standing wave comprised of the forward and reflected voltages will result if the transmission lines and their associated loads are not

impedance matched. This can be done by ensuring the source impedance (Z_S), line impedance (Z_0) and load impedance (Z_L) as shown in figure 2-14 are all matched.

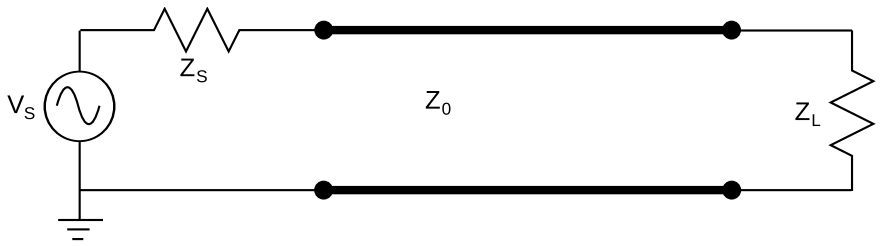

Figure 2-14: Schematic of a generic transmission line circuit. Z_S is source impedance, Z_0 is the line impedance, Z_L load impedance, and V_S is the source voltage.

The amplifier is our source. It has a 50 Ω termination on its output. So to prevent reflections, it needs to "see" a 50 Ω load. Thus we use 50 Ω cables. These selections are simple, and the components are commonly available. This real problem is that the load, which primarily contains the coil, does not necessarily have an impedance of 50 Ω. In general the impedance of the coil is both a function of the frequency $Z_L = Z_L(\omega)$, and the other elements in the circuit, like the connectors, and in close proximity to the coil which affect the "back Emf" by altering the electric field (E). All of this put together can be modeled with an RLC (resistance, inductance, capacitance) circuit. An impedance analyzer like Agilent E4991A can be used to get a number of potential models for the load. As an example, I determined that one coil in the CD drawer can be modeled as in figure 2-15. Another way to account for the

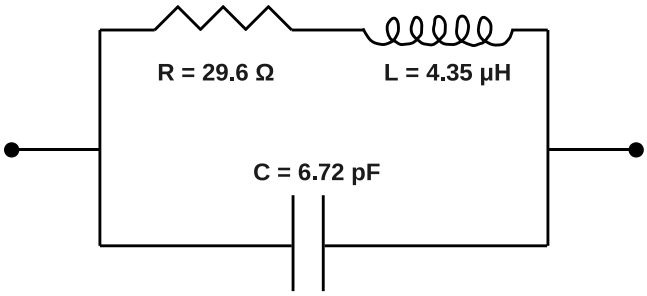

Figure 2-15: Schematic of the model of a RFMF producing coil as determined from an impedance analyzer.

impedance of the load is to use a vector network analyzer (VNA) like Agilent 8753ES to determine $Z_L(\omega)$. The coil (same coil as the one modeled in figure 2-15) most

closely approaches the 50 Ω impedance value at ∼ 875, 940, 1110 and 1225 MHz (see figure 2-16). This data suggests that the highest energy transmittance to the coil will be at these frequency, thus limiting the potential for varying the field.

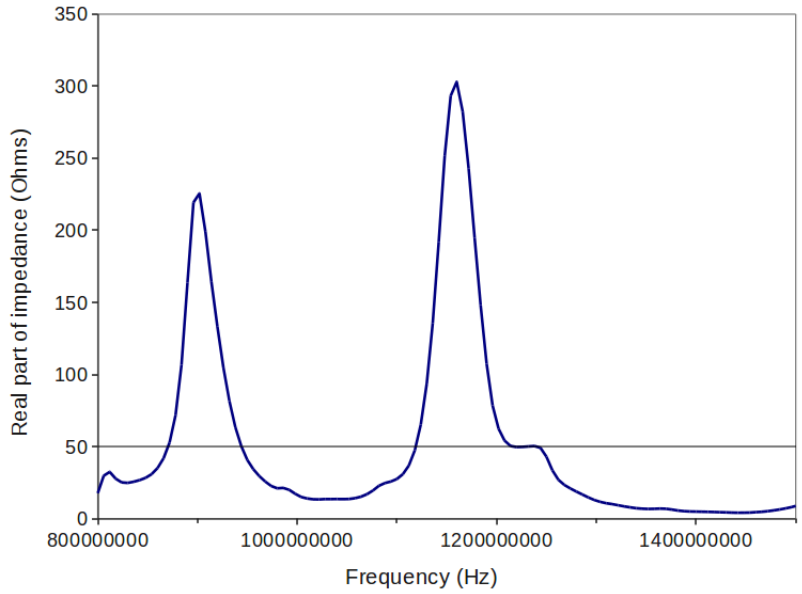

Figure 2-16: VNA output for the coil in the CD drawer. The system is impedance matched when the real part of the load's impedance is 50 Ω.

If the frequencies that happen to satisfy the impedance matching are unsatisfactory for the application, there are some circuits design techniques to improve the situation. The simplest solution is to use what is known as "stub matching."[122] This modifies $Z_L(\omega)$ by adding either shorted or open length of coaxial cable to the load at particular locations. Stubs can broaded the matched regions as well as shift them. Another method is to introduce a secondary set of electrical elements that provide either passive broadband impedance matching or reactive impedance matching,[122] known as a matching network.

Careful consideration of the electrical engineering and RF engineering design must be considered to build a circuit that can successfully deliver the field to the biological switch. There are simulation tools to help with this design including Cadence Design Systems PSpice student version, which enables the prediction of the current as a function of the frequency (figure 2-17).

To maximize the current at the coil, I used a combination of all these techniques,

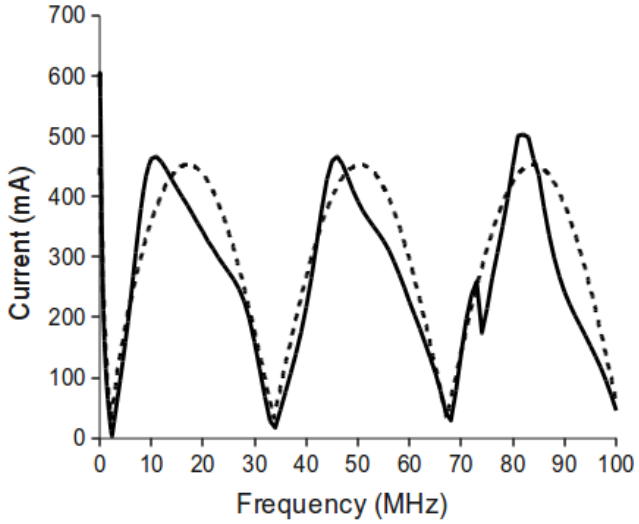

Figure 2-17: Current passing through the coil in the CD drawer as a function of the frequency. Solid line is experimental data, dashed line is a simulation using the impedance analyzer determined RLC circuit model of the load (see figure 2-15). The model is an output from PSpice.

other than making a matching circuit. If the reader is interested in matching circuits I would direct you to Shahriar Khushrushahi's Master's Thesis.[91]

2.4 Global heating of ferrofluids

To experimentally determine the power output per particle (SAR), I used global heating experiments. The procedure is to subject a very highly concentrated solution of magnetic nanoparticles to a RFMF, and measure the temperature as a function of time. From this data, and a few other known parameters, I calculate the power output of the average particle (P). I then assume that this is the power output per particle in the biomolecular control system, when the concentration of NPs is much lower.

The primary assumption of this calculation is that each particle heats the solvent in the control volume immediately surrounding it. The boundary between these control volumes is adiabatic. This is is a no flux, or symmetric, boundary condition (see figure 2-18) on the spherically symmetric heat conduction equation (Fourrier's

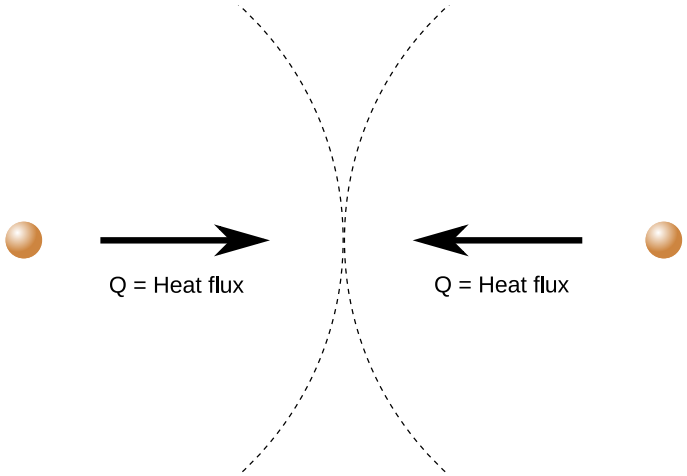

Figure 2-18: Schematic diagram of the heat flux in a global heating experiment. The boundary between control volumes (shown as the dotted line) is at $r = r_0$.

Law: $q = -k \bigtriangledown T$) at $r = r_0$ where

$$r_0 = \frac{d_0}{2} = \left(\frac{3}{4\pi C_x N_A} \right)^{\frac{1}{3}} \tag{2.18}$$

and d_0 is the mean particle spacing (see figure 2-19) and N_A is Avogadro's number. As seen in figure 2-19, a concentration of 1 nM corresponds to about 1.5 μm and 1 mM corresponds to about 15 nm.

Therefore, based on conservation of energy, the power output per particle (P) is

$$P = \frac{(\rho_{NP} C_{p,NP} \phi_{NP} + \rho_{solvent} C_{p,solvent} \phi_{solvent})}{C_{NP} N_A} \frac{dT}{dt}. \tag{2.19}$$

Equation 2.19 suggests that, given all other parameters are constant with time, the temperature of a ferrofluid evolves linearly with time

$$T = T_0 + \frac{P}{(\rho_{particle} C_{p,particle} V_{particle} + \rho_{solvent} C_{p,solvent} V_{solvent})} t, \tag{2.20}$$

where T_0 is the initial temperature of the NP solution.

I performed global heating experiments with all particles of interest (see section 2.1), but as a representative example, I will show the results using EMG 507 magnetite NPs. The sample (39 μM) was placed in a glass tube and held at the

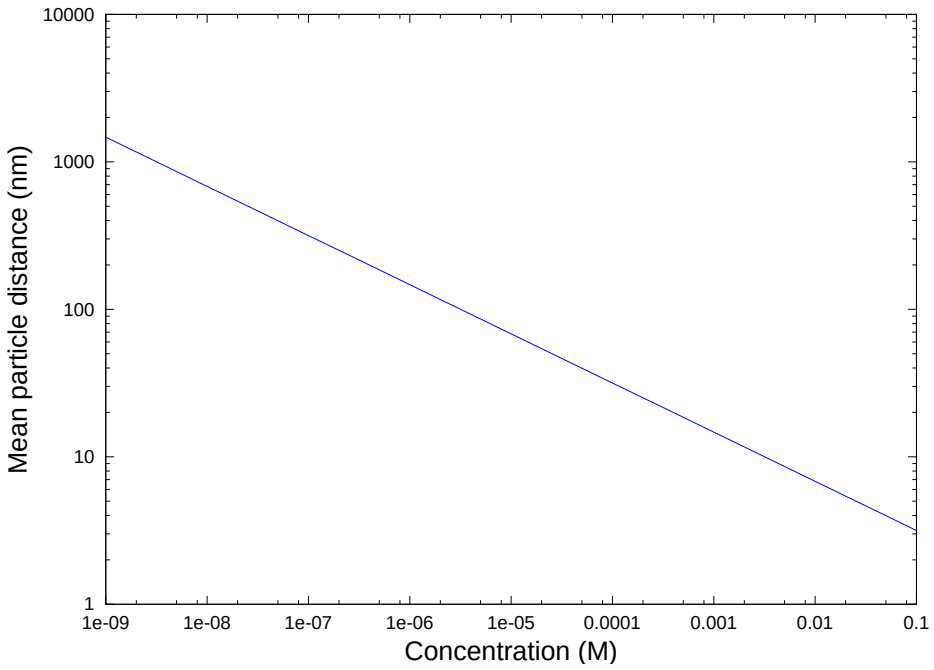

Figure 2-19: Plot of the mean particle spacing as a function of concentration.

axis of the coil. A Luxtron FOT temperature probe system was used to record the temperature as a function of time. A probe, which consists of a thermally sensitive fluorescent ceramic that fluoresces as a function of the temperature jacketed in Teflon at the end of a fiberoptic cable, was placed in the fluid to probe its temperature. This type of fluorescent temperature probe is necessary because of the high electric and magnetic fields within the sample. A standard thermocouple would not give accurate results because of the currents that would be induced within the thermocouple by the RFMF.

As seen in figure 2-20, the temperature does not evolve linearly with time. Equation 2.20 predicts that the sample will never reach a steady state temperature ($T(t) \rightarrow \infty$ as $t \rightarrow \infty$). There are a number of factors affecting this, but the primary factor is the heat flux out of the sample. Based on the geometry of the sample and a fixed temperature boundary condition at the edge of the sample, the analytical solution to Fourrier's Law yields the temperature as a function of time,

$$T = \triangle T_{SS} \left(1 - \exp\left(-\frac{t}{\tau_{SH}}\right)\right) + T_{\infty}, \tag{2.21}$$

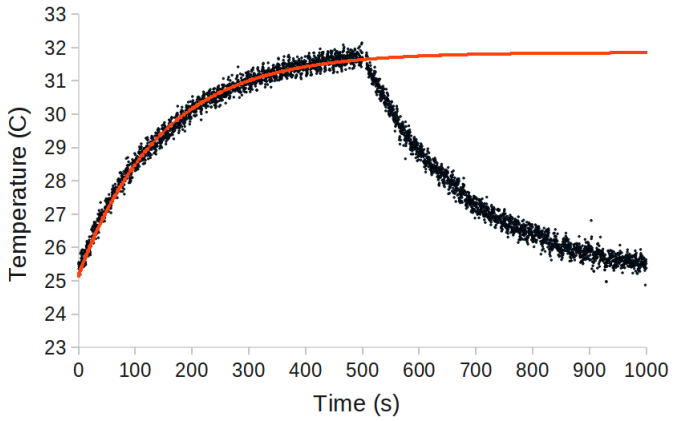

Figure 2-20: Example global heating data (EMG 507 - black dots) with best fit line (red line). $\triangle T_{SS} = 6.7°$ C, $\tau_{SH} = 145$ s where τ_{SH} is the time constant associated with dissipation from the sample holder, and $T_\infty = 25.2°$C with $R^2 = 0.9896$. RFMF of frequency = 1.1 MHz was turned on at $t = 0$ and turned off at $t = 500$ s.

where $\triangle T_{SS}$ is the temperature rise of the sample at steady state, τ_{SH} is the characteristic thermal diffusion time constant of the sample holder in the coil, and T_∞ is the ambient temperature far from the sample and the initial temperature of the entire system. Recall that in equation 2.19 P is proportional to $\frac{dT}{dt}$ under adiabatic conditions. Taking the first derivative of equation 2.21,

$$\frac{dT}{dt} = \frac{\triangle T_{SS}}{\tau_{SH}} \exp\left(-\frac{t}{\tau_{SH}}\right) \tag{2.22}$$

and solving for $t \to 0$, the time that most closely approaches the adiabatic solution (at $t = 0^+$ the flux out of the sample is 0), we get

$$\left.\frac{dT}{dt}\right|_{t\to 0} = \frac{\triangle T_{SS}}{\tau_{SH}}. \tag{2.23}$$

So, we simply need to find the initial slope of $T(t)$ data as in figure 2-20 to calculate the power output of each particle as a function of the frequency. It should be noted that there are a number of factors that need to be carefully controlled in this non-adiabatic formulation of the global heating experiment including the affect of the temperature probe and the environment close proximity to the sample.[121]

At this point it is critically important to recall the transmission line effects. If

the coil is not impedance matched for all frequencies, there will be clear peaks in $P(f)$ not predicted by equation 2.7, because without broadband impedance matching $H = H(f)$. This is seen clearly in figure 2-21.

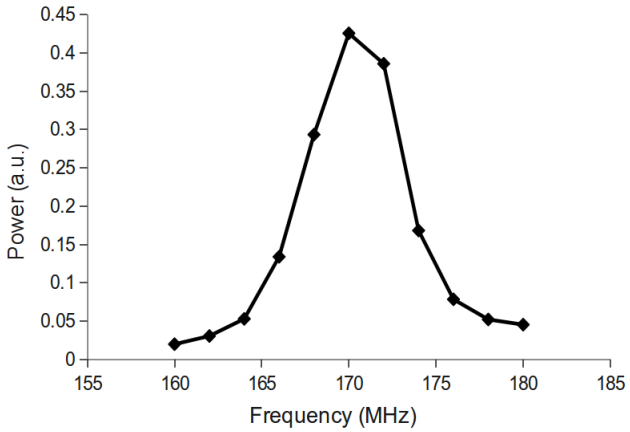

Figure 2-21: Power output per particle of EMG 507 ferrofluids near an impedance matched frequency.

Though these values are highly dependent on the field ($P \sim H^2$ from equation 2.7), table 2.3 has some of the highest power outputs per particle I measured with the CD coil. Note that these values are representative, and are provided just to give an idea of the order of magnitude possible of heat dissipation that is practically feasible from the setup described above. Some of the data were obtained under less than optimal conditions. The EMG 507 data is the maximum feasible power output per particle for these particles on this setup. The value was obtained at a frequency were the coil was closely impedance matched. Any higher current through the coil and thus larger H results in melting of the coil due to resistive heat dissipation.

Table 2.3: Power output for selected magnetic nanoparticles

Magnetic NP	Power output per particle $\left[\frac{\text{W}}{\text{particle}}\right]$	Power output per NP mass $\left[\frac{\text{W}}{\text{g}}\right]$
EMG 507	3.1×10^{-16}	80
EMG 705	1.3×10^{-17}	3.3
Au doped Fe	1.9×10^{-17}	4

2.5 Local heating of magnetic nanoparticles

To characterized the biomolecular control system, I performed experiments looking at the structure of a protein in close proximity to the NP as it is exposed to an RFMF. The idea being that if the structure is changed from the native conformation to a denatured state when the field is on, and if it recovers its native conformation when the field is removed, then a biomolecular activity switch has been achieved as in the local denaturation model (section 1.5.1 and figure 1-11).

2.5.1 Theoretical analytical temperature profiles in magnetic field heating

The solution to the heat conduction problem in which a heat generating sphere is suspended in an infinite solvent has an analytical form.[53] Under the assumption that the magnetic nanoparticles are spherical, that there is infinite thermal interface conductance between the particle and the solvent, that the continuum approximation holds, and that the primary mode of heat transfer is conduction, the temperature within the particle is

$$T(r) = \frac{r_{NP}^2 \frac{P}{V_{NP}}}{k_{NP}} \left[\frac{k_{NP}}{3k_{solvent}} + \frac{\left(1 - \frac{r^2}{r_{NP}^2}\right)}{6} - \frac{2r_{NP}b}{r\pi} \int_0^\infty \Phi(y)\, dy \right] \tag{2.24}$$

where $\Phi(y) = \dfrac{\exp\left(-\frac{\alpha_{NP} t y^2}{r_{NP}^2}\right)}{y^2} \dfrac{(\sin y - y\cos y)\sin\left(\frac{ry}{r_{NP}}\right)}{[c\sin y - y\cos y]^2 + b^2 y^2 \sin^2 y}$.[53] The temperature of the solvent is

$$T(r) = \frac{r_{NP}^3 \frac{P}{V_{NP}}}{r k_{NP}} \left[\frac{k_{NP}}{3k_{solvent}} - \frac{2}{\pi} \int_0^\infty \Psi(y)\, dy \right] \tag{2.25}$$

where $\Psi(y) = \dfrac{\exp\left(-\frac{\alpha_{NP} t y^2}{r_{NP}^2}\right)}{y^3} \dfrac{(\sin y - y\cos y)[by\sin y\cos(\sigma y) - [c\sin y - y\cos y]\sin(\sigma y)}{[c\sin y - y\cos y]^2 + b^2 y^2 \sin^2 y}$

with parameters $b = \dfrac{k_{solvent}}{k_{NP}} \sqrt{\dfrac{\alpha_{NP}}{\alpha solvent}}$, $\sigma = \left(\dfrac{r}{r_{NP}} - 1\right) \sqrt{\dfrac{\alpha_{NP}}{\alpha solvent}}$, and $c = \left(1 - \dfrac{k_{solvent}}{k_{NP}}\right)$ true for both equations 2.24 and 2.25. These equations are based on the initial conditions that the temperature within the sphere and the solvent is

0 everywhere (thus $T(r)$ is actually temperature rise). The boundary conditions are that $T(r)$ as r approaches 0 is finite and that $T(r)$ as r approaches infinity is 0. The continuity conditions are that the temperature and the heat flux ($k\frac{\partial T}{\partial r}$) are equal at $r = r_{NP}$. The treatment of the boundary condition at $r = r_{NP}$ is somewhat uncommon. In classical texts, when the analysis is for macro-scale spheres, the assumption that $T(r = r_{NP}) = T_\infty$ is ok for many problems, but at the nm length and the ps time scales, this is not the case.

Just a quick note on the continuum approximation for heat. When classical laws are applied at the nanometer length-scales care must be taken to ensure they still hold. For example, the definition of temperature is somewhat dubious at the atomic scale because, for a solid, it is a measure of the average kinetic energy of material lattice points about their mean. Additionally, the concept of a continuous temperature field is somewhat suspect within a nanoparticle. In general, a material can be assumed to be continuous if it is significantly larger than the mean free path of the primary energy carrier, which in the case of conduction is the quantized vibration unit - the phonon.[26] Within the nanoparticle this is probably not true. The phonon mean free path is assumed to be on the order of the distance between grain boundaries, but can also be affected by lattice vacancies, impurities, and other forms of local disorder.[157] In a 10 nm particle is likely either to be single crystal or to have a small number of boundaries. In some magnetic materials the phonon mean free path could be as large as $0.1 - 5.0\mu$m. However, for a liquid, the phonon mean free path may be just a couple angstroms.[26] Even though equation 2.24 may not hold for our system, equation 2.25 does. This approximation is acceptable because the particle's temperature is nearly uniform because the thermal conductivity of the NP is much greater than the solvent, and the timescale for phonon scattering is much shorter than energy dissipation so temperature fluctuations are averaged out over a longer period of time. Additionally, we are not generally concerned with the details of the temperature distribution within the particle when investigating the biomolecular control mechanism.

2.5.2 Magnetoferritin experiments

To test the ability of RFMFs to control the confirmation of a biomolecule, I used magnetoferritin (see section 2.1 and figure 2-2) as both the NP and the protein. This is an ideal system because there is no chemical conjugation necessary, as ferritin is a protein shell around a NP in nature, and it has spherical symmetry. Additionally, ferritin is primarily α-helical (see figure 2-2B), so that its naturation state can be easily assayed by with CD. The change in the α-helicity is can be monitored by changes in the CD signal at 222 nm (see figure 2-9).

Magnetoferritin synthesis

The chemistry behind growing the magnetite particle in the magnetoferritin synthesis procedure is an oxidation reaction.[24]

$$3Fe^{2+} + 2O_2 \longrightarrow Fe_2^{3+}Fe^{2+}O_4 \tag{2.26}$$

The ferritin acts as oxidation enzyme. The enzymatic action of ferritin is not fully understood, but it is thought to be a relatively complicated mechanism. First, there are iron uptake channels due to the 3-fold symmetry of the arrangements of ferritin subunits. The distribution of charge in and around these channels are highly conserved across all forms of life. This distribution of charge results in an electrostatic "funnel" that is thought to guide Fe^{2+} ions to the channels.[37] Once inside, other charged amino acids (6 glutamic acid residues E61, E64 and, E67 from each of two neighboring monomers primarily on the light chain) guide the Fe^{2+} to the nucleation centers.[24, 37] Those nucleation centers consist of three amino acids, E27, E62 and H65, found only on the heavy chain.[96] There, the iron nanoparticle is started and grown.

The synthesis of magnetoferritin[111] takes advantage of the native particle formation mechanism. The conditions are altered such that the resulting particle takes a different form. The synthesis procedure can be broken down into two primary steps. First the native particle needs to be removed. Second, the magnetite particle needs

to be grown within the protein shell (see figure 2-22). I did this in two ways. For

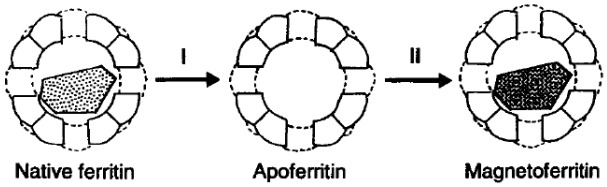

Figure 2-22: Schematic of magnetoferritin synthesis procedure. From F. C. Meldrum, B. R. Heywood, and S. Mann. Magnetoferritin: *in vitro* synthesis of a novel magnetic protein. *Science*, 257(5069):522, 1992. Reprinted with permission from AAAS.

some samples I purchased apoferritin, the ferritin molecule without the particle, from Sigma directly. For others I performed both steps in the lab.

Horse spleen ferritin in a saline solution at 38 $\frac{\text{mg}}{\text{mL}}$ (or 86 μM based on 440 kDa molecular weight of ferritin) was obtained from Sigma. 2 mL of as supplied ferritin was added to 10 mL of 100 mM sodium acetate buffer at pH 4.5. This solution was dialyzed against 1 L of 100 mM thioglycolic acid (TGA) plus 1 L of 100 mM sodium acetate using a 10 kDa dialysis bag. After 5 hours the dialysis was stopped because the sample turned clear, indicating the loss of the NP from the ferritin. About half way through this time the TGA/sodium acetate was refreshed. The sample was then dialyzed against 150 mM saline solution for 12 hours, changing the saline once. The final solution was concentrated using a Savant Speed Vac Plus rotary evaporator. The concentration was measured using the Cary 100 and the extinction coefficient for ferritin ($\epsilon_{ferritin}(280\text{ nm}) = 396{,}000\ \frac{1}{M\,cm}$).

To grow the magnetite particle within the apoferritin, 4 mL of 1 μM apoferritin in 50 mM AMPSO (N-(1,1-Dimethyl-2-hydroxyethyl)-3-amino-2-hydroxypropanesulfonic acid) at pH = 8.5 were degassed. The degassing procedure involves preparing AMPSO well ahead of time and storing it under vacuum. Just before use, argon is bubbled through the apoferritin in AMPSO for 15 minutes. Degassing is critical because addition of the Fe^2+ in an environment rich in oxygen results in rapid oxidation. The iron is not incorporated into the particles and falls to the bottom of the flask in a rust colored precipitate. A solution of 24 mM Fe^2+ was prepared by dissolving ferrous ammonium sulfate [$(NH_4)_2Fe(SO_4)_2 \cdot 6\ H_2O$] in deaerated water. This solution was

added to the apoferritin sample under argon with a syringe pump at the rate of 1 drop every 1 minute. To encourage the formation of the magnetite nanoparticle, the pH was 8.5 while the temperature of the solution was held between 55° and 60° C. Slow oxidation was achieved by bubbling of air into the solution at a rate of 1 bubble every 15 minutes. The addition of ferrous ammonium sulfate to the apoferritin solution resulted in increasing cloudiness and increasingly greenish black discoloration.

After the synthesis, the magnetoferritin was purified. Any iron not taken up by the apoferritin forms an aggregate and falls to the bottom of a tube under light centrifugation. The supernatant contains the magnetoterritin. We did not have a way to remove any remaining apoferritin. We had tried magnetic separation, but because the particles are so small, a magnetic field does not generate a large enough force to cause separation.

Characterization

The characterization of magnetoferrin is necessary to determine the size of the particle, the naturation state of the protein component, and the magnetic properties. To do this I used a variety of techniques including CD, SQUID, XPS, ICP-OES, and UV-Vis spectrophotometry.

Since CD is used to monitor the denaturation state of the ferritin in the local heating experiments, baseline data was taken on ferritin in the CD. The folded room temperature spectra (see figure 2-23 blue lines) shows the characteristics of a primarily α-helical protein, with a clear minimum at 222 nm. Also from figure 2-23, it is clear that a temperature rise of $\sim 10°$ C is sufficient to assay changes in secondary structure.

We are also interested in the determining the size of the particles within the magnetoferritin cage. The simplest way to measure this is with TEM, but iron atoms have a relatively small nucleus so they do not scatter many electrons. With particle sizes of less than 8 nm in diameter, TEM was prohibitively difficult. So, I used a combination of spectrophotometry and inductively coupled plasma atomic emission spectroscopy (ICP-OES). The Cary 100 spectrophotometer was used to quantify the protein content of the sample using $\epsilon_{ferritin}(280\text{ nm})$ and Beer-Lambert's Law (equa-

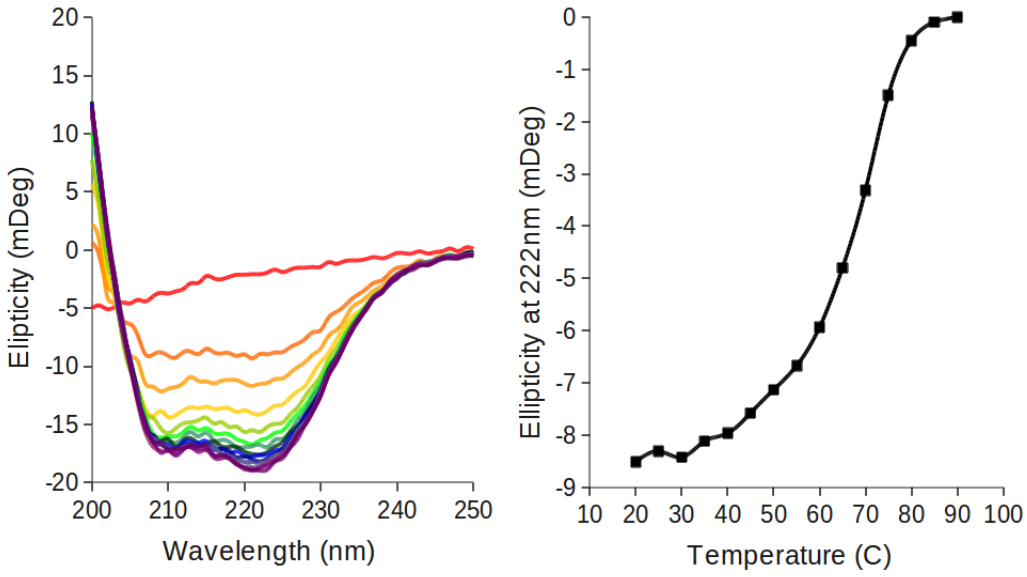

Figure 2-23: Effects of temperature on CD spectra of ferritin. Temperature ranges from 20° C (purple) to 95° C (red). The melting curve, plot on the right, indicates a melting point of 65° C.

tion 2.15). ICP-OES uses the inductively coupled plasma to excite the atoms and ions of the sample so that they emit light at wavelengths characteristic of a particular element and chemical state.[159] The intensity is directly proportional to the concentration of the element within the sample. We found that a typical 1 μM solution of magnetoferritin contains about 1.4 mM iron atoms. Thus the average particle, assuming that each ferritin molecule has a particle, has 1400 atoms. I estimate that the average size of these particles is about 5.5 nm in diameter. This is quite a bit short of the optimal theoretical loading of 4500 atoms and about 8 nm particles.

In an attempt to determine the chemical state of the iron within the magnetoferritin's particle and thus understand its magnetic properties, I performed x-ray photoelectron spectroscopy (XPS) using a Kratos AXIS Ultra Imaging X-ray Photoelectron Spectrometer in the CMSE. XPS is used to determine the elemental composition, empirical formula, chemical state or electronic state of the elements within a material by measuring the kinetic energy (KE) and the number of electrons that escape from the top 1 to 10 nm of the material being irradiated by an x-ray beam with known energy. If the NP within the magnetoferritin were FeOOH (the native particle) the binding

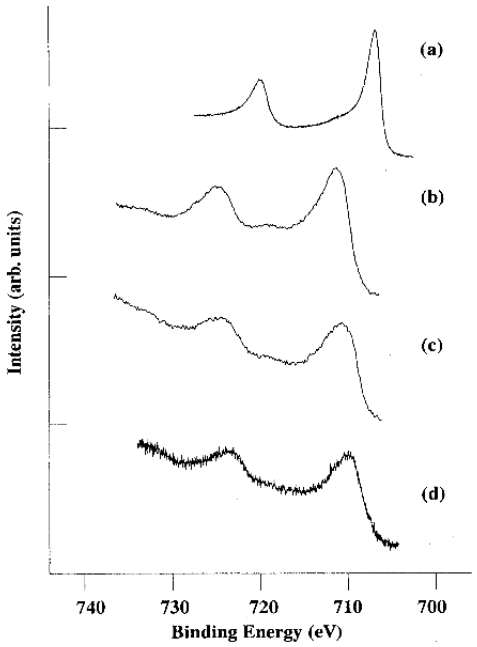

Figure 2-24: XPS spectra of various iron compounds. (a) BE of Fe $2p_{3/2} = 706.8$ eV. (b) BE of FeOOH $2p_{3/2} = 711.4$ eV. (c) BE of Fe_2O_3 $2p_{3/2} = 710.7$ eV. (d) BE of Fe_3O_4 $2p_{3/2} = 710.1$ eV. Copyright 1989 by The American Physical Society.[176]

energy (BE) of the Fe 2p would be 711.4 eV.[176] If the NP within the magnetoferritin were Fe_3O_4 (magnetite) the BE of the Fe 2p would be 710.1 eV (see figure 2-24).[176] So the change in binding energy between FeOOH and Fe_3O_4 is 0.74 eV. The results of XPS on native ferritin and magnetoferritin (see figure 2-25) show a change in binding

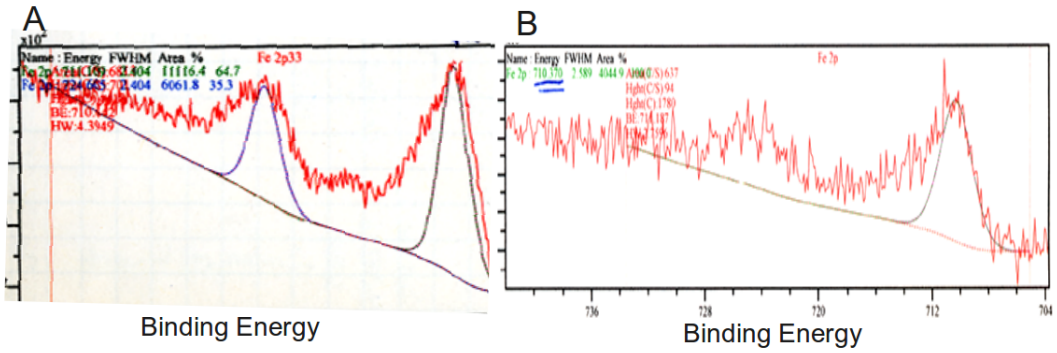

Figure 2-25: XPS spectra of A) native ferritin and B) magnetoferritin. BE of ferritin $2p_{3/2} = 711.10$ eV. (b) BE of magnetoferritin $2p_{3/2} = 710.37$ eV.

energy between of 0.73 eV. That the difference in BE is nearly identical indicates a high likelihood that the ferritin contains an FeOOH particle and the magnetoferritin

contains a magnetite particle.

The final physical characterization of the magnetoferritin I did was magnetometry using a superconducting quantum interference device (SQUID) on the Quantum Design AC and DC Magnetic Property Measurement System at CMSE. SQUID is used to measure extremely small magnetic fields, and the technology is based on superconducting loops containing Josephson junctions.[16] The output is a magnetization curve of the sample like that shown in figure 2-3.

I performed SQUID magnetometry on the magnetoferritin, ferritin, and EMG 507 NPs. The primary challenge associated with performing SQUID (at least in the CMSE facility) is that $\geq$ 10 mg of NP is required to get a signal. The results (see

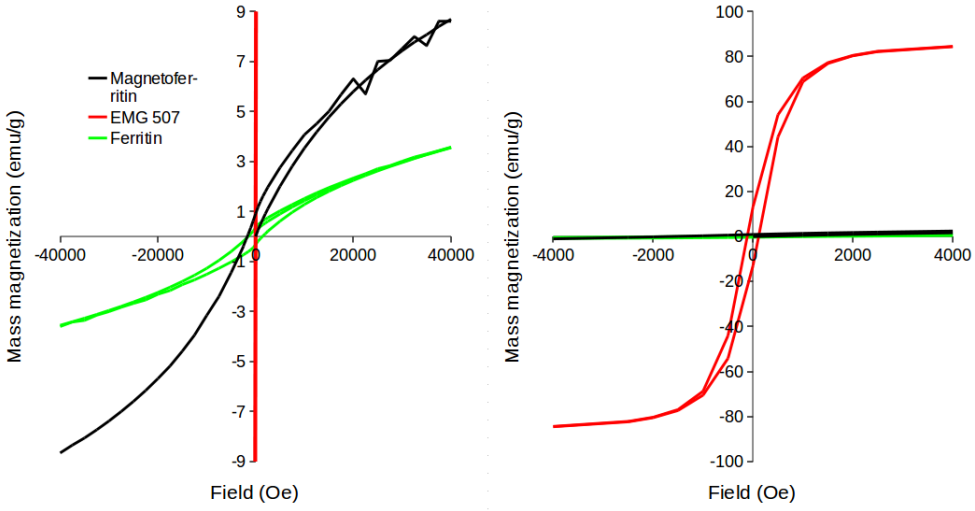

Figure 2-26: SQUID data of magnetoferritin, ferritin, and EMG 507 NPs. Note that the right plot has a different scale on both axes.

figure 2-26) show that the magnetoferritin is slightly more magnetic than ferritin, but significantly less so than EMG 507. There is some indication that the magnetoferritin NPs are superparamagnetic, but the SQUID was not conclusive. A major source of error here could be the amount of sample. It is easy to get enough EMG 507, but there may not have been enough magnetoferritin to adequately trust the SQUID results.

When taking account for all the characterization data on magnetoferritin, it appears that magnetoferritin is likely to have magnetite nanoparticles, but they are smaller than is ideal for the biomolecular switch demonstration.

Local experiment results

I put a sample of $\sim$ 10 nM magnetoferritin, despite the questionable characterization results detailed above, in the CD cuvette and loaded it into the coil inside the custom CD drawer. The drawer was placed into the CD and the cooling air was started. The CD was setup to record the ellipticity at 222 nm as a function of time. After 5 minutes of baseline data, the field was turned on at 67.5 MHz, a frequency predetermined to be impedance matched by the VNA, and the maximum field practical for the setup. Data was collected for 10 minutes (see figure 2-27) and no changes were observed.The magnetoferritin does not heat up locally in sufficient magnitude to alter the secondary structure.

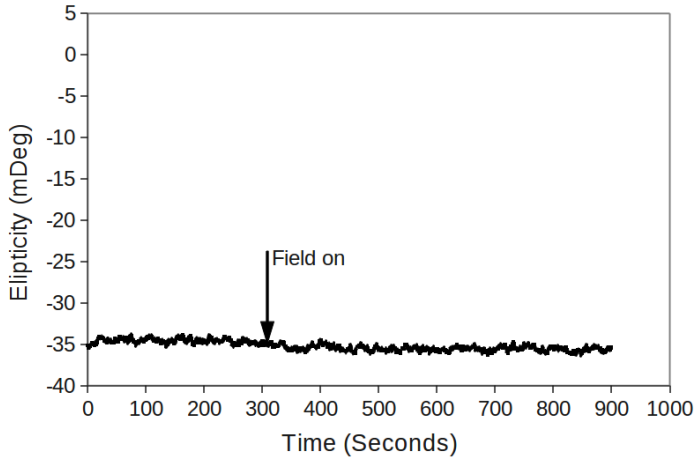

Figure 2-27: Local heating results for Magnetoferritin. The field was turned on at the arrow, but no changes in secondary structure were noted.

2.5.3 Discussion of local heating using magnetic fields

The experimental results indicate that the system I tried is not sufficient to demonstrate that an RFMF can be used to control biomolecular structure and thus activity. There are questions that remain. Did the biomolecular activity switch fail because one or two parameters are out of the "operating window"? Did it fail because the field generating setup used is not sufficient? Did it fail because RFMFs and the Néel, Brownian and hysteresis heating modes cannot heat a particle locally?

Time scales

One way to think about the thermal requirements of the biomolecular activity switch is by comparing time constants. Recall that in the discussion about local thermal confinement (section 1.4.5) I introduced the dissipation time constant (τ_D). In the local heating experiment (section 2.5.2) $d \sim 10^{-8}$ nm and $\alpha \sim 1.4 \times 10^{-7}\ \frac{m^2}{s}$ so $\tau_D \sim 25 - 100$ ps. The effective dissipation time constant $\tau_{eff} \sim 10^{-8} - 10^{-6}$ s. Even if τ_{eff} is at the short end of this range, it is still at least 2 orders of magnitude greater than τ_D. This means that during the time of relaxation, the energy transport out of the particle is more rapid than conversion of magnetic field energy to heat. Thus the temperature of the particle cannot rise above the solvent.

The global heating samples do show a significant temperature rise because $\tau_D << \tau_{\mathrm{SH}} = 145$ s (see figure 2-20). Based on this analysis, for very small particles, $\tau_D \sim \tau_{eff}$ if the effected zone $d \geq 200$ nm. For larger particles $\tau_D \sim \tau_{eff}$ if the effected zone $d \geq 2\ \mu$m. So if the goal were to affect entire cells, this analysis predicts that there are some set of parameters that should work.

Another consequence of this analysis is for applications where larger areas are to be heated in a hyperthermia application, for instance in tumor hyperthermia, the concentration of NPs must be such that the distance between particles is at most 200 nm to 2 μm, depending on the particle size. This corresponds to a concentration range from 500 nM to 0.5 nM NPs depending on particle size. Thus the physical and practical limits of RFMF heated NP hyperthermia are sensitive to the NP size.

This analysis does not take into consideration the magnitude of the energy converted by to heat by the NPs per unit time (the specific power output of the particles).

Power scales

Based on the CD spectra as a function of temperature, a temperature rise of about 10° C is necessary to see any appreciable change in secondary structure of ferritin. This analysis uses this as an order of magnitude estimate for any conjugated biomolecule. The energy necessary to raise the particle and the next nearest 5 nm 10°C assuming

adiabatic heating is $\sim 1.7 \times 10^{-16}$ J. Note that from conservation of energy and the definition of specific heat, the energy (E) necessary is

$$E = \sum_i \rho_i C_{p,i} V_i \triangle T \tag{2.27}$$

where i represents each of the elements in the heated zone.

There are a couple ways to think about this number in the context of this system. First, based on the calculated max power output per particle (see table 2.3), it takes 2 seconds to heat this zone. Recall that $\tau_D \sim 25 - 100$ ps. So before the particle can convert enough energy to heat to elevate the temperature of the particle, the heat has dissipated. Second, based on the calculated max power output per particle (see table 2.3), the temperature of the zone rises $\sim 2 \times 10^{-9\circ}$ C. Finally, to get the required 10° C temperature rise of the nearest 5 nm to a NP it would require about 1.7×10^{-6} $\frac{\text{W}}{\text{particle}}$. In each of these formulations it is clear that the setup cannot deliver enough energy fast enough to get a local temperature rise.

There is one additional resource to which I would point the interested reader to analysis by Pawel Keblinski et al.[88] They come to the same conclusions about using RFMFs to heat NPs in a slightly different way. They alos point out that for the same reasons, continuous wave laser heating of NPs cannot be used to heat on the nanometer length scale.

What it would take to make RFMF work

The simplest solution is to use the setup as is in an application that is physically and practically possible. Basically this would involve using the RFMF and a ferrofluid to heat a system, as in direct thermal control (see section 1.2.3). If the ferrofluid could be spatially localized, it could provide a control system in much the same way other "local" heating systems can, like those using MEMS devices to deliver heat locally.[184] This is a recast application of hyperthermia, which has been used to selectively heat cells,[65] and to treat cancer.[130, 64, 33, 170]

Another potential solution is to increase the field strength such that the power is

sufficient to achieve local thermal confinement. The power needs to be $\sim 5.5 \times 10^9$ times higher than it is now. Recalling that power scales with H^2 (see equation 2.7), H would have to be increased by a factor of $\sim 7.4 \times 10^4$. Though this is technically challenging, it is possible. Amplifier Research sells amplifiers as high as 50,000 W (ours is 100 W). For about $1,000,000 we could get two and a half of the 4 and a half orders of magnitude improvement necessary. By changing the coil design and improving the matching networks, it is possible to get within an order of magnitude. This could work out, but it is not practically possible for our lab.

Of course there are potential problems with this plan. The generated fields would be extremely high, so lots of safety assurances would have to be implemented. The coil would certainly need to be redesigned to carry the very high current, and lots of lab infrastructure would need to be improved (power supply, cooling capacity, etc.).

Even beyond the practical, with such a high power input the temperature of the entire sample could rise if the particles are not far enough apart. Recall that the time constant associated with the sample holder (τ_{SH}) is 145 s. Clearly the sample holder would almost certainly need to be redesigned, but lets assume it would have a similar time constant. To ensure the whole sample does not heat, the heat dissipation time constant associated with the solvent area around each nanoparticle must be greater than τ_{SH}. Based on equation 1.1 the particle spacing needs to be 20 mm, or have a concentration of order 10^{-21} M. This means that one particle would be sufficient to measurably heat the entire sample over time. To mitigate this problem, we could reduce the duty cycle of the field. In effect, this recommendation is to apply a "ultrafast-pulsed" RFMF field.

The final conclusion is that the RFMF cannot work for an ideal biomolecular switch as defined in chapter 1. The dissipation time constants are just too fast compared to the relaxation time constants. Even if this were not the case (if the NPs were very small), producing the power necessary to affect a change in a conjugated biomolecule requires a RFMF with such a high magnitude magnetic field and such a low concentration of particles, that it is simply not practical as a bench-top laboratory biological engineering tool.

Chapter 3

Laser mediated control

As I showed at the end of the last chapter, heating nanoparticles by RFMFs is not sufficiently rapid to heat the particle appreciably above the immediate surroundings. To accomplish this temperature rise, the energy to heat the NP must be absorbed significantly faster than energy dissipates. One way to deliver energy to NPs this fast is with pulsed laser irradiation which have peak powers (P_{max})

$$P_{max} = \frac{E_{pulse}}{t_{pulse}} \tag{3.1}$$

on the order of 10^{11} W where the energy per pulse $E_{pulse} \sim 10$ mJ and the length of the pulse $t_{pulse} \sim 100$ fs.

Put another way, the dissipation of heat from a NP is governed by a diffusive process where the coefficient of thermal diffusion in an aqueous solvent is $\alpha = 1.38 \times 10^{-3} \frac{m^2}{s}$. It is governed by the heat equation

$$\frac{\partial \theta}{\partial t} = \alpha \nabla^2 \theta \tag{3.2}$$

where θ is the temperature rise as a function of space and time. From a scaling analysis, the characteristic length (L) scales with the square root of characteristic time (τ)

$$L \sim \sqrt{\alpha \tau}. \tag{3.3}$$

For the biomolecular switch $L \sim 10^{-8}$ m so the relevant characteristic time $\tau \sim 10^{-13}$ s. This indicates the need for ultrafast pulsed lasers. Continuous wave (CW) lasers have $\tau \sim 10^{1}$ s so they can generate temperature changes on the characteristic length scale $L \sim 10^{-2}$ m. This is why CW lasers are useful for medical applications on the tissue scale, but are not feasible on the molecular or cellular length scales.

In this chapter, I will discuss the theoretical basis of using pulsed laser irradiation to control biomolecular activity. I will discuss the mechanism by which laser light generates a local temperature rise in the nanoparticle. I will also discuss a number of the critical elements of a laser actuated biomolecular control system. These include a discussion about the laser specifications, critical characteristics of the nanoparticle, and nanoparticle interfaces with the biological element. Finally I discuss my experimental results, including characterization of the thermal properties of the NR ligand layer.

3.1 Optically active NPs

Nearly all NPs interact with light as a function of the light's wavelength. Some are types of NPs particularly interesting. Quantum dots (QDs) are inorganic semiconductor nanocrystals (diameter = 2 – 8 nm) that possess unique luminescent properties. They are smaller than the exciton Bohr radius which leads to a quantum confinement effect and thus their unique optical and electronic properties.[21, 4] QDs are often used in place of molecular fluorophores, in biological imaging,[90] FRET,[110] and therapeutic[186] applications because their thermal efficiencies are higher. Metallic NPs also possess unique optical properties due to their absorption and scattering properties.[89] In particular the noble metal NPs are of interest, including various shapes of silver and gold NPs.

3.1.1 Gold nanoparticles

The optical properties of gold nanoparticles were known about and used as early as the 4th and 5th centuries to color glass, and later in the middle ages for diagnosis

and treatment of diseases. More recently, gold nanoparticles have been studied extensively for potential biological applications that exploit their optical and electronics characteristics along with their biocompatibility, ease of conjugation, and stability.[30]

Gold nanoparticles are spherical clusters of gold atoms 1 – 100 nm in diameter. It is this size that gives rise to a natural frequency of the mobile electrons in the gold lattice equal to the frequency of visible photons. This resonance frequency of electrons along the NP surface is called surface plasmon resonance (SPR), and it is the physical characteristic most responsible for the optical properties of gold nanoparticles.

Gold NPs are only soluble in water if stabilized by a ligand. The aqueous, organic, or two-phase chemical synthesis procedures for gold NPs always include a ligand, often citrate, but also alkane thiols, lipids and polymers.[30]

Gold particles have been successfully used in a number of biomolecular applications, including DNA delivery,[25] DNA antisense amplification,[149] sensing amplification,[120, 180] and medical applications like imaging.[19] The chemical nature gold NPs enables site-specific conjugation to proteins, which is key to maintaining the structure and function of conjugated biomolecules.[12]

3.1.2 Gold nanorods

Even when compared to spherical gold particles, Au nanorods (NRs), due to their lack of spherical symmetry, have unique optical properties. NR synthesis conditions control the NR's aspect ratio (AR),[118] and, because the AR determines the surface plasmon resonance,[105, 112, 45] NRs can be tuned to absorb in the near infrared "optical window," where water and tissue do not absorb light strongly.[72]

Because of the NR specific absorption spectra and the thermal confinement phenomenon, picosecond (ps) and femtosecond (fs) pulsed laser excitation at the SPR specifically heats Au NRs and not the surroundings.[105, 47, 7] Consequently, NRs have been used for applications such as photothermal cancer therapy,[124, 9] triggered delivery,[68, 92, 25, 179, 163] and targeted destruction of microorganisms.[127, 139] The optical properties also make NRs attractive surface enhanced Raman spectroscopy (SERS) substrates,[141, 126] and imaging applications.[71, 2]

I selected gold NRs to focus the energy of the laser onto the target biomolecule in the biomolecular activity switch for their biocompatibility, ease of conjugation, and optical properties. For this reason, the remainder of this thesis will focus on the techniques and methods used to design a biomolecular activity switch using gold NRs excited by ultrafast pulsed laser irradiation.

3.1.3 The "optical window"

The optical properties of Au NRs make them particularly attractive for this application because, by slightly adjusting the synthesis procedure, the SPR of Au NRs can be tuned to the "optical window" (see figure 3-1). The "optical window" is the band

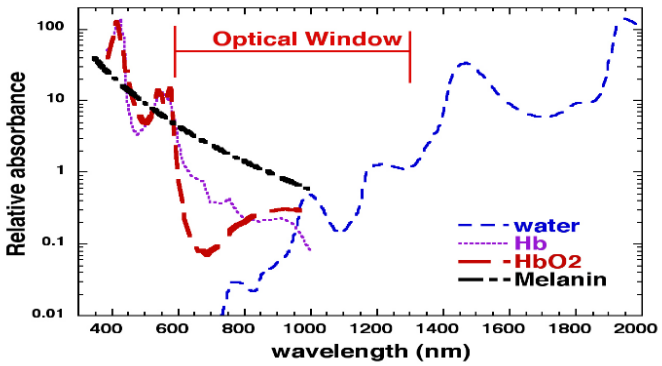

Figure 3-1: The "optical window." Hb: hemoglobin, HbO_2: oxygenated hemoglobin, and melamin. Figure adapted from Huang et al. 2009.[72]

of light wavelengths in the near infrared (NIR) between 600 nm and 1200 nm where penetration of light into tissue is maximal. Neither the primary tissue chromophores (hemoglobin, oxygenated hemoglobin, and melamin) nor water absorb light strongly within this band. Ultrafast laser systems are often near in the 700 – 1200 nm range. This ensures that the energy from the laser is indeed absorbed preferentially by the NRs.

Even though NIR light is not strongly absorbed by tissue, the laser intensity, φ, is attenuated as a function of the characteristic optical penetration depth (δ) of the tissue.[160]

$$\varphi = \varphi_0 \exp\left(-\frac{x}{\delta}\right) \tag{3.4}$$

where φ is the laser intensity, φ_0 is the incident intensity, and x is the distance into the tissue. See table 3.1 for some values of δ at $\lambda = 780$ nm for various tissues.

Table 3.1: Penetration depth (δ) of selected tissues at $\lambda = 780$ nm. All data from [160] except * from [8].

Tissue	δ [mm]
Blood	0.42
Liver	1.04
Lung	1.86
Mammary	3.12
Brain	2.17
Muscle	3.46
Dermis	0.06*

3.1.4 Mie/Gans theory

The features of the absorption spectrum of gold nanoparticles are primarily attributed to the plasmon resonance of electrons in the conduction band of the gold lattice. Mie first solved Maxwell's equations for the radiation of an electromagnetic field interacting with a spherical gold particle under the appropriate boundary conditions.[112] Gans extended Mie's theory to account for ellipsoids,[45] which gold NRs closely resemble. The extinction coefficient (ϵ_{AuNR}) of randomly oriented gold NRs according to Gans is[104]

$$\epsilon_{AuNR} = \frac{2\pi[\text{NRs}]V_{NR}\epsilon_m^{\frac{3}{2}}}{3\lambda}\sum_j \frac{\frac{\text{Im}(\epsilon_{Au})}{P_j^2}}{\left(\text{Re}(\epsilon_{Au}) + \frac{1-P_j}{P_j}\epsilon_m\right)^2 + \text{Im}(\epsilon_{Au})^2} \tag{3.5}$$

where ϵ_m is the relative dielectric constant of the medium immediately surrounding the particle, ϵ_{Au} is the wavelength dependent relative complex dielectric constant of gold,[80] λ is the wavelength of the interacting light, and P_j are the depolarization

factors for the three axes A, B, and C of the rod with $A > B = C$. They are

$$P_A = -\frac{1}{1-AR^2}\left[\frac{1}{2\sqrt{1-\frac{1}{AR}^2}}\ln\left(\frac{1+\sqrt{1-\frac{1}{AR}^2}}{1-\sqrt{1-\frac{1}{AR}^2}}\right)-1\right] \tag{3.6}$$

and

$$P_B = P_C = \frac{1-P_A}{2}. \tag{3.7}$$

Note that the complex dielectric constant of gold, when the particle size approaches the mean free path of a conduction electron ($\sim$ 10 nm), deviates from the bulk gold values.[161]

Equations 3.5, 3.6, and 3.7 predict that as the AR approaches 1 (the particles are spherical) there is a peak in ϵ_{AuNR} near $\lambda = 530$ nm. As the AR increases, this peak splits in two. The redder peak, due to the plasmon resonance of the longitudinal direction of the NR, red shifts as a function of the AR (see figure 3-2), while the bluer peak, due to the plasmon resonance of the transverse direction of the NR, is relatively insensitive to the AR. As the longitudinal plasmon resonance redshifts, the extinction

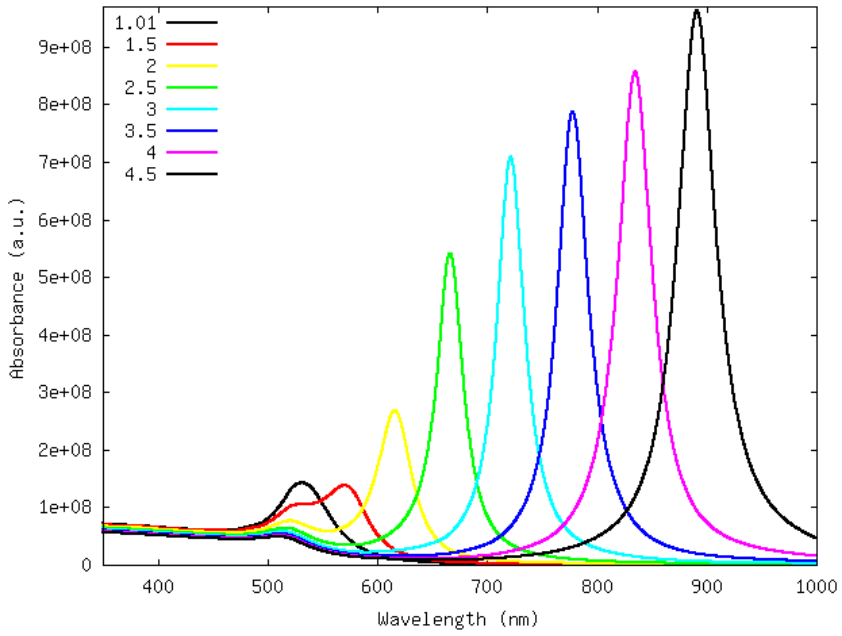

Figure 3-2: Calculated absorption spectra of gold NRs using equation 3.5 for various aspect ratio NRs. The NRs have the same volume, but different aspect ratios.

coefficient also gets bigger. In contrast, the extinction coefficient at wavelengths to the blue side of the transverse plasmon resonance are relatively independent of aspect ratio.

3.1.5 Synthesis techniques

The wet chemistry synthesis of gold nanorods was pioneered primarily by the Murphy and El-Sayeed groups at the University of South Carolina and Georgia Institute of Technology respectively.[76, 77, 125] For the interested reader there are a number of nice reviews on Au NRs that include excellent sections on synthesis.[136, 118] Independent of the actual chemical technique, the basics of NR synthesis remain the same. It is a two step chemical synthesis. First, NRs are nucleated by the addition of a fast reducing agent to a solution of gold salt. Second, the NRs are grown by the further reduction using a slow reducing agent in the presence of hexadecylammonium bromide (CTAB). The CTAB coordinates to particular crystal planes on the gold particles stronger than others. This allows for growth on the faces with the weakest coordination. NRs grow along the [100] axis, and the sides are the {110} and {100} crystal facets.[107]

NR growth is assisted by a small amount of silver which seems to act in concert with the CTAB as a surface ligand on the sides preventing further growth in that direction.[107] NR growth can be additionally regulated by altering the surfactant. For example, using a binary surfactant, CTAB/BDAC where BDAC is benzyldimethylammonium chloride, yields long aspect ratio NRs.[125]

There are other synthesis techniques including electrochemical growth and templates syntheses. Since I did not use these techniques, they will not be covered here. The interested reader should refer to [136].

Seed mediated synthesis

The most commonly used synthesis procedures are seed mediated syntheses.[117] The two step process consists first of making ~ 4 nm Au nanoparticles by rapidly reducing

gold salt rapidly with $NaBH_4$ in the presence of hexadecyltrimethylammonium bromide (CTAB) or sodium citrate. Then the gold seeds are added to a growth solution containing primarily $_L$-ascorbic acid, gold salt and CTAB. The second stage takes much longer due to the slower reducing nature of ascorbic acid. Over a period of about 20 minutes, the solution takes on the characteristic reddish, brownish purple color of Au NRs. The entire growth process is completed in about 3 hours.

Seedless synthesis

A less common synthesis procedure is a non-seeded method.[78] NRs can be synthesized in relatively small quantity (just a couple mL of a 1 – 5 nM solution) or in gram-scale.[78] All of the NRs used in the experiments that follow were synthesized using this seedless procedure.

The basics of the procedure are given here. For specifics of any particular NRs used in a particular experiment, see the experimental details of that experiment. First, a CTAB and sodium chloride solution was made up. Generally the CTAB concentration is high enough (>100 mM) that it is marginally stable at room temperature. So, the CTAB solution was heated and stirred to get all the CTAB to dissolve. To that solution small volumes of relatively high concentrations Au (III) chloride trihydrate ($HAuCl_4 \cdot 3\ H_2O$) and silver nitrate ($AgNO_3$) were added. Upon agitation, this turns the solution yellow-brown. Next, $_L$-ascorbic acid (AA) was added, which turned the solution clear after $\sim$ 30 s of agitation by inversion. Finally ice cold sodium borohydride ($NaBH_4$) was added, and the solution was agitated by inversion for $\sim$ 30 s. The solution was left at room temperature for $>$ 3 h while it turned deep purplish brown, but the final color is highly dependent on the NRs' aspect ratio. It is critical that the temperature of the NR sample remain at or above 25° C for the duration of synthesis or the CTAB will crash and affect the final NRs.

NRs were washed and concentrated by centrifugation for a time and speed dependent on the size of the sample, i.e. 15 min and 10,000 relative centrifugal force (RCF) for a 1.5 mL solution. With higher volume synthesis centrifugation was done in 40 mL batches in 50 mL tubes six at a time on a Sorvall Evolution Superspeed centrifuge

(thank you Prof. Van Vliet and the Van Vliet lab!) for 1 hour at 7000 RCF. It is critical that the temperature of the NR sample remain at or above 25° C for the duration of centrifugation or the CTAB will crash and foul the highly concentrated NR sample in the pellet. After centrifugation, the supernatant was removed and replaced with 1 mM CTAB. NRs were washed 3 × to remove excess reagents. The NR solution was stored at 100 nM in 1 mM CTAB. They are stable for at least 6 months in this state.

Tuning Au NR aspect ratio

A critical aspect of the synthesis is the NR's size and shape sensitivity to the exact synthesis protocol. By adjusting the concentration of silver, and the relative amounts of the two reducing agents, the aspect ratio and size can be adjusted. This is critical for optical applications because the optical properties are highly dependent on the NR's size and shape (see section 3.1.4).

I performed a brief experiment to examine the effect of SPR on the amount of silver. I synthesized five samples all exactly the same, except for varying the silver content. As expected, the NR's SPR is a strong function of silver (see figure 3-3). Note that the exact ratio of Ag to Au in the solution that maximizes the wavelength of the longitudinal SPR may not be the same for all syntheses. In this example (see figure 3-3), a ratio of 0.175 : 1 maximized the longitudinal SPR. So, by simply adjusting the synthesis, the SPR can be easily changed, and depending on the planed end use of the NRs, they can be tuned up to about 805 nm. To get higher SPRs, a two surfactant synthesis is needed.[125]

3.1.6 Ligands

Like any nanoparticle, gold NRs must be stabilized in solution or they will aggregate and precipitate out of solution. The most energetically favorable configuration for gold is to reduce surface area and form bulk gold. To avoid this, a ligand layer is used on the surface of the NRs. The ligand layer stabilizes the NR in two primary ways. First, it can sterically hinder aggregation by physically separating NRs. Second, ligands can

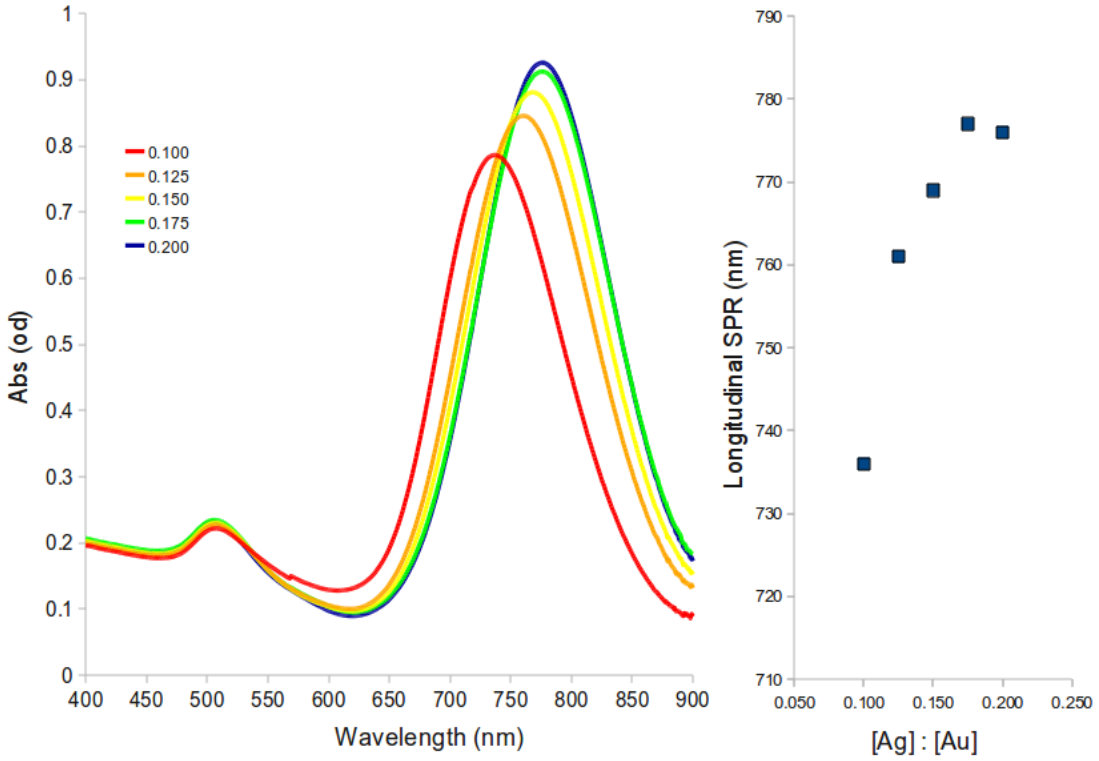

Figure 3-3: The effect of silver in NR synthesis. Left: Absorption spectra of NRs synthesized with various silver to gold ratios ($\frac{[\mathrm{Ag}]}{[\mathrm{Au}]}$). Right: Longitudinal SPR as a function of $\frac{[\mathrm{Ag}]}{[\mathrm{Au}]}$.

electrostatically repel neighboring NRs by being charged. Derjaguin and Landau,[36] and Verwey and Overbeek [172] developed what is know as DLVO theory to describe the energy of interaction between nanoparticles, V_T. It is the sum of electrostatic repulsion due to Debye double layer and the van der Waal's attraction:

$$V_T = 2\pi\epsilon_0\epsilon_m a\zeta^2 \exp(-\kappa d_0) - \frac{A_h a}{12 d_0} \tag{3.8}$$

where ϵ_0 is the electrical permittivity of free space, ϵ_m is the relative permittivity of the medium, ζ is the surface potential (zeta potential), κ^{-1} is the Debye length, d_0 is the mean particle separation and a is the particle radius. $A_h = \pi^2 C\rho_1\rho_2$ where A_h is the Hamaker constant, C is the coefficient in the particle-particle pair interaction, and ρ_1 and ρ_2 are the number of atoms per unit volume of two adjacent particles. Note, $\kappa a << 1$ in equation 3.8. A total energy barrier of 15 – 20 $k_B T$ is required to keep the particles stable.[63]

CTAB

As was mentioned above, the most common gold NR synthesis protocols require the ligand hexadecyltrimethylammonium bromide (CTAB, see figure 3-4).[118] Note that CTAB actually stands for the general cetyltrimethylammonium bromide. The specific cetyltrimethylammonium bromide necessary used in the synthesis of NRs is one with a 16 carbon alkyl tail, technically C_{16}TAB, but CTAB will be used for brevity.

Figure 3-4: Hexadecyltrimethylammonium bromide (CTAB)

CTAB is a surfactant, and, like all surfactants, it is amphiphilic. The prevailing theory in the literature is that the tertiary amine headgroup of CTAB coordinates preferentially to certain facets of Au nanoparticles which directs NP growth along the [110] crystal direction.[118] How it does this is still largely unknown. There is

some evidence that the 16 carbon chain length is critical.[46] It is also possible the bromine ion is also necessary for NR growth.[118] Additionally there is a clear role of Ag in all this (see section 3.1.5) What is known is that coordination of the amine head to the Au leaves the hydrophobic alkyl chain tails of the CTAB protruding from the surface of the NRs. In the presence of enough free CTAB in aqueous solution, additional CTAB molecules coordinate with these tails to form a bilayer. This bilayer stabilizes the NRs, and it prevents their aggregation through steric and electrostatic interactions.

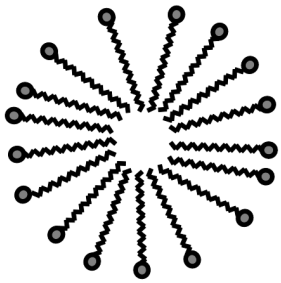

Figure 3-5: CTAB micelle schematic. The hydrophobic tails aggregate together leaving only the hydrophilic heads exposed to the water. This creates a hydrophobic pocket in aqueous solution.

Free in solution, CTAB will form micelles (see figure 3-5). The critical micelle concentration (cmc), the concentration necessary for spontaneous formation of micelles, is $\sim$ 1.2 mM,[14, 168] though this is a function of ionic strength and temperature. The cmc is a critical parameter because the physical and chemical properties of the CTAB ligand layer vary greatly near the cmc. As an example, CTAB-NRs are stable in the aqueous phase at room temperature for months if the concentration of CTAB is kept at or above the cmc. However, if the concentration of CTAB is significantly below the cmc, the NRs will aggregate.

Though CTAB does an excellent job at keeping the NRs stable, for many biological applications, including many of the strategies using the biomolecular activity switch, CTAB is not a desirable ligand. CTAB is toxic, and CTAB coated NRs are highly unstable in most biological buffers. For these reasons, we performed ligand exchange on the NRs to get other molecules on the surface.

Mercaptoalkyl acids

Mercaptoalkyl acids (MCAs, see figures 3-6, 3-7, and 3-8) are another commonly used ligand for gold NPs. They consist of a carboxyl functional group at one end and a thiol functional group at the other of carbon chain. MCAs covalently bond to gold NPs by virtue of the strong affinity of the gold thiol bond. At nearly all relevant pH ranges they are negatively changed, thus they stabilize NPs primarily by electrostatic repulsion.

Figure 3-6: Mercaptohexanoic acid (MHA), carbon chain length = 6 carbons

Figure 3-7: Mercaptoundecanoic acid (MUDA), carbon chain length = 11 carbons

Figure 3-8: Mercaptohexadecanoic acid (MHDA), carbon chain length = 16 carbons

The challenge in using MCAs, or really any ligand other than CTAB, on NRs is replacing the CTAB bilayer. It is difficult to displace the CTAB because the bilayer's affinity for the gold is due to both the coordination of the amine to the gold, and the hydrophobic interactions between two layers of 16 carbon length chains. To displace CTAB, I use a "round-trip" ligand exchange protocol developed by Andy Wijaya.[178] Described here briefly, 1 mL of 10 – 100 nM CTAB coated NRs are extracted from the aqueous phase to the organic phase by 1 mL of dodecane thiol (DDT) in the presence of acetone (4 : 1 ratio – acetone : NR solvent). The DDT displaces the CTAB. This is favorable because the Au-thiol bond is stronger than the Au-amine, and the bilayer

is disrupted by the hydrophobic solvent. The excess DDT is then washed away by 5 : 1 methanol : toluene. NRs are then washed in toluene. The NRs are extracted back to the aqueous phase by 9 mL of 1 mM MCA in toluene. This extraction is done at $\sim 90^{\circ}$ C and while being stirred. When the NRs settle to the bottom, they are no longer stable in the organic phase indicating the presence of the MCAs on the surface. The excess MCA in toluene was removed after light centrifugation, and the NRs were washed in toluene. After at least 3 washing cycles, the NRs were washed once in isopropyl alcohol to deprotonate the MCAs. The isopropyl alcohol is then washed out, and the NRs are finally resuspended in 1 $\times$ tris-borate-EDTA buffer (TBE).

For various experiments, I used any of three MCAs, including mercaptohexanoic acid (MHA - figure 3-6), mercaptoundecanoic acid (MUDA - figure 3-7) and mercaptohexadecanoic acid (MHDA - figure 3-8). As described in reference [178] exchanging the shorter MCAs is difficult. It fails a large percentage of the time. The hypothesis is that the MCAs have trouble replacing the DDT, even in great excess of the MCA, if the MCA's alkyl chain is significantly shorter than the DDT. So, for ligand exchange of MHA, I used hexanethiol instead of DDT with great success.

Polyetholyene glycol

Polyethylene glycol (PEG) is another very common nanoparticle ligand. PEG (see figure 3-9) is a neutral ligand often used to passivate surfaces to minimize fouling with biological materials. When used on gold particles, PEG is generally thiolated so

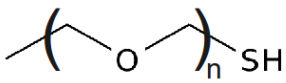

Figure 3-9: Methyl-polyethylene glycol-thiol (mPEG-Thiol)

it covalently conjugates to gold. The other end of PEG can also be functionalized, however we primarily used methylated PEG to prevent reaction with other elements in the system. PEG is a highly hydrophilic molecule. It is very useful in aqueous

solution. PEG can come in a variety of lengths, usually specified by molecular weight. The experiments detailed in this thesis use one of three lengths: 356, 1000, or 5000 Da which correspond to n = 7, 22, 112 (see figure 3-9) respectively.

The ligand exchange procedure for PEG is relatively simple. When incubated in 1 mM mPEG-thiol, the MCA coat will be displaced by the PEG from MCA-NRs. Incubation overnight at room temperature is sufficient to do the ligand exchange.[178] After exchange, the PEG-NRs were washed by changing out the supernatant of repeated centrifugation cycles.

Polyelectrolytes

Another way of functionalizing NRs is to coat them with polyelectrolytes. A polyelectrolyte is a polymer whose repeating units have an electrolyte group. These groups dissociate in aqueous solutions leaving the polymers charged. The most common way of putting polyelectrolyte layers on surfaces is with the layer-by-layer (LbL) deposition method. The fundamental principle of LbL is that negatively charged poleyelctrolytes adsorb onto positive surfaces. They are so highly charged that the net charge of the surface is changed from positive to negative. Then another, oppositely charged polyelectrolyte can be introduced, and it will adsorb on the first layer. This can be repeated to form many layers. As long as both polyelectrolytes are strong polyelectrolytes, then the properties of the thin film formed from LbL deposition is not a strong function of the solvent pH or ionic strength.[40] There are many applications that use this technique, but it has most promisingly been used in controlled drug release applications.[28]

The polyelectrolytes we used were both strong polyelectrolytes. Specifically they are polysodium 4-styrenesulfonate (PSS) and poly(diallyldimethylammonium) chloride (PDADMAC) (see figure 3-10). To deposit the polyelectrolyte layers on the NRs I loosely followed a procedure in the literature.[54] I prepared 10 $\frac{\text{mg}}{\text{mL}}$ stock solutions of PSS (70 kDa, 30% by weight in water) and PDADMAC (100 kDa, 35% by weight in water) both from Sigma. First 100 μL of either 100 nM CTAB-NRs or MCA-NRs were washed to remove any free CTAB or other contaminants. They were resuspended

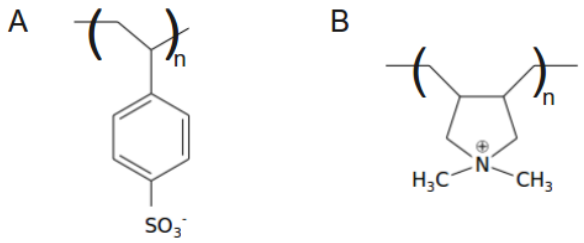

Figure 3-10: Polyelectrolytes for coating NRs. A. Polysodium 4-styrenesulfonate (PSS). B. Poly(diallyldimethylammonium) chloride (PDADMAC).

in 1 mL of water. 200 μL of 10 $\frac{\text{mg}}{\text{mL}}$ polyelectrolyte was added. If the CTAB-NRs are used, then the surface charge is positive, so the PSS (the negative polyelectrolyte) was used for the first layer. If MCA-NRs were used, then the surface charge is negative, so the PDADMAC (the positive polyelectrolyte) was used for the first layer. The NRs were briefly agitated and left at room temperature for 20 minutes. After incubation, they were centrifuged and the supernatant was discarded. 1 mL of water was added to the pellet and 200 μL of 10 $\frac{\text{mg}}{\text{mL}}$ of the oppositely charged polyelectrolyte was added. This procedure was repeated as many times as desired, each cycle adding another layer to the NR.

3.1.7 Characterization Techniques

The physical characteristics of the particles used in the biological activity switch help determine the remainder of the key components of the biomolecular switch. The physical characteristics of the NRs we are most interested in are length, diameter, aspect ratio, optical properties, ligand thickness, surface charge. Additionally we are interested in the purity, concentration, and polydispersity of sample.

Transmission electron microscopy

The most accurate way to measure the physical characteristics of NRs is to analyze transmission electron micrographs (TEM) of them. Gold has a relatively large nucleus and NRs tend to be about 10 nm in diameter, so NRs scatter electrons very efficiently.

This makes TEM relatively simple (especially when compared to TEM of magnetic nanoparticles or gold particles less than 4 nm). All of the TEM data and images used in this thesis were taken on the JEOL 200CX TEM in the Center for Material Science and Engineering at MIT using copper grids with a thin carbon film from Ted Pella.

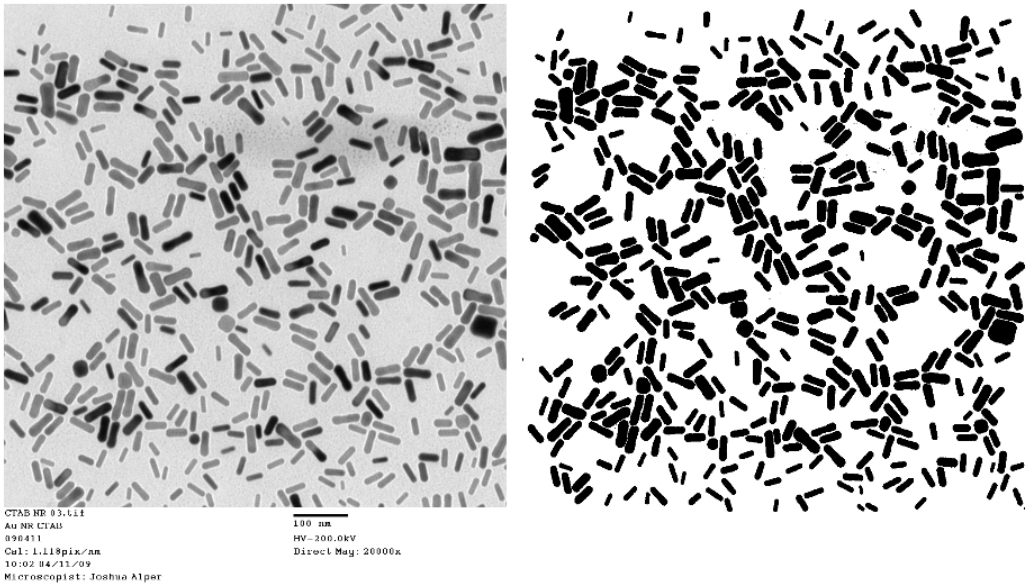

Figure 3-11: Sample TEM image as it comes from the camera on the left. Sample TEM image that has been image processed and is ready for analysis with ImageJ on the right.

I primarily used TEM to measure the size of the NRs. By using image processing software ImageJ,[142] some of the sizing process can be automated. ImageJ needs an image that is black for particles and white where there are no particles. The particles must not be touching in the image file or ImageJ will assume touching particles are just one particle. Thus, depending on the spacing of the NRs on any particular TEM image there is often a fair amount of pre-processing of the image necessary. To do the preprocessing I generally used GIMP - open source image processing software (see figure 3-11 for an example). Once the image is loaded into ImageJ, the software can be set to count, find the major and minor diameters, aspect ratio, and area of the NRs. I generally aggregate the data from at least five images taken from five different locations on the grid for a total of at least 1000 particles. I then calculate the mean and standard deviations of the length, width and AR.

Additionally I can calculate the yield, which is calculated by dividing the number of NRs by the total number of nanoparticles (rods and spheres). Au nanoparticles are considered spheres if their aspect ratio ($AR = \frac{\text{length}}{\text{diameter}}$) is < 1.75.

UV/Vis spectrophotometry

Because the optical properties of NRs are sensitive to so many of the physical characteristics of the NR (see section 3.1.4, optical absorbance is often a valuable analysis technique. It can be used to find the concentration of the sample and the optical properties of the NRs. Additionally, it can give insight into the NR's aspect ratio, stability, purity, and polydispersity.

To get the concentration of NRs we can use Beer-Lambert's law (equation 2.15) and the molar extinction coefficient. As is clear from Gans theory, the extinction coefficient of the NRs at their longitudinal SPR is a function of the AR (see figure 3-2). However, they absorb strongest there, so using this point to get the concentration could be easier than any other wavelength. For this reason, the extinction coefficient at the longitudinal SPR is most often used to calculate the concentration of NRs. Table 2 in reference [128] gives the molar extinction coefficient for a number of AR of NRs. Since the NRs I tend to use have their SPR near 785 nm, I used $\epsilon_{NR} = 4.6 \times 10^9 \frac{1}{\text{M cm}}$. Nearly all of the UV/Vis spectrophotometry data in this thesis comes from the Cary 100, however some of the data does come from a Cary 50. To assay longer aspect ratio NRs, a UV/Vis/NIR spectrophotometry might be necessary since the UV/Vis spectrophotometry generally does not go to wavelengths longer than 900 nm.

The optical properties are obviously easily determined from the absorbance spectra. The longitudinal and transverse SPRs can be found by locating the two local maximums in the data. Upon closer observation of the absorbance spectra, we can learn about the sample polydispersity. There is a clear difference between the absorption spectra of a sample, and the simulation of its absorption spectra using the AR as determined from TEM (see figure 3-12). The extinction coefficient of the NR simulation is $\sim 4 \times$ the actual extinction coefficient. Further simulations show

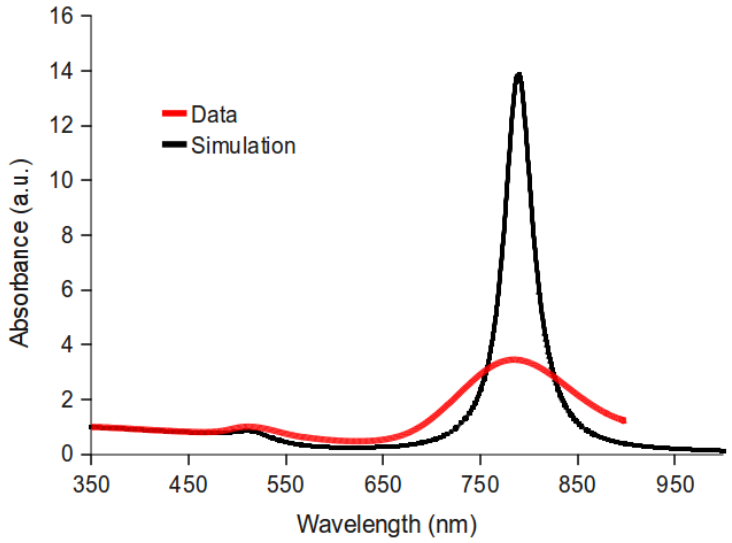

Figure 3-12: Simulated absorption spectrum of a NR with AR equal to the mean AR of a sample (as determined by TEM analysis) and the actual absorption spectrum data of that sample using the Cary 100 UV/Vis spectrophotometer.

that this difference can be most easily explained by accounting for the distribution of NRs about their mean AR (see figure 3-13). Also, because NRs with larger AR have a higher extinction coefficient, as the standard deviation increases, so does the wavelength of the absorption peak of the a sample of NRs.

Another key piece of information that can be found in the absorption spectra of NRs is their aggregation state. Because NRs that are in close proximity electrically couple,[44, 79] the SPR of aggregated NRs tends to shift. Also, since they tend to aggregate end to end, the longitudinal SPR tends to red shift. Aggregation results in a broadening and a redshift of the longitudinal SPR, much like if the polydispersity were higher. So by comparing absorbance spectra over time or as a function of other chemical operations (ligand exchange, biomolecule conjugation, etc.) we can determine if the NRs remain stable in solution.

Along these same lines, absorbance can be used to assay the ligand exchange. In particular, the full width half max of the longitudinal plasmon resonance directly relates to the aggregation state of the NRs. That these NRs do not show a broadening as compared to the CTAB stabilized NRs (figure 3-14) is indicative of their stability without aggregation. Due to the difference in dielectric constant (and also

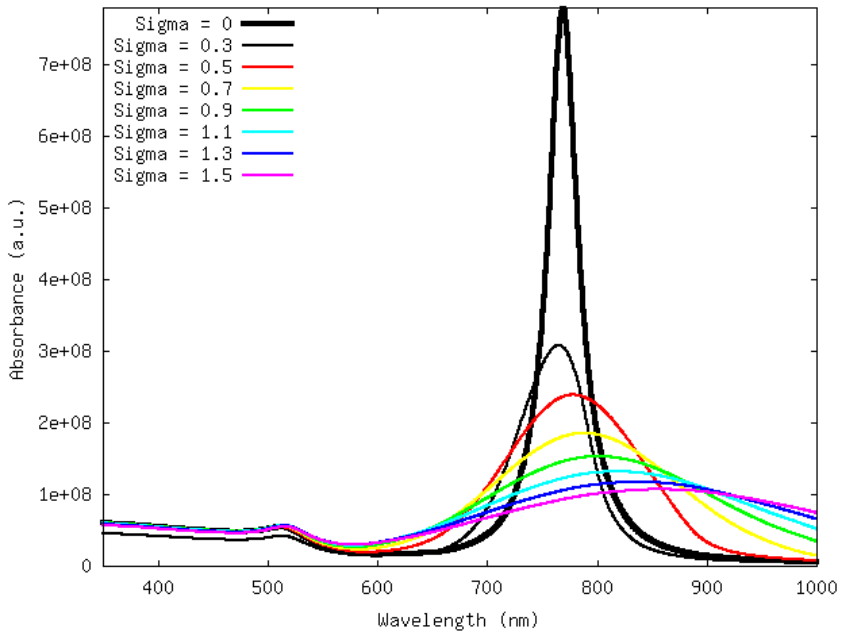

Figure 3-13: Simulated absorption spectra of NRs with AR equal to the mean AR of a sample (as determined by TEM analysis) and various standard deviations of about that mean. The actual standard deviation of this sample is 0.7, as determined by TEM analysis.

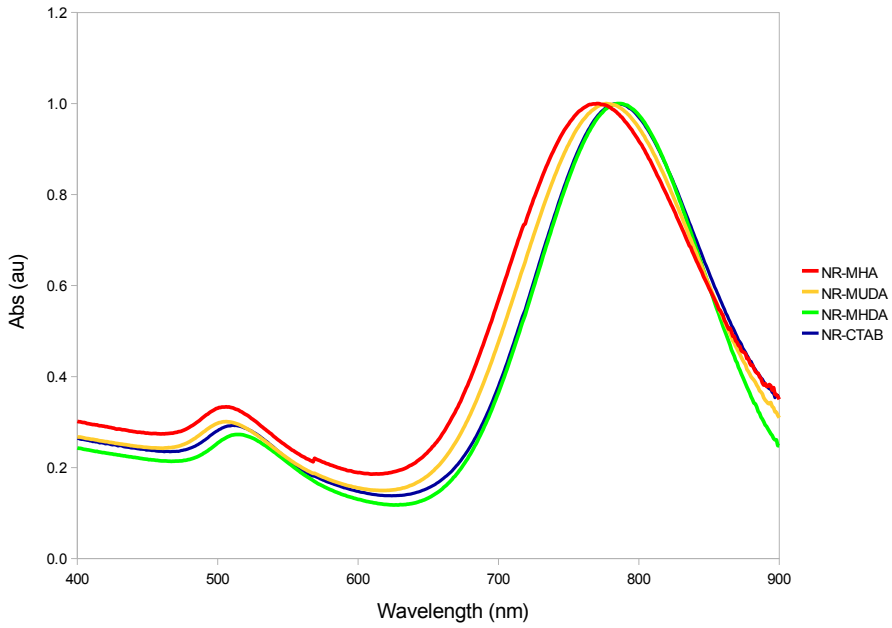

Figure 3-14: Absorption spectrum of MCA coated NRs. All spectra are normalized at their SPR.

the refractive index) in the immediate vicinity of the NR, the longitudinal surface plasmon resonance changes (see equation 3.5). The linear red shift in the SPR with the length of the alkyl chain (figure 3-15) is expected.

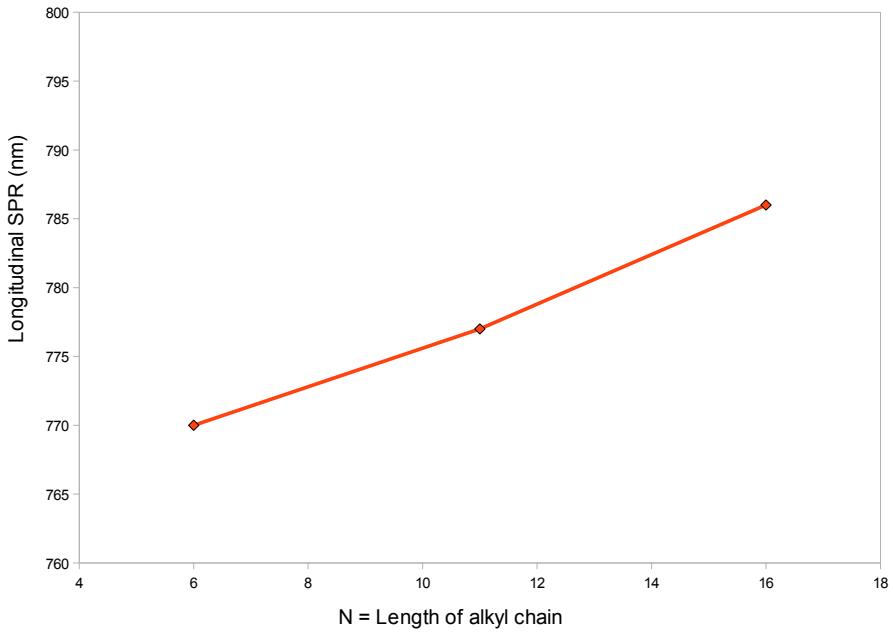

Figure 3-15: Longitudinal SPR of mercaptoalkyl acid stabalized Au NRs a function of the length of the alkyl chain (n).

Analytical gel electrophoresis

Another technique to learn about the size and charge of the NRs and their ligand layer is analytical gel electrophoresis. Additionally gel electrophoresis can be used to help assay conjugation of the target biomolecule to the NR.

Gel electrophoresis separates particles based on their size and charge. The samples are loaded into the wells of an agarose gel, and they are exposed to an electric field. The field causes the particles to migrate in the gel. Negatively charged particles move toward the positive electrode. The gel serves to separate the particles by size, restricting the paths of larger particles more. Often I use gel electrophoresis to compare two similar samples and look at relative mobilities in the gel. However, analytical gel electrophoresis using Ferguson plots of nanoparticles is also possible.[133]

Analytical gel electrophoresis using Ferguson plot analysis is used to determine the size, mobility and charge of a particle.[147] This can be useful for understanding the changes associated with various ligands. The mobility of a NP changes in a gel with different charged and sized ligands, and Ferguson plot analysis is, in many cases, the most accurate way to determine both the thickness and zeta potential of a ligand layer,[133] particularly when TEM analysis is not feasible. It has been shown to be more accurate than dynamic light scattering (DLS), the more commonly used size and charge technique in the literature.[133] Ferguson plot analysis does tends to consume a significantly larger amount of NPs than either DLS or TEM. Additionally it can take a long time to get 6 - 10 data points necessary to get good characterization of the NPs.

The mobility is

$$M = \frac{l_{migration}}{tE_{field}} \tag{3.9}$$

where E_{field} is the electric field strength, t is the total time the sample was exposed to the field, and $l_{migration}$ is the distance the sample moved in the gel as measured from the leading edge of the well to the peak intensity of sample as determined using ImageJ. Ferguson plot analysis is based on the observation that the log of the mobility of a sample in a gel is a linear function of the gel percentage, T_{gel},[147]

$$\log_{10}(M) = \log_{10}(M_0) - K_R T_{gel} \tag{3.10}$$

where M_0 is the free mobility and the slope is the retardation coefficient, K_R. K_R is a function of the gel parameters and the effective hydrodynamic radius of the particle in the gel

$$\sqrt{K_R} = C_1 + C_2 r_{eff} \tag{3.11}$$

where C_1 and C_2 are functions of the gel parameters.

Agarose gels were prepared by adding an appropriate amount of agarose for the desired gel percentage ($\frac{1 \text{ g}}{100 \text{ mL}} = 1\%$) to 0.5 $\times$ TBE. The suspension was then heated in a microwave oven to boiling. The agarose solution was then poured into a gel box

to cool. Samples were loaded with $\sim$ 5 μL glycerol to help keep the samples in the well. A voltage was applied across the gel for a measured time. The time and field were recorded for each gel.

Before Ferguson plot analysis can be done on unknown samples, the gel must be calibrated. I used four samples of NP with diameter determined from TEM analysis. They were run in gels ranging from about $T_{gel} = 0.75 - 2.0\%$. The slope of the Ferguson plot (figure 3-16, left), K_R, was found for each sample, and then plotted as a function of the known particle size (figure 3-16, right). From the K_R plot, the gel parameter constants were found and applied to all calculations on unknown samples using equation 3.11.

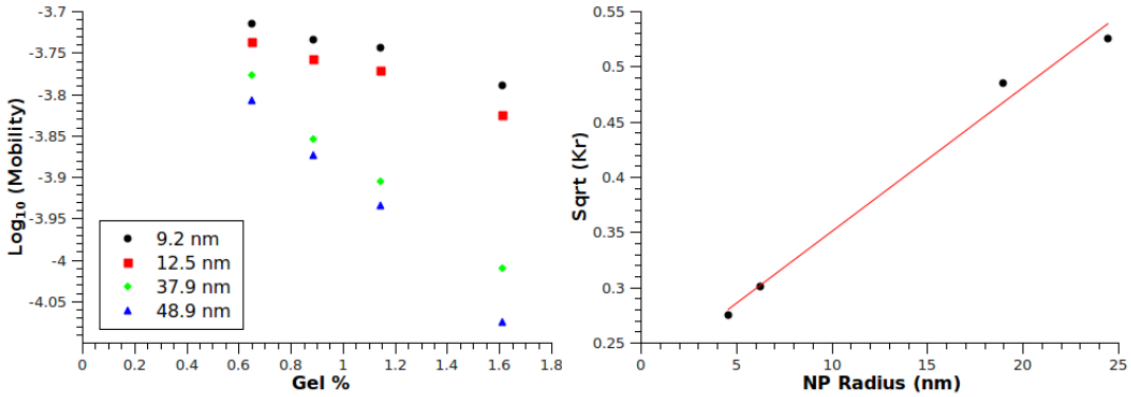

Figure 3-16: Ferguson plots of the size standards (left). Retardation coefficient (K_R) plot of the size standards on the left. $C_1 = 2.20 \times 10^{-1} \pm 1.53 \times 10^{-2}$ and $C_2 = 1.30 \times 10^{-2} \pm 9.61 \times 10^{-4}$ (see equation 3.11).

I used Ferguson plot analysis to determine the thickness of the ligand layer on a NR. The mobilities of the samples were calculated for a number of gel percentages. These data were plotted on Ferguson plots, and using equations 3.10 and 3.11 the effective hydrodynamic radius of the nanoparticles were determined. The major drawback of this technique is that NRs are not spherical, so the calculated effective hydrodynamic radius needs to be converted to the length and diameter of a nanorod. The mobility of a particle through the gel is, like many nanometer length scale phenomena, dominated by the particle's surface area.[147, 23] So, to convert from effective hydrodynamic radius (r_{eff} in equation 3.11 to ligand layer thickness

(t_{lig}) I use

$$4\pi r_{eff}^2 = 2\pi \left((r_{NR} + t_{lig})(l_{NR} - 2r_{NR}) + 2(r_{NR} + t_{lig})^2\right) \tag{3.12}$$

where r_{NR} is the NR radius and l_{NR} is the NR length.

One major drawback of gel electrophoresis of NRs is that CTAB coated NRs are not stable in TBE so they do not run in the gel. This is equally true for NRs with PDADMAC as the outer layer. So any analytical gel electrophoresis may only be done if ligand allows it.

3.1.8 Analysis of limits on NR AR

Before I leave the specific topic of gold NRs, I want to discuss a the operating window of a couple NR parameters.

It is clear based on the Gans theory, if the NRs are to efficiently absorb the laser, the absorbance due to the longitudinal SPR must overlap the spectral output of the laser. This ensures NRs absorb as much energy as possible, which in turn helps ensure specificity. Gans theory predicts that the longitudinal SR is highly dependent on the NRs' aspect ratio, which, as I have shown (see section 3.1.5), can be controlled by adjusting the synthesis procedures.

For this analysis, I assume that the spectral output of the laser has a FWHM width in the wavelength of about 50 nm (see figure 4-4). The goal of the synthesis is to get NRs that match the laser exactly, so the target mean AR is determined by the matching of the longitudinal SPR with peak laser output. However, exact overlap is difficult, so I assume the overlap is good enough if the NR absorption peak falls within the 50 nm FHWM band. Based on Gans theory (see figure 3-2) the AR shifts by about 50 nm if the AR were to change by 0.5. Thus, the NRs need to fall within the operating window of ± 0.25 of the target mean AR if the NR SPR is to be within the $\sim$ 50 nm FWHM wavelength width of the laser.

3.1.9 Analysis on the effect of NR polydispersity

The best NR syntheses I have done, and the best I have seen in the literature, have a standard deviation on the mean AR of about 0.5. Given the analysis done above on the limits of NR AR, this is not ideal. The following analysis assumes that the spectral output of the laser has a FWHM width in the wavelength of about 50 nm, and NRs that have their SPR peak within this 50 nm range absorb the light. Given these assumptions, based on a normal distribution of NRs and the cumulative distribution function, only $\sim$ 40% of the NRs are actually excited. It is difficult to assign an operating window on polydispersity. The primary conclusion is that it is a critical factor, and that the AR's standard deviation should be minimized.

A related issue is that of synthesis yield. Discussed in a couple places elsewhere, yield is the ratio of NRs to total particles (NRs plus spherical NPs) in solution. The synthesis is never 100% efficient. I found that a good yield is around 95% for the nonseeded synthesis. This means that about 5% of the particles will not be affected by the laser, and thus any target biomolecules on those particles will not be actuated.

Polydispersity, and to a lesser extent yield, greatly affects the efficiency of the biomolecular activity switch (see section 1.4.7). The analysis done above is just a first order analysis because of the binary assumption (NRs whose SPR falls within the FWHM width absorb, others don't). This is clearly just an assumption. Both the absorption spectra of the NRs as predicted by Gans, and the spectral output of the laser have a non-step function shape. This means that many NRs will absorb less than the optimal amount of light (never mind that any individual NR will absorb a different amount of light based on its relative orientation to the beam path).

Polydispersity and yield have been well studied and can be controlled in spherical gold NP synthesis along with many other metallic and semiconductor NPs. Gold NR synthesis is a significantly newer procedure, and many of the techniques do not transfer to NRs easily. Recently there has been some progress reported in the literature on improving polydispersity after synthesis,[156, 155] but the synthesis used in this thesis remain state of the art.

3.2 Analysis of heating mechanisms

Light that is incident on matter is either reflected, refracted, transmitted, scattered or absorbed.[114] Metallic nanoparticles predominantly absorb light. The energy in the photons absorbed by nanoparticles is converted to heat through a number of processes. First, the photons excite the electron cloud to a higher energy level, approaching 1000° K.[102] This causes an energy imbalance between the electrons and the lattice structure of the NPs. Energy is transfered in a ballistic manner to quantized units called phonons in the lattice. The kinetic energy of vibrations of the lattice about their mean position in space is what is commonly thought of as heat. This heat is dissipated to the surrounding fluid primarily by phonon-phonon interactions.[102]

3.2.1 Photon-electron thermalization

When a nanoparticle is irradiated by light, the fastest mode of energy transfer is from the photons to the electron cloud. This is the absorption of energy, and it happens on the femtosecond time scale ($\tau_{\hbar\nu-el} \sim$ 4 fs).[101] Since even the fastest lasers have a 20 – 150 fs pulse width, it is safe to assume the NP can efficiently absorb the light because $\tau_{\hbar\nu-el} \ll 100$ fs.

3.2.2 Electron-phonon thermalization

Once the electron cloud raises its temperature, there is an imbalance in the energy level of the electrons and the crystal lattice. This imbalance is relaxed on the picosecond time scale ($\tau_{el-ph} \sim$ 1.5 − 4 ps).[102, 3] The energy transfer to the lattice excites vibrations of the lattice about their mean position. This leads to thermal expansion of the nanoparticle. Additionally, the rapid nature of this transfer can lead to other, lower frequency vibration modes. In NRs, the lowest energy vibration mode is an extension mode. NRs can also have a significant portion of the energy partition into a breathing mode, too (see figure 3-17).[70]

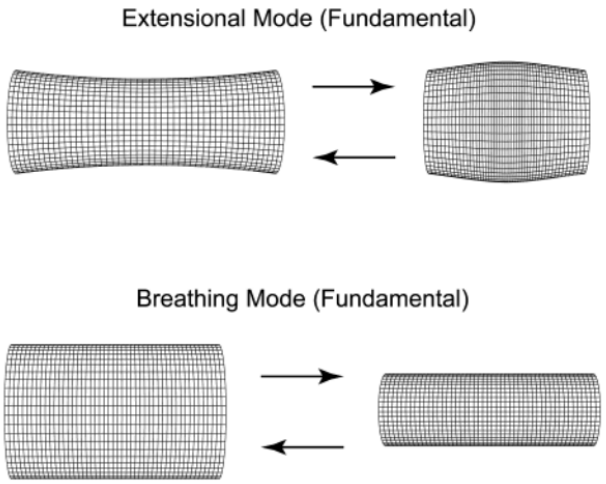

Figure 3-17: Schematic of NR vibration modes. Reprinted with permission from M. Hu, X. Wang, G. V. Hartland, P. Mulvaney, J. P. Juste, and J. E. Sader. Vibrational response of nanorods to ultrafast laser induced heating: Theoretical and experimental analysis. *J. Am. Chem. Soc.*, 125(48):1492514933, 2003. Copyright 2003 American Chemical Society."

3.2.3 Phonon-phonon thermalization

As the lattice starts to vibrate, there is an energy imbalance between the phonons in the nanoparticle lattice and the surrounding fluid. This energy imbalance relaxes through phonon-phonon interactions. Since the characteristic length of the particles ($L \sim 10$ nm) is above the mean free path of a phonon in the fluid (5 Å), the energy transfer is well described by classical heat transfer. Because the energy dissipation is on the order of hundreds of picoseconds ($\tau_D \sim 100$ ps), conduction dominates other potential modes of heat transfer. Thus classical heat diffusion equations (see equation 3.2) well characterize nanoparticle cooling.

3.3 Finite element analysis of NR heating

The analysis of NR heating is a very nice forum to explore some of the laser parameters that are difficult to change experimentally, including changing the pulse length and the repetition rate of the laser.

Despite the questionable treatment of the temperature distribution within the NR

as a continuum, the continuum assumption is a good approximation within the solvent (see section 2.5.1 for a more detailed discussion). Additionally, because the timescale for thermal dissipation is much larger then the timescale for phonon-phonon interactions within the particle, and the thermal conductivity of the particle is significantly higher than the solvent, it is not unreasonable to use the continuum approximation as long as we look at average NR temperature and not the spatial distribution of heat within the particle. Thus we can use continuum methods to analyze the heating of a NR and the solvent.

The first order analysis is to assume that a NR is approximately a sphere, and thus use equations 2.24 and 2.25 to determine the temperature as a function of time and space outside the NR. Alternatively, there are similar analytical solutions for an infinitely long rod in solution. However, on the length scale of nm and the time scale of ps neither of these are good assumptions.

An analytical solution for the time dependent temperature field, $T(\mathbf{r}, t)$, for a finite length rod or an ellipse in solution is not available (at least to my knowledge).

So, to get $T(\mathbf{r}, t)$ I used a numerical simulation. Because of the non-trivial geometry, I solved the differential equations defining heat diffusion in the NR-solvent system using a finite element model (see figure 3-18). The model is a 2-D representation of the 3-D NR. It is an axisymmetric model, and the corresponding boundary condition was applied to the left most edge of the model. No flux boundary conditions were applied along the outer diameter of the solvent. To reduce computation time, only half of the model is actually represented in finite elements. The other half is accounted for by applying symmetric boundary conditions along the bottom edge of the model. The interior consists of three regions: 1. a Au NR with a size as determined by TEM analysis (see section 3.6.2) and the physical properties of bulk gold; 2. a ligand with the corresponding physical properties of the modeled molecule and a thickness determined from Ferguson plot analysis; and 3. a region of solvent containing water, and if necessary, CTAB with thermal conductivity between 0.55 and 0.6 $\frac{W}{mK}$ as determined by transient hotwire[116] measurements of CTAB solutions. The solvent region of the model is approximately 3 μm in diameter, approximately equal in size to the average

rod separation due to the sample concentration of 1 nM NRs. The adiabatic (no flux) boundary condition was used because of the periodic nature of the NR solvent system within the overall model of the sample. The initial condition of the transient simulation was that all elements are at room temperature.

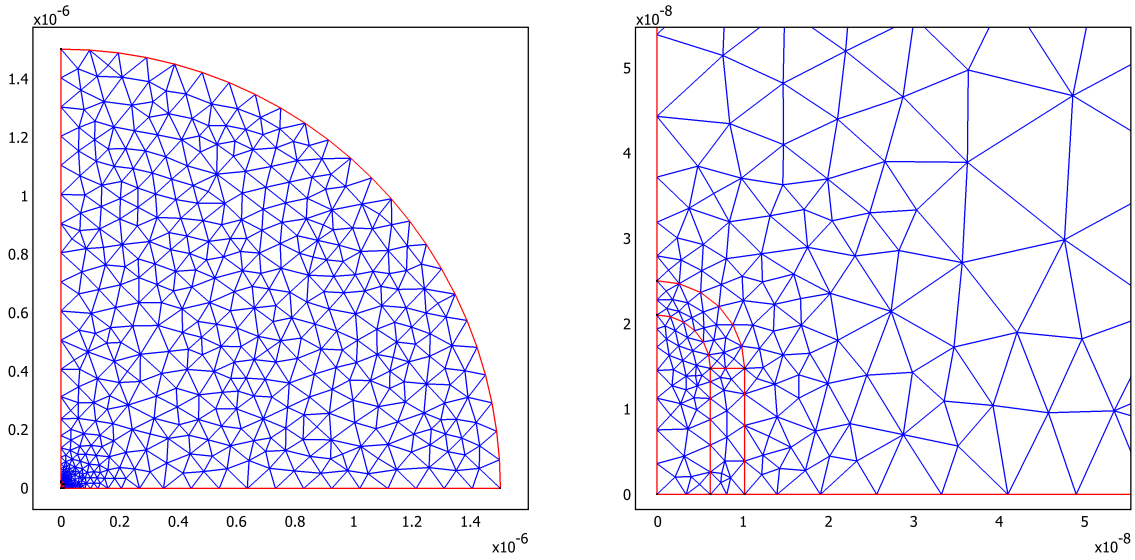

Figure 3-18: NR FEA model and mesh. The right shows a detail of the NR and ligand region.

I used COMSOL's automatic mesh generating routine to mesh the model. The refinement of the mesh was optimized to ensure that any errors were less than 1% while minimizing computation time. Optimization was done by analyzing finer and finer meshes until there is no significant difference in the results, or the results converge. The model needed very little refinement.

3.4 Temperature as a function of space and time

Upon absorption of a laser pulse, the NR's lattice very quickly ($\tau_{el-ph} \sim 1.5 - 4$ ps) reaches its maximum temperature if the pulse duration is $\leq \tau_{el-ph}$. However, heating the NR is not the primary goal of this biomolecular activity switch. We actually want to heat the molecules in the immediate surroundings, which is a slightly different

problem. Furthermore, if the NR gets too hot too fast, then it could melt, break apart, send shock waves, or some other probably undesirable effect.

We modeled the laser input as uniform volumetric heat generation within the NR. The heat generation was Gaussian in time with standard deviation equal to half of the full width at half maximum (FWHM) time of the pulse. For the simulations of the fs laser, this is effectively an impulse of energy because of the relative time constants of the laser and τ_{el-ph}.

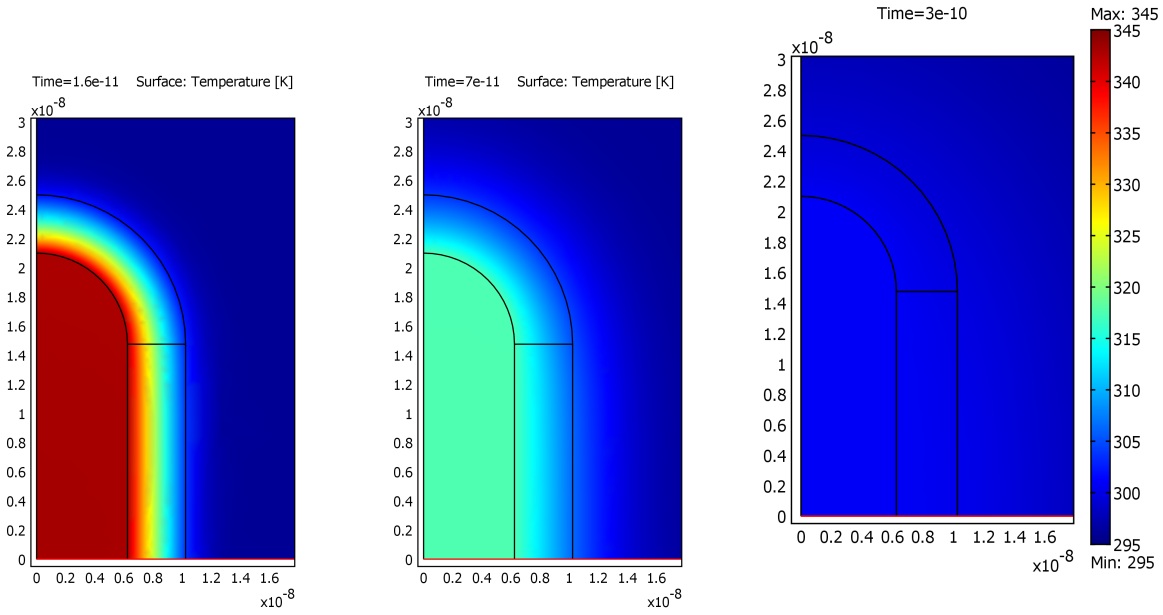

Figure 3-19: FEA output of the temperature field around NR after irradiation by a 100 fs laser pulse. Left: t = 16 ps, Center: t = 70 ps, Right: t = 300 ps. The temperature scale is arbitrary. The temperature rise above T_∞ is directly proportional to the magnitude of the pulse. The scale bar shown is applicable to all plots, and is given to aid in interpreting the relative temperatures near the NR. Just these details are shown because the remainder of the solvent has negligible temperature rise.

Thermal confinement is clear from the FEA results (see figures 3-19 and 3-20). This confirms numerically what the order of magnitude estimates indicated, that the target molecule must be within about 1 – 5 nm of the NR for the temperature to appreciably rise.

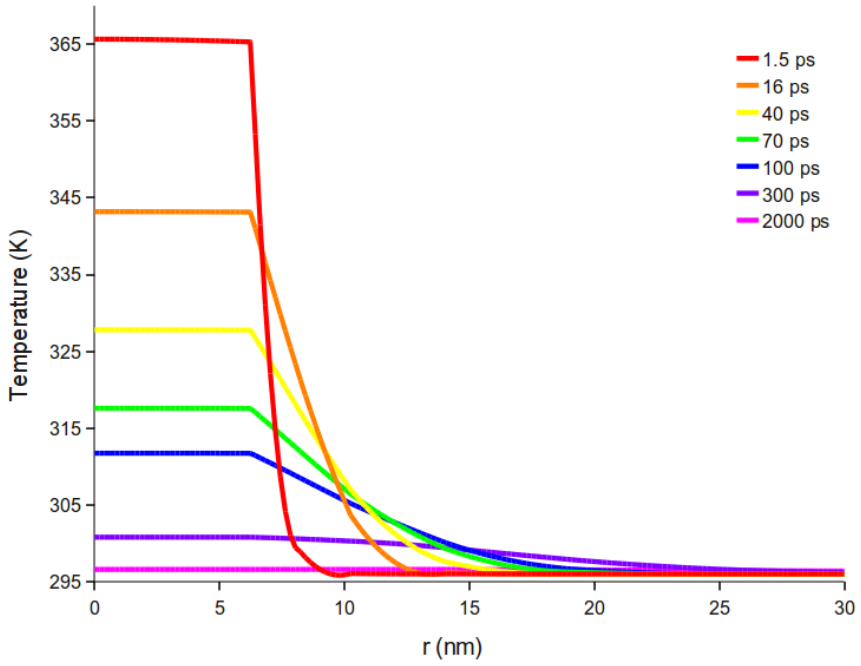

Figure 3-20: Temperature as a function of r (the length along the r axis in figure 3-18 at multiple times after laser.

3.4.1 Analysis of pulse length

Further FEA analysis leads to additional insights about the limits on the laser parameters. As can be seen by comparing the time constants of energy conversion, the fs speed of our laser systems is not necessary. The energy is only converted to the lattice on the order of 1.5 – 4 ps, so a laser with this pulse width would yield no different results than the fs laser. The FEA results help us understand what would happen if the laser were even slower, say on the order of heat dissipation to the solvent (see figure 3-21). These results indicate that by increasing the pulse length to 10 ps, the maximum temperature rise of the NR can be reduced by about a third without any changes to the maximum temperature of the target biomolecule. Increasing the length of the pulse beyond 10 ps results in lower peak temperature of the protein. However, as the pulse is slowed, the ratio between the peak temperature of the protein to the NR keeps increasing. This suggests that a slower pulse can be used if it is of higher magnitude to help avoid NR melting but maximize effects on the protein. The tradeoff is that as the pulse is extended, so is the heating zone, and specificity

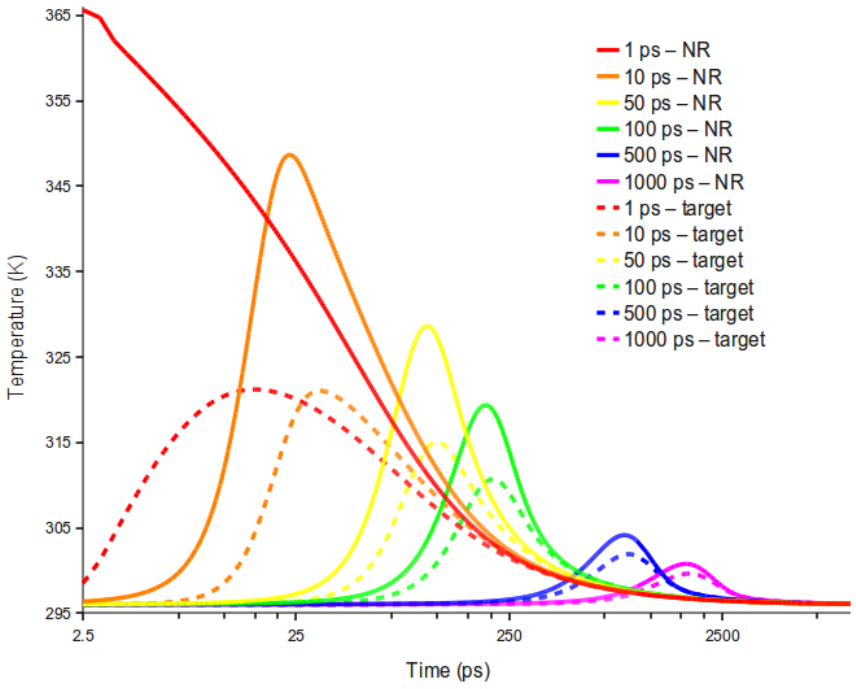

Figure 3-21: FEA results on the laser pulse length. Solid lines are the temperature of the NR, assuming $T(\mathbf{r} = 1 \text{ nm}) = T_{\text{NR}}$, for various possible pulse lengths as predicted by finite element analysis. Dashed lines are the temperature of the biomolecule assuming it is 2 nm from the side of the NR. Note that due to $\tau_{el-ph} \sim 1.5 - 4$ ps, all pulse lengths shorter than $\sim 1.5 - 4$ ps have approximately the same $T(\mathbf{r})$ as a 1 ps pulse. Also note that the energy per pulse is equal in all cases and arbitrary. The temperature rises scale linearly with power.

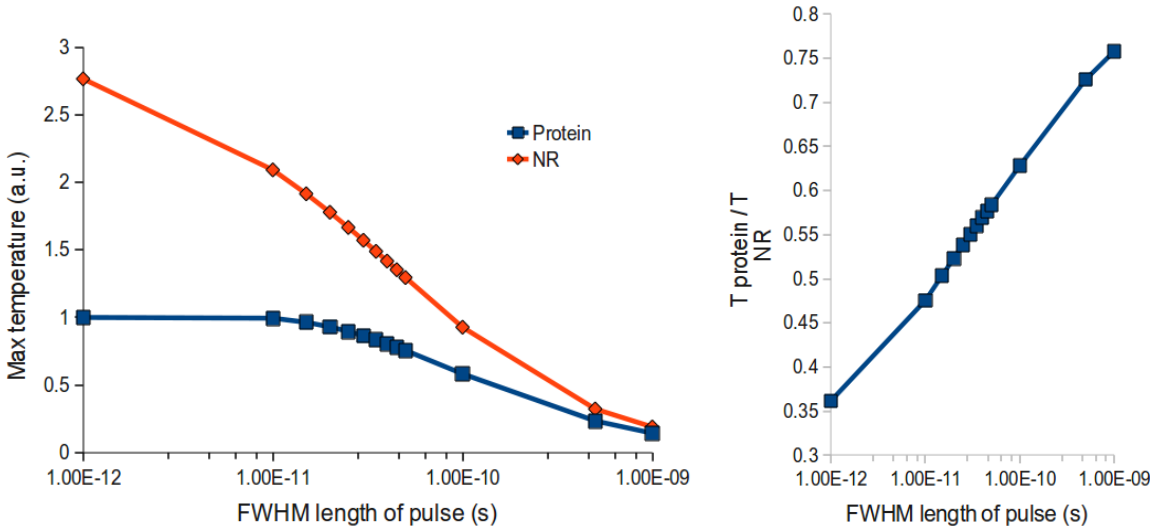

Figure 3-22: Relative peak temperatures of NR and protein with varying pulse length. Left: The peak temperature (see figure 3-21) of the NR and protein (2 nm from the NR surface) both normalized by the peak temperature of the protein. Right: $\left(\frac{\text{Temperature of the Protein}}{\text{Temperature of the NR}}\right)$

of the biomolecluar switching mechanism is sacrificed.

Therefore I conclude that the optimum pulse length is 10 ps, because it would lower the temperature of the NR without sacrificing anything on the maximum temperature of the protein or risking reducing specificity. My experimenter were subjected to and additional a practical limit in that our collaborators in the Chen lab and Tokmakoff labs had femtosecond lasers available for us to use, so all the experiments have been done on fs lasers.

3.4.2 Multiple pulses

The timescale of heating is critical to making an efficient biomolecular switch that meets all the hallmarks. Since the thermal dissipation time (τ_D) scale is of order 10s – 100s of ps, the target is only at the heated temperature for $\sim$ 200 ps (see figure 3-21). This may not be long enough to actuate the target efficiently. Recall that for an efficient switch, $\tau_{switching}$ must be longer than τ_D. Additionally, since it takes 1 ms for the next pulse to hit, it is possible that $\tau_{recovery}$ is much faster,

particularly if the target is not hot long and may not be far from the default state on the energy landscape (see section 1.4.7 for further discission of switch efficiency).

The simplest solution to mitigate the recovery time constant part of this problem is to increase the repetition rate of the laser. When the repetition rate is increased, the energy per pulse goes down such that the average (over many pulses) power is unchanged. Based on some of the data I will present later on the operating window for laser fluence, this may be feasible, however for reasons beyond your control, this may be impractical.

The simplest solution to mitigate the switching time constant part of this problem may be to divide the pulse into multiple smaller pulses with beam splitting optics. Then the various pieces can be run through a delay path, and finally be recombined to form a "pulse train." The concept here is that if the pulse energy necessary to actuate is low enough (say 100 mW) there may be enough power in the original laser pulse to have 10s of pulses in the "train." The pulse train cannot keep the temperature of the target constant, but it could keep it between some bounds for significantly longer than a single pulse. Using the same models as in section 3.3, I modeled this scenario (see figure 3-23), and the results look promising.

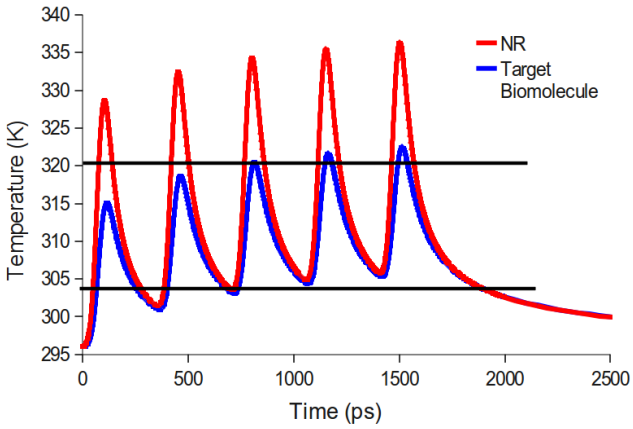

Figure 3-23: Simulation of the NR temperature and the protein temperature (2 nm from the side of the NR) subjected to a pulse train. The black, horizontal solid represent the upper and lower bounds on the protein temperature necessary to achieve efficient biomolecluar switching. All the pulses have equal magnitude, FWHM time is 50 ps, and the time between each pulse in the train is 350 ps. The model used is for CTAB coated NRs above the cmc.

3.5 The laser setup

The experiments I performed for this thesis were primarily done on two different laser setups. They are both ultrafast pulsed lasers in the NIR ($\lambda \sim$ 800 nm), but they have greatly different pulse powers due to the difference is repetition rate.

3.5.1 Femtosecond laser

To generate the ultrafast pulsed laser irradiation for demonstrating the biomolecular switch I used a laser in the Tokmakoff lavatory in the Chemistry Department at MIT. The 82 MHz output from a Ti:sapphire oscillator (Tsunami, Spectra-Physics) was amplified by a Ti:sapphire regenerative amplifier (Spitfire, Spectra-Physics) to produce 100 fs full width at half max, $\lambda = 792$ nm pulses at 1 kHz. The oscillator was pumped with a continuous wave 532 nm laser (Millennia, Spectra-Physics), and the amplifier was pumped with 1 kHz, 527 nm ns pulses (Empower, Spectra-Physics). The average max laser power for this configuration is about 7 W, but I only used up to 3 W for the NR melting experiments. For the which resulted in the fluence varying from 110 – 550 $\frac{\mu J}{cm^2}$.

3.5.2 Pump-probe system

The pump probe technique is widely used to probe the properties of a system in the hundreds of fs to tens of ns time scales after being excited by a laser pulse. The principle is that a high energy pulse, the pump pulse excites the sample. Then a much lower energy probe pulse also hits the sample. This is used to probe for changes in the sample's optical properties. The time between these pulses is often controlled by routing the probe pulse through a slightly longer path, controlled by a movable stage on the optical table. Given the additional length of the light path and the speed of light, the time delay of the probe pulse can be calculated.

When a gold NR is excited by the pump laser, it rapidly converts the energy from the photons to lattice vibrations. The three lowest energy level vibration modes are: 1. the extension mode where the NR gets longer and skinnier and then shorter and

fatter, and, like a tension test, this mode can be used to probe the Young's modulus of the NR, 2. the breathing mode where the NR gets longer and fatter and then shorter and skinnier, and, like a confined compression test, this mode can be used to probe the bulk modulus of the NR, and 3. thermal vibration of the lattice points about their mean position (note that vibration modes 1 and 2 translate the mean lattice point location as they vibrate (see figure 3-17).[70, 60] The vibrations in mode 3 get larger with more energy, thus mode 3 is the molecular basis for thermal expansion.[26]

All three of these vibration modes can have an effect on the absorbance of the NR. The simplest to envision is that the extension vibration mode changes the AR of the NR as a function of time (see figure 3-17). Since the SPR is a strong function of the AR, the SPR shifts with time. Modes 2 and 3 change the complex dielectric constant of the NR because the electron density changes. This is due to the conservation of electrons and the change in volume of the NR due to thermal expansion. The pump-probe system can detect these changes if the longitudinal SPR is near, but not at, the wavelength of the probe beam because the abosrbance changes due to small SPR shifts are pretty large at a fixed wavelength (see figure 3-25).

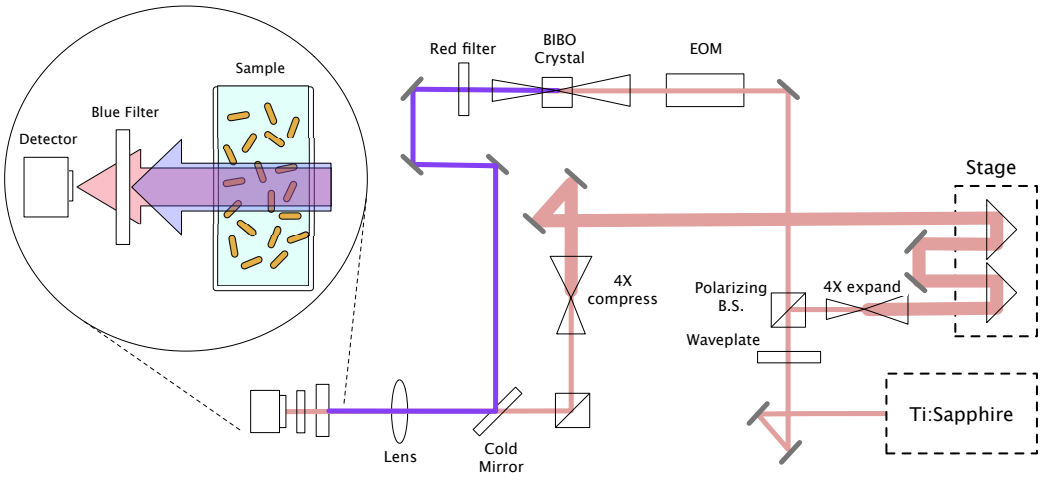

Figure 3-24: Pump-probe system.

The pump-probe system (see figure 3-24) in the Gang Chen lab in the Mechanical Engineering Department at MIT is built around a Ti-sapphire laser that emits 150 fs pulses at a repetition rate of 80 MHz, and an energy per pulse of $\sim$ 15 nJ. Each pulse is divided into pump and probe pulses with a polarizing beam splitter. The probe

beam then passes through a 4 × beam expander and to a delay stage with a range of up to 7 ns. Once leaving the delay stage, it is compressed before being focused through the sample which is held in a 3 × 3 mm cuvette. The pump beam passes through an electro-optic modulator (EOM) and then a bismuth triborate (BIBO) crystal where it is frequency-doubled to 400 nm. The doubled light is directed through the same lens, coaxial with the probe beam. The pump beam is significantly larger in diameter than the probe beam. This ensures that the probed particles have all been evenly heated. Any diffusion of particles into or out of the probe beam during the course of the experiment should all have been heated by the larger pump beam. A color filter placed just before the detector prevents any pump light from reaching the detector. The typical laser fluence at the sample is $\leq$ 200 $\frac{\mu J}{cm^2}$.

This unamplified system, when compared to more commonly used amplified pump-probe systems, has the advantage that high frequency modulation and lock-in detection can be used to give a very high signal-to-noise ratio.[47] The measurement is sensitive to changes in absorption on the order of one part in 10^7. This allows resolution of fine details in the cooling process following pulsed laser heating. In addition, unlike previously reported unamplified systems,[47, 48, 49, 181] the pump beam is frequency-doubled. This allows us to prevent scattered pump light from reaching the detector by using color filters with greater efficiency than polarization-based techniques, and without the additional complexity of double-modulation schemes. The spatial resolution of our delay stage translates into better than 0.5 ps temporal resolution of the timing of the probe pulse. The center probe wavelength is 800 nm. More details on the experimental system can be found in Schmidt et al. 2008.[151]

3.6 Thermal properties of NR ligands

In this section, I present a sensitive and systematic study of the role ligand molecules play in thermal transport processes in Au NR systems. Understanding the thermal transport from the NR in suspension to the surrounding fluid and thus biomolecules near to the NR is essential for designing not only the biomolecular switch, but

also other biological applications requiring spatial thermal confinement[59, 73] and nanofluids with enhanced bulk thermal conductivity.[31, 32, 39] This thermal transport depends critically on heat transfer across solid-fluid interfaces. The chemical and physical properties of the ligand molecules at the solid-fluid interface heavily influence the thermal transport at the macroscopic and microscopic levels.[47, 48, 49, 70, 74, 181]

The optical pump-probe technique (described in section 3.5.2) is an established tool to study the transient absorption of nanoparticles. It has been used to investigate many physical phenomena of NPs including the excitation of the electron cloud,[100] the thermalization of the electron cloud with the nanoparticle lattice phonons,[99, 103] the acoustic vibrations in the lattice,[70, 137] and the thermal decay due to heat diffusion to the solvent.[47, 48, 49, 74, 181, 69] The referenced thermal decay studies concluded that the structural and chemical properties of the ligand layer and its interaction with the surrounding solvent can strongly influence the thermal interface[48] especially if the particle is less than 40 nm in diameter.[47]

It is important to understand the magnitude of the effect that subtle differences in the ligand layer can make. It is additionally important to understand why these differences occur. In particular, there is a need to analyze quantitatively how the nature of ligands commonly used on NR in biological applications (CTAB, MCAs, PEG, and polyelectrolyte layers) affects the thermal transport between Au NRs and solvent. In close collaboration with Aaron Schmidt and Kimberlee Collins both from Prof. Gang Chen's lab, I investigated this need.[152]

3.6.1 NR synthesis

NRs were synthesized for this study using the non-seeded synthesis procedure (see section 3.1.5). The final concentrations of each reactant are shown in table 3.2.

Ligand exchange was preformed according to the protocols detailed in section 3.1.6.

Table 3.2: Final concentrations of NR synthesis components in mM unless otherwise noted. Synthesis # : 1 - CTAB, 2 - PEG, 3 - MCA and polyelectrolytes.

Synthesis #	CTAB	NaCl	Au^3+	Ag^+	AA	$NaBH_4$ (μM)
1	150	2.250	0.900	0.135	1.800	2.000
2	150	2.500	0.900	0.158	1.800	2.000
3	150	2.250	0.900	0.158	1.800	2.000

3.6.2 NR characterization

Three different syntheses of NRs were used in these experiments, but they all have approximately the same characteristics.

Optical properties and TEM

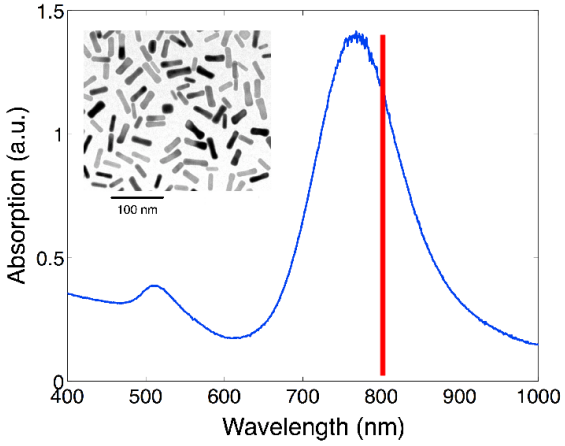

Figure 3-25: Optical absorption spectrum of NRs in 10 mM CTAB with longitudinal SPR peak at 768 nm. The red line represents the peak of the probe laser (800 nm) and the pump laser is at 400 nm (the left edge of this chart). Inset is the TEM of these NRs.

The CTAB NRs have their longitudinal SPR peak at 768 nm (see figure 3-25). Transmission electron microscope (TEM) imaging shows (see figure 3-25, inset) that the NRs are 10.3 $\pm$ 2.6 nm in diameter and are 34.9 $\pm$ 7.4 nm long, with an average aspect ratio of 3.7 $\pm$ 0.5. Our sample's yield is 93%.

The PEG coated NRs all have their longitudinal SPR peak at 775 nm (see figure 3-26B). TEM analysis indicated (TEM not shown) that the NRs are 12.3 $\pm$ 3.2 nm in

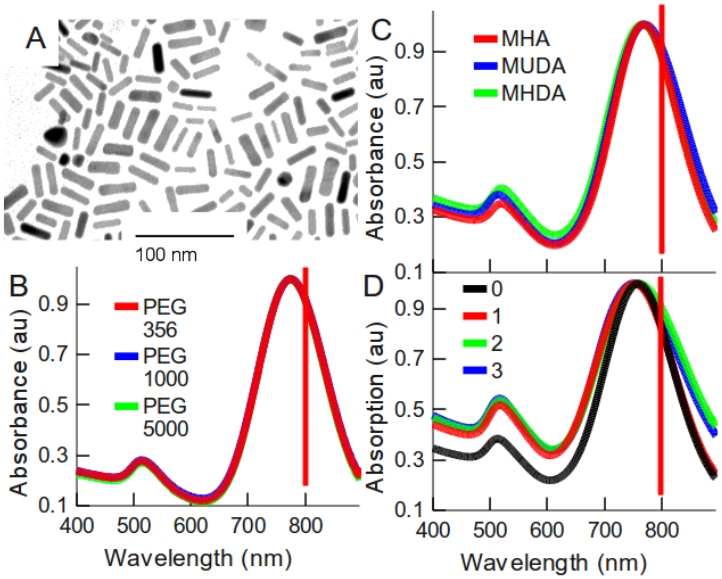

Figure 3-26: Characterization of NRs used in determining the surface conductance of PEG, MCAs and polyelectrolytes. A. Example TEM image of NRs. B. Optical absorption of NR-PEG. C. NR-MCA. D. NR-polyelectrolyte were the number corresponds to the number of layers. The 0 layer sample has MUDA on it. Note that the spectra obscure each other because the data are nearly coincident. This is indicative of NR stability after ligand exchange. The red line represents the peak of the probe laser in B, C, and D.

diameter and are 42.1 ± 9.4 nm long, with an average aspect ratio of 3.5 ± 0.4. Our sample's yield is 96%.

The MCA coated NRs have their longitudinal SPR peak at 770, 771, and 768 nm (see figure 3-26C) for MHA, MUDA, and MHDA respectively. TEM analysis shows (see figure 3-26A) that the NRs are 9.5 ± 2.0 nm in diameter and are 31.0 ± 7.3 nm long, with an average aspect ratio of 3.3 ± 0.5. Our sample's yield is 93% (see figure 3-27A).

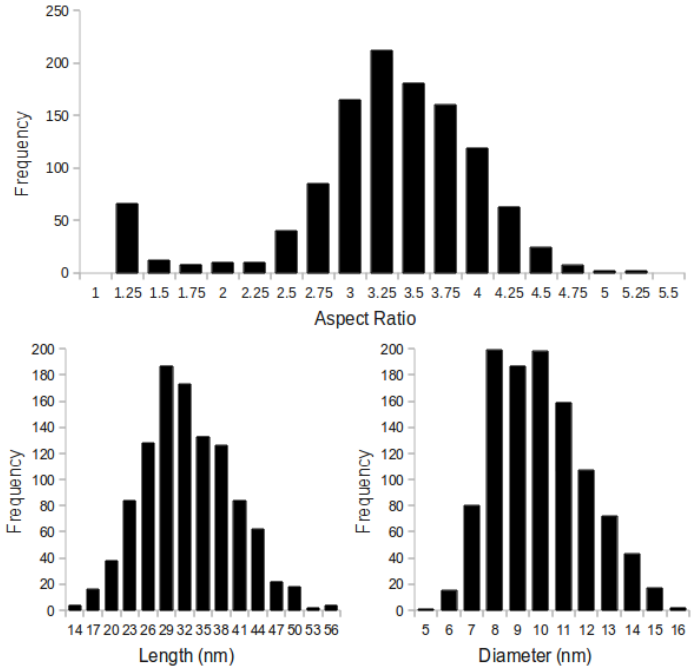

Figure 3-27: Example distributions of NR aspect ratios, lengths, and diameters. These distributions are typical. The NRs are the ones used in the MCA and polyelectrolyte experiments.

The polyelectrolyte coated NRs have their longitudinal SPR peak at 751, 760, and 751 nm (see figure 3-26D) for 1, 2,and 3 layers respectively. They are from the same NR synthesis as the MCA NRs, so they are the same size (see above and figure 3-27A).

Thickness of the ligand

We need to know the thickness of the ligand layer to accurately determine its thermal interface resistance. There are not many techniques to measure the thickness of a ligand on a nanoparticle, but since electrophoretic mobility is sensitive to the

hydrodynamic radius of a particle, it is also sensitive to the ligand thickness. We used quantitative gel electrophoresis to determine the particle hydrodynamic radius in the gel, r_{eff}, and thus the ligand layer thickness (see section 3.1.7). The mobility of the NRs was measured in varying gel percentages ($T_{gel} = 0.75 - 2.0\%$). NRs show expected shifts in their gel electrophoretic mobility (see figure 3-28), where thicker ligand layers and less charges surfaces lead to lower mobilities.

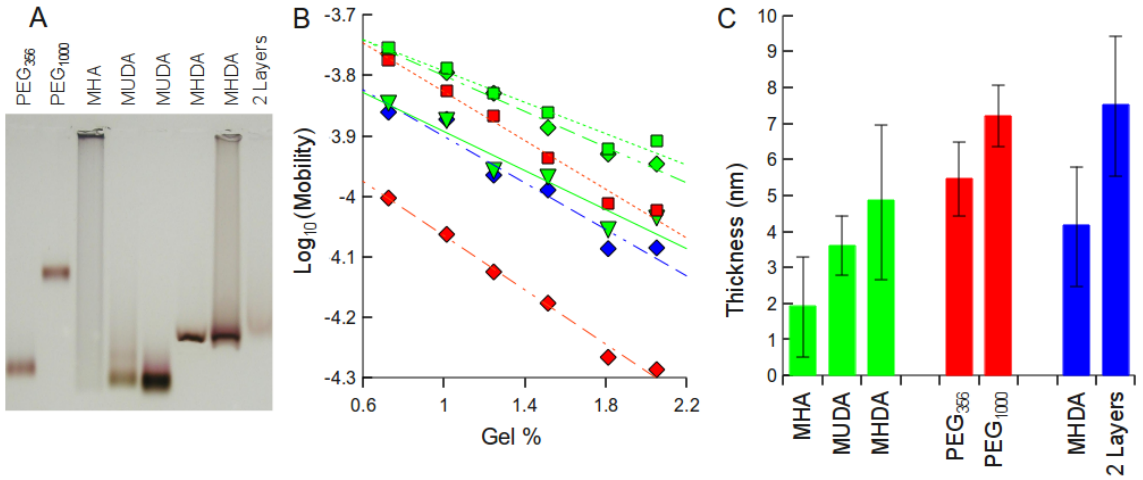

Figure 3-28: Size of gold nanorods by Ferguson plot analysis. A. Image of a 0.75% agarose gel run for 2 hours with negative electrode at the top and positive electrode at the bottom. Negatively charged particles migrate down the gel. This gel is representative of all gels used for analytical gel electrophoresis. B. Ferguson plot where the color correlates to ligand chemistry. Green = MCAs, red = PEG, blue = polyelectrolyte. The shape and fit line correlates to relative size. Square and fine dashes are the smallest ligand of a particular chemistry (MHA, and PEG_{356}), diamonds and dot-dot-dash-dash-dash lines are the middle sized ligand (MUDA, PEG_{1000}, and 2 polyelectrolyte layers), and down triangles and solid lines are the largest ligand in the class (MHDA). C. Final results of Ferguson analysis is the thickness of the ligand. The error bars represent the upper and lower bounds on thickness as calculated from the statistical error on the fitting parameter, K_R.

Some of the ligands are not in the data shown in figure 3-28. CTAB is not shown because CTAB-NRs aggregate in TBE, and will not migrate in the gel. In our analysis, we used a thickness of 4 nm for CTAB.[77] PEG_{5000} cannot be run in the same gels as the other NRs. They are so big and have such little charge that they barely move at all, so they need to be run for 6+ hours. When they do, they migrate as if they were slightly positively charged. Separate Ferguson plot analysis revealed that the

thickness of PEG_{5000} on NRs is 8.5 nm $\pm$ 1.2 nm. 1 and 3 polyelectrolyte layers-NRs also cannot be run in the gel because the PDADMAC outer layer causes them to aggregate in TBE. Based on the thickness of the 0 and 2 layer results, we extrapolate the thickness of 1 and 3 polyelectrolyte layers to be 5.9 and 9.7 nm respectively.

3.6.3 Transient absorption procedure

We used the pump-probe technique (see figure 3-24 and section 3.5.2) to obtain the transient absorption of $\sim$ 3 nM NR solutions. We used CTAB-NRs with the free CTAB concentration varying from $<$ 0.1 mM to 100 mM, spanning CTAB's critical micelle concentration of $\sim$ 1.2 mM (see figure 3-29).[14, 168] Above 300 mM, CTAB crystallizes very rapidly at room temperature, preventing stable measurements. We also used three MCA-NRs, specifically MHA, MUDA, and MHDA; three PEG-NRs, specifically PEG_{356}, PEG_{1000}, and PEG_{5000}; and three polyelectrolyte layers, specifically 1 layer-NRs have PDADMAC, 2 layer-NRs have PDADMAC/PSS, and 3 layer-NRs have PDADMAC/PSS/PDADMAC adsorbed on MUDA-NRs. These ligands were selected because they are biologically relevant, and the effects of both ligand chemistry and thickness could be tested.

The practical adjustments in the pump-probe system was adjusted until reaching an acceptable "operating window." We were careful with the transient absorption measurements because too rapid of a delay stage movement and too slow of a time constant of data collection leads to artifacts in the data. Additionally, we were careful to ensure the power of the pump laser was not too high. All our analysis is predicated on the assumption that, for small temperature rises, the absorption of the Au NR solution is linearly proportional to the temperature of the rods.[47] When the magnitude of the transient absorption data was linear with the pump power, we were satisfied that this condition was met. Finally, we were careful with the NR concentration. If the concentration were too low the signal would be small because the probe was probing fewer NRs. If the concentration were too high, the heated zone of one NR would influence the heated zone of the neighboring NR, which violates the modeling assumption necessary to perform continuum finite element analysis on

this system. We found that $\sim$ 3 nM NR solutions were sufficient. We estimate that $\sim$ 120 individual NRs are probed with every pulse.

Modeling thermal decay in NRs

To calculate the effective thermal interface conductance of the ligand, we fit the transient absorption data, assumed to be directly proportional to temperature rise, to the temperature of the NR, ($T_{NR}(t)$) as determined by a finite element, numerical model for transient heat conduction from the NR to the surrounding liquid using COMSOL (see section 3.3). We averaged the temperature of all nodal points within the Au NR region at each time-step. The average NR temperature plotted as a function of time represents the cooling curve, and we compared it with the experimental data. Using a custom written COMSOL script, we used a least squared error regression to determine the best fit on the thermal conductivity of the ligand layer. This approach accounts for the thermal mass of the ligand layer in the thermal decay, thus the need for the layer's thickness. It is important to note that it also lumps the thermal conductance of the ligand layer together with the NR-ligand and ligand-fluid thermal interface conductances into one parameter: thermal interface conductance (G).

3.6.4 Results and discussion

We performed baseline transient absorbance measurements on the buffers used, water, and CTAB solutions ranging from $<$ 0.1 mM to 300 mM CTAB with no NRs. Buffers and CTAB alone produced no signal, indicating that any transient absorption signal in experimental data is due to the NRs. Additionally, we find that increasing or decreasing the laser fluence did not alter the shape of the transient absorption curve of NRs, only its amplitude. This verifies the necessary assumption that the temperature increases of the NR after laser excitation are sufficiently small to linearize any potentially complex, unknown relationship between the change in absorption and the change in temperature of the NR.[47]

The initial $\sim$ 3 ps of the transient absorption spectra for each sample exhibit

bleaching characteristic of electron-phonon relaxation[99] (data not clearly shown) followed by oscillations that are associated with the extensional vibration mode of the NR (see figure 3-29).[60] The transient absorption data at time $<$ 300 ps are

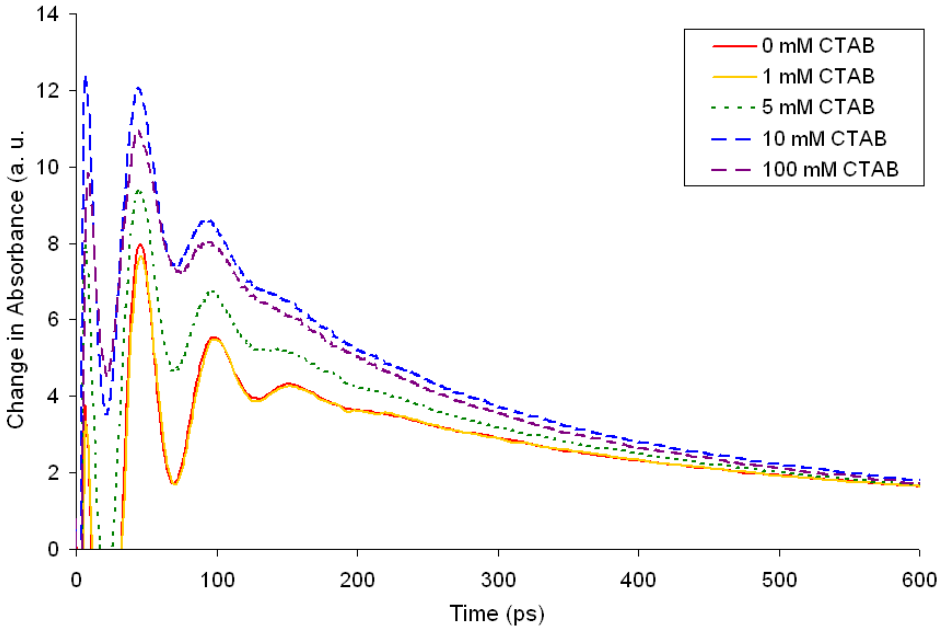

Figure 3-29: Transient absorption curves for 3 nM NR solutions with concentrations of free CTAB of $\sim$ 0 mM (red solid line), 1 mM (yellow solid line), 5 mM (green dotted line), 10 mM (blue dashed line), and 100 mM (purple dashed line). All data are normalized at t = 600 ps.

dominated by these effects,[131] so we did not attempt to fit our thermal diffusion model in the regime. However, from these vibrations, the Young's modulus of the NR can be extracted.[70]

Despite being convoluted with other vibration modes, the thermal expansion of the NR is observable even within the first 300 ps as the background on which the vibrations reside. There are clear differences in this background as a function of free CTAB concentration; there is a transition in the cooling behavior of the NRs between 1 mM and 10 mM free CTAB (see figure 3-29). The transition in behavior corresponds to the critical micelle concentration, and thus can be attributed to the formation of a stable CTAB bilayer on the NR.

Once the initial oscillations dissipate, presumably by viscous damping, all the

energy remaining in the NR resides in the lattice vibration mode. As this leads to thermal expansion of the NR, we can monitor this energy as a change in absorbance. Thus the transient absorption signal from 300 ps to the end of our experiments is directly proportional to the NR's temperature. Thermal diffusion dominates the energy transport out of the NR. We applied the finite element model to the diffusion regime

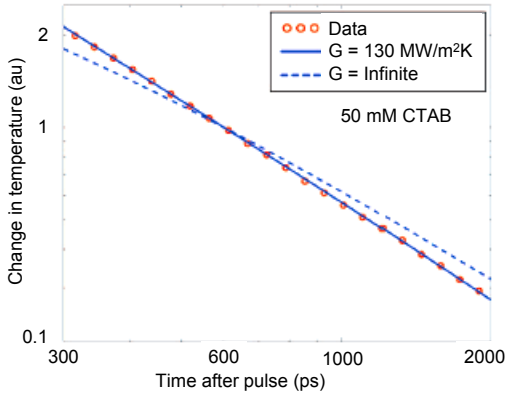

Figure 3-30: Temperature of NRs after CTAB NRs in 50 mM CTAB were irradiated with the pump beam. Measured (red dots) and calculated (blue lines) results were normalized at t = 600 ps. The calculated data represent the best fit (solid line) and the infinite thermal interface conductance results (dashed line).

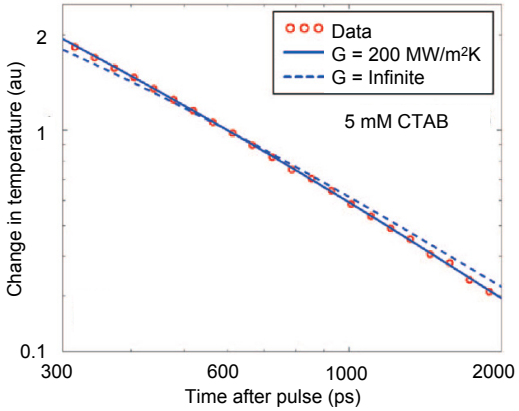

Figure 3-31: Temperature of NRs after CTAB NRs in 5 mM CTAB were irradiated. Measured (red dots) and calculated (blue lines) results were normalized at t = 600 ps. The calculated data represent the best fit (solid line) and the infinite thermal interface conductance results (dashed line).

(time > 300 ps), iterated on a variety of values for thermal interface conductance, G, and evaluated the results based on minimizing the sum of squared errors. We find

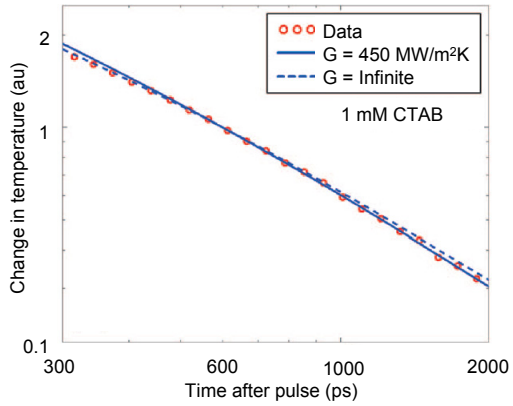

Figure 3-32: Temperature of NRs after CTAB NRs in 1 mM CTAB were irradiated. Measured (red dots) and calculated (blue lines) results were normalized at t = 600 ps. The calculated data represent the best fit (solid line) and the infinite thermal interface conductance results (dashed line).

that a CTAB-NR solution in 50 mM free CTAB has a G for the CTAB bilayer of $130 \pm 20 \frac{MW}{m^2K}$ (see figure 3-30). Similarly, a NR solution with 5 mM free CTAB has a G of $200 \pm 50 \frac{MW}{m^2K}$ (see figure 3-31), and a NR solution with 1 mM free CTAB has a G of $450 \pm 300 \frac{MW}{m^2K}$ (see figure 3-32). Note that the errors quoted were not determined in any quantitative way. They were based on the judgment of the team involved in performing these fits.

Note that in figures 3-30, 3-31, and 3-32, the models of $G \rightarrow \infty$ are shown to give an indication of the sensitivity of the fits. As the value of G increases, the fit becomes less sensitive, leading to the much larger bounds on the best fit values. At these higher values of G, it becomes difficult to statistically differentiate a value of G from infinity. For this reason, any fit that yield a value of $G > 1000 \frac{MW}{m^2K}$ is assumed to be infinite.

For the 50 mM CTAB solution (see figure 3-30) the infinite conductance line is significantly different from the best fit curve with $G = 130 \frac{MW}{m^2K}$, showing that the interface layer is controlling the cooling process. For the 1 mM CTAB solution, the cooling curve is very close to the infinite conductance case, making hard to distinguish the results from infinity. It is therefore dominated by the thermal effusivity of the surrounding fluid, or, said another way, the NR cools as if the ligand were not even

there.

Similar to the results of the CTAB experiments, we can see clear differences between the NRs as a function of MCA length. The shortest MCA (MHA) is noticeably different from the other two, which seem to be similar (see figure 3-33A). We again

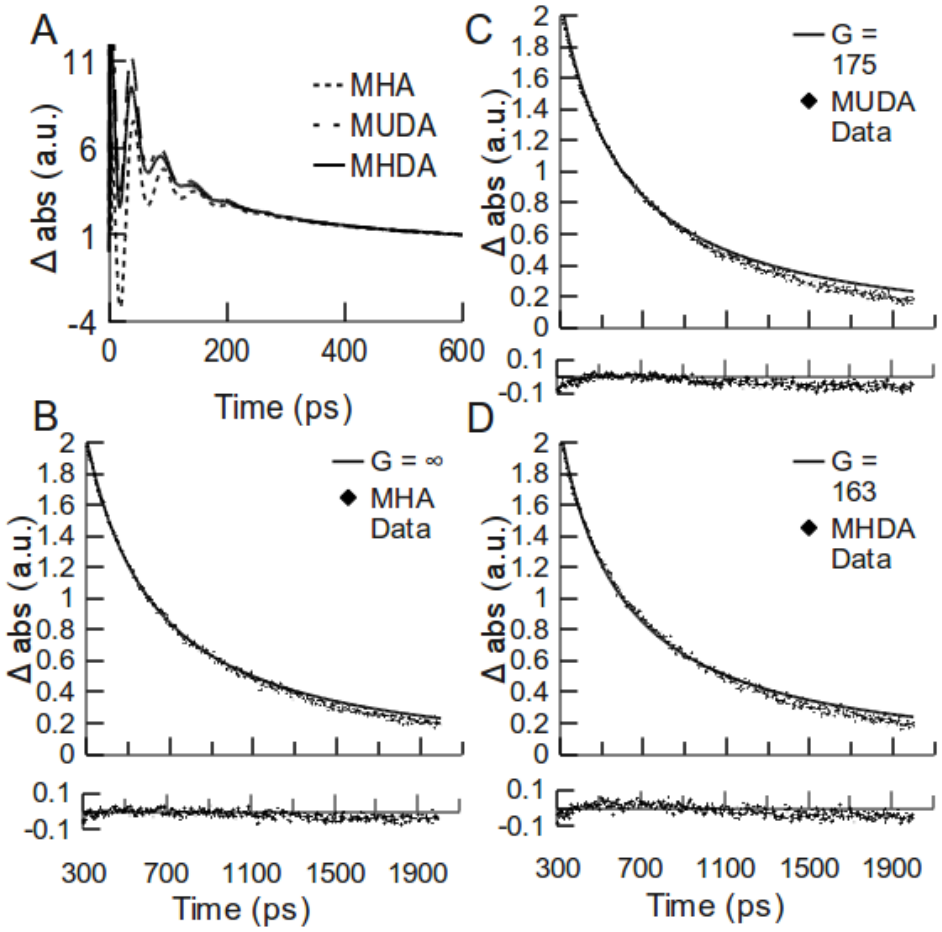

Figure 3-33: Transient absorption spectra of 3 nM MCA-NRs solutions. A. NR vibration regime. Transient diffusion regime: B. MHA-NRs, C. MUDA-NRs, D. MHDA-NRs. The transient absorbance data are the point, and the best fits are the lines. Residuals are shown below. All results were normalized at t = 600 ps.

used our finite element model to determine the thermal interface conductance, G. We find that a MHA ligand layer has a value for G that approaches infinite $\frac{MW}{m^2K}$ (see figure 3-33B). In contrast, the MUDA ligand has a G of 175 $\pm$ 75 $\frac{MW}{m^2K}$ (see figure 3-33C), and the MHDA ligand has a G of 163 $\pm$ 35 $\frac{MW}{m^2K}$ (see figure 3-33D). All three of these fits has an R^2 0.99.

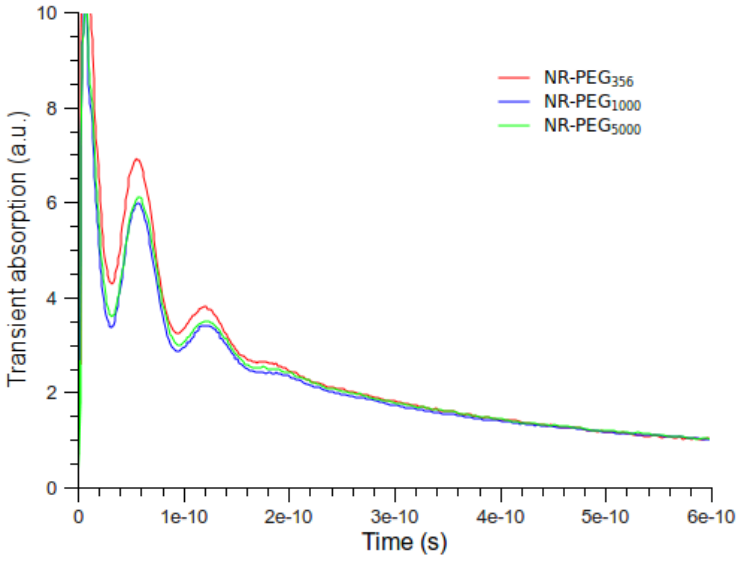

Figure 3-34: Transient absorption spectra of 3 nM PEG-NRs solutions. The NR vibration regime is shown. All results were normalized at t = 600 ps.

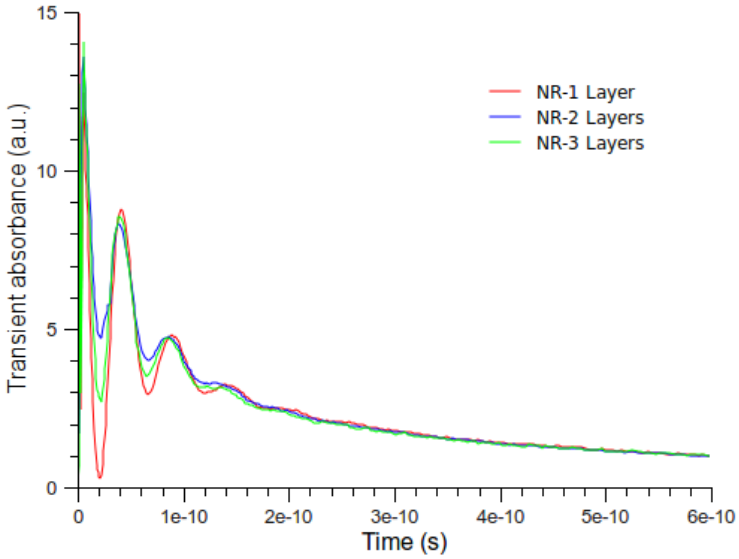

Figure 3-35: Transient absorption spectra of 3 nM polyelectrolyte-NRs solutions. The NR vibration regime is shown. All results were normalized at t = 600 ps.

As opposed the CTAB and MCA data, we cannot see clear differences between the PEG-NRs and polyelectrolyte-NRs as a function of ligand size or chemistry. With the possible exception of PEG_{356}, all of these data sets are remarkably similar (see figures 3-34 and 3-35).

Finally, we used our finite element model to determine the thermal interface conductance of PEG and polyelectrolyte layers assembled by the layer-by-layer method. We find that all thicknesses of these ligand chemistries have a value for G that approaches infinite $\frac{MW}{m^2K}$ (see figure 3-36). All of these fits have an $R^2 > 0.99$ except for PEG_{356} and the 3 layer polyelectrolyte sample who had $R^2 \sim 0.98$.

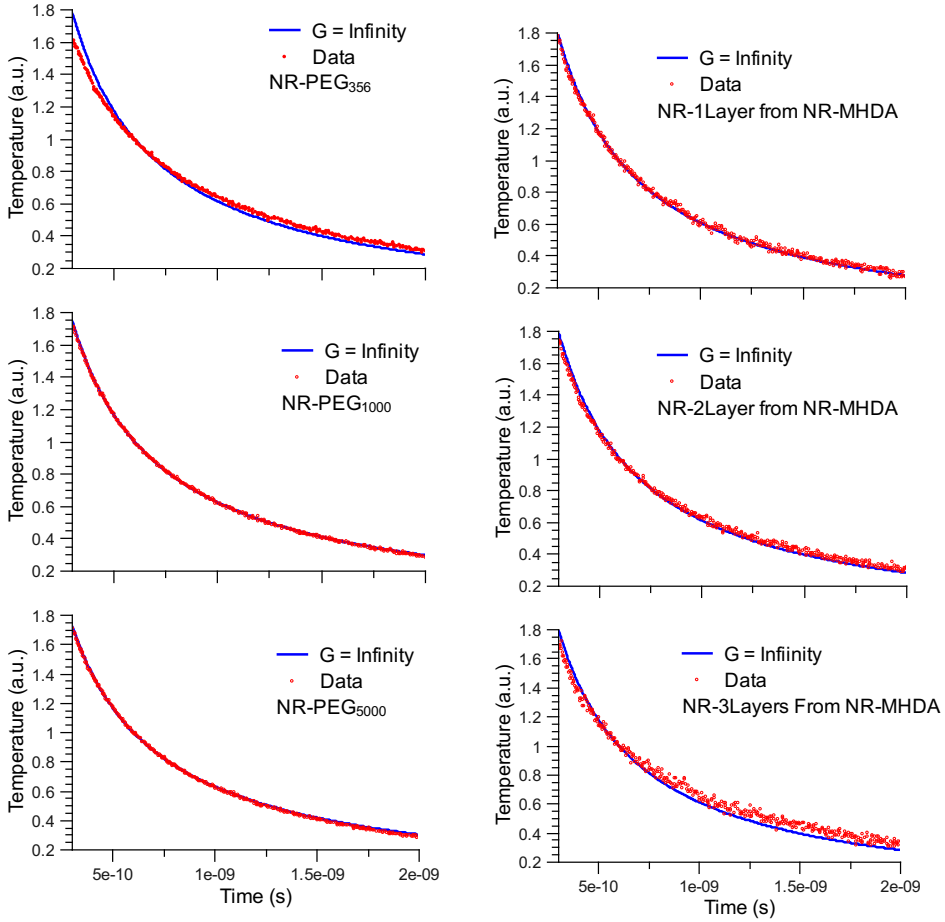

Figure 3-36: Transient absorption spectra of 3 nM PEG-NR and polyelectrolyte-NRs solutions. The NR dissipation regime is shown. The transient absorbance data are the point, and the best fits are the lines. All results were normalized at t = 600 ps.

Previously reported values of the effective thermal interface conductance, G, for

Pt and AuPd spherical nanoparticles in aqueous solution stabilized by thioalkylated ethylene glycol, tiopronin, and CTAB are between 145 – 250 $\frac{MW}{m^2K}$.[47] Others found that G = 220 ± 100 $\frac{MW}{m^2K}$ for mercaptoalkanethiolates, independent of the length.[175, 174] Our results (see table 3.3) are similar, within a reasonable margin of error, to these published results.

Table 3.3: Thermal interface conductance for all tested ligands

Ligand	G $\left[\frac{MW}{m^2K}\right]$
MHA	∞
MUDA	175 ± 75
MHDA	163 ± 35
PEG_{356}	∞
PEG_{1000}	∞
PEG_{5000}	∞
1 Layer	∞
2 Layers	∞
3 Layers	∞
CTAB below cmc	450 ± 300
CTAB near cmc	200 ± 50
CTAB above cmc	130 ± 20

The thermal interface conductance of the longer MCAs are close to, but somewhat different from, the results from mercaptoalkanethiolates.[175, 174] This is not unexpected because, despite a similar NR-ligand interaction, the different ligand-water interactions for the COO^- and CH_3 terminations could lead to differences. That the MCAs have a lower G is somewhat surprising given that hydrophobic interfaces have been shown to have lower thermal interfacial conductance than hydrophilic ones.[49] This difference could be within the experimental error. Note that the values are not statistically different based on the reported ± errors.

We find that the thermal interface conductance is independent of chain length, if the chain is long enough. These results match well with the results reported by Wang et al.[175, 174] They find that G is independent of chain length. Their experi-

mental technique (vibration sum-frequency generation spectroscopy) allows them to additionally investigate the molecular effect of heating an alkyl chain. They find that heat propagates ballistically along the chains at a velocity of 0.95 $\frac{nm}{ps}$ by measuring the delay time as a function of alkyl chain length before the heat is detectable at the terminal methyl group. By extrapolation of this time delay data back to t=0, they find that the initial step in the heat transfer from the Au to the alkyl chain is of length equal to 4 – 5 carbon segments. They note that this is in agreement with data indicating that the phonons delocalize over 4 – 5 carbon segments.[153] For this reason, it is not surprising that the MHA, with only 5 carbons before the terminal carboxyl group, has a thermal interface conductance approaching infinity. Phonons leaving the NR can directly couple with the solvent with such a short ligand.

The thermal interface conductance of all lengths of PEG and all numbers of layers of polyelectrolyte show infinite thermal interface conductance. This is significantly different than the results for CTAB or MCAs, but the chemistry of these ligands is also very different from CTAB and MCAs. Both CTAB and MCAs have a well defined, ordered, and packed hydrophobic layer. This prevents the penetration of water molecules into the ligand layers. This contrasts with PEG and polyelectrolyte layers which are entirely hydrophilic and allow for water impregnation. Others have experimentally[62] and with modeling by molecular dynamics simulations[81] concluded that water molecules are excluded from hydrophobic self-assembled monolayers and allowed to penetrate hydrophilic ones. Their results show that PEG layers consist of 83% water by volume.[62] In the restricted confines of a self-assembled monolayer, water tends to coordinate closely with atoms on the ligand. This coordination gives the water an ordered structure, almost like ice.[94] Without the disorder of liquid water, phonon transport is much more efficient. Thus it is due to the hydrophilic nature of the PEG and polyelectrolyte ligands that lead to their thermal interface conductances being not statistically different from infinity.

The change in the thermal conductance of the ligand layer above and below the cmc of CTAB leads us to conclude that the thermal behavior is associated with the formation of the bilayer.[169, 119] Below the critical micelle concentration of 1 mM,

NRs are partially passivated by CTAB. This presumably allows water to penetrate the layer more efficiently than a bilayer. Between 1 mM and 10 mM CTAB the ligand layer undergoes a transition to form a fully stable bilayer on the NR. At this point increasing the CTAB concentration produces no further change in thermal transport. A 12

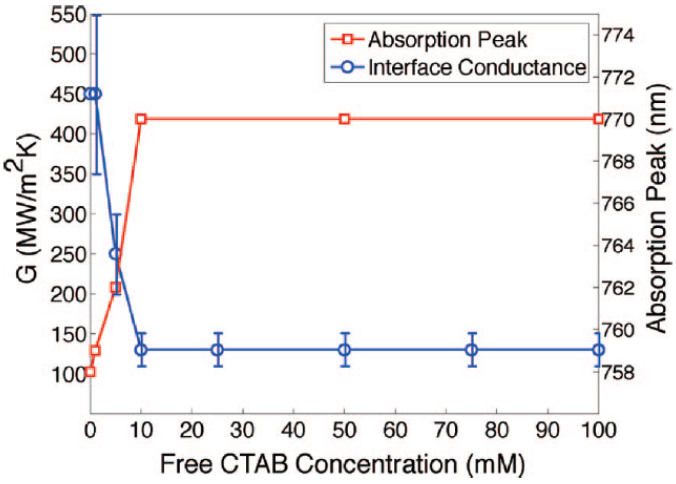

Figure 3-37: Effective thermal conductance, G, of the CTAB layer (blue circles) and SPR absorption peak (red squares) plotted as a function of free CTAB concentration.

nm red shift of the longitudinal SPR with increasing free CTAB concentration below 10 mM (see figure 3-37) also supports the conclusion that the ligand layer undergoes a phase transition. The shift coincides with the change in thermal interface conductance. It has been theoretically and experimentally demonstrated that the SPR peak wavelength in Au NRs is a strong function of the local dielectric constant,[116, 185] and therefore it is reasonable that a phase change in the CTAB ligand layer would cause the SPR to shift.[105] A similar phenomenon has been observed in Au-polymer core-shell nanoparticles, where the addition of an organic cosolvent to the suspension caused the polymer shell to swell, red shifting the SPR peak by approximately 20 nm.[48]

3.6.5 Conclusions

We demonstrated that a sensitive optical pump-probe technique can be used to study the thermal properties of Au NR ligands. Thermal conductance of the ligand layer

depends on the free ligand concentration in solution near the ligand's critical micelle concentration. Changes in the ligand layer's thermal conductance with ligand concentration correlate with a shift in the SPR and the transition associated with the critical micelle concentration of CTAB. We believe that these results are general for all metallic nanoparticles with amphiphilic ligands, independent of size or shape, and highlight the sensitivity of a nanoparticle's thermal decay to the nature of the ligand layer at the nanoparticle fluid interface. The results have utility in the design of biological applications like hyperthermia, heat transfer applications like electronic cooling utilizing nanoparticles, and studies that employ the concept of nanoscale thermal confinement.

3.7 Global heating effects

Like the global heating of the magnetic samples using RFMF (see section 2.4), if the concentration of NRs is high enough the entire sample will heat.

I quantified the magnitude of this effect by subjecting various concentrations of NRs to the laser and measuring the temperature as a function of time. The samples were exposed to a fluence of 2.4 $\frac{mJ}{cm^2}$. Note that this is more than sufficient to melt the NRs. A K-type thermocouple was used to monitor the temperature of laser irradiated NR and solvent control samples. Since water does not absorb strongly at 792 nm, the temperature rise of the control solution (see figure 3-38) is attributable to the thermocouple directly absorbing the laser. The bulk temperature rise due to the NRs was calculated by subtracting the temperature measured in the control solution from the NR solution.

Even at these very high fluences, a 1 nM NR solution (see section 3.8.2 for a discussion on NR concentration) only shows a 5.5° C temperature rise. This indicates that as long as the laser is kept low enough to not melt the NRs, there are other, more restrictive limits on the concentration than global sample heating resulting in the loss of specificity of the biomolecular switch.

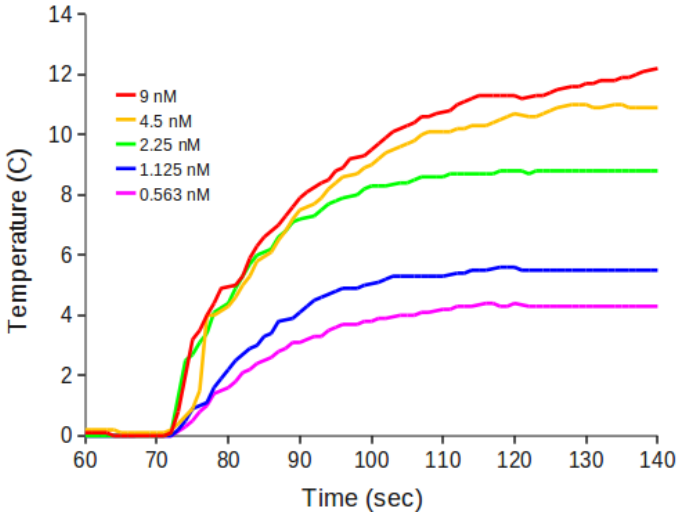

Figure 3-38: Global heating experiment results on NRs. Temperature rise of the sample as a function of time. The laser was turned on at $t = 70$ s. The data shown has had the effect of the laser on the thermocouple in a water sample subtracted.

3.8 Local heating effects

The primary reason for using ultrafast pulsed laser irradiation is to achieve local thermal confinement. There are some limits on the parameters closely related to the local heating effects. This include limits on fluence that could cause NR melting, and the concentration of NRs in the solution leading to sample auto-absorption.

3.8.1 Nanorod melting

The zeroth order experiment for the biomolecular control switch is to observe evidence of local thermal confinement. The simplest way to do this is to melt the NRs without significantly heating the entire solution. I first performed a baseline experiment with NRs in 10 mM CTAB. I heated the bulk sample up for 10 minutes at 40, 60, and 80° C using a water bath. Then I used the Cary 50 to get the absorption spectra of these NRs, and I compared them to the absorption spectrum of NRs not heated (see figure 3-39). The data shows that there is basically no effect on the NRs after exposure to this level of heat.

I next subjected the NRs to laser fluence up to 2.42 $\frac{mJ}{cm^2}$ using the biomolecular switch laser (see section 3.5.1) for 60 seconds. Again I used the Cary 50 to get the

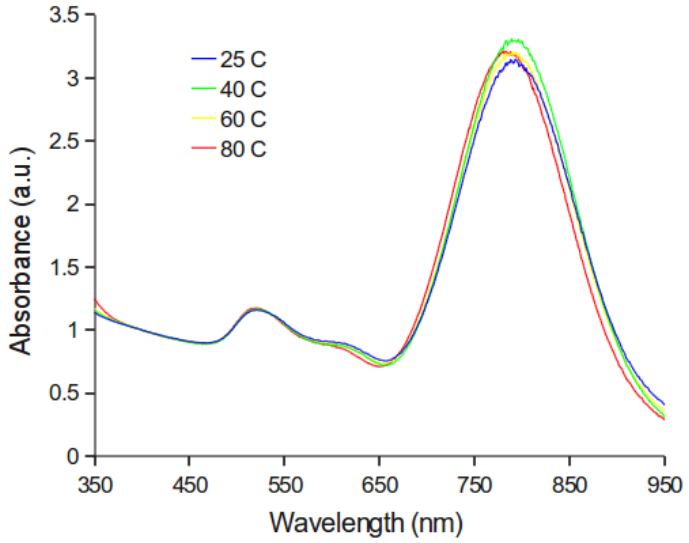

Figure 3-39: Effect of bulk heating a NR sample as assayed by comparing absorption spectra.

absorption spectra of these NRs (see figure 3-40). That the absorption near 800 nm drops, and the SPR peak blue shifts are clear evidence of NR melting because as NRs melt they tend to become more spherical. Recall that spherical particles have a longitudinal SPR closer to the transverse SPR (see section 3.1.4). This shape change was further verified by TEM analysis of the samples before and after being subjected to the laser (see figure 3-41).

Since bulk heating of the NRs up to 80° C does not have an effect on their shape, and the laser does not elevate the temperature of the sample to anywhere near boiling (see section 3.7), I conclude that the local temperature of the NRs must have been high to melt the NRs. I also conclude that there must be a steep temperature gradient, because the solution temperature did not significantly rise. Thus the biomolecular switch laser is sufficient to have local effects on a NR.

The NR melting experiments are very nice demonstrations of the ability to deliver energy specifically to a target. The experiments also demonstrate the potential power of the ultrafast laser. If not carefully controlled, the energy delivery to the NRs can cause a lot of damage. This damage could adversely affect the target molecules, thus reducing the observed efficiency of the switching mechanism. If one is not careful, this could be wrongly interpreted as the laser fluence below operating window. Addi-

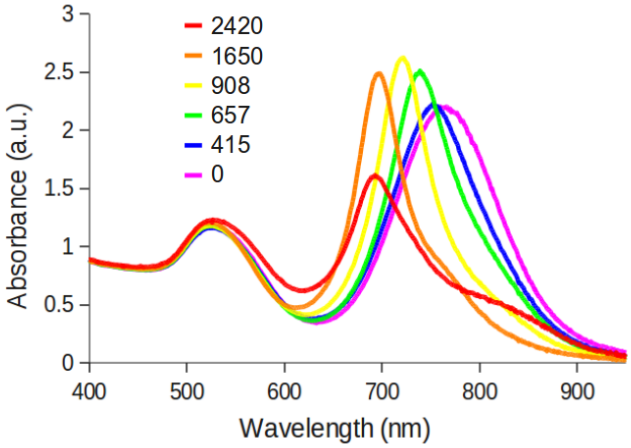

Figure 3-40: Absorption spectra of NRs after being exposed to the laser at a variety of fluences. The fluences shown in the legend all have the unit $\frac{\mu J}{cm^2}$. The results show clear evidence of NR melting.

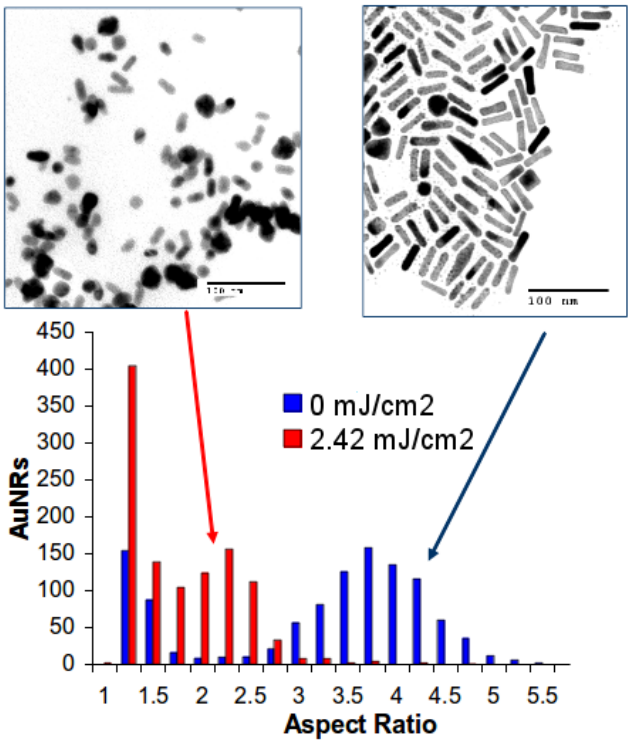

Figure 3-41: Before and after TEM of the same sample of NRs when subjected to a high fluence of ultrafast pulsed irradiation (fluence = 2.42 $\frac{mJ}{\text{cm}^2}$). It is clear that the NRs are almost all gone, but the spherical particle appear unchanged. Note that the scale bar in both plots is 100 nm. The histograms show the aspect ratio of the NRs with and without the laser exposure. The AR shift is clear.

tionally, this damage could change the shape of the NRs and thus their sensitivity to future pulses of light. This would reduce the repeatability of the biomolecular switch. Recall that real goal of the ultrafast laser system within the biomolecular switch is not to melt the NRs, but to affect the targets. Based on the disparity between the temperature of the particles and the biomolecules just a few nm away (see section 3.4), one way to possibly mitigate this problem is deliver the energy a little slower using ps lasers to reduce the possibility of melting without negatively impacting the amount of heat reaching the target biomolecule (see section 3.4.1).

3.8.2 The effect of NR concentration

Based on the Beer-Lambert law (equation 2.15) a higher concentration will lead a larger absorbance. Thus, as a function of the concentration, the particles closer to the laser will absorb all the light, and those behind will not be heated. This causes spatial variation of the control mechanism within the sample, and the specificity of the control system goes down. The extinction coefficient of NRs with $AR \sim 3.5$ at the longitudinal SPR is $4.6 \times 10^9 \frac{1}{M\,cm}$.[128] Given that samples are 3 mm in depth and laser intensity uniformity of $\geq 90\%$ is desirable, based on equations 2.15 and 2.16 the concentration would have to be $\leq 3 \times 10^{-11}$ M (see figure 3-42). For

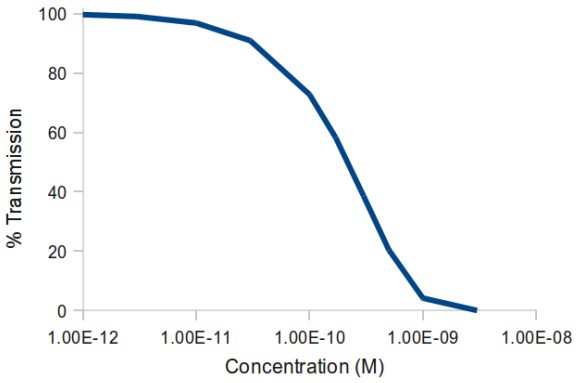

Figure 3-42: Effect of concentration on biomolecular switch specificity. Assumes that $\epsilon_{NR} = 4.6 \times 10^9 \frac{1}{M\,cm}$, and $l_p = 3$ mm. Percent transmission is $100 \times \frac{I_1}{I_0}$.

many applications 3×10^{-11} M is below the practical limit of detection. Often the controlled affect will require a greater concentration to be detectable, or the target

molecule exists in the biomolecular system to be controlled in a higher concentration than this. Based on a diffusion coefficient of $D_{\mathit{eff}} = 2 \times 10^{-11}$ from Einstein's relation assuming the hydrodynamic diameter of a NR is $D = 23$ nm, where Einstein's relation is

$$D_{\mathit{eff}} = \frac{k_B T}{3\pi\eta D}, \tag{3.13}$$

the characteristic diffusion time of a NR across the sample is longer than 5 days. To address this issue and ensure that specificity of the biomolecular switch is achieved, sample stirring is required.

I found that using approximately 1 nM NRs stuck a workable balance between uniformity (granted not very good), and the ability to assay any changes in the sample.

Chapter 4

Proof of concept using the release strategy : operating window and mechanism description

In this chapter, I describe a proof of concept experiment for the release strategy introduced in section 1.5.3 that quantifies the release mechanism, and defines the operating window for some of the key parameter using ultrafast laser excitation system. Recall that the idea behind the release strategy is that the NP suppresses the activity of the biomolecule in the default (conjugated) state. When the switch is actuated, energy from the irradiating field is converted to heat by the NP. This heat disrupts the conjugation, and it releases the biomolecule. In the released state, the NP is no longer present to suppress biomolecular activity, and the biomolecule is activated. When the field is removed, the entire system relaxes back to its default, inactive state.

The results in this chapter are presented in the context of the biomolecular control mechanism, but they can be applied to other optically triggered release applications, like drug delivery. This concept has been used for gene delivery,[68, 25, 163] protein release,[92] and combination therapies.[179]

With either framing of the problem, the key issue remains the same. Because biomolecules are sensitive to heat and prone to denaturation, particularly on nanoparticle surfaces,[10] the heat from NR melting may permanently damage the released

species, substantially reducing delivery yield. Temperature increases of the NR upon absorption of ultrafast pulsed laser irradiation in the current state of the art release studies have been estimated to be $\sim 100 - 1000^{\circ}$ C.[138, 137, 101] This level of heat either limits the payload to molecules robust enough to withstand these conditions, or forces the acceptance a low delivery yield. Therefore, determining an operating window on laser fluence that maximizes release while minimizes thermal degradation is desirable. Particularly when applied to the control system, defining an operating window on fluence that does not lead to melting will allow for one of the hallmarks of control, reversibility, to remain possible.

The other key issue often overlooked in the literature is the role surface chemistry of the NR can affect the release strategy. CTAB, the ligand that is required for NR synthesis (see section 3.1.5), is amphiphilic and forms a bilayer on the NR (see section 3.1.6). CTAB is fluxional, meaning it goes on and off the NR surface in chemical equilibrium, so the CTAB concentration most likely plays a role in release. Furthermore, the CTAB bilayer is known to affect the local thermal confinement of the NR upon laser excitation (see section 3.6),[47, 152] which could also influence release. Therefore, the CTAB layer's effect on release also needs to be determined.

Note that the majority of this chapter can be found our 2009 JPCC paper.[6] It is adapted with permission from Joshua Alper, Monica Crespo, and Kimberly Hamad-Schifferli.

4.1 Experimental plan

As a first order proof of concept, I demonstrate the release strategy using octadecyl-rhodamine B (R_{18} see figure 4-1A) as the target molecule to be released from Au NRs using ultrafast-pulsed laser excitation (see figure 4-1B). I chose to use R_{18} primarily to simplify the conjugation. Its hydrophilic head and alkyl tail mimics the chemical structure of CTAB so when incubated together, R_{18} intercalates into the CTAB bilayer on the NR or CTAB micelles in solution. It also fits the release strategy model. When in the CTAB bilayer on a NR, it is close enough to the NR to be quenched by

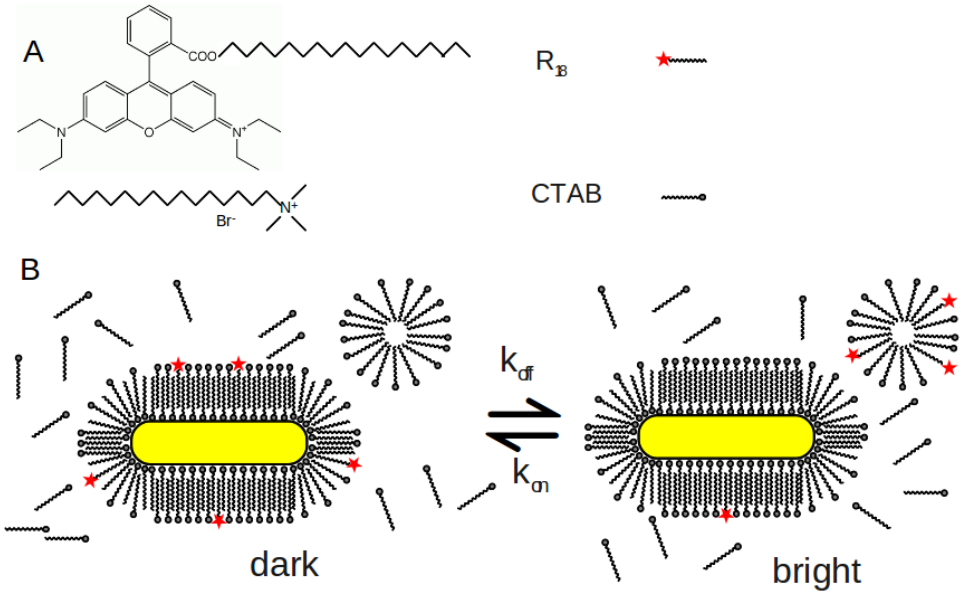

Figure 4-1: A. Octadecylrhodamine B (R_{18}) and CTAB. B. Schematic of R_{18} release as a chemical reaction.

a phase-induced suppression of the radiative rate.[38] The "dark" state corresponds to inactivity. When it is released, R_{18} is no longer quenched and fluoresces. The "bright" state corresponds to activity. The switching between quenching and unquenching allows us to use standard, static fluorescence spectroscopy to quantify the release rates.

We quantified the R_{18} release rate as a function of ultrafast pulsed laser fluence and CTAB concentration. We determined the operating window for laser fluence that limits thermal degradation while maximizes the release rate due to local heating. We compared these rates to the global heating case when the sample is heated in a water bath. Additionally, we describe how the release mechanism involves exchange of the R_{18} between the CTAB layer on the NR surface and free CTAB micelles.

4.2 Materials and methods

4.2.1 NR synthesis

The nanorods used for these experiments were synthesized using the non-seeded synthesis procedure[78] described in detail in section 3.1.5. For this experiment I used two different synthesis of NR. The final concentration of each component of the syntheses is given in table 4.1.

Table 4.1: Final concentrations of NR synthesis components in mM unless otherwise noted.

NR	CTAB	NaCl	Au^{3+}	Ag^{+}	AA	$NaBH_4$ (μM)
Long AR	150	2.25	0.90	0.14	1.80	2.00
Short AR	100	7.50	2.50	0.50	5.00	1.00

4.2.2 NR characterization

NR samples were prepared for transmission electron microscopy (TEM, JEOL 200CX) by drying $\sim$ 15 μL of 100 nM Au NR solution on a copper grid with a carbon film (Ted Pella). >1400 NRs from five images were sized with ImageJ version 1.37[142] (see section 3.1.7 for details).

Optical absorption (Cary 50 UV/Vis Spectrophotometer) samples were $\sim$ 0.5 nM NR solutions in 10 mM CTAB. NR concentration was calculated using an extinction coefficient for the longitudinal SPR of $1.9 \times 10^9 \ \frac{1}{M\,cm}$.[98]

4.2.3 R_{18} loading of NRs

The fluorescent dye octadecylrhodamine B chloride (R_{18}, Sigma-Aldrich - Fluka) was bound to the NRs by incubating 10 μL of 5 μM R_{18} in dimethyl sulfoxide with 1 mL of a 10 nM NR, 1 mM CTAB solution overnight at room temperature. Loading occurs because the hydrophobic octadecyl group on the R_{18} packs in the CTAB layer on the surface of the NR.[5, 42, 66] The R_{18} loaded NRs were washed 2$\times$ by centrifugation

to remove $\sim 99\%$ of the R_{18} not bound to NRs. The supernatant from that first wash was saved to quantigy the loading of R_{18} on NRs. The final stock solution consisted of 10 nM NR-R_{18} in 0.1 - 1 mM CTAB.

4.2.4 Laser induced release

For laser induced release, 13 μL of 10 nM NR-R_{18} stock were added to 104 μL of water. 13 μL of 100 mM CTAB were added to raise the CTAB concentration to 10 mM. A 65 μL aliquot of the sample was set aside at room temperature. The remaining 65 μL aliquot was placed in a 3 $\times$ 3 mm cuvette at the center of a 10 mm diameter laser spot. The sample was exposed to 60 - 1200 s of pulsed laser irradiation using the biomolecular switch laser in the Tokmakoff lab (see section 3.5.1). Immediately after exposure, both aliquots were centrifuged to separate the NRs from the released R_{18}. The supernatant and precipitate from both aliquots were saved for analysis.

4.2.5 Laser accelerated loading

The laser accelerated loading procedure was identical to laser induced release, except that the sample consisted of 1.3 μL of 100 nM NRs added to 130 μL of a 150 nM R_{18} and 1 mM CTAB solution. The sample was split, and all further processing of the sample was identical to the laser induced release procedure (section 4.2.4).

4.2.6 Water bath induced release

The water bath induced release procedure was identical to the laser induced release procedure (section 4.2.4), except that one aliquot was heated in a water bath instead of being exposed to laser irradiation.

4.2.7 Water bath accelerated loading

The water bath accelerated loading procedure was identical to water bath induced release (section 4.2.6) except that the sample consisted of a 1.3 μL aliquot 100 nM Au NR stock added to 130 μL of a 150 nM R_{18} 1 mM CTAB solution.

4.2.8 Fluorescence spectroscopy

One of the primary benefits of using R_{18} instead of a protein is that R_{18} is highly fluorescent. The fluorescence intensity of R_{18} ($I_{R_{18}}$) dissolved in CTAB is linear with concentration. Thus, by measuring the peak fluorescence intensity of R_{18} ($I_{R_{18},\lambda=583nm}$) I can calculate $C_{R_{18}}$ (see figure 4-2).

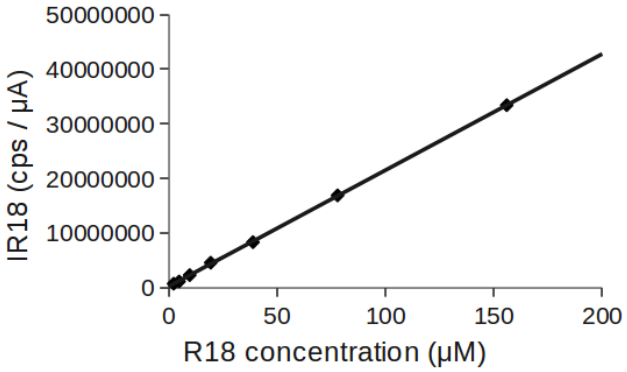

Figure 4-2: Fluorescence intensity calibration curve, $I_{R_{18}}$ vs $C_{R_{18}}$ in 10 mM CTAB. $\lambda_{excitation} = 559$ nm. $I_{R_{18}}$ is the peak fluorescence (at $\lambda_{emission} = 583$ nm) normalized by the lamp current.

Fluorescence spectroscopy was done on a HORIBA Jobin Yvon FluoroMax 3. The slit sizes were set to 2 nm for both the excitation and emission wavelengths, and the sample was placed in a 3 × 3 mm special optical glass (SOG) cuvette. These conditions are true for all fluorescence measurements in this chapter.

Fluorescence spectroscopy was used to measure the R_{18} released per NR for each sample. Fluorescence spectra of each sample's supernatant diluted in 10 mM CTAB to 130 μL were taken at $\lambda_{excitation} = 559$ nm. The fluorescence intensity of the un-exposed, room-temperature aliquot was subtracted from the exposed aliquot yielding the change in supernatant intensity. Using the calibration curve (see figure 4-2), the change in concentration of R_{18} was calculated. Dividing the change in concentration of R_{18} by the concentration of NR equals the number of R_{18} molecules released per NR. The rate of R_{18} release is found by calculating the slope of the R_{18} released vs time data. The rate of release, in units of $\frac{R_{18}}{NR \cdot s}$, can be converted to release per pulse by dividing by the repetition rate of the laser (1 kHz). This also represents the probability of releasing an R_{18} molecule with a single pulse, or the average number of

R_{18} molecules released per NR per pulse. Note that because the room temperature release rate was slow compared to the laser irradiated and water bath release rates, I assume it to be zero over the timescale of release and loading experiments.

4.2.9 Coverage of NRs

The coverage of R_{18} on NRs is defined as the average number of R_{18} molecules on each NR. To calculate this, I measured the fluorescence intensity of the supernatant after the first round of centrifugation in the washing procedure to calculate the concentration of R_{18} not bound to NRs. This concentration is subtracted from the concentration of R_{18} used in the synthesis. The key assumption is that any R_{18} molecules not remaining in the supernatant were stuck to the NRs when they were precipitated out during the centrifugation. The coverage of R_{18} on NRs is then the concentration of R_{18} not remaining in the supernatant divided by the concentration of NRs in the synthesis.

4.3 Results and discussion

4.3.1 Characterization of NRs

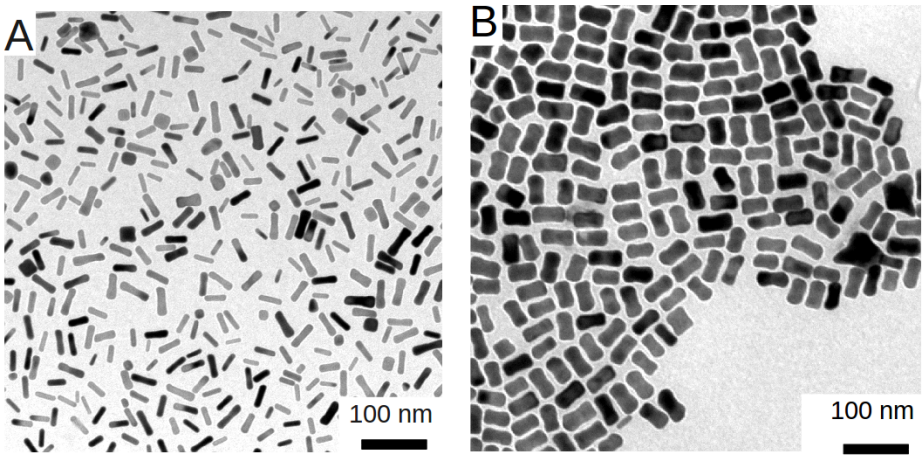

Figure 4-3: TEM of NRs. A Long AR NRs. B Short AR NRs.

All of the NRs were approximately cylindrical with hemispherical caps and monodis-

perse (figure 4-3). Long aspect ratio NRs (from here on called simply NRs) were 34.9 $\pm$7.4 nm long by 10.3 $\pm$2.6 nm in diameter, with a mean $AR = 3.6 \pm 0.7$ (figure 4-4A). The NR longitudinal SPR (figure 4-4B, solid line) coincided with the 792 nm spectral output of the fs pulsed laser (dashed line). Short AR NRs were 48.0 $\pm$ 7.7 nm long by 21.5 $\pm$ 3.9 nm in diameter, with a mean $AR = 2.3 \pm 0.4$ (figure 4-4C). The optical absorption spectrum (figure 4-4D, solid line) confirms the longitudinal SPR, 639 nm, does not coincide with the 792 nm spectral output of the femtosecond pulsed laser (figure 4-4D, dashed line).

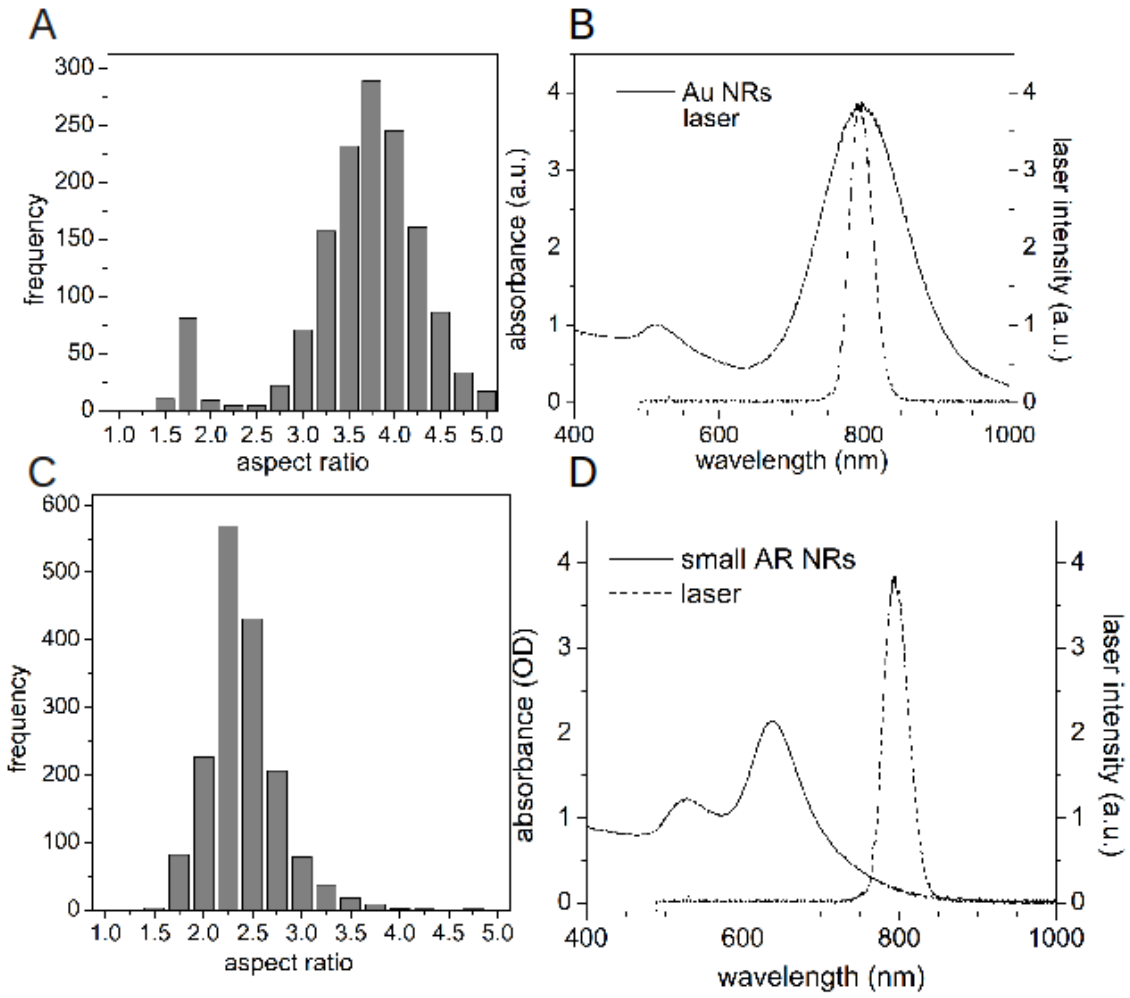

Figure 4-4: Histograms and absorption spectra of NRs. A. Histogram of long AR NRs. B. Absorption spectrum of long AR NRs. C. Histogram of short AR NRs. D. Absorption spectrum of short AR NRs.

The number of R_{18} molecules bound to NRs varied between 100 - 400 R_{18} per NR

depending on the NRs used and the conjugation parameters. Recall from section 4.2.9, to calculate the yield of R_{18} loading, I used the change in fluorescence intensity of the R_{18} loaded NR solutions solvent. The fluorescence intensity of 5 μM R_{18}, the concentration used during NR-R_{18} conjugation, and the supernatant of the first wash from the NR-R_{18} conjugation (figure 4-5, red line and black line respectively), were measured. The difference in fluorescence intensity of these two samples indicates that

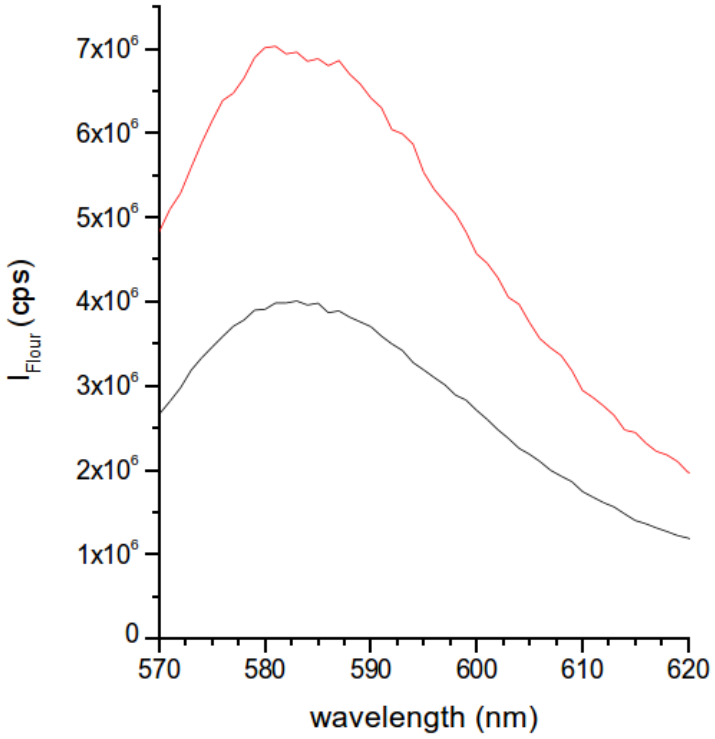

Figure 4-5: R_{18} coverage assay example data. Fluorescence intensity of R_{18} used in conjugation is the red line, and fluorescence intensity of R_{18} in the supernatant of the first wash from is the and black line.

the concentration of R_{18} conjugated to NRs is 2.12 muM. Since the concentration of NRs was 10 nM, there are an average of 212 $\frac{R_{18}}{NR}$.

4.3.2 Pulsed laser irradiation accelerates R_{18} release

We excited R_{18} loaded NRs with pulsed laser irradiation and quantified the amount of R_{18} released per NR ($R_{18,released}$) from the change in fluorescence intensity (ΔI) of

the supernatant after NR separation by centrifugation,

$$R_{18,released} = \frac{(\Delta I)_{\lambda,emissionpeak}}{\zeta C_{NR}} \tag{4.1}$$

where $\zeta = 1.39 \times 10^{12} \frac{cps_{\lambda=583nm}}{M}$ in 10 mM CTAB is the fluorescence intensity per M of R_{18} for the fluorometer parameters detailed above, and $(\Delta I)_{\lambda,emissionpeak} = I_{exposed} - I_{unexposed}$ where $I_{exposed}$ and $I_{unexposed}$ are the fluorescence intensities of the supernatant of the irradiated and unexposed aliquots of the sample respectively. After 20 min of irradiation at a fluence of 110 $\frac{\mu J}{cm^2}$, ΔI was positive (figure 4-6, purple line), indicating release of R_{18}. The ΔI was higher after irradiation with 220 $\frac{\mu J}{cm^2}$ (blue

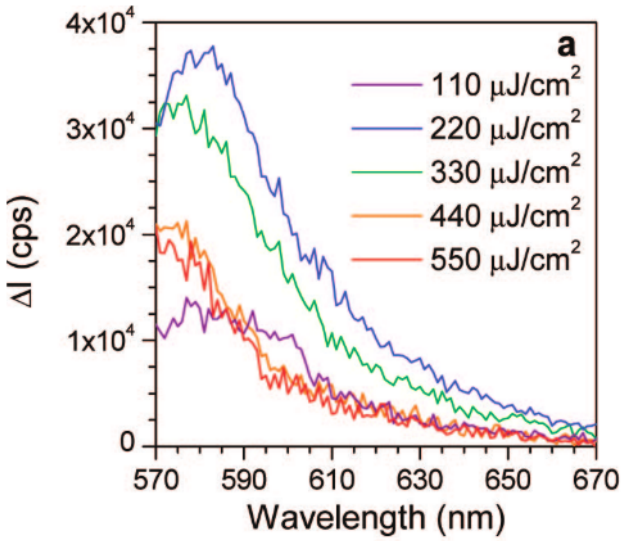

Figure 4-6: Release of R_{18} from NRs under laser irradiation. The difference between the supernatant fluorescence intensity of the laser irradiated and unexposed samples after NRs were separated from released R_{18} by centrifugation. Data for 20 min of laser exposure are shown.

line). However, under higher laser fluences of 330, 440, and 550 $\frac{\mu J}{cm^2}$ (green, orange, and red lines, respectively), the ΔI decreased. A shift of the peak fluorescence from 583 nm to 575 nm accompanied the increase in laser fluence.

I calculated the R_{18} release rate from the initial slope of the $R_{18,released}$ vs laser irradiation time (figure 4-7). At 110 $\frac{\mu J}{cm^2}$ (figure 4-7, purple diamonds) the release rate was low, 0.006 ± 0.009 $\frac{R_{18}}{NR \cdot s}$. It increased to 0.028 ± 0.019 $\frac{R_{18}}{NR \cdot s}$ at 220 $\frac{\mu J}{cm^2}$

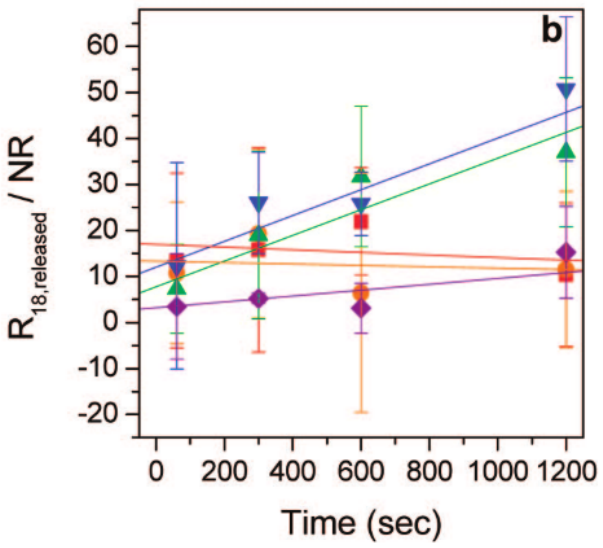

Figure 4-7: Release rate of R_{18} from NRs under laser irradiation. R_{18} per NR released as a function of laser irradiation time. Laser fluence: 110 (purple diamonds), 220 (blue down triangles), 330 (green up triangles), 440 (orange circles), $\frac{\mu J}{cm^2}$ (red squares). Error bars are the standard deviation of 3 repeats of data, and lines are the least-squares regression fit.

(blue triangles). However, at 330 $\frac{\mu J}{cm^2}$, (green triangles) the release rate was slightly lower, 0.025 ± 0.016 $\frac{R_{18}}{NR \cdot s}$. Increasing the fluence beyond 330 $\frac{\mu J}{cm^2}$ (440 $\frac{\mu J}{cm^2}$ and 550 $\frac{\mu J}{cm^2}$, orange circles and red squares, respectively) resulted in an insignificant amount of apparent release (see table 4.2).

Table 4.2: R_{18} release rates due to laser irradiation

Laser Fluence $\left(\frac{\mu J}{cm^2}\right)$	Release rate $\left(\frac{R_{18}}{NR \cdot s}\right)$	Probability of release $\left(\frac{R_{18}}{NR \cdot pulse}\right)$
110	0.006 ± 0.009	0.6×10^{-5}
220	0.028 ± 0.019	2.8×10^{-5}
330	0.025 ± 0.016	2.5×10^{-5}
440	-0.002 ± 0.007	
550	-0.003 ± 0.007	

These results indicate that the fs-pulsed laser irradiation of R_{18} loaded NRs ac-

celerates the apparent release rate of R_{18}. The apparent release rate increases with laser fluence until 220 $\frac{\mu J}{cm^2}$, after which it begins to decrease. I hypothesize that at fluences > 220 $\frac{\mu J}{cm^2}$, the apparent release rate decrease is due to thermal degradation of the R_{18} while the actual release rate is probably increasing. Thus, I refer to the observable release rate as the "apparent release rate." Further evidence of degradation is in the fluorescence intensity peak shift (figure 4-6) of the R_{18} at the high laser fluences.

The spread in the apparent release rate data represents the standard error weighted by the standard deviations of each individual data point. Thus, despite the wide error bars shown in figure 4-7, there is greater than 85% statistical confidence (Student's t-test) in the increased apparent release rate between 110 and 220 $\frac{\mu J}{cm^2}$. However, since the apparent release rate values are very sensitive to the released molecule (R_{18}) and all the experimental and laser parameters, I suggest the general trend is more important than the actual values. This trend is apparent in data in figure 4-7, and it is reflected in the raw fluorescence data taken across all similar experiments (see figure 4-8).

With all the parameters as specified above, the optimal apparent release rate is 0.028 $\frac{R_{18}}{NR \cdot s}$. Given a 1 kHz laser repetition rate, the probability of releasing an R_{18} from a NR with any given pulse is 2.8 $\times 10^{-5}$. This suggests that the apparent release rate can be doubled by doubling the repetition rate of the laser to 2 kHz while keeping all the other parameters constant.

4.3.3 Controls on the release of R_{18}

There are a number of possible explanations for the apparent release other than the local heating effect of NRs tuned to absorb the laser light. To test for some of these I performed a series of control experiments. These include testing the effect of the laser on the R_{18} alone, determining the global temperature rise due to the laser and NRs, and testing what happens if the NRs are not tuned to the laser.

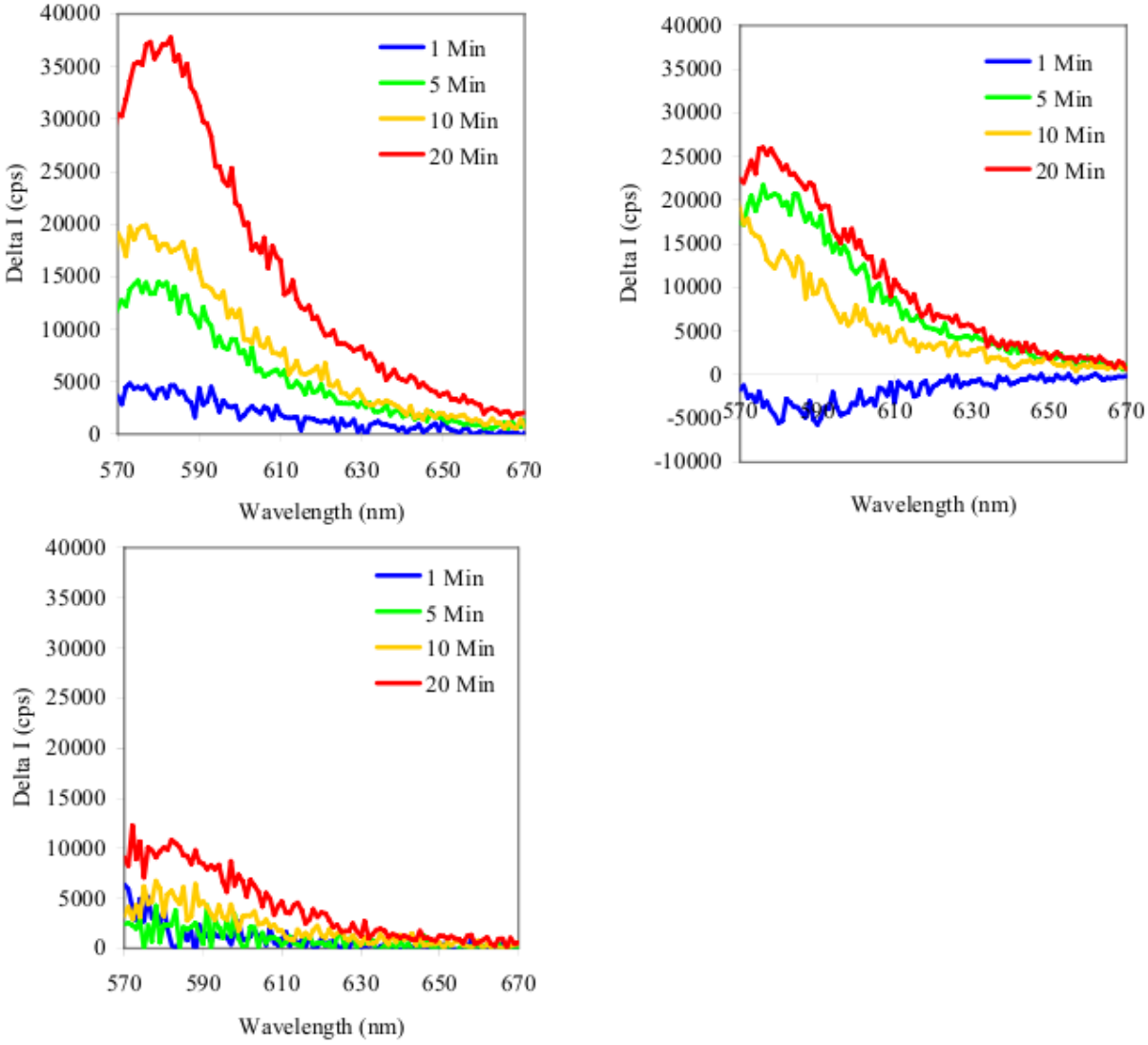

Figure 4-8: Additional example data (see figure 4-6) from release of R_{18} from NRs under laser irradiation experiments. Plotted here is the difference between the supernatant fluorescence intensity of the laser irradiated and unexposed samples after NRs were separated from released R_{18} by centrifugation. In all plots, time length of laser irradiation: 1 min (blue), 5 min (green), 10 min (orange), 20 min (red). a) and b) Data from 2 separate trials at a laser fluence of 220 $\frac{\mu J}{cm^2}$. c) Data taken at a laser fluence of 110 $\frac{\mu J}{cm^2}$.

Global heating effect

I performed a control the see if the bulk temperature rise of the solution upon laser irradiation was responsible for the apparent R_{18} release rates. I measured the temperature rise of a 1 nM NR solution when irradiated at 330 $\frac{\mu J}{cm^2}$ to be $\Delta T \sim 0.7°$ C (figure 4-9A). To determine if this temperature rise can explain the observed R_{18} release, we heated an aliquot of an R_{18} loaded NR sample to 30° C ($\Delta T = 7°$ C) in a water bath and quantified the R_{18} release. The fluorescence intensity of the heated aliquot (dots,figure 4-9B) was the same as the unheated aliquot (line). This suggests that the increased apparent release rate is due to spatially confined temperature effects at the NR specific to ultrafast laser irradiation, not direct solvent heating by the laser.

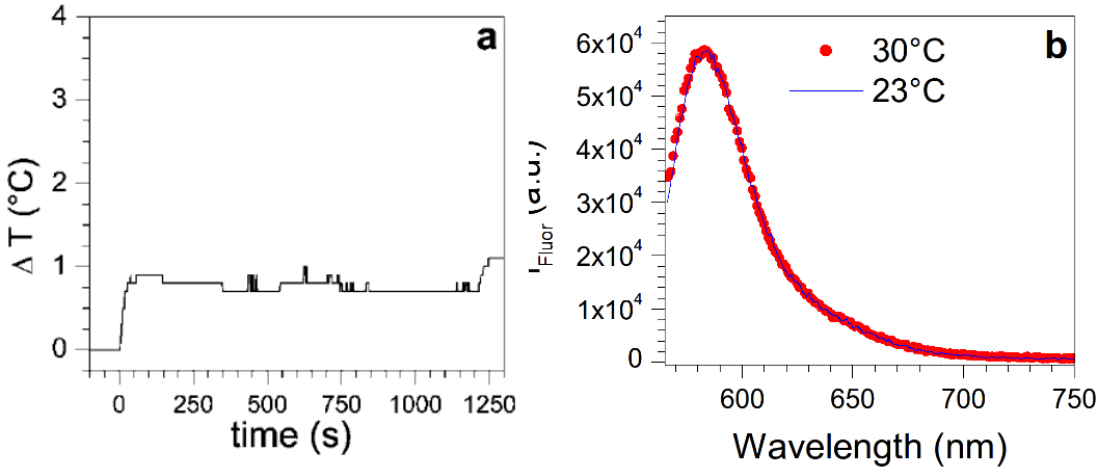

Figure 4-9: Controls for bulk heating due to the laser. A. The bulk temperature rise of the sample due to NR heating. Pulsed laser irradiation began at time = 0 and continued for the duration of the test. The fluence was 330 $\frac{\mu J}{cm^2}$, the wavelength 792 nm, and the repetition rate 1 kHz. B. Fluorescence intensity of the supernatant of an aliquot of sample heated to 30° C ($\Delta T = 7°$ C, points) in a water bath and an aliquot left at room temperature, 23°, (line) for 20 min.

Effect of laser irradiation on the R_{18}

I also performed experiments to test whether laser irradiation of the R_{18} alone can explain the apparent R_{18} release rates. I selected R_{18} as a model for a biological

molecule to study laser induced release because it, like most biological material, does not absorb light in the near infra red (see figure 4-10). 50 nM R_{18} in 10 mM CTAB was

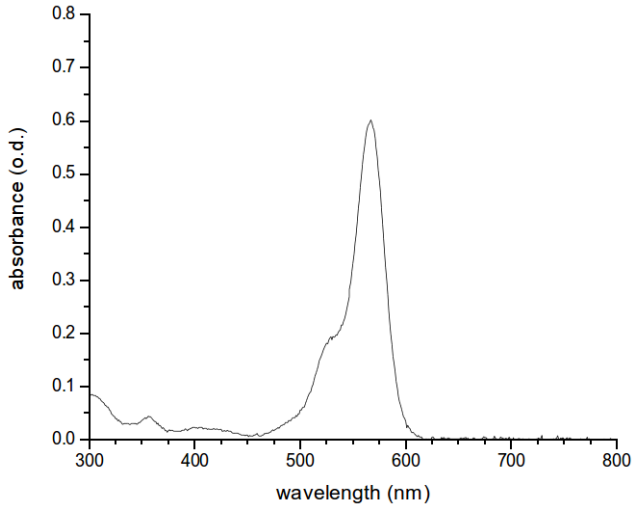

Figure 4-10: Absorption spectrum of R_{18}.

exposed to the laser with a fluence up to 550 $\frac{\mu J}{cm^2}$ for 10 minutes. The fluorescence intensity of each sample was measured (see figure 4-11). The data indicates that laser irradiation does not affect the fluorescence intensity free R_{18}. This result indicates that the changes in fluorescence intensity of the solvent cannot be explained by direct absorption of laser irradiation by R_{18} and thus the observed R_{18} release is specific to excitation of the NR.

Effect of NR aspect ratio on release

For the last major control experiment, I explored whether the apparent R_{18} release rate is dependent on the aspect ratio of the NRs. Recall that I synthesized NRs (see section 4.2.1) used in the release experiments (section 4.3.2) intended to focus the heat generated by the laser onto target molecules. This focusing occurs because the absorption peak of the Au NRs, as determined by the aspect ratio of the NRs, corresponds to the lasers spectral output. I also synthesized NRs with a smaller aspect ratio (see section 4.2.1 for synthesis and section 4.3.1 for characterization including figures with TEM and UV/Vis). Note that the she optical absorption spectrum (see

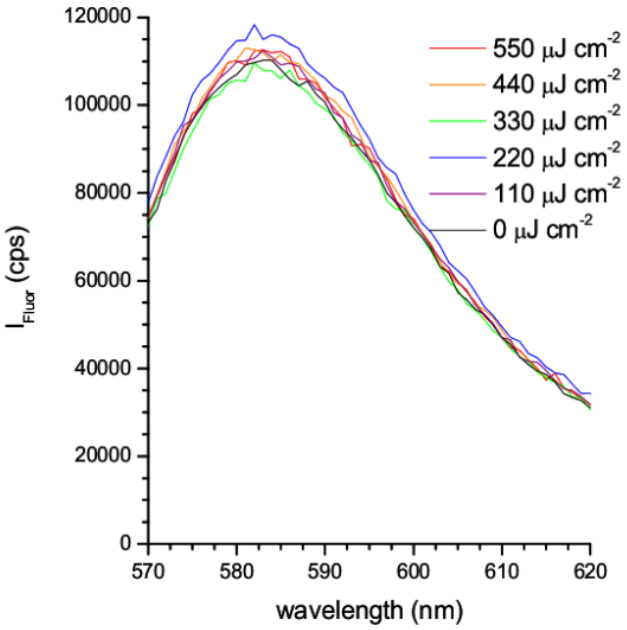

Figure 4-11: Fluorescence intensity of R_{18} in 10 mM CTAB after 10 minutes of laser irradiation.

figure 4-4D, solid line) confirms the longitudinal SPR, 639 nm, does not coincide with the 792 nm spectral output of the femtosecond pulsed laser (figure 4-4D, dashed line).

R_{18} release experiments were performed on R_{18}-NR conjugates (see section 4.2.4). Even after 20 min at any fluence tested, there is no observed change in fluorescence intensity of the supernatant (see figure 4-12). This is in contrast to the larger aspect ratio NRs, which showed a strong dependence on the laser fluence (figures 4-7 and 4-6). Based on this contrast, we conclude that laser irradiation does not affect the release rate of R_{18} from smaller aspect ratio NRs, whose longitudinal SPR absorption peak of 639 nm does not overlap the laser excitation. Thus, laser irradiation did not accelerate the apparent release rate of R_{18}. The laser release results are specific to NR-R_{18} conjugates where the NRs have their longitudinal SPR tuned to the spectral output of the laser.

4.3.4 Exchange Mechanism

CTAB is amphiphilic and fluxional, and it forms a bilayer at the NR-solvent interface.[118] Even at equilibrium CTAB molecules, as a fluxional ligand, continuously exchange

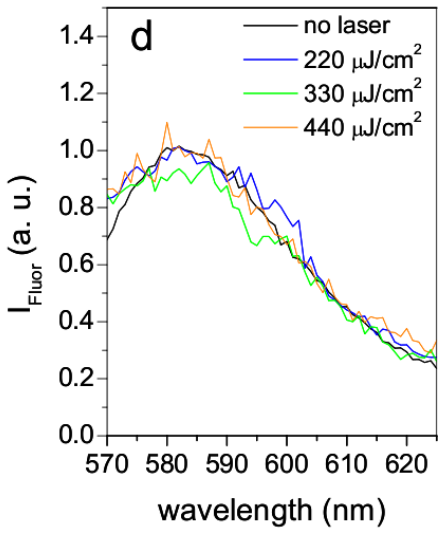

Figure 4-12: Fluorescence intensity of R_{18} in the supernatant after release from small aspect ratio NRs.

from the bilayer on the NR surface to the solution, where it exists as isolated molecules or forms micelles. Because R_{18} is also amphiphilic, it too continuously exchanges from the CTAB bilayer on the NR surface to the solution, where a CTAB micelle stabilizes it (see figure 4-1). Similar exchange mechanisms have been observed for the movement for other hydrophobic dyes interspersed in sodium dodecyl sulfate (SDS) and Triton X-100 micelles.[42] Because R_{18} is minimally soluble in water, it has a strong tendency to intercalate into a CTAB micelle. Fluorescence spectroscopy showed that

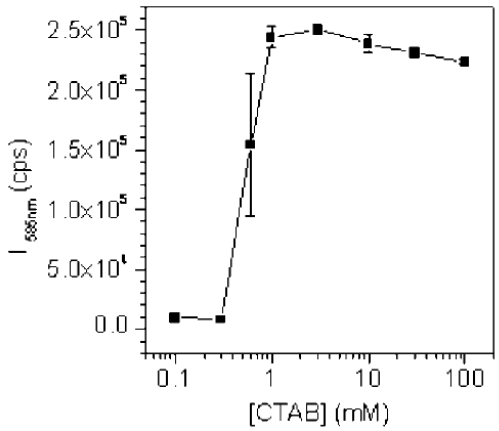

Figure 4-13: Fluorescence intensity of 100 nM R_{18} as a function of CTAB concentration. Error bars are the standard deviations of 3 sets of data.

R_{18} was not fluorescent at low concentration of CTAB (see figure 4-13) and that the fluorescence intensity of R_{18} had a clear transition at CTAB's critical micelle concentration (cmc $\sim$ 1.2 mM[14, 168]) suggesting that free, isolated R_{18} in solution is minimal. This exchange of R_{18} at the NR-solvent interface can be described by

$$R_{18,bound} + M_{site} \underset{k_{on}}{\overset{k_{off}}{\rightleftharpoons}} NR_{site} + R_{18,micelle} \tag{4.2}$$

where M_{site} and NR_{site} are an unoccupied R_{18} binding sites on CTAB micelles and NRs respectively, and the rate of release is

$$\frac{d[R_{18,micelle}]}{dt} = k_{off}\left[R_{18,bound}\right]\left[M_{site}\right] - k_{on}\left[NR_{site}\right]\left[R_{18,micelle}\right] \tag{4.3}$$

where $[R_{18,micelle}]$ is the concentration of R_{18} solvated by CTAB micelles, $[R_{18,bound}]$ is the concentration of R_{18} loaded into the CTAB bilayer on NRs. The concentration of unoccupied R_{18} binding sites in micelles is

$$[M_{site}] = n_{CTAB}[M] - [R_{18,micelle}]\,, \tag{4.4}$$

the concentration of unoccupied R_{18} binding sites on NRs is

$$[NR_{site}] = n_{NR}[NR] - [R_{18,bound}]\,, \tag{4.5}$$

n_{NR} and n_{CTAB} are the valency numbers of NRs and CTAB micelles respectively, $[NR]$ is the concentration Au NRs. $[M]$ is the concentration of CTAB micelles, and is defined as

$$[M] = \frac{[CTAB] - cmc}{n} \tag{4.6}$$

where n is CTAB's aggregation number and $[CTAB]$ is the concentration of CTAB.

4.3.5 CTAB influences the binding and release of R_{18}

The details of the exchange mechanism suggest that release and binding may be influenced according to Le Chatelier's principle. Given that the $cmc \sim 1.2$ mM and $n \sim 20$,[14, 168] at 1 nM NR and above the cmc ($[CTAB] \sim 10mM$), the concentration of CTAB micelles is much greater than the concentration of NRs ($[M] \gg [NR]$). Thus, R_{18} tends to go into free micelles because the positive term in equation 4.3 dominates. However, just below the cmc, $[M]$ approaches zero, and R_{18} tends to bind to the NRs because the negative term in equation 4.3 dominates. Thus, according to equation 4.3, the CTAB concentration influences the rate at which R_{18} exchanges on and off the NR, particularly for $[CTAB] \sim cmc$.

Using Le Chatelier's principle, I exploited the dependence of the release rate on $[CTAB]$ during the process of loading R_{18} onto NRs and its release. Since maintaining $[CTAB] < cmc$ favors R_{18} binding to the NRs, a low $[CTAB]$ helps to load R_{18} onto NRs and maintain a low rate of R_{18} release once loading is complete, with negligible R_{18} loss over a period of days. However, if the $[CTAB]$ is too low, the NRs are not stable, and they will aggregate. Additionally, since maintaining $[CTAB] > cmc$ favors R_{18} release off the NRs, immediately prior to release experiments $[CTAB]$ is increased to accelerate the rate of exchange to a measurable value.

4.3.6 Bulk heating accelerates R_{18} release and binding

I heated R_{18} loaded NRs in a water bath, and I measured the rate at which R_{18} both bound to and came off the NR. Released R_{18} ($[R_{18,micelle}]$) increased with time (see figure 4-14a), and the rate of release $\left(\frac{d[R_{18,micelle}]}{dt}\right)$ increased with increasing temperature (see table 4.3). By fitting the rate of release at various temperatures to the Arrhenius equation (see figure 4-14a, inset), I obtained the activation energy of release, $E_{a,off} = 25.2\ \frac{kcal}{mol}$. R_{18}-NR association showed similar results (see figure 4-14b, table 4.3), with a binding activation of $E_{a,on} = 26.1\ \frac{kcal}{mol}$. These E_a values are comparable to those observed for the exchange of pyrene-containing triglycerides in Triton X-100 micelles, $E_a = 38.2\ \frac{kcal}{mol}$.[145]

Table 4.3: R_{18} release and binding rates due to water bath heating

Release		Binding	
Water bath (T ° C)	Release rate $\left(\frac{R_{18}}{NR \cdot s}\right)$	Water bath (T ° C)	Release rate $\left(\frac{R_{18}}{NR \cdot s}\right)$
30	0.004 ± 0.007	30	-0.042 ± 0.004
40	0.012 ± 0.012	40	-0.217 ± 0.048
50	0.066 ± 0.012	50	0.470 ± 0.091
60	0.135 ± 0.005	60	2.56

I compared the rate of release of water bath heated and laser-irradiated samples. The maximum apparent release rate (0.032 $\frac{R_{18}}{NR \cdot s}$ for 220 $\frac{\mu J}{cm^2}$ laser fluence) for specific, local heating using fs pulsed laser irradiation before the effects of NR melting dominated corresponded to globally heating the sample using a water bath temperature between 40 and 50° C.

4.3.7 Pulsed laser irradiation accelerates R_{18} binding

That the binding rate increases with water bath temperature suggests that laser irradiation can accelerate not only the rate of release but also the reverse reaction, binding to the NRs. I added 1 nM NRs to 150 nM R_{18} in the presence of 1 mM CTAB and irradiated it with fluences of 220 and 330 $\frac{\mu J}{cm^2}$ (see figure 4-15, blue filled triangles and green circles, respectively). $[R_{18,micelle}]$ decreased as a function of time due to binding to the NR, with a rate $\left(\frac{d[R_{18,micelle}]}{dt}\right) = -0.069$ and $-0.094\frac{R_{18}}{NR \cdot s}$, respectively (see table 4.4). However, higher fluence (440 $\frac{\mu J}{cm^2}$, orange squares) did not increase the rate further. This behavior is similar to other laser irradiated samples at high fluence (figure 4-7) and can be attributed to R_{18} thermal degradation.

4.3.8 Excess CTAB inhibits laser induced R_{18} binding

$[CTAB]$ plays a key role in optimizing release and binding. Equations 4.3 and 4.6 suggest high $[CTAB]$ can inhibit R_{18} binding $\left(-\frac{d[R_{18,micelle}]}{dt}\right)$. To test this, I irradiated

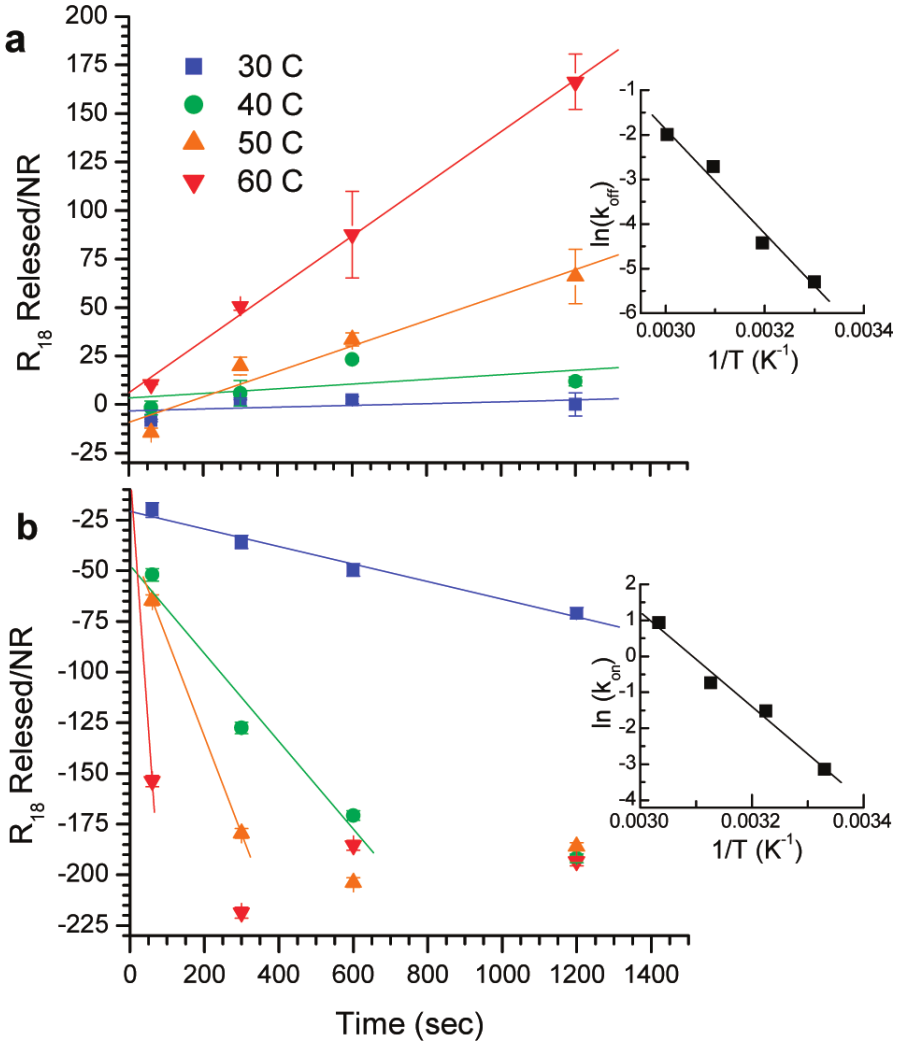

Figure 4-14: Induced release and binding of R_{18} when heated in a water bath. In both plots, water bath temperatures: 30° C (blue squares), 40° C (green circles), 50° C (orange up triangles), 60 °C (red down triangles). Insets: Arrhenius plots. (a) Release of R_{18} as a function of time. Error bars are the standard deviation of 2 repeats of data. (b) Release of R_{18} as a function of time (negative numbers indicate binding). Samples are 1 nM NR, 1 mM CTAB, and 150 nM R_{18}. Lines are the least-squares regression fit for the initial, linear portions of these data.

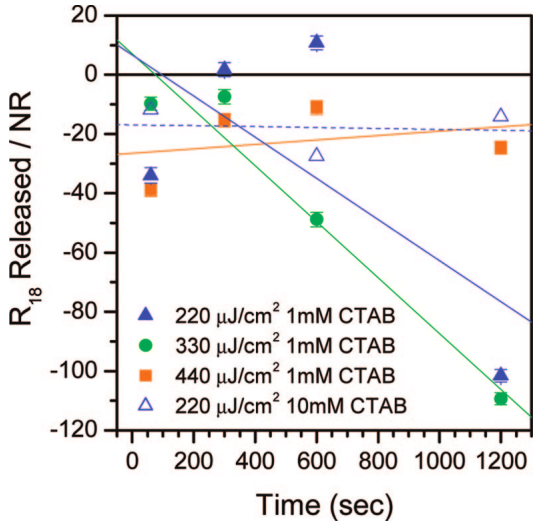

Figure 4-15: Binding of R_{18} to NRs under laser irradiation. Cumulative release (negative numbers indicate binding) of R_{18}. Filled data points are 1 nM NR, 1 mM CTAB, and 150 nM R_{18}. Open data points are 1 nM NR, 10 mM CTAB, and 150 nM R_{18}. Laser fluence: 220 $\frac{\mu J}{cm^2}$ (blue triangles), 330 $\frac{\mu J}{cm^2}$ (green circles) and 440$\frac{\mu J}{cm^2}$ (orange squares). Lines are the least-squares regression fit and the binding rate is the initial slope of these data (table 4.4).

Table 4.4: R_{18} binding rates due to laser irradiation

Laser Fluence $\left(\frac{\mu J}{cm^2}\right)$	Binding rate $\left(\frac{R_{18}}{NR \cdot s}\right)$	Probability of binding $\left(\frac{R_{18}}{NR \cdot pulse}\right)$
220	-0.069 ± 0.054	6.9×10^{-5}
330	-0.094 ± 0.015	9.4×10^{-5}
440	0.007 ± 0.017	

1 nM NRs and 150 nM R_{18} in the presence of 10 mM CTAB. At 220 $\frac{\mu J}{cm^2}$ the rate of R_{18} binding to the NR was 0.002 $\frac{R_{18}}{NR \cdot s}$ (figure 4-15, blue dashed line and empty triangles), $\sim 35\times$ slower than when $[CTAB] = 1$ mM (figure 4-15) blue solid line and filled triangles). These results, in combination with the fact that $[CTAB]$ strongly influences the NR thermal interface conductance,[152] demonstrate that maintaining an appropriate $[CTAB]$ is critical for controlling release.

4.3.9 NR melting correlates to the upper limits of laser accelerated release

Ultrafast-pulsed laser irradiation can melt Au NRs. Because the longitudinal SPR is a strong function of NR AR,[105] it can be used to monitor the onset of melting as a function of laser fluence [25, 67, 100] (see figure 4-16). The SPR peak position (inset)

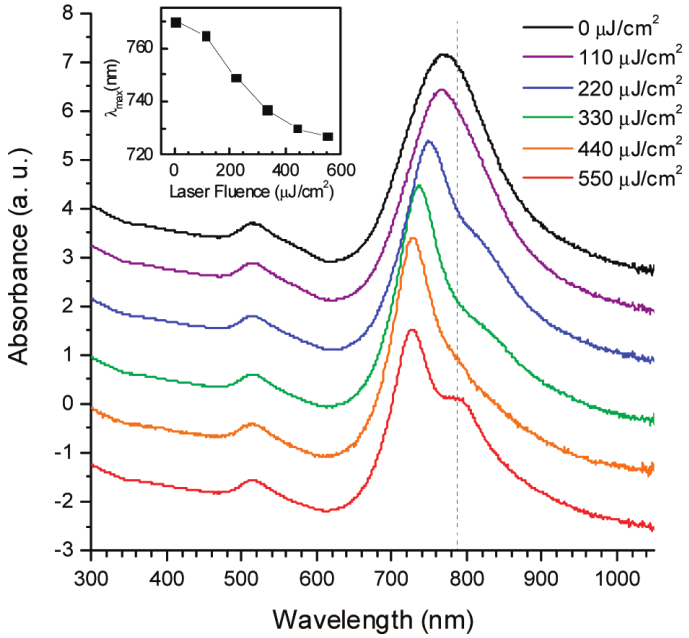

Figure 4-16: Optical absorption of NRs after 20 min of femtosecond pulsed laser exposure. All data were normalized at $\lambda = 375$ nm. Dotted vertical line corresponds to the max laser output, and the spectra are offset for clarity. Laser fluence: 0 (black line), 110 (purple), 220 (blue), 330 (green), 440 (orange), 550 $\frac{\mu J}{cm^2}$ (red). Inset: longitudinal SPR wavelength ($\lambda_{mathitmax}$) as a function of laser fluence.

shifted under laser fluence as low as 220 $\frac{\mu J}{cm^2}$, indicating the onset of melting. This

coincides with the transition between an accelerated and decelerated exchange rate, suggesting that the observed decelerated exchange rate is primarily due to thermal degradation. Therefore, the fluence of 220 $\frac{\mu J}{cm^2}$ maximizes the apparent release rate while minimizing R_{18} and NR destruction.

4.4 Summary and broader impact of the proof of concept experiment

Ultrafast-pulsed laser irradiation accelerates the release of R_{18} from a NR surface. The effect is specific to NRs excited at their longitudinal SPR absorption band. Laser induced bulk solvent heating is not sufficient to accelerate release, so the release is due to local heating of the NR. This demonstrates that the ultrafast pulsed laser system employing a release strategy is feasible.

As expected, there are physical and practical limits that govern the operating windows on the key release parameters. Thermal degradation of the R_{18} and the Au NRs defines the upper limit on the laser fluence. Additionally, there are limits on the ligand chemistry. A simple model explains the relationship between the kinetics of R_{18} release and the concentration of CTAB. While the mechanism presented is a simplified model of what occurs upon laser excitation of the NRs, it shows that by judicious choice of free ligand concentration, either release or capture of the target molecules by NRs can be achieved with laser irradiation.

These results emphasize the importance of ligand surface chemistry and laser fluence on release rates. They have important implications beyond the biomolecular activity switch for using ultrafast laser irradiation of NRs to deliver a broad range of molecules. Because laser-induced release from NRs is complex and involves multiple processes, future studies will examine how these processes independently influence release and binding rates.

Chapter 5

Conclusions and future considerations

The desire to engineer biology grows every day. As new applications of biological engineering are thought of, the need for specific external control of biomolecular activity also grows. Previous studies have demonstrated control using techniques such as chemical,[106] electrical,[182] laser induced thermal,[82, 86, 143] direct thermal,[113, 134, 135] and photoactivated [109] means. However, each of these studies lacks at least one of the key hallmarks of an ideal biomolecular activity control system: that it be external, specific, and reversible.

We proposed a biomolecular activity switch. The switch consists of four key components: a target biomolecule, a nanoparticle, an electromagnetic field, and conjugation technique. To achieve all three hallmarks of ideal control the parameters governing each of these components must be carefully controlled.

There are two primary goals of this thesis. First, to demonstrate that biomolecular control using electromagnetic field irradiated NPs to locally heat and actuate the activity of a conjugated biomolecule is feasible. Second, to define a set of rules on how to accomplish this type of biomolecular control. Specifically, the goal is to provide the physical and practical limits on the parameters governing the key components of the biomolecular activity switch.

5.1 Major conclusions

Many of this thesis's conclusions are found throughout the previous 4 chapters. In this section only the key conclusions will be summarized.

5.1.1 The biomolecular switch is feasable

First and foremost, this thesis demonstrates using a "first order" proof-of-concept experiment that the biomolecular activity switch is feasible. The key components of this experiment were octadecylrhodamine B as a model for a biomolecule where the fluorescence of the R_{18} represents the biomolecular activity that is actuated, CTAB passivated gold nanorods (NRs) tuned to absorb light in the near infrared, an infrared femtosecond pulsed laser, and a conjugation between the R_{18} and the NR due to hydrophobic interactions between the R_{18}'s alkyl tail, and the CTAB bilayer on the NR. The demonstration was done using the "release" strategy where R_{18}'s activity was suppressed by the NR's quenching ability when conjugated. R_{18} was activated by the release because the released R_{18} was far from the NR and no longer quenched.

The demonstration showed that the biomolecular activity switch achieves all of the hallmarks of an ideal biomolecular control system. It showed that the actuation is external because release was triggered by initiation of laser irradiation outside of the biological system. It is specific because local thermal confinement ensured only conjugated R_{18} were effected, and because the laser did not affect the R_{18} in the absence of the NR. It is reversible because the laser was able to accelerate binding as well as release.

5.1.2 Limits on the electromagnetic field

Like any of the key components, the electromagnetic field must work in concert with the other key components of the system. The field needs to be tuned to match the physical properties of the NPs that allow for specific absorption of the field's energy.

Radio frequency magnetic fields are not a feasible means of energy delivery

Despite the highly specific nature of magnetic nanoparticles to absorb RFMFs, using them in the biomolecular control system is not feasible. The time scale of energy conversion in the magnetic NP-RFMF system (τ_{eff}) is at least two orders of magnitude slower than the heat dissipation time (τ_D) over length scale of nanometers necessary to achieve specificity in biomolecular systems.

The RFMF system could be useful as a control system to compete with other technologies that heat specific regions on the cellular scale, $\geq 10\mu$m.[113, 134, 135] If the technical challenges, including transmission line effects and shield requirements, can be overcome, this is a very promising technology for systems where the lower bound on the characteristic length of the temperature gradient is 10μm. It would compete favorably with the previously reported direct thermal control systems.

Ultrafast laser fluence must be carefully controlled

Ultrafast pulsed laser irradiation is a feasible means of energy delivery. The "first order" proof-of-concept experiment demonstrated this, as mentioned above. There are limits on the laser parameters if ultrafast pulsed lasers are to be an energy source that achieves each of the hallmarks for an ideal biomolecular control system.

The experiments showed that the lower limit on laser fluence is defined by the onset of measurable release. I found that the lower bound on laser fluence is between 110 – 220 $\frac{\mu J}{cm^2}$. One way to think about achieving the onset of release is increasing likelihood that the target biomolecules overcome the energy barrier keeping them from being actuated. This suggests two ways to decrease the the lower bound on the fluence, thus increasing the parameter's operating window and making the biomolecular switch more robust. The first way is to decrease the the energy barrier keeping the target biomolecule from being actuated probably by altering the conjugation technique, the NR ligand, or the system's environment. The second way is to increase the frequency of laser pulses thus increasing the likelihood that the target will be actuated in the timescale of order seconds. This can take the form of introducing a "pulse chain,"

where the duration of elevated temperature at the target is extended thus increasing the probability of actuation. This could also take the for of increasing the repetition rate, which does not affect the probability of the actuation event, but it increases the number of potential actuation events in a given time.

The experiments also show that the upper limit on laser fluence is defined by both the onset of NP melting and the thermal degradation of the target biomolecule. I found that the upper bound on laser fluence is $\sim 330\frac{\mu J}{cm^2}$. NP melting defines the upper bound because NR melting changes its aspect ratio and thus its optical properties change. To ensure switch repeatability energy, the absorbing and converting properties of the NP must not change. More difficult to quantify, but equally important, thermal degradation of the target defines an upper bound on fluence because destruction of the biomolecules also limits the repeatability of the biomolecular activity switch. The upper bound on fluence could be raised if the laser pulse were made longer.

This thesis concludes that the helpful and destructive effects of the laser must be balanced. Thus an optimum may exits. I found that the optimum was between 220 – 330 $\frac{\mu J}{cm^2}$.

This optimum is not a generally applicable result. The optimum fluence and the bounds on fluence are highly dependent on each of the key components of the biomolecular switch, thus they need to be determined on a case-by-case basis. They will have to be determined experimentally, because the physical models that govern the interactions between metallic NPs, biomolecules, and electromagnetic fields are not good enough to be predictive to the necessary level of certainty. However, many of the trends and analyses given in this work are generally applicable. The 220 – 330 $\frac{\mu J}{cm^2}$ is probably as good as any place to start looking for an optimum for any particular system.

5.1.3 Limits on the nanoparticle

The choice of nanoparticle is critical to the biomolecular switch's success. My work demonstrated some of these limits including those on the concentration of particles,

their size and shape, and the sample polydispersity.

Limits on magnetic nanoparticles

Theoretical analysis and experimental results confirm that the primary limit on the RFMF system is the size of the heated zone. To minimize the heated zone, and thus achieve the hallmark of specificity through local thermal confinement, the energy conversion time constant ($\tau_{mathiteff}$) must be minimized. The NP needs to be small such that the Néel relaxation mode dominates. For smaller particles, this time constant can be $\sim 10^{-6}$ s. However, the trade off is a lower power output per particle for any given magnetic field strength. Thus, the need for larger H which could lead to practical limits on the field producing equipment.

Limits on NR aspect ratio

The results from the proof-of-concept experiments show that the spectral output of the laser must overlap with the NRs' longitudinal absorbance peak. This ensures NRs will absorb as much energy as possible, which in turn helps ensure specificity. The longitudinal absorbance peak is highly dependent on the NRs' aspect ratio, which can be controlled by adjusting the synthesis procedures. My analysis indicates that the NRs need to hit the target mean AR, as determined by the matching of the longitudinal SPR with the peak laser output, within ± 0.25 if the NR SPR peak is to be within the ~ 50 nm FWHM wavelength width of the laser.

The polydispersity of NR AR needs to be kept to a minimum. For the same reasons that matching the SPR to the laser is important, so is keeping polydispersity to a minimum. Polydispersity is difficult to control, but purification by centrifugation can help, as well as ensuring that ligand exchange does not significantly broaden the longitudinal SPR absorption peak. Polydispersity, even on a relatively monodisperse sample, can lead to only $\sim 40\%$ of the particles being significantly heated by the laser.

NR yield needs to be maximized. With similar consequences as polydispersity, the number of spherical NPs should be kept to a minimum in NR samples.

The quantitative upper and lower bounds on SPR to laser matching, polydispersity, and NR yield are impossible to state generally. Minimizing the former two and maximizing the latter parameter are desirable. Anything deviation from perfect matching, monodispersity, and 100% yield will reduce the efficiency of the biomolecular switch. The limits therefore will be determined by how important efficiency of the switch is to the final application.

Limits on NP concentration

In a laser irradiated sample, if the concentration is too high, the particles closer to the laser will absorb all the light, and those behind will not be heated. This causes spatial variation of the control mechanism within the sample, and the specificity of the control system goes down. For the case of NRs, a 3 mm sample size, and the need to have at least 90% of the incident light intensity affecting all NRs, the upper limit on NRs concentration needs is 3×10^{-11} M. This is often not practical, so for the laser irradiated biomolecular switch, the concentration of NP should be kept at a minimum. If the minimum practical concentration is higher than calculated upper limit, stirring, if practical, will help reduce spatial variation of laser intensity within the sample.

Secondly, with any irradiating field type, if the concentration is too high the NPs will be too close together and the heated zones will overlap before the heat can dissipate from the sample. This causes the entire solution to heat and the specificity of the control system goes down. Both experiments and analysis indicate this limit is less restrictive than the upper limit on concentration determined by specificity. In the rare case that it is less restrictive, the upper limit on concentration is around 10 nM.

5.1.4 Limits on the conjugation

The interplay between the conjugation chemistry, the NP ligand, the biomolecule, and the control strategy is critical. Conjugation is often dictated by the other key

parameters, like chemistry of the biomolecule, so it may be a parameter the system designer has very little control over. However, it can have some of the highest impact. The energy associated with the interactions between the NPs and target biomoelcules is probably the most important parameter when trying to achieve a particular control strategy. For the "release" strategy I demonstrated, the conjugation had to be weak enough to allow for release without destruction of the NR or the biomolecule. For a "denaturation" strategy, the conjugation would have to be strong enough to withstand the effects of the laser pulse.

Limits on free CTAB

In the "release" strategy demonstration using R_{18} and NRs, the concentration of free CTAB in solution is critical to release. To achieve release, the concentration of CTAB should be above CTAB's cmc. To achieve binding, the concentration of CTAB should be near or just below CTAB's cmc. The trade off to dropping the concentration of free CTAB too far is a reduction in NR stability.

Thermal properties of ligands

Because the surface to volume ratio of NPs is so very high, the thermal interface resistance between the NP and the solvent has a large effect on the time varying temperature field around the NP. Above the cmc, a CTAB bilayer has a low thermal conductance. At or below the cmc, a CTAB bilayer has a high thermal conductance. Mercaptoalkyl acids that are long enough ($>$ 6 carbons) also have a low thermal conductance, while shorter ones have a thermal conductance approaching infinity. Additionally, PEG and polyelectrolyte layers have a thermal conductance approaching infinity. The ligand layers with low thermal conductance have well defined separation between the metallic NP and the solvent. This provides insulation and a higher energy interface between the particle and the solvent. The ligand layers with high thermal conductance tend to allow infiltration of the solvent molecules into the ligand layer. This provides a better conduction path and a lower energy interface between the NP and the solvent.

Depending on the release strategy and the details of the biomolecule there could be thermal considerations that would lead to the selection of one ligand chemistry over another. This work on the thermal properties of the ligand allows the biomolecluar switch designer to make intelligent choices that could help open up the operating window for laser fluence, ligand chemistry or conjugation chemistry leading to a more robust biomolecular switching system.

Interaction between ligand and biomolecule

Though I do not have a lot of positive results to describe the interactions between the ligands and biomolecules, I do have lots of negative results. My conjugation failures lead me to conclude that conjugation between the NP and the biomolecule is not trivial. It can be difficult to achieve conjugation without aggregation, to quantify or even assay the coverage, and to control the confirmation state of the biomolecule when it is conjugated.

Some nice work was done by others in the Hamad-Schifferli lab on this front, particularly Marie-Eve Aubin-Tam's work.[12, 11, 10]

5.1.5 Limits on the biomolecule

For the biomolecular switch to be reversible, the time constant associated with recovery, $\tau_{recovery}$, must be longer than the repetition rate of the laser. A key characteristic of the R_{18}-CTAB-NR system is that the CTAB provided another hydrophobic area for the R_{18} to reside. This provided an energy barrier to reversal that was difficult for the R_{18} to overcome. If the system relied on diffusion alone to carry the R_{18}, it is likely that it would rebind to the NP before the next pulse could hit the system and cause release again.

The operating window could be opened up on this limit if either the repetition rate of the laser were increased or a "pulse train" were used.

5.2 Broader implications

The primary goals of this work were to demonstrate a biomolecular switch and to provide some insight into the operating windows for many of the parameters governing the switching mechanism. But much of the experimental and theoretical work done has implications beyond the biomolecular control switch. Many of these studies could be applied to drug release applications. There is much interest in the literature for targeted drug theraperies, and NP systems are promising. They allow for decoration with both the drug and targeting molecules. They have high contrast in both optical and magnetic imaging systems, and their properties allow for heating to accelerate drug release. It is for these applications that this work is broadly applicable, including the studies on R_{18} release from CTAB, and thermal properties of ligands.

Even beyond drug delivery, this work is valuable to those interested in nanometer length-scale thermal systems of all kinds. Many of the analyses I have done are generally applicable, and the role of thermal interfaces is a key concept lost on many working in the field.

5.3 Future considerations

This work demonstrated the feasibility of using ultrafast pulsed laser irradiation in biomolecular control, but it really only represents a first order proof-of-concept. The work will hopefully be a useful starting point for many future studies.

5.3.1 Near term "enabling" studies key to achieving external biomolecular control

This thesis, and those of my colleagues in the Hamad-Schifferli lab, are just starting to reveal how the biomolecular switch could work. All of our work has been useful in quantifying particular aspects of the switch, but there is still a lot of work that needs to happen before making the biomolecular switch into a useful biological engineering tool. Here are some of the next steps, as I see them:

The rules governing biomolecule metallic nanoparticle conjugation need to be extended to the challenges specific to NRs. This is an extension of Marie-Eve Aubin-Tam's work. This will help guide site specific biomolecule conjugation. This will also help guide conjugation that can either specifically preserve biomolecule activity or disrupt it.

The CTAB used in NR synthesis is incompatible with biological systems, so the NR ligand exchange procedure needs to be made more general. This would allow for a greater diversity of ligands and thus biomolecule conjugation techniques, which would, in turn, enable a greater diversity of switching strategies and allow for finer resolution on control.

The conclusions of this work indicate that the operating window on the power generated in the NR is be small. The upper bound on the fluence is to ensure specificity and reversibility, while the lower bound is to ensure the switch actually actuates when desired. To improve this aspect, further work needs to be done to characterize and optimize the nanoscale heat generation and transport. One area that my analysis indicates should be pursued is to use a longer pulse. Additionally, by adjusting the repetition rate or using a pulse train, the efficiency of the actuation could be greatly improved.

Another immediate next step is to characterize various biomolecule nanoparticle conjugation techniques. The strength of the binding, the characteristic time of release, and the characteristic time of reversal are all critical parameters that will be a strong function of specific biomolecule and the conjugation technique. General rules governing some of these parameters would enable an analytical approach to switch design.

5.3.2 Near term demonstration of biomolecular switch with a biological target

In parallel with these suggested enabling studies, the switch should be demonstrated with a more biological sample. In this section I provide some suggestions for possible

systems.

Gramicidin used to control bactericidal system

The idea here is to demonstrate the switch using the release strategy. Gramicidin is a 15 amino acid peptide that is a bactericide. It is active against Gram-positive and select Gram-negative bacteria. It naturally has 3 forms: A 80%, B 6%, C 14% which together make D, the naturally occurring mixture. The primary structure is formyl-L-X-Gly-L-Ala-D-Leu-L-Ala-D-Val-L-Val-D-Val-L-Trp-D-Leu-L-Y-D-Leu-L-Trp-D-Leu-L-Trp-ethanolamine where X = valine or isoleucine, Y = Trp in gramicidin A, Y = Phe in B, and Y = Tyr in C. It has no secondary structure in H_2O, but takes on a β-helix in hydrophobic bilayers (see figure 5-1A) where it dimerizes to form a channel for monovalent cations (its bactericidal mechanism, see figure 5-1B).

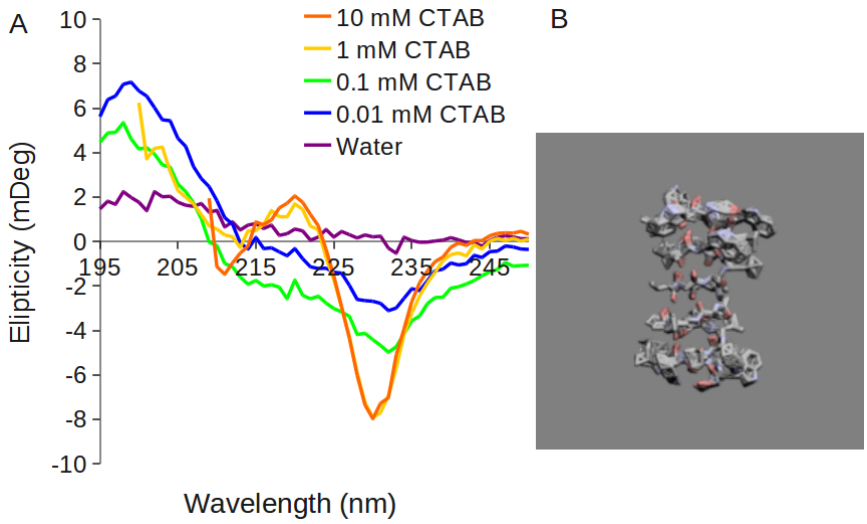

Figure 5-1: A. CD spectra of gramicidin D in various concentrations of CTAB above and below the cmc. Above the cmc it displays the characteristic β-helix structure. Below the cmc, it is unstructured. B. Diagram of gramicidin D dimer showing the β-helix structure.[108]

Gramicidin is a nice model molecule because it conjugates to NRs in a manner similar to R_{18} as evidenced by its preference to enter CTAB micelles (see figure 5-1). Also, it has a place to go in solution if either there are CTAB micelles present, or if there are target bacteria. Additionally, a nice assay would be to monitor its activity

by the rate at which it kills bacteria.

The primary output from this experiment would be to show that a biological molecule could remain active after release from a NR by ultrafast pulsed laser irradiation. My preliminary experiments were inconclusive about whether gramicidin conjugates to CTAB. Using an actual lipid bilayer on the NR may prove more successful.[97]

Microperoxidase-11 used to control catalysis of peroxide lysis

The idea here is to demonstrate the switch using the release strategy. Microperoxidase-11 (MP-11) is a peptide (Val-Glu-Lys-(Cys-Ala-Gln-Cys)Heme-His-Thr-Val-Glu) that is amino acids (11 – 21) of Cyt C, including the heme. It is prepared by enzymatic degradation of equine heart cytochrome c. MP-11 has been shown to preferentially enter CTAB micelles where its peroxidase activity is enhanced.[140]

MP-11 is a nice model molecule because it is part of the well studied protein cytochrome C, the Hamad-Schifferli lab has a lot of experience with it, it conjugates to NRs in a manner similar to R_{18} as evidenced by its preference to enter CTAB micelles[140], it has a highly sensitive fluorogenic assay (N-Acetyl-3,7-dihydroxyphenoxazine - which fluoresces in the presence of the products of split H_2O_2)[115], and its heme is highly absorptive so its released concentration can be determined independently of enzymatic activity.

The primary output from this experiment would be to show that a biological molecule could remain active after release from a NR by ultrafast pulsed laser irradiation. It would allow for further characterization of the system. My preliminary experiments seemed to indicate that MP-11 tended to aggregate in the presence of CTAB and did not enter the bilayer on the NR. We eventually abandoned this in favor of other pursuits, but the technical obstacles around conjugation could be solved. Then, I believe this would be an excellent system.

Thrombin-aptamer system used to control blood clotting

Depending on how some preliminary experiments turn out, this system could be used to demonstrate one of two switching strategies. The root concept here is to conjugate

a thiolated DNA aptamer[18, 167] to the NR with gold-thiol chemistry (see figure 5-2) and use that system to control blood clot formation.

Figure 5-2: Schematic of NR-thrombin-aptamer system. The NR (yellow) is shown coordinated with the 3' end of the aptamer. The ribbon diagram of human thrombin (purple)[150] has the active site cleft with the active site Ser shown in gray. The ribbon diagram of the DNA ligand (turquoise), is positioned such that nucleotide T12 (green) in the second loop of the G-quadruplex can establish a contact with Phe245 (green) of thrombin. The A at position 4 of the G-quadruplex (pink) which plays a role in determining the binding site of this DNA and the first G of the 3H spacer (orange) which contributes to high-affnity binding are shown directed toward the positive charged residues (red) of the heparin-binding exosite. Adapted from Journal of Molecular Biology, Vol 272, Diane M. Tasset, Mark F. Kubik, and Walter Steiner, Oligonucleotide inhibitors of human thrombin that bind distinct epitopes, Pages 688 – 698 , Copyright 1997, with permission from Elsevier.

If free thrombin tends to stick to the aptamers when they are conjugated to the NRs,[129] then the switching strategy would really be the denaturation strategy, and the target would be the aptamer. The aptamers form a G-tetraplex to bind to the thrombin. Without that structure the affinity drops dramatically.[43] So when excited by the laser, the aptamer could lose its structure and release the thrombin activating it. When the laser is removed the aptamer could reform its structure and rebind the

thrombin. This could work if the characteristic time of refolding is greater than the time between pulses.

If free thrombin does not stick to the aptamers when they are conjugated to NRs, then the switching strategy would be the release strategy. There are a couple ways to do this. First, if the aptamer could be conjugated to the NR in a non-covalent manner, it could be reversibly released. When free from the NR, it would inhibit the thrombin's activity. Second, the aptamer could be thiolated, tagged with a poly-T spacer, and conjugated to the NR in a covalent manner. Then it could be released with very high fluence laser pulses that melt the NR.[179] The poly-T spacer is necessary to ensure the aptamer is not damaged by the very high local temperatures necessary to break the covalent bond. The reversal could then happen by releasing the aptamer's conjugate, shown to reactivate thrombin in solution,[144, 17] from a NR with a different AR and a second laser.[179]

The aptamer-thrombin-NR system is nice for a couple reasons. Aptamers are a technology currently at their height of scientific interest, and if they could be locally denatured by heating the NR there would be much interest. It would enable many other very interesting applications. Also it is good because there are two nice assays. There is a highly sensitive fluorogenic assay,[84] and clot formation itself can be monitored.

The primary output of these experiments would be to demonstrate the full utility of the biomolecular switch. When combined with the "enabling" studies recommended in section 5.3.1 and the results of this thesis, this would provide a basis for future implementation of the biomolecular switch. Our preliminary experiments demonstrate the ability to conjugate thrombin aptamers to NRs. Based on the NR ligand, the thrombin has shown varying degrees of affinity to the NR-aptamer conjugates.

5.3.3 The potential of this biomolecular control mechanism

The biomolecular switch could theoretically have both clinical and research applications. The allure of clinical applications is appealing. It could be advantageous in the

treatment of disease, or performing surgery like medical operations. If practical, there would be many exciting possibilities for biomolecular control at the human scale. The primary obstacle to most *in vivo* applications is that despite the near IR being called the "tissue window," in practice light is attenuated by tissue at a depth $\delta \sim 3$ mm.

The more promising applications for the biomolecular switch are those outside of an entire organism. The biomolecular switch is more likely to have a real impact on applications using small tissue samples, cells, and *in vitro* biochemical samples. It would be a valuable control mechanism in bench top or even manufacturing scale biotech applications, perhaps in pharmaceutical manufacturing. It could be useful in the future as a key control component in nanoscale machinery. Finally, the biomolecular switch would make a valuable research tool. It would allow a particular biomolecule to be actuated in real time as the output of a biological system is monitored. This could have far reaching affects on understanding biology at the submolecular, molecular, cellular, and systems scales. It is as a research tool that I believe this biological switching technique could have a significant impact. I hope that with the dedication of future graduate students and post doctoral researchers in the Hamad-Schifferli lab and other academic labs this goal will be achieved.

Appendix A

Symbols and acronyms

These are the symbols used in this thesis.

Table A.1: Definition of symbols used

Symbol	Definition
α_N	Damping coefficient
α	Thermal diffusivity
χ_0	Magnetic susceptibility
δ	Optical penetration depth
ϵ_0	Permittivity of free space
ϵ_m	Relative permittivity (dielectric constant) of the medium
ϵ_x	Molar extinction coefficient of molecule x
η	Viscosity
$\hbar\nu$	Energy in a photon
κ^{-1}	Debye length
λ_p	Persistence length
λ	Wavelength
AR	Aspect ratio
μ_0	Permeability of free space
μ_r	Relative magnetic permeability
μ	Magnetic permeability

Table A.1: Definition of symbols used, continued.

Symbol	Definition
ω	Angular frequency $[\frac{rad}{s}]$
ϕ	Volume fraction
ρ	Mass density
$\tau_{\hbar\nu-el}$	Photon-electron relaxation time
τ_{el-ph}	Electron-phonon relaxation time
τ_0	$\sim 10^{-7}10^{-9}$
τ_B	Brownian relaxation time constant
τ_D	Thermal dissipation time constant
τ_eff	Effective magnetic relaxation time constant
τ_N	Neel relaxation time constant
τ	Characteristic time
φ	Laser intensity
ζ	Surface electrical potential (Zeta potential)
A_h	Hamaker constant
A	Absorbance
B	Magnetic flux density
C_p	Specific heat at constant pressure
C_x	Concentration of molecule x
c	Speed of light
d_0	Average particle spacing
d	Size of heated zone
D	Diameter of nanoparticle
E	Energy
f	Frequency (Hz)
G	Thermal interface conductance
H	Magnetic field strength
I_0	Intensity of incident light

Table A.1: Definition of symbols used, continued.

Symbol	Definition
I_1	Intensity of transmitted light
I_x	Fluorescence intensity of molecule x
I	Current
k_B	Boltzmann's constant
k_BT	Characteristic energy of thermal fluctuations
k_{off}	Disassociation rate constant
k_{on}	Binding rate constant
K_1	Anisotropy energy density
k	Thermal conductivity
l_p	Path length
L	Inductance
l	Length
M_0	Free mobility
M_d	Domain magnetization
m_S	Saturation magnetization
M	Electrophoretic mobility
N_A	Avogadro's number
N_H	Number of turns in a Helmholtz coil
n_x	Valency number of x
N	Number of turns in a coil
n	Aggregation number
P	Power
Q	Heat energy
q	Heat flux
R^2	Statistical goodness of fit parameter for least-squares regression
r_0	Radius of control volume
r	Radius

Table A.1: Definition of symbols used, continued.

Symbol	Definition
T_{gel}	Gel percentage
t_{lig}	Thickness of the ligand
T	Temperature
t	Time
V_H	Hydrodynamic volume
V	Volume
v	Voltage
Z_0	Impedance of a transmission line
Z_L	Impedance of the load
Z_S	Impedance of the source
Z	Impedance

These are the acronyms used in this thesis.

Table A.2: Definition of acronyms used

Acronym	Definition
ATP	Adenosine triphosphate
AA	Ascorbic acid
AMPSO	N-(1,1-Dimethyl-2-hydroxyethyl)-3-amino-2-hydroxypropanesulfonic acid
AR	Aspect Ratio
BDAC	Benzyldimethylammonium chloride
BE	Binding energy
BIBO	bismuth triborate (BIBO)
BNC	Bayonet Neill-Concelman connector
CD	Circular dichrosim

Table A.2: Definition of acronyms used, continued.

Acronym	Definition
cmc	Critical micelle concentration
CMSE	Center for Materials Science and Engineering at MIT
CTAB	Hexadecyltrimethylammonium bromide (C_{16}TAB)
DMNPE	1-(4,5-dimethoxy-2-nitrophenyl)ethyl ester
DNA	Deoxyribonucleic acid
dsDNA	Double stranded DNA
EMI	Electromagnetic Interference
emu	Electromagnetic unit (Unit of magnetic moment $1 emu = 10^{-3} Am^2$)
EOM	Electro-optic modulator
FRET	Fluorescence resonance energy transfer
fs	Femtosecond
FWHM	Full width at half maximum
GMP	Guanosine monophosphate
GPIB	General purpose interface bus
Hb	Hemoglobin
HbO_2	Oxygenated hemoglobin
HP	Hewlett-Packard
ICP-OES	Inductively coupled plasma - atomic emission spectroscopy
IR	Infrared
KE	Kinetic energy
LbL	Layer by layer (polyelectrolyte deposition technique)
MEMS	Micro electro-mechanical system
MP-11	Microperoxidase-11
MRI	Magnetic resonance imaging
NIR	Near infrared
NP	Nanoparticle

Table A.2: Definition of acronyms used, continued.

Acronym	Definition
NR	Nanorod
Oe	Oersted (unit of field strength $1 Oe = 79.6 \frac{A}{m}$)
OP	1,10-phenanthroline
PDADMAC	Poly(diallyldimethylammonium) chloride
PID	Proportional, integral, and differential control system
PNIPAm	poly(N-isopropylacrylamide)
ps	Picosecond
PSS	Polysodium 4-styrenesulfonate
QD	Quantum dot
RFMF	Radio frequency alternating magnetic field
RLC	Resistance, inductance, and capacitance circuit
RNA	Ribonucleic acid
SAR	Specific absorption rate
SCFH	Standard cubic feet per hour
SDS	Sodium dodecyl sulfate
SERS	Surface enhanced Raman spectroscopy
SOG	Special optical glass
SPR	Surface plasmon resonance
SQUID	Superconducting quantum interference devices magnetometer
ssDNA	Single stranded DNA
TBE	tris-borate-EDTA buffer
TEM	Transmission electron micrograph
TGA	Thioglycolic acid
UV	Ultraviolet
XPS	X-ray photoelectron spectroscopy
XRD	X-ray diffraction

Bibliography

[1] Leonard M. Adleman. Molecular computation of solutions to combinatorial problems. *Science*, 266(5187):1021–1024, November 1994.

[2] A. Agarwal, S. W. Huang, M. O'Donnell, K. C. Day, M. Day, N. Kotov, and S. Ashkenazi. Targeted gold nanorod contrast agent for prostate cancer detection by photoacoustic imaging. *Journal of Applied Physics*, 102(6):064701–4, 2007.

[3] T. S. Ahmadi, S. L. Logunov, and M. A. El-Sayed. Picosecond dynamics of colloidal gold nanoparticles. *J. Phys. Chem.*, 100(20):8053–8056, 1996.

[4] A. P. Alivisatos. Semiconductor clusters, nanocrystals, and quantum dots. *Science*, 271(5251):933–937, February 1996.

[5] Alaaldin M. Alkilany, Rebecca L. Frey, John L. Ferry, and Catherine J. Murphy. Gold nanorods as nanoadmicelles: 1-Naphthol partitioning into a nanorod-bound surfactant bilayer. *Langmuir*, 24(18):10235–10239, 2008.

[6] Joshua Alper, Monica Crespo, and Kimberly Hamad-Schifferli. Release mechanism of octadecyl rhodamine B chloride from Au nanorods by ultrafast laser pulses. *The Journal of Physical Chemistry C*, 113(15):5967–5973, April 2009.

[7] R. R. Anderson and J. A. Parrish. Selective photothermolysis: precise microsurgery by selective absorption of pulsed radiation. *Science*, 220(4596):524, 1983.

[8] Volker Andresen, Stephanie Alexander, Wolfgang-Moritz Heupel, Markus Hirschberg, Robert M. Hoffman, and Peter Friedl. Infrared multiphoton microscopy: subcellular-resolved deep tissue imaging. *Current Opinion in Biotechnology*, 20(1):54–62, February 2009.

[9] A. S. Angelatos, B. Radt, and F. Caruso. Light-responsive polyelectrolyte/gold nanoparticle microcapsules. *J. Phys. Chem. B*, 109(7):3071–3076, 2005.

[10] Marie-Eve Aubin-Tam and Kimberly Hamad-Schifferli. Gold nanoparticle-cytochrome c complexes: The effect of nanoparticle ligand charge on protein structure. *Langmuir*, 21(26):12080, 2005.

[11] Marie-Eve Aubin-Tam and Kimberly Hamad-Schifferli. Structure and function of nanoparticle-protein conjugates. *Biomedical Materials*, 3(3):034001, 2008.

[12] Marie-Eve Aubin-Tam, Wonmuk Hwang, and Kimberly Hamad-Schifferli. Site-directed nanoparticle labeling of cytochrome c. *Proceedings of the National Academy of Sciences*, 106(11):4095–4100, March 2009.

[13] Pan K. Bae, Kyung N. Kim, Seung J. Lee, Hyun J. Chang, Chong K. Lee, and Joung K. Park. The modification of quantum dot probes used for the targeted imaging of his-tagged fusion proteins. *Biomaterials*, 30(5):836–842, February 2009.

[14] Mohamed A. Bahri, Maryse Hoebeke, Angeliki Grammenos, Lisiane Delanaye, Nicolas Vandewalle, and Alain Seret. Investigation of SDS, DTAB and CTAB micelle microviscosities by electron spin resonance. *Colloids and Surfaces A: Physicochemical and Engineering Aspects*, 290(1-3):206, 2006.

[15] Bernard Barbara. Magnetization reversal of nano-particles. In *Magnetism and Synchrotron Radiation*, pages 157–208. 2001.

[16] Antonio Barone and Gianfranco Paterno. *Physics and Applications of the Josephson Effect*. Wiley, New York, 1982.

[17] Stefan Beyer and Friedrich C. Simmel. A modular DNA signal translator for the controlled release of a protein by an aptamer. *Nucl. Acids Res.*, 34(5):1581–1587, March 2006.

[18] Louis C. Bock, Linda C. Griffin, John A. Latham, Eric H. Vermaas, and John J. Toole. Selection of single-stranded DNA molecules that bind and inhibit human thrombin. *Nature*, 355(6360):564–566, February 1992.

[19] Elodie Boisselier and Didier Astruc. Gold nanoparticles in nanomedicine: preparations, imaging, diagnostics, therapies and toxicity. *Chemical Society Reviews*, 38(6):1759–1782.

[20] Katherine A. Brown, Andy Wijaya, Joshua D. Alper, and Kimberly Hamad-Schifferli. Synthesis of water-soluble, magnetic Fe/Au nanoparticles. volume 900 of *Materials Research Society Symposium Proceedings*, page 205, Boston, MA, United States, 2005. Materials Research Society, Warrendale, PA 15086, United States.

[21] Tracie J. Bukowski and Joseph H. Simmons. Quantum dot research: Current state and future prospects. *Critical Reviews in Solid State and Materials Sciences*, 27(3):119, 2002.

[22] James D. Byrne, Tania Betancourt, and Lisa Brannon-Peppas. Active targeting schemes for nanoparticle systems in cancer therapeutics. *Advanced Drug Delivery Reviews*, 60(15):1615–1626, December 2008.

[23] Banani Chakraborty, Ruojie Sha, and Nadrian C. Seeman. A DNA-based nanomechanical device with three robust states. *Proceedings of the National Academy of Sciences*, 105(45):17245–17249, November 2008.

[24] N. Dennis Chasteen and Pauline M. Harrison. Mineralization in ferritin: An efficient means of iron storage. *Journal of Structural Biology*, 126(3):182–194, June 1999.

[25] C. C. Chen, Y. P. Lin, C. W. Wang, H. C. Tzeng, C. H. Wu, Y. C. Chen, C. P. Chen, L. C. Chen, and Y. C. Wu. DNA-gold nanorod conjugates for remote control of localized gene expression by near infrared irradiation. *J. Am. Chem. Soc.*, 128(11):3709–3715, 2006.

[26] Gang Chen. *Nanoscale energy transport and conversion : a parallel treatment of electrons, molecules, phonons, and photons*. MIT-Pappalardo series in mechanical engineering. Oxford University Press, New York, NY, 2005.

[27] Brian Choi, Giovanni Zocchi, Yim Wu, Sum Chan, and L. Jeanne Perry. Allosteric control through mechanical tension. *Physical Review Letters*, 95(7):078102, 2005.

[28] Helen F. Chuang, Rene C. Smith, and Paula T. Hammond. Polyelectrolyte multilayers for tunable release of antibiotics. *Biomacromolecules*, 9(6):1660–1668, June 2008.

[29] Jos Luis Corchero and Antonio Villaverde. Biomedical applications of distally controlled magnetic nanoparticles. *Trends in Biotechnology*, 27(8):468–476, August 2009.

[30] Marie-Christine Daniel and Didier Astruc. Gold nanoparticles: Assembly, supramolecular chemistry, quantum-size-related properties, and applications toward biology, catalysis, and nanotechnology. *Chemical Reviews*, 104(1):293–346, 2004.

[31] Sarit Kumar Das. *Nanofluids : science and technology*. Wiley-Interscience, Hoboken, N.J., 2008.

[32] Sarit Kumar Das, Stephen U. S. Choi, and Hrishikesh E. Patel. Heat transfer in nanofluids - a review. *Heat Transfer Engineering*, 27(10):3 – 19, 2006.

[33] Emily S. Day, Jennifer G. Morton, and Jennifer L. West. Nanoparticles for thermal cancer therapy. *Journal of Biomechanical Engineering*, 131(7):074001–5, July 2009.

[34] Mrinmoy De, Subinoy Rana, and Vincent M. Rotello. Nickel-Ion-Mediated control of the stoichiometry of His-tagged protein/nanoparticle interactions. *Macromolecular Bioscience*, 9(2):174–178, 2009.

[35] P. F de Chatel, I. Nandori, J. Hakl, S. Meszaros, and K. Vad. Magnetic particle hyperthermia: Néel relaxation in magnetic nanoparticles under circularly polarized field. *J. Phys. : Condens. Matter*, 21:124202, October 2008.

[36] B. Derjaguin and L. Landau. Theory of the stability of strongly charged lyophobic sols and of the adhesion of strongly charged particles in solutions of electrolytes. *Acta Physico chemica URSS*, 14:633, 1941.

[37] T. Douglas and D. R. Ripoll. Calculated electrostatic gradients in recombinant human h-chain ferritin. *Protein Science*, 7(5):1083, 1998.

[38] E. Dulkeith, M. Ringler, T. A. Klar, J. Feldmann, A. Munoz Javier, and W. J. Parak. Gold nanoparticles quench fluorescence by phase induced radiative rate suppression. *Nano Letters*, 5(4):585–589, April 2005.

[39] J. A. Eastman, S. R. Phillpot, S. U. S. Choi, and P. Keblinski. Thermal transport in nanofluids. *Annual Review of Materials Research*, 34(1):219–246, 2004.

[40] Magdalena Elzbieciak, Marta Kolasinska, and Piotr Warszynski. Characteristics of polyelectrolyte multilayers: The effect of polyion charge on thickness and wetting properties. *Colloids and Surfaces A: Physicochemical and Engineering Aspects*, 321(1-3):258–261, 2008.

[41] Omid C. Farokhzad and Robert Langer. Nanomedicine: Developing smarter therapeutic and diagnostic modalities. *Advanced Drug Delivery Reviews*, 58(14):1456–1459, December 2006.

[42] Marta S. Fernandez and Peter Fromherz. Lipoid pH indicators as probes of electrical potential and polarity in micelles. *J. Phys. Chem.*, 81(18):1755–1761, 1977.

[43] Marketa Fialova, Jaroslav Kypr, and Michaela Vorlickova. The thrombin binding aptamer GGTTGGTGTGGTTGG forms a bimolecular guanine tetraplex. *Biochemical and Biophysical Research Communications*, 344(1):50–54, May 2006.

[44] Alison M. Funston, Carolina Novo, Tim J. Davis, and Paul Mulvaney. Plasmon coupling of gold nanorods at short distances and in different geometries. *Nano Letters*, 9(4):1651–1658, April 2009.

[45] R. Gans. ber die form ultramikroskopischer goldteilchen. *Annalen der Physik*, 342(5):881–900, 1912.

[46] Jinxin Gao, Christopher M. Bender, and Catherine J. Murphy. Dependence of the gold nanorod aspect ratio on the nature of the directing surfactant in aqueous solution. *Langmuir*, 19(21):9065–9070, October 2003.

[47] Z. Ge, D. G. Cahill, and P. V. Braun. AuPd metal nanoparticles as probes of nanoscale thermal transport in aqueous solution. *J. Phys. Chem. B*, 108(49):18870–18875, 2004.

[48] Z. Ge, Y. Kang, T. A. Taton, P. V. Braun, and D. G. Cahill. Thermal transport in Au-core polymer-shell nanoparticles. *Nano Lett.*, 5(3):531–535, 2005.

[49] Zhenbin Ge, David G. Cahill, and Paul V. Braun. Thermal conductance of hydrophilic and hydrophobic interfaces. *Physical Review Letters*, 96(18):186101–4, 2006.

[50] R. K. Gilchrist, Richard Medal, William D. Shorey, Russell C. Hanselman, John C. Parrott, and Bruce Taylor. Selective inductive heating of lymph nodes. *Annals of Surgery*, 146(4):596 – 606, October 1957.

[51] Dominique Givord. Introduction to magnetism and magnetic materials. In *Magnetism and Synchrotron Radiation*, pages 3–23. 2001.

[52] Anita Goel and Viola Vogel. Harnessing biological motors to engineer systems for nanoscale transport and assembly. *Nat Nano*, 3(8):465–475, 2008.

[53] H. Goldenberg and C. J. Tranter. Heat flow in an infinite medium heated by a sphere. *British Journal of Applied Physics*, 3(9):296, 1952.

[54] A. Gole and C. J. Murphy. Polyelectrolyte-coated gold nanorods: Synthesis, characterization and immobilization. *Chem. Mater.*, 17(6):1325–1330, 2005.

[55] T Granier, B Gallois, A Dautant, B Langlois d'Estaintot, and G Prcigoux. Comparison of the structures of the cubic and tetragonal forms of horse-spleen apoferritin. *Acta Crystallographica. Section D, Biological Crystallography*, 53(Pt 5):580–587, September 1997.

[56] Adrienne C. Greene, Amanda M. Trent, and George D. Bachand. Controlling kinesin motor proteins in nanoengineered systems through a metal-binding on/off switch. *Biotechnology and Bioengineering*, 101(3):478–486, 2008.

[57] Norma Greenfield and Gerald Fasman. Computed circular dichroism spectra for the evaluation of protein conformation. *Biochemistry*, 8(10):4108–4116, 1969.

[58] Itaru Hamachi, Takashi Hiraoka, Yasuhiro Yamada, and Seiji Shinkai. Photoswitching of the enzymatic activity of semisynthetic ribonuclease S bearing phenylazophenylalanine at a specific site. *Chemistry Letters*, 27(6):537–538, 1998.

[59] Kimberly Hamad-Schifferli, John J. Schwartz, Aaron T. Santos, Shuguang Zhang, and Joseph M. Jacobson. Remote electronic control of dna hybridization through inductive coupling to an attached metal nanocrystal antenna. *Nature*, 415(6868):152, 2002.

[60] Gregory V. Hartland. Coherent vibrational motion in metal particles: Determination of the vibrational amplitude and excitation mechanism. *The Journal of Chemical Physics*, 116(18):8048–8055, 2002.

[61] Henry Hess, John Clemmens, Dong Qin, Jonathon Howard, and Viola Vogel. Light-controlled molecular shuttles made from motor proteins carrying cargo on engineered surfaces. *Nano Letters*, 1(5):235–239, May 2001.

[62] M. Heuberger, T. Drobek, and J. Voros. About the role of water in surface-grafted poly(ethylene glycol) layers. *Langmuir*, 20(22):9445–9448, October 2004.

[63] P. Hiemenz. *Principles of Colloid and Surface Chemistry*. Marcel Dekker, New York, NY, 1986.

[64] I. Hilger, R. Hergt, and W.A. Kaiser. Use of magnetic nanoparticle heating in the treatment of breast cancer. *IEE Proceedings - Nanobiotechnology*, 152(1):33–39, 2005.

[65] Ingrid Hilger, Andreas Kiessling, Erik Romanus, Robert Hiergeist, Rudolf Hergt, Wilfried Andra, Martin Roskos, Werner Linss, Peter Weber, Werner Weitschies, and Werner A. Kaiser. Magnetic nanoparticles for selective heating of magnetically labelled cells in culture: preliminary investigation. *Nanotechnology*, 15(8):1027–1032, 2004.

[66] Dick Hoekstra, Tiny de Boer, Karin Klappe, and Jan Wilschut. Fluorescence method for measuring the kinetics of fusion between biological membranes. *Biochemistry*, 23:5675–5681, 1984.

[67] Yukichi Horiguchi, Kanako Honda, Yuichi Kato, Naotoshi Nakashima, and Yasuro Niidome. Photothermal reshaping of gold nanorods depends on the passivating layers of the nanorod surfaces. *Langmuir*, 24(20):12026–12031, 2008.

[68] Yukichi Horiguchi, Takuro Niidome, Sunao Yamada, Naotoshi Nakashima, and Yasuro Niidome. Expression of plasmid DNA released from DNA conjugates of gold nanorods. *Chemistry Letters*, 36(7):952, 2007.

[69] M. Hu and G. V. Hartland. Heat dissipation for Au particles in aqueous solution: Relaxation time versus size. *J. Phys. Chem. B*, 106(28):7029–7033, 2002.

[70] M. Hu, X. Wang, G. V. Hartland, P. Mulvaney, J. P. Juste, and J. E. Sader. Vibrational response of nanorods to ultrafast laser induced heating: Theoretical and experimental analysis. *J. Am. Chem. Soc.*, 125(48):14925–14933, 2003.

[71] X. Huang, I. H. El-Sayed, W. Qian, and M. A. El-Sayed. Cancer cell imaging and photothermal therapy in the near-infrared region by using gold nanorods. *Journal of the American Chemical Society*, 128(6):2115–2120, 2006.

[72] Ying-Ying Huang, Michael Hamblin, and Aaron C.-H. Chen. Low-level laser therapy: an emerging clinical paradigm. *SPIE Newsroom*, July 2009.

[73] Gereon Huettmann, Benno Radt, Jesper Serbin, and Reginald Birngruber. Inactivation of proteins by irradiation of gold nanoparticles with nano- and picosecond laser pulses. *Proceedings of SPIE - The International Society for Optical Engineering*, 5142:88, 2003.

[74] Scott T. Huxtable, David G. Cahill, Sergei Shenogin, Liping Xue, Rahmi Ozisik, Paul Barone, Monica Usrey, Michael S. Strano, Giles Siddons, Moonsub Shim, and Pawel Keblinski. Interfacial heat flow in carbon nanotube suspensions. *Nat Mater*, 2(11):731, 2003.

[75] Wonmuk Hwang and Matthew Lang. Mechanical design of translocating motor proteins. *Cell Biochemistry and Biophysics*, 54(1):11–22, July 2009.

[76] N. R. Jana, L. Gearheart, and C. J. Murphy. Seed-mediated growth approach for shape-controlled synthesis of spheroidal and rod-like gold nanoparticles using a surfactant template. *Advanced Materials*, 13(18):1389–1393, 2001.

[77] N. R. Jana, L. Gearheart, and C. J. Murphy. Wet chemical synthesis of high aspect ratio cylindrical gold nanorods. *J. Phys. Chem. B*, 105(19):4065–4067, 2001.

[78] Nikhil R. Jana. Gram-scale synthesis of soluble, near-monodisperse gold nanorods and other anisotropic nanoparticles. *Small*, 1(8-9):875–882, 2005.

[79] Jiang Jiang, Ken Bosnick, Mathieu Maillard, and Louis Brus. Single molecule raman spectroscopy at the junctions of large ag nanocrystals. *The Journal of Physical Chemistry B*, 107(37):9964–9972, 2003.

[80] P. B. Johnson and R. W. Christy. Optical constants of the noble metals. *Physical Review B*, 6(12):4370, 1972.

[81] Yuzo Kanari, Yusuke Shoji, Hirotaka Ode, Takeo Miyake, Takashi Tanii, Tyuji Hoshino, and Iwao Ohdomari. Protein adsorption on self-assembled monolayers induced by surface water molecule. *Japanese Journal of Applied Physics*, 46(9B):6303 – 6308, 2007.

[82] Hirokazu Kato, Takayuki Nishizaka, Takashi Iga, Jr. Kinosita, Kazuhiko, and Shin'ichi Ishiwata. Imaging of thermal activation of actomyosin motors. *Proceedings of the National Academy of Sciences*, 96(17):9602–9606, 1999.

[83] Eugenii Katz and Itamar Willner. Integrated nanoparticle-biomolecule hybrid systems: Synthesis, properties, and applications. *Angewandte Chemie International Edition*, 43(45):6042–6108, 2004.

[84] Shun-Ichiro Kawabata, Takako Miura, Takashi Morita, Hisao Kato, Kazuo Fujikawa, Sadaaki Iwanaga, Katsumi Takada, Terutoshi Kimura, and Shumpei Sakakibara. Highly sensitive peptide-4-methylcoumaryl-7-amide substrates for blood-clotting proteases and trypsin. *European Journal of Biochemistry*, 172(1):17–25, 1988.

[85] Kenji Kawaguchi and Shin'ichi Ishiwata. Temperature dependence of force, velocity, and processivity of single kinesin molecules. *Biochemical and Biophysical Research Communications*, 272(3):895–899, June 2000.

[86] Kenji Kawaguchi and Shin'ichi Ishiwata. Thermal activation of single kinesin molecules with temperature pulse microscopy. *Cell Motility and the Cytoskeleton*, 49(1):41–47, 2001.

[87] Euan R. Kay, David A. Leigh, and Francesco Zerbetto. Synthetic molecular motors and mechanical machines. *Angewandte Chemie - International Edition*, 46(1-2):72, 2007.

[88] Pawel Keblinski, David G. Cahill, Arun Bodapati, Charles R. Sullivan, and T. Andrew Taton. Limits of localized heating by electromagnetically excited nanoparticles. *Journal of Applied Physics*, 100(5):054305, 2006.

[89] K. L. Kelly, E. Coronado, L. L. Zhao, and G. C. Schatz. The optical properties of metal nanoparticles: The influence of size, shape, and dielectric environment. *J. Phys. Chem. B*, 107(3):668–677, 2003.

[90] Armen R Kherlopian, Ting Song, Qi Duan, Mathew A Neimark, Ming J Po, John K Gohagan, and Andrew F Laine. A review of imaging techniques for systems biology. *BMC Systems Biology*, 2:74, 2008.

[91] Shahriar Khushrushahi. *A Quantitative Design and Analysis of Magnetic Nanoparticle Heating Systems*. PhD thesis, Massachusetts Institute of Technoloty, February 2006.

[92] Rumiko Kitagawa, Kanako Honda, Hirofumi Kawazumi, Yasuro Niidome, Naotoshi Nakashima, and Sunao Yamada. Formation of gold nanorod–myoglobin aggregates by electrostatic interactions and their photochemical properties. *Japanese Journal of Applied Physics*, 47(2):1374–1376, 2008.

[93] Shigeki Kiyonaka, Seiji Shinkai, and Itaru Hamachi. Combinatorial library of low molecular-weight organo- and hydrogelators based on glycosylated amino acid derivatives by solid-phase synthesis. *Chemistry - A European Journal*, 9(4):976–983, 2003.

[94] Roland Kjellander and Ebba Florin. Water structure and changes in thermal stability of the system poly(ethylene oxide)water. *Journal of the Chemical Society, Faraday Transactions 1: Physical Chemistry in Condensed Phases*, 77:2053 – 2077, 1981.

[95] Kaoru Konishi, Taro Q.P. Uyeda, and Tai Kubo. Genetic engineering of a Ca^{2+} dependent chemical switch into the linear biomotor kinesin. *FEBS Letters*, 580(15):3589–3594, June 2006.

[96] David M. Lawson, Amyra Treffry, Peter J. Artymiuk, Pauline M. Harrison, Stephen J. Yewdall, Alessandra Luzzago, Gianne Cesareni, Sonia Levi, and Paolo Arosio. Identification of the ferroxidase centre in ferritin. *FEBS Letters*, 254(1-2):207, 1989.

[97] Somin Eunice Lee, Darryl Y. Sasaki, Thomas D. Perroud, Daniel Yoo, Kamlesh D. Patel, and Luke P. Lee. Biologically functional cationic Phospholipid-Gold nanoplasmonic carriers of RNA. *Journal of the American Chemical Society*, 131(39):14066–14074, October 2009.

[98] Hongwei Liao and Jason H. Hafner. Gold nanorod bioconjugates. *Chemistry of Materials*, 17:4636–4641, 2005.

[99] S. Link, C. Burda, M. B. Mohamed, B. Nikoobakht, and M. A. El-Sayed. Femtosecond transient-absorption dynamics of colloidal gold nanorods: Shape independence of the electron-phonon relaxation time. *Physical Review B*, 61(9):6086, 2000.

[100] S. Link, C. Burda, Z. L. Wang, and M. A. El-Sayed. Electron dynamics in gold and gold–silver alloy nanoparticles: The influence of a nonequilibrium electron distribution and the size dependence of the electron–phonon relaxation. *The Journal of Chemical Physics*, 111(3):1255, 1999.

[101] S. Link and M. A. El-Sayed. Size and temperature dependence of the plasmon absorption of colloidal gold nanoparticles. *J. Phys. Chem. B*, 103(21):4212–4217, 1999.

[102] S. Link and M. A. El-Sayed. Spectral properties and relaxation dynamics of surface plasmon electronic oscillations in gold and silver nanodots and nanorods. *J. Phys. Chem. B*, 103(40):8410–8426, 1999.

[103] S. Link, D. J. Hathcock, B. Nikoobakht, and M. A. El-Sayed. Medium effect on the electron cooling dynamics in gold nanorods and truncated tetrahedra. *Advanced Materials*, 15(5):393–396, 2003.

[104] S. Link, M. B. Mohamed, and M. A. El-Sayed. Simulation of the optical absorption spectra of gold nanorods as a function of their aspect ratio and the effect of the medium dielectric constant. *J. Phys. Chem. B*, 103(16):3073–3077, 1999.

[105] Stephan Link and Mostafa A. El-Sayed. Shape and size dependence of radiative, non-radiative and photothermal properties of gold nanocrystals. *International Reviews in Physical Chemistry*, 19(3):409, 2000.

[106] Haiqing Liu, Jacob J. Schmidt, George D. Bachand, Shahir S. Rizk, Loren L. Looger, Homme W. Hellinga, and Carlo D. Montemagno. Control of a biomolecular motor-powered nanodevice with an engineered chemical switch. *Nat Mater*, 1(3):173, 2002.

[107] M. Z. Liu and P. Guyot-Sionnest. Mechanism of silver(I)-assisted growth of gold nanorods and bipyramids. *J. Phys. Chem. B*, 109(47):22192–22200, 2005.

[108] A.L. Lomize, V.I.u Orekhov, and A.S. Arsen'ev. Refinement of the spatial structure of the gramicidin a ion channel. *Biol.Membr. (USSR)*, 18:182 – 200, 1992.

[109] Gunter Mayer and Alexander Heckel. Biologically active molecules with a "light switch". *Angewandte Chemie International Edition*, 45(30):4900–4921, 2006.

[110] Igor L Medintz and Hedi Mattoussi. Quantum dot-based resonance energy transfer and its growing application in biology. *Physical Chemistry Chemical Physics: PCCP*, 11(1):17–45, 2009. PMID: 19081907.

[111] F. C. Meldrum, B. R. Heywood, and S. Mann. Magnetoferritin. *in vitro* synthesis of a novel magnetic protein. *Science*, 257(5069):522, 1992.

[112] Gustav Mie. Beitrge zur optik trber medien, speziell kolloidaler metallsungen. *Annalen der Physik*, 330(3):377–445, 1908.

[113] Goran Mihajlovic, Nicolas M. Brunet, Jelena Trbovic, Peng Xiong, Stephan von Molnar, and P. Bryant Chase. All-electrical switching and control mechanism for actomyosin-powered nanoactuators. *Applied Physics Letters*, 85(6):1060–1062, 2004.

[114] Michael I. Mishchenko, Larry D. Travis, and Andrew A. Lacis. *Scattering, Absorption, and Emission of Light by Small Particles*. Cambridge University Press, 2002.

[115] J. G. Mohanty, Jonathan S. Jaffe, Edward S. Schulman, and Donald G. Raible. A highly sensitive fluorescent micro-assay of H_2O_2 release from activated human leukocytes using a dihydroxyphenoxazine derivative. *Journal of Immunological Methods*, 202(2):133–141, March 1997.

[116] P. Mulvaney. Surface plasmon spectroscopy of nanosized metal particles. *Langmuir*, 12(3):788–800, 1996.

[117] C. J. Murphy, T. K. Sau, A. M. Gole, C. J. Orendorff, J. Gao, L. Gou, S. E. Hunyadi, and T. Li. Anisotropic metal nanoparticles: Synthesis, assembly, and optical applications. *J. Phys. Chem. B*, 109(29):13857–13870, 2005.

[118] Catherine J. Murphy, Tapan K. Sau, Anand Gole, and Christopher J. Orendorff. Surfactant-directed synthesis and optical properties of one-dimensional plasmonic metallic nanostructures. *MRS Bulletin*, 30(5):349, 2005.

[119] Y. Nagasaka and A. Nagashima. Absolute measurement of the thermal conductivity of electrically conducting liquids by the transient hot-wire method. *Journal of Physics E: Scientific Instruments*, (12):1435, 1981.

[120] Nidhi Nath and Ashutosh Chilkoti. Label free colorimetric biosensing using nanoparticles. *Journal of Fluorescence*, 14(4):377–389, July 2004. PMID: 15617380.

[121] Eva Natividad, Miguel Castro, and Arturo Mediano. Adiabatic vs. non-adiabatic determination of specific absorption rate of ferrofluids. *Journal of Magnetism and Magnetic Materials*, 321(10):1497–1500, May 2009.

[122] Charles G. Nelson. *High frequency and microwave circuit design*. CRC Press, 2000.

[123] Christof M. Niemeyer. Nanoparticles, proteins, and nucleic acids: Biotechnology meets materials science. *Angewandte Chemie International Edition*, 40(22):4128–4158, 2001.

[124] Takuro Niidome, Masato Yamagata, Yuri Okamoto, Yasuyuki Akiyama, Hironobu Takahashi, Takahito Kawano, Yoshiki Katayama, and Yasuro Niidome. PEG-modified gold nanorods with a stealth character for in vivo applications. *Journal of Controlled Release*, 114(3):343, 2006.

[125] B. Nikoobakht and M. A. El-Sayed. Preparation and growth mechanism of gold nanorods (NRs) using seed-mediated growth method. *Chem. Mater.*, 15(10):1957–1962, 2003.

[126] Babak Nikoobakht, Jianping Wang, and Mostafa A. El-Sayed. Surface-enhanced raman scattering of molecules adsorbed on gold nanorods: off-surface plasmon resonance condition. *Chemical Physics Letters*, 366(1-2):17, 2002.

[127] R. S. Norman, J. W. Stone, A. Gole, C. J. Murphy, and T. L. Sabo-Attwood. Targeted photothermal lysis of the pathogenic bacteria, pseudomonas aeruginosa, with gold nanorods. *Nano Lett.*, 8(1):302–306, 2008.

[128] C. J. Orendorff and C. J. Murphy. Quantitation of metal content in the silver-assisted growth of gold nanorods. *J. Phys. Chem. B*, 110(9):3990–3994, 2006.

[129] H. Pandana, K.H. Aschenbach, and R.D. Gomez. Systematic aptamer-gold nanoparticle colorimetry for protein detection: Thrombin. *Sensors Journal, IEEE*, 8(6):661–666, 2008.

[130] Q. A. Pankhurst, J. Connolly, S. K. Jones, and J. Dobson. Applications of magnetic nanoparticles in biomedicine. *Journal of Physics D: Applied Physics*, 36(13):R167, 2003.

[131] Sungnam Park, Matthew Pelton, Mingzhao Liu, Philippe Guyot-Sionnest, and Norbert F. Scherer. Ultrafast resonant dynamics of surface plasmons in gold nanorods. *Journal of Physical Chemistry C*, 111(1):116, 2007.

[132] Sunho Park, Katherine A. Brown, and Kimberly Hamad-Schifferli. Changes in oligonucleotide conformation on nanoparticle surfaces by modification with mercaptohexanol. *Nano Letters*, 4(10):1925, 2004.

[133] Sunho Park and Kimberly Hamad-Schifferli. Evaluation of hydrodynamic size and zeta-potential of surface-modified Au nanoparticle-DNA conjugates via ferguson analysis. *The Journal of Physical Chemistry C*, 112(20):7611–7616, May 2008.

[134] Tao Peng, Chikara Dohno, and Kazuhiko Nakatani. Bidirectional control of gold nanoparticle assembly by turning on and off DNA hybridization with thermally degradable molecular glue. *ChemBioChem*, 8(5):483–485, 2007.

[135] S. S. Pennadam, M. D. Lavigne, C. F. Dutta, K. Firman, D. Mernagh, D. C. Gorecki, and C. Alexander. Control of a multisubunit dna motor by a thermoresponsive polymer switch. *J. Am. Chem. Soc.*, 126(41):13208–13209, 2004.

[136] Jorge Perez-Juste, Isabel Pastoriza-Santos, Luis M. Liz-Marzan, and Paul Mulvaney. Gold nanorods: Synthesis, characterization and applications. *Coordination Chemistry Reviews*, 249(17-18):1870, 2005.

[137] M. Perner, S. Gresillon, J. Mrz, G. von Plessen, J. Feldmann, J. Porstendorfer, K. J. Berg, and G. Berg. Observation of hot-electron pressure in the vibration dynamics of metal nanoparticles. *Physical Review Letters*, 85(4):792, 2000.

[138] Hristina Petrova, Jorge Perez Juste, Isabel Pastoriza-Santos, Gregory V. Hartland, Luis M. Liz-Marzan, and Paul Mulvaney. On the temperature stability of gold nanorods: comparison between thermal and ultrafast laser-induced heating. *Physical Chemistry Chemical Physics*, 8(7):814–821, 2006.

[139] D. Pissuwan, S. M. Valenzuela, C. M. Miller, and M. B. Cortie. A golden bullet? Selective targeting of toxoplasma gondii tachyzoites using antibody-functionalized gold nanorods. *Nano Lett.*, 7(12):3808–3812, 2007.

[140] Tatiana Prieto, Rodrigo O. Marcon, Fernanda M. Prado, Antonio C. F. Caires, Paolo Di Mascio, Sergio Brochsztain, Otaciro R. Nascimento, and Iseli L. Nantes. Reaction route control by microperoxidase-9/CTAB micelle ratios. *Physical Chemistry Chemical Physics*, 8(16):1963–1973, 2006.

[141] X. M. Qian and S. M. Nie. Single-molecule and single-nanoparticle SERS: from fundamental mechanisms to biomedical applications. *Chemical Society Reviews*, 37(5):912–920, 2008.

[142] W. S. Rasband. Imagej. *U. S. National Institutes of Health, Bethesda, Maryland, USA, http://rsb.info.nih.gov/ij/*, 1997-2009.

[143] Helke Reinhardt, Petra Stephanie Dittrich, Andreas Manz, and Joachim Franzke. m-hotplate enhanced optical heating by infrared light for single cell treatment. *Lab on a Chip*, 7(11):1509–1514, 2007.

[144] A. Reuter, W.U. Dittmer, and F.C. Simmel. Kinetics of protein-release by an aptamer-based DNA nanodevice. *The European Physical Journal E*, 22(1):8 pages, 2007.

[145] Yahya Rharbi and Mitchell A. Winnik. Solute exchange between surfactant micelles by micelle fragmentation and fusion. *Advances in Colloid and Interface Science*, 89-90:25, 2001.

[146] Frederic M. Richards and Paul J. Vithayathil. The preparation of subtilisin-modified ribonuclease and the separation of the peptide and protein components. *J. Biol. Chem.*, 234:1459–1465, 1959.

[147] D. Rodbard and A. Chrambach. Estimation of molecular radius, free mobility, and valence using polyacrylamide gel electrophoresis. *Analytical Biochemistry*, 40(1):95–134, March 1971.

[148] R. E. Rosensweig. Heating magnetic fluid with alternating magnetic field. *Journal of Magnetism and Magnetic Materials*, 252(1-3):370, 2002.

[149] Nathaniel L. Rosi, David A. Giljohann, C. Shad Thaxton, Abigail K. R. Lytton-Jean, Min Su Han, and Chad A. Mirkin. Oligonucleotide-modified gold nanoparticles for intracellular gene regulation. *Science*, 312(5776):1027–1030, 2006.

[150] TJ Rydel, KG Ravichandran, A Tulinsky, W Bode, R Huber, C Roitsch, and JW Fenton. The structure of a complex of recombinant hirudin and human alpha-thrombin. *Science*, 249(4966):277–280, July 1990.

[151] Aaron Schmidt, Matteo Chiesa, Xiaoyuan Chen, and Gang Chen. An optical pump-probe technique for measuring the thermal conductivity of liquids. *Review of Scientific Instruments*, 79(6):064902, 2008.

[152] Aaron J. Schmidt, Joshua D. Alper, Matteo Chiesa, Gang Chen, Sarit K. Das, and Kimberly Hamad-Schifferli. Probing the gold nanorod-ligand-solvent interface by plasmonic absorption and thermal decay. *The Journal of Physical Chemistry C*, 112(35):13320–13323, 2008.

[153] Dvira Segal, Abraham Nitzan, and Peter Hanggi. Thermal conductance through molecular wires. *The Journal of Chemical Physics*, 119(13):6840–6855, October 2003.

[154] Shiladitya Sengupta, David Eavarone, Ishan Capila, Ganlin Zhao, Nicki Watson, Tanyel Kiziltepe, and Ram Sasisekharan. Temporal targeting of tumour cells and neovasculature with a nanoscale delivery system. *Nature*, 436(7050):568–572, July 2005.

[155] Vivek Sharma, Kyoungweon Park, and Mohan Srinivasarao. Colloidal dispersion of gold nanorods: Historical background, optical properties, seed-mediated synthesis, shape separation and self-assembly. *Materials Science and Engineering: R: Reports*, 65(1-3):1–38, May 2009.

[156] Vivek Sharma, Kyoungweon Park, and Mohan Srinivasarao. Shape separation of gold nanorods using centrifugation. *Proceedings of the National Academy of Sciences*, 106(13):4981–4985, March 2009.

[157] Glen A. Slack. Thermal conductivity of MgO, Al_2O_3, $MgAl_2O_4$, and Fe_3O_4 crystals from 3° to 300°K. *Physical Review*, 126(2):427, April 1962.

[158] Narasimha Sreerama, Robert W. Woody, Ludwig Brand, and Michael L. Johnson. Computation and analysis of protein circular dichroism spectra. In *Numerical Computer Methods, Part D*, volume Volume 383, pages 318–351. Academic Press, 2004.

[159] Andri Stefansson, Ingvi Gunnarsson, and Niels Giroud. New methods for the direct determination of dissolved inorganic, organic and total carbon in natural waters by Reagent-Free ion chromatography and inductively coupled plasma atomic emission spectrometry. *Analytica Chimica Acta*, 582(1):69–74, 2007.

[160] S. Stolik, J. A. Delgado, A. Perez, and L. Anasagasti. Measurement of the penetration depths of red and near infrared light in human "ex vivo" tissues. *Journal of Photochemistry and Photobiology B: Biology*, 57(2-3):90–93, September 2000.

[161] Patrick Stoller, Volker Jacobsen, and Vahid Sandoghdar. Measurement of the complex dielectric constant of a single gold nanoparticle. *Optics Letters*, 31(16):2474–2476, 2006.

[162] Makoto Suto, Yasutake Hirota, Hiroaki Mamiya, Asaya Fujita, Ryo Kasuya, Kazuyuki Tohji, and Balachandran Jeyadevan. Heat dissipation mechanism of magnetite nanoparticles in magnetic fluid hyperthermia. *Journal of Magnetism and Magnetic Materials*, 321(10):1493–1496, May 2009.

[163] Hironobu Takahashi, Yasuro Niidome, and Sunao Yamada. Controlled release of plasmid DNA from gold nanorods induced by pulsed near-infrared light. *Chemical Communications*, (17):2247–2249, 2005.

[164] Kiyo Takaoka, Yoshiro Tatsu, Noboru Yumoto, Terumi Nakajima, and Keiko Shimamoto. Synthesis and photoreactivity of caged blockers for glutamate transporters. *Bioorganic & Medicinal Chemistry Letters*, 13(5):965–970, March 2003.

[165] Kiyo Takaoka, Yoshiro Tatsu, Noboru Yumoto, Terumi Nakajima, and Keiko Shimamoto. Synthesis of carbamate-type caged derivatives of a novel glutamate transporter blocker. *Bioorganic & Medicinal Chemistry*, 12(13):3687–3694, July 2004.

[166] Candan Tamerler and Mehmet Sarikaya. Molecular biomimetics: nanotechnology and bionanotechnology using genetically engineered peptides. *Philosophical Transactions of the Royal Society A: Mathematical, Physical and Engineering Sciences*, 367(1894):1705–1726, 2009.

[167] Diane M. Tasset, Mark F. Kubik, and Walter Steiner. Oligonucleotide inhibitors of human thrombin that bind distinct epitopes. *Journal of Molecular Biology*, 272(5):688–698, October 1997.

[168] A. M. Tedeschi, L. Franco, M. Ruzzi, L. Paduano, C. Corvaja, and G. D'Errico. Micellar aggregation of alkyltrimethylammonium bromide surfactants studied by electron paramagnetic resonance of an anionic nitroxide. *Physical Chemistry Chemical Physics*, 5(19):4204–4209, 2003.

[169] Stephanie Tristram-Nagle and John F. Nagle. Lipid bilayers: thermodynamics, structure, fluctuations, and interactions. *Chemistry and Physics of Lipids*, 127(1):3–14, 2004.

[170] H.-Y. Tseng, G.-B. Lee, Y.-H. Shin, and X.-Z. Lin. Localised heating of tumours utilising injectable magnetic nanoparticles for hyperthermia cancer therapy. *Nanobiotechnology, IET*, 3(2):46–54, 2009.

[171] M. Uchida, M. L. Flenniken, M. Allen, D. A. Willits, B. E. Crowley, S. Brumfield, A. F. Willis, L. Jackiw, M. Jutila, M. J. Young, and T. Douglas. Targeting of cancer cells with ferrimagnetic ferritin cage nanoparticles. *J. Am. Chem. Soc.*, 128(51):16626–16633, 2006.

[172] EJW Verwey and JThG Overbeek. *Theory of the stability of lyophobic colloids*. Elsevier, Amsterdam, 1948.

[173] Donald Voet, Judith G. Voet, and Charlotte W. Pratt. *Fundamentals of biochemistry : life at the molecular level*. Wiley, Hoboken, NJ, 2006.

[174] Zhaohui Wang, David G. Cahill, Jeffrey A. Carter, Yee Kan Koh, Alexei Lagutchev, Nak-Hyun Seong, and Dana D. Dlott. Ultrafast dynamics of heat flow across molecules. *Chemical Physics*, 350(1-3):31–44, June 2008.

[175] Zhaohui Wang, Jeffrey A. Carter, Alexei Lagutchev, Yee Kan Koh, Nak-Hyun Seong, David G. Cahill, and Dana D. Dlott. Ultrafast flash thermal conductance of molecular chains. *Science*, 317(5839):787–790, August 2007.

[176] I. D. Welsh and Kansas State University Manhattan Kansas 66502 I. Department of Chemistry, Willard Hall. Photoemission and electronic structure of FeOOH: distinguishing between oxide and oxyhydroxide. *Physical Review B*, 40(9):6386.

[177] Andy Wijaya, Katherine A. Brown, Joshua D. Alper, and Kimberly Hamad-Schifferli. Magnetic field heating study of Fe-doped Au nanoparticles. *Journal of Magnetism and Magnetic Materials*, 309(1):15, 2007.

[178] Andy Wijaya and Kimberly Hamad-Schifferli. Ligand customization and DNA functionalization of gold nanorods via round-trip phase transfer ligand exchange. *Langmuir*, 24(18):9966–9969, 2008.

[179] Andy Wijaya, Stefan B. Schaffer, Ivan G. Pallares, and Kimberly Hamad-Schifferli. Selective release of multiple DNA oligonucleotides from gold nanorods. *ACS Nano*, 3(1):80–86, 2009.

[180] Itamar Willner, Bernhard Basnar, and Bilha Willner. Nanoparticle-enzyme hybrid systems for nanobiotechnology. *The FEBS Journal*, 274(2):302–309, 2007.

[181] Orla M. Wilson, Xiaoyuan Hu, David G. Cahill, and Paul V. Braun. Colloidal metal particles as probes of nanoscale thermal transport in fluids. *Physical Review B*, 66(22):224301, 2002.

[182] Ian Y. Wong, Matthew J. Footer, and Nicholas A. Melosh. Dynamic control of biomolecular activity using electrical interfaces. *Soft Matter*, 3(3):267–274, 2007.

[183] K. K. W. Wong, T. Douglas, S. Gider, D. D. Awschalom, and S. Mann. Biomimetic synthesis and characterization of magnetic proteins (magnetoferritin). *Chem. Mater.*, 10(1):279–285, 1998.

[184] Satoshi Yamaguchi, Shinji Matsumoto, Koji Ishizuka, Yuko Iko, Kazuhito Tabata, Hideyuki Arata, Hiroyuki Fujita, Hiroyuki Noji, and Itaru Hamachi. Thermally responsive supramolecular nanomeshes for on/off switching of the rotary motion of F_1-ATPase at the single-molecule level. *Chemistry - A European Journal*, 14(6):1891–1896, 2008.

[185] Jian Yang, Jen-Chia Wu, Yi-Chou Wu, Juen-Kai Wang, and Chia-Chun Chen. Organic solvent dependence of plasma resonance of gold nanorods: A simple relationship. *Chemical Physics Letters*, 416(4-6):215–219, 2005.

[186] Hua Zhang, Douglas Yee, and Chun Wang. Quantum dots for cancer diagnosis and therapy: biological and clinical perspectives. *Nanomedicine (London, England)*, 3(1):83–91, February 2008.

[187] Giovanni Zocchi. Controlling proteins through molecular springs. *Annual Review of Biophysics*, 38(1):75, 2009.